RESONANCE PRODUCTION IN 16 GeV/c PROTON-PROTON COLLISIONS

by

Kulya Pongpoonsuksri

A Thesis Presented for the Degree of Doctor of Philosophy of the University of London.

Department of Physics,
Imperial College of
Science & Technology,
London, S.W.7.

March 1970.

ABSTRACT

The investigations reported in this thesis concern particular decay products of proton-proton collisions recorded by the 2 Metre Hydrogen Bubble Chamber at CERN, using an incident proton beam momentum of 16.08 GeV/c. An analysis is made of the resonance production and a search is made for higher isobars, in particular, those decaying into $P\pi^+\pi^-$.

The basic data were taken at CERN during September 1966 and then analysed at Imperial College. The yield was 27,000 useful frames with 16733 four-prong events.

Data reduction procedures are described first in Chapters 2, 3 and 4 and this is followed by a general discussion of the dynamic properties of produced particles and a brief survey of current models.

Despite a serious and, as yet, unexplained distortion in the bubble chamber, 10.75% of the four-prong events yielded significant results in a 4-constraint fit, of which 52% are dominated by Δ^{++}. Estimates are presented for the cross-section of the resonances observed in the present experiment. It is concluded that the associated high resonances are mostly decaying into $\Delta^{++}\pi^-$.

In Chapter 7 the high energy aspects of inelastic three- and four-body processes are studied, and this is followed by a review of nucleon resonance in other experiments similar to the one described. The Cambridge share of the data, reduced independently, is in general agreement with the results presented here and a general comparison is made in Chapter 8. A suggested programme of further work is outlined.

PREFACE

The author joined the High Energy Nuclear Physics Group of Imperial College in October 1965 and spent the first year attending the departmental Ph.D qualifying course. She initially assisted in the 10 GeV/c K^-p experiment then in progress and also became briefly involved with both the 1.65 GeV/c K^-D and 6 GeV/c K^-p experiments.

In September 1966 a proton-proton experiment at 16 GeV/c was commenced at CERN where the author participated in the beam tuning and film exposure.

This experiment was a collaborative effort between Imperial College, London, and the Cavendish Laboratory, Cambridge, and the CERN 2 Metre Hydrogen Bubble Chamber was used throughout.

This thesis is based on the Imperial College share of the data. The author was solely responsible for all the compilation and data processing as well as for the analysis of the $pp \longrightarrow pp\pi^+\pi^-$ data.

CONTENTS

CONTENTS (Cont'd)

CONTENTS (Cont'd)

FIGURE CAPTIONS

FIGURE CAPTIONS (Cont'd)

CHAPTER 3

CHAPTER 4

FIGURE CAPTIONS (Cont'd)

CHAPTER 5

FIGURE CAPTIONS (Cont'd)

FIGURE CAPTIONS (Cont'd)

FIGURE CAPTIONS (Cont'd)

CHAPTER 7 (Cont'd)

FIGURE CAPTIONS (Cont'd)

CHAPTER 7 (Cont'd)

FIGURE CAPTIONS (Cont'd)

CHAPTER 7 (Cont'd)

CHAPTER 8

LIST OF TABLES

CHAPTER 1

INSTRUMENTATION OF THE EXPERIMENT

1.1 Introduction

The following instruments are required for a modern bubble chamber experiment:-

(i) An accelerator[1-4] associated with assemblies for magnetic and electrostatic field generation with remote control of collimators, to produce a flux of required particles, or a particle beam at the desired momentum, with a reasonably good purity.

(ii) A large and high magnetic field bubble chamber[5-8; 49] with the appropriate illumination system[9-11] where photographs of particle interactions are recorded.

(iii) Magnifying scanning tables are needed in examining the films which are investigated visually for interesting interactions or "events". A rough measurement of particle tracks recorded on the film can be attached at this stage, should this be considered necessary.

(iv) The other important mechanical aids are measuring machines; these are essentially projectors for digitising photographic track points for events of interest. The coordinates of each measured point can be punched out on command, as well as salient book-keeping information in a suitable form for further processing.

All operations - photography, processing, scanning and measurement - are organized to accommodate a high volume of data in order to keep up with the physicists' demand for good statistical significance. This general problem leads ultimately to the demand for a reasonably large Digital Electronic Computer.

The rest of this chapter describes the consequences of some salient features of the instruments used in the present experiment.

1.2 The Beam

In September 1966 for the first time a 16 GeV* proton beam became available at the CERN Proton Synchrotron (CPS). The CERN 2 Metre Hydrogen Bubble Chamber (2-M HBC) was exposed to this beam and set-up for 100,000 pictures. However, owing to a chamber fault which developed in the refrigeration and pressure control, a total of only 57,000 useful photographs was obtained. The first half of these films exhibited on average about 10 proton tracks per picture while the second half averaged about 16 per picture.

A general purpose beam known as the "U3" beam line[(18)] (developed originally from the "O2" beam[(12-17)]) incorporated both Electrostatic and Radiofrequency separators[(17-19)] and

* The convention $\hbar=c=1$ will be used throughout the following text

was constructed in the East Experimental Area of CPS. It was designed to provide the CERN 2-M HBC with reasonably pure beams of kaons, pions, protons and antiprotons upto a momentum of about 20 GeV.

A simpler approach to proton production is based on the assumption that there is no contamination of muons for stable positive particle beams(13). The actual beams used for this experiment were operated as unseparated particle beams, taking protons directly from CPS by means of some of the bending magnets operating at maximum field(15) to provide sufficient flux. When the momentum of 16 GeV was reached in CPS, the beam was deflected by the Rapid Beam Deflector onto an internal target (target 6). The elastically scattered secondary protons were produced in a cone shape at essentially zero production angle. These protons continued to circle in the CPS on deflected orbits, so that part of the reflection cone passed through a Fast Ejection Septum located in the ring. The current in the Septum could be adjusted to control the appropriate proton flux down the beam line as close as necessary to the 16 GeV momentum value with a distribution determined by the magnetic field provided in the CPS. The beams were kept to within about 5 cms of the beam axis to minimise aberrations arising from non-paraxial optics. The independent, adjustable, remotely controlled, collimator jaws were used throughout and provided easy and more accurate tuning of the beam. The complete lay-out of the beam, approximately 180 metres in length, is shown in fig. 1.1. The proton beam may be conveniently regarded as being made up of two main parts. A phase space acceptanc and momentum bite which serves to regulate the flux in the first part. In the last section the phase space and momentum bite are approximately redefined until the beam is approximatel shaped. Beams of reasonable purity are expected before enterin into the bubble chamber.

Proper shielding (BP) is provided for the beam, from the magnetic effect of the CPS magnet unit, as it leaves the accelerator and enters the series of 9 collimators, 15 CERN standard quadruple magnets, 8 bending magnets and 2 radio-frequency separator cavities. Features of the proton beam will be described without consideration of the separators. In order to reduce the scattered particle background, the independent vertical and horizontal collimators were used everywhere in the beam line to separate the images into two planes. After passing through the lens Q_4, an arrangement of mangets M_1, M_2, M_3 and M_4 forms a conjugate focus at Q_6. This facility permits the transmission of a large momentum bite if so desired. The bending magnets M_5 and M_6 together with the quadruple lenses Q_{14}, Q_{15} are incorporated in the final momentum analysis in the horizontal plane. To avoid overlapping of too many beams, the lenses Q_{14} and Q_{15} are used to produce a divergent beam in the vertical plane. Finally, the last two bending magnets M_7 and M_8 were used to steer the beam into the bubble chamber.

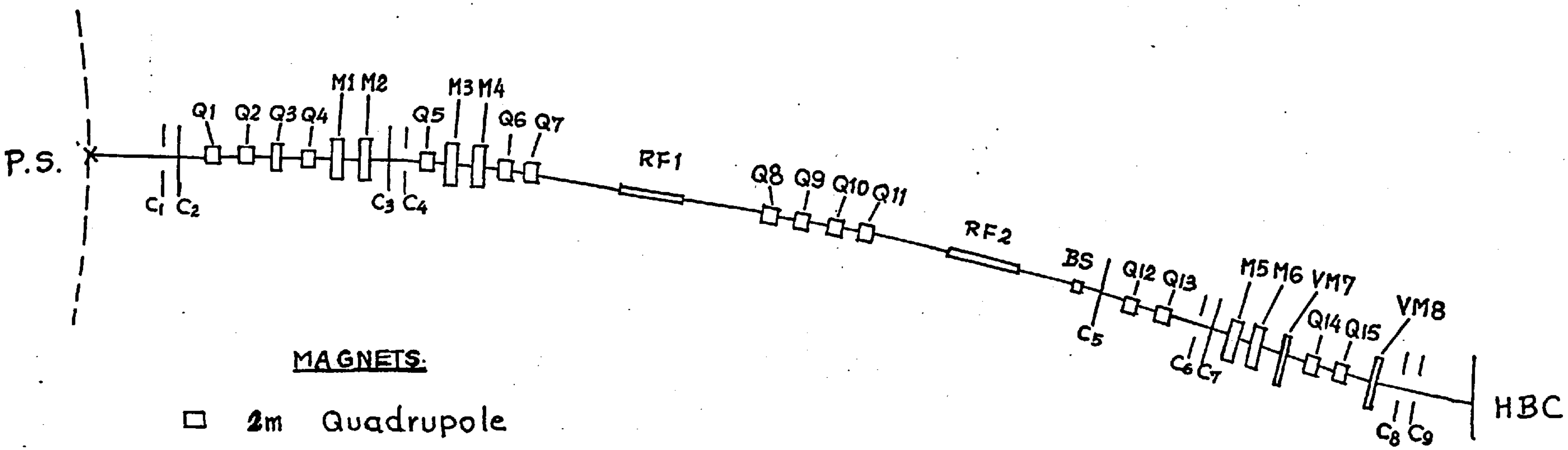

MAGNETS:

2m Quadrupole

1m Quadrupole

1m Special vertical magnet

2m Bending magnet

COLLIMATORS

Horizontal

Vertical

P.S. = Proton Synchroton

BS = Beam stopper

HBC = Hydrogen Bubble Chamber

Fig. 1·1

1.3 The Bubble Chamber

The general details of this hydrogen bubble chamber have been described elsewhere(5,6,21) and only a brief description of the CERN 2-M HBC used for this experiment is given here.

Essentially, the bubble chamber is a vessel containing a transparent superheated liquid (hydrogen). The dimensions and some important parameters(22,23) are listed in table 1.1.

The actual liquid hydrogen tank is made of two vertical borosilicate BK7 crown glass windows(10,28). The top and bottom of the chamber are metal, thus permitting good temperature control. Fiducial crosses are engraved on the inner side of the windows; these are used as survey marks and are important references needed later in the reconstruction stage (see section 2.4). Radiation is reduced by a hydrogen and nitrogen shield surrounding the chamber, and the whole assembly is suspended in a large stainless steel vacuum tank. The temperature of the chamber is controlled by refrigeration loops at a working temperature of 26°K. The slightly different values of refractive index(26) for glass/vacuum and glass/liquid window interfaces are also listed in table 1.1. The vacuum tank is enclosed in an electromagnet giving an average field of 17.343K-gauss(24,25).

The chamber is expanded upwards. The purpose of the expansion system is to make the bubble chamber sensitive to charged particles. This is achieved by bringing the liquid in the chamber to a superheated state for a short time by momentarily lowering the pressure.

In a large hydrogen chamber it is preferable from the cryogenic point of view to vary the pressure by means of a piston rather than by gas expansion (used in the previous small British chamber). The expansion system forms an oscillating system which will be operated at its resonant frequency. This frequency can be adjusted within certain limits to suit the experimental requirements by varying the spring rate of the gas cushion[49].

The liquid hydrogen in the visible volume is separated from the colder liquid hydrogen over the expansion piston by the flexible suspended separation disc. This disc improves the optical conditions in the visible volume, and maintains a more even distribution of pressure in it during expansion.

In order to ensure that the flashes for track illumination are synchronized with the passage of the particles through the chamber, a signal taken from the P.S., initiated the expansion of the chamber for each cycle of arrival of the beam pulse. The recycle time was typically about 1-2 seconds.

Without doubt the amount of useful data increases with picture quality. Therefore the optical design plays an important part from the experimentalist's point of view. This is especially true for a large chamber. The illumination[10,11] of the CERN 2-M HBC will be described briefly. Figure 1.2a shows a schematic view of the bubble chamber optics. The illumination is of a straight-through dark field type. The chamber illuminated by three independent demountable flash-tubes with the help of a condensing lens system[29]. The three flash-tubes illuminate a cone-shaped useful volume of about 500 litres. Some general parameters for a conventional bubble chamber are given in table 1.1. Some newer points will be discussed briefly, in particular the advantages of the light sources and the two big plano-convex condensers. The light source of figure 1.2b was designed by F.Frungel, H.Kohler and H.R.Reinhard[10] and developed and built at CERN for the 2-M HBC. It was used for this experiment and provided a good combination of high energy (upto 2500 J) and short flash duration. The radiating plasma approximated to a point source and the lamp had a long lifetime (defined as the time for the useful light in the second focus to be reduced to 60% of its initial value). High intensity and shorter flash delay also allow a reduction in image distortions arising from turbulence in the liquid. With the distribution of point sources described, images are confined to a circular region of 15 cms diameter, thus providing a free choice of camera position. The ideal situation of four cameras was used, placed on a circle of 60 cms diameter. The resulting images produce a scattering angle of 7° which leads to a good compromise between the conflicting requirement of adequate intensity and sufficient stereo angle. Operation of the three synchronous lamps is controlled by a light monitor, yielding a uniform illumination for the whole chamber. In addition to the advantages described, the flash tubes are less costly and more durable than those used in earlier system.

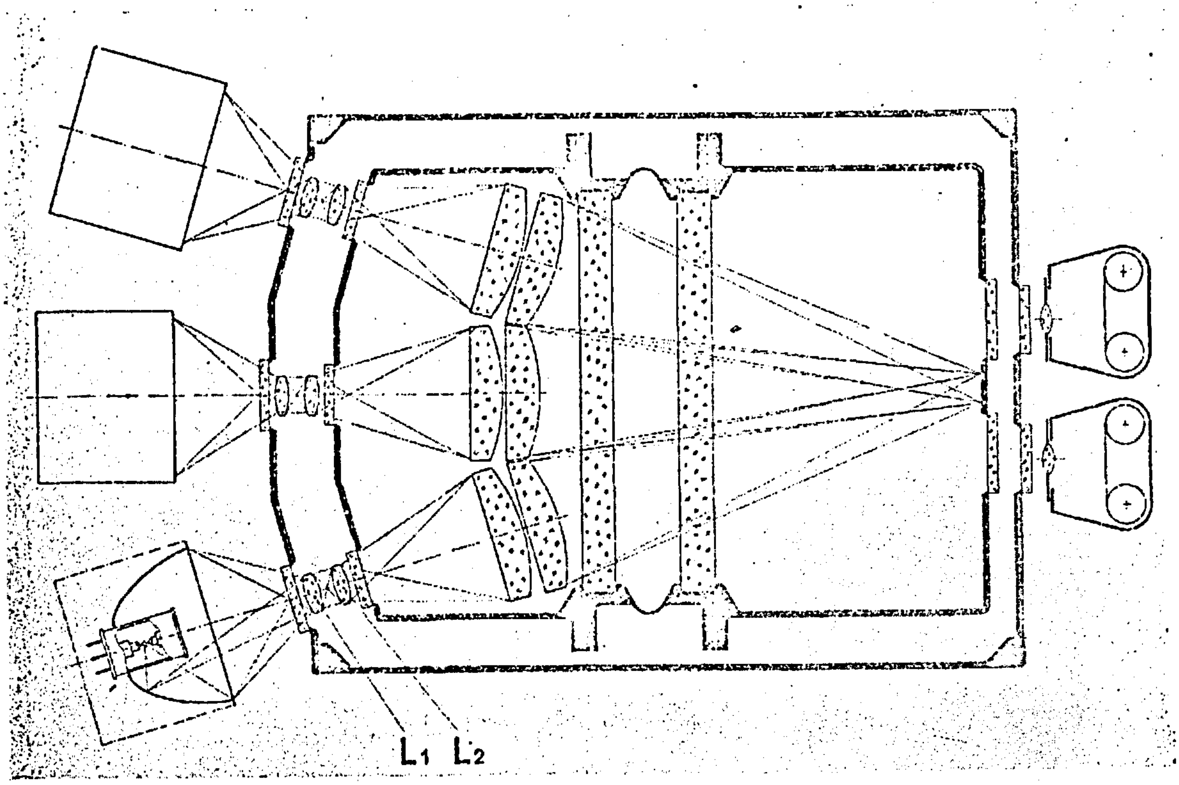

Fig. 1.2a

SCHEMATIC VIEW OF THE OPTICAL SYSTEM OF THE CERN 2-M HBC

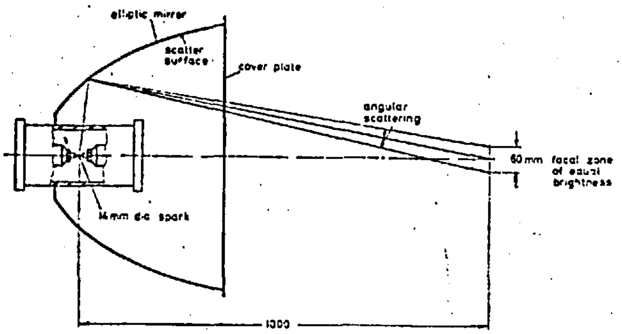

Fig. 1.2b

VIEW OF THE FLASH TUBE AND ELLIPTIC MIRROR

To ensure that the final image of the light source yields a perfect dark field illumination for the best film contrast, two plano-convex lenses of approximately equal power are used. They have one external aspheric surface for, according to experience and optical computations, the lateral aberration for non-axial points due to astigmatism and coma may be corrected by adjusting asphering constants. From figure 1.2 L1 and L2 are the first and second collector lenses respectively for the image. Then the main condenser subsequently brings the image to each camera aperture with the minimum of stray light due to geometric optical aberrations. The parasitic images due to double reflection are suppressed by anti-reflection coatings. In order to help beam tuning, there are two direct viewing windows. Polaroid photographs were often taken and closed circuit television monitors the chamber.

1.4 Scanning and Measuring Machine

Essentially, the scanning table consists of high quality multiple projectors. The film transport mechanism, table and optical illumination system produce the necessary degree of film magnification at a convenient position for visual investigation. In practice, the facilities allow three stereoscopic views of the same picture. These are mounted side by side for comparison purposes as well as a referance in the case of difficult events. The film can be moved at a controlled speed either on one view at a time or on all three views simultaneously

A partial vacuum causes the film to be pressed down flat to the guide and released when film movement is required.

British National Measuring machines[27] were used to measure the films for the present experiment. These were built and developed under the general direction of Professor C.C. Butler, FRS, at Imperial College. The measuring machine consists basically of a moving stage bearing Moire Fringe digitizers. A projection system displays a complete magnified stationary image of the frame onto a screen at a convenient position for the measurers to find events. Part of the image may be magnified on a separate screen to facilitate accurate measurement to within a limit of 5 microns on the film. The stage moves parallel to the length of the film (the X-ccordinate) the position of which is recorded. The carriage bearing the projection lens moves transversely and measures the Y-coordinate. A number of evenly spaced points are measured on each track for each of three sterioscopic views in turn. These numbers and the control character information of an event are punched out on five-hole paper tape in binary coded octal format. The semi-automatic control of measuring fixed fiducial marks was attached later[30] under the supervision of Dr S.J. Goldsack.

Table 1.1

GENERAL PARAMETERS OF CERN 2-M HBC

1) Optical system: 3 light sources, 3 condenser systems, 2 big windows and 4 cameras.

2) Chamber:

illumination region in the front plane	520 X 1620	mm
illumination region in the black plane	600 X 1920	mm
depth	500	mm
useful volume	465 litres = 82% total volume.	

3) Windows: (BK7)

dimensions	2170 X 770 X 170 mm
weight	660 Kg.

4) Refractive index:

Glass/vacuum	1.5168
Glass/liquid	1.5267

5) Beam properties: circulating proton beam in P.S.

Intensity	5×10^{11}
Energy	28 GeV.

6) Film: 50 mm wide, unperforated, medium speed.

The photographs were taken approximately 1.5 msec after the arrival of the beam pulse, in order to allow the bubble to grow to the desired size (2 bubbles per mm).

CHAPTER 2

DATA PROCESSING

2.1 Introduction

Efficient processing of the data from modern bubble chamber experiments requires large scale facilities involving a multi-step handling process (e.g. scanning, measuring, etc). It is also necessary to set up an efficient book-keeping system in order to accumulate all the information as it progresses and thus minimise the loss of events. Figure 2.1 is a rough flow diagram of the data processing system used for the present experiment.

Imperial College received approximately 27,000 frames of film from CERN made up of alternative rolls. Each roll consisted of about 1500 pictures in four stereoscopic views (the four projected camera positions are shown in figure 2.3). For the convenience of the existing scanning and measuring machines, each roll was sub-divided into two-half rolls of approximately 750 pictures each. The quality of the film had initially been investigated visually during the run at CERN by taking "test strips"[31]. Before transferring film into the measuring stages it was selectively scanned and predigitised once for events of interest (4-prong events with no neutral and strange particles). This was done at Imperial College. The proper scanning[32] was performed later. A sequence of reconstruction procedures and full kinematic fitting was carried out by a chain of CERN standard

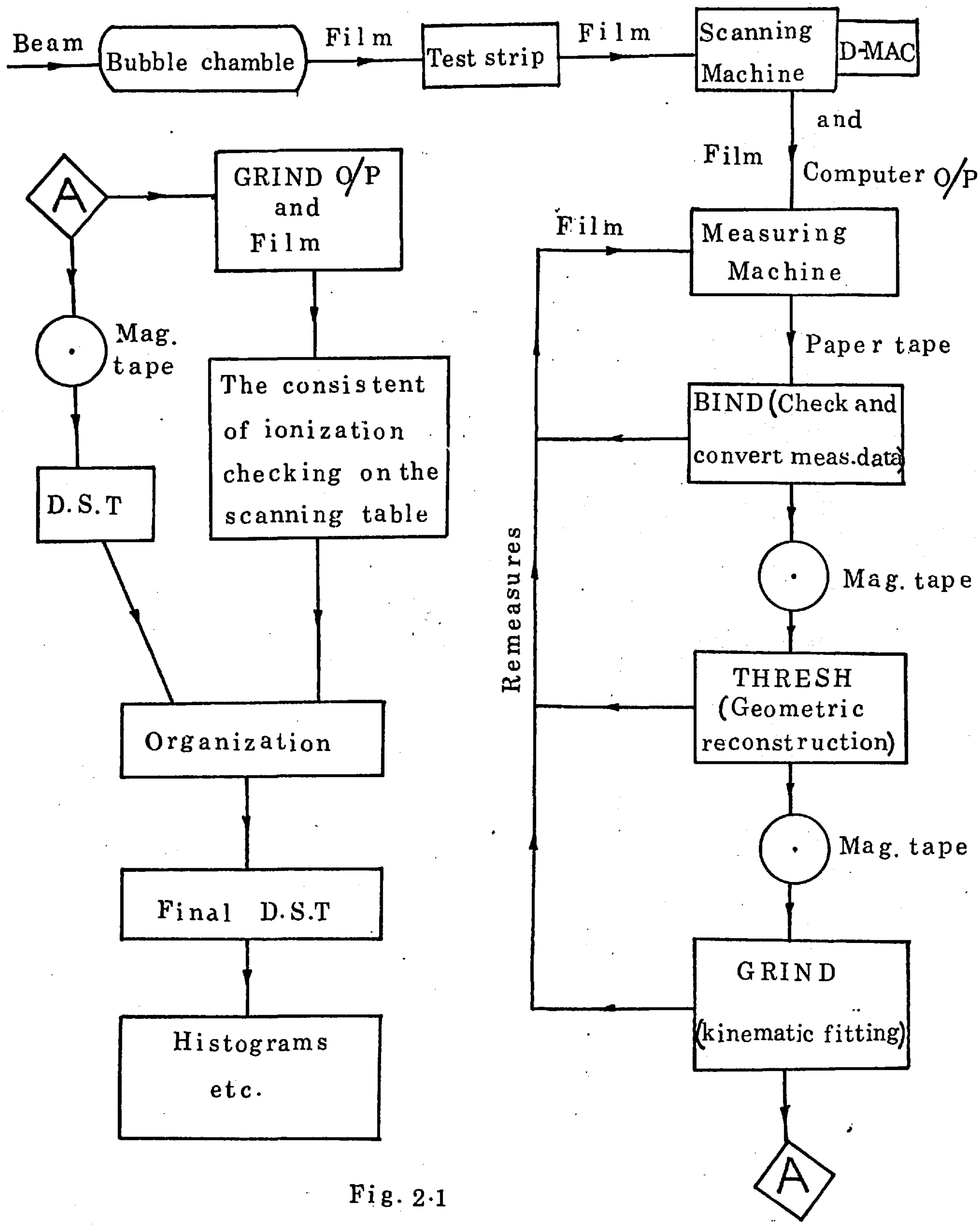

Fig. 2·1

Flow Chart of the Data Processing System programmes THRESH-GRIND, adapted for use on IBM-7090 and PDP6 computers. The post kinematical analysis was performed with the aid of the NIRNS Programmes[33]. Unfortunately these programmes failed to identify separately the two protons in the final state. Thus, for the first time in the H.E.N.P. Group at Imperial College an experiment dependent Data Summary Tape (D.S.T.) and statistics programme was commenced and developed called "POOR MAN'S SUMX"[34].

2.2 Scanning and Fiducial Volume

2.2.1 Quality of Film - An initial idea about frame quality was achieved from test strips and a summary is given in Table 2.1. In effect, the "test strip" was one of the additional methods of improving the quality of film in the system described in Chapter 1. During the experiment as soon as one roll of photographic film was finished, about ten frames in each view were immediately developed and scanned. They were then examined under the microscope for a bubble density analysis. Figure 2.2a shows the distribution of the average number of bubbles per cm, while the average number of beam tracks per frame is shown in figure 2.2b. The number of each type of interaction was recorded, based on the assumption that there was no limitation on the fiducial volume required. This gave a reasonably good prediction for the number of tracks and the number of events per picture, especially for 4-prong events. In this case the test-strip gave a value of 42% for 4-prong events out of the total number of interactions

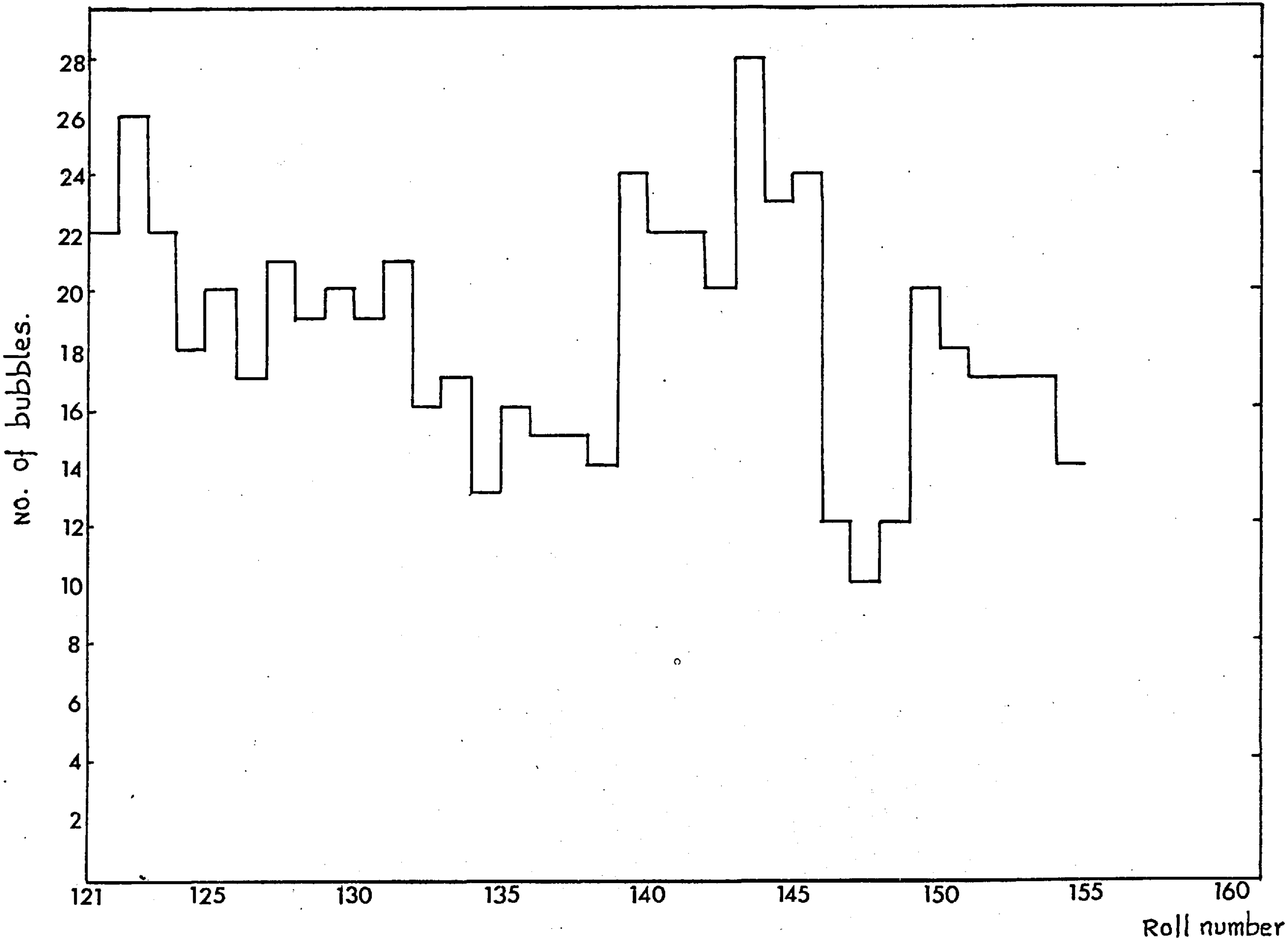

Fig. 2·2a Distribution of average number of bubbles per cm. from test strips

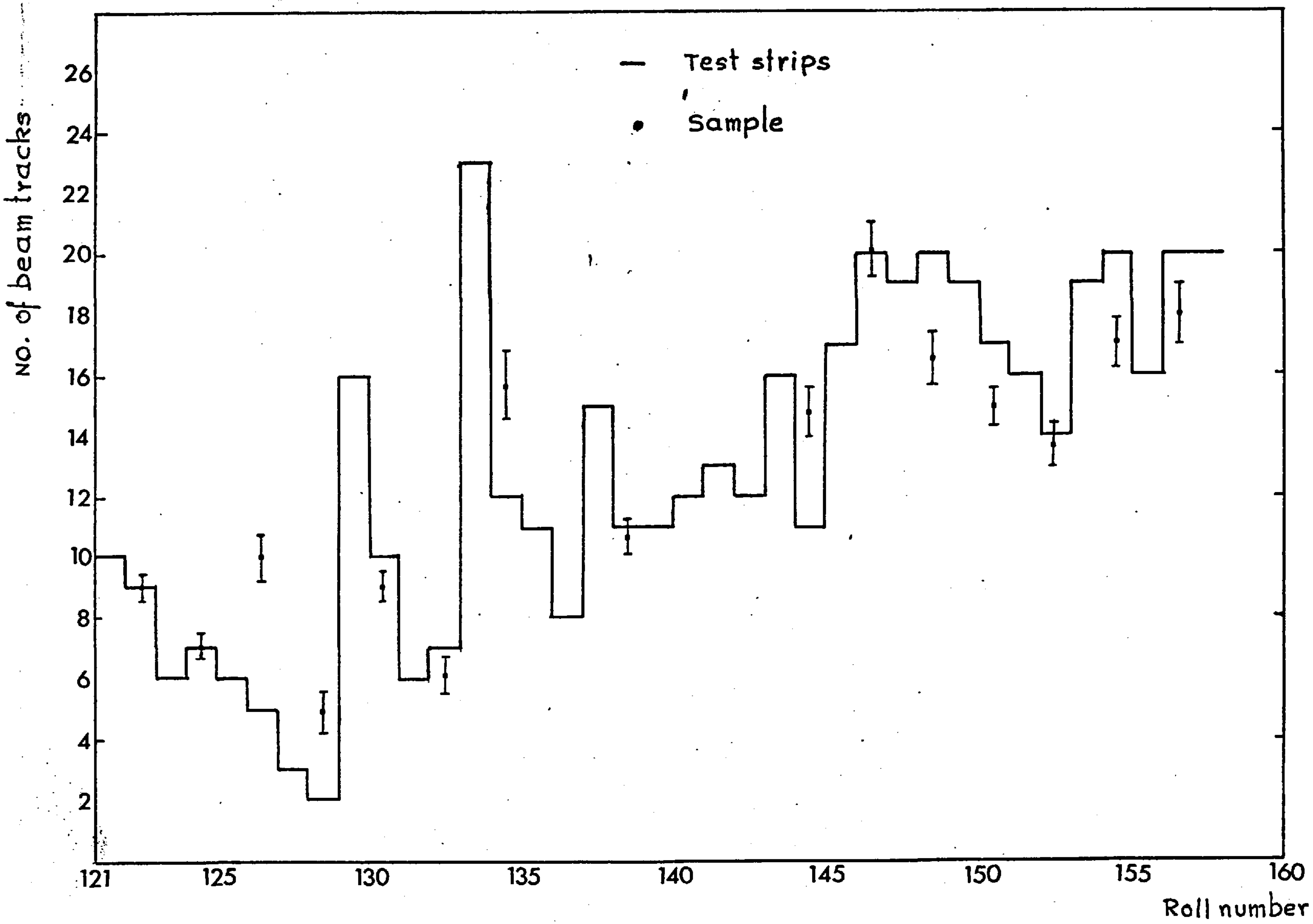

Fig. 2·2b Distribution of average beam tracks per frame per roll compared with a subsequent result of 40.5% from a random sample of 10 half rolls of film scanned once for every type of collision as listed in table 2.1 within the specified region (see figure 2.3b).

A similar comparison of the average number of beam tracks per frame is illustrated in figure 2.2b. Since the present experiment was concerned only with 3 and 4-prong events no further consideration was paid to those of higher multiplicity.

Unfortunately a compensating magnet which controlled the beam azimuthal angle at the entrance of the chamber was accidentally switched on after three rolls of film had been taken. This effect can be seen in fig.2.3a as a difference in beam azimuth angle of about 20 m-radians. It incidentally caused the value of the field at the chamber centre to increase by 0.2%. However this change was neglected as it was within the error on the value of the magnetic field[25]. Collimator C3 was adjusted frequently to compensate for a fault which had developed in the injection system causing the number of beam tracks per frame to vary considerably from roll to roll Some scattered non-beam protons (discussed later in Chapter 3) entered the chamber. The picture quality deteriorated during the end of the run as a consequence of poor chamber operation and, furthermore, during this period of time[22,23] the chamber had undergone distortion.

After reconstruction (described in section 2.4.1) of the measured events, several hundred beam tracks were carefully studied in order to determine essential parameters

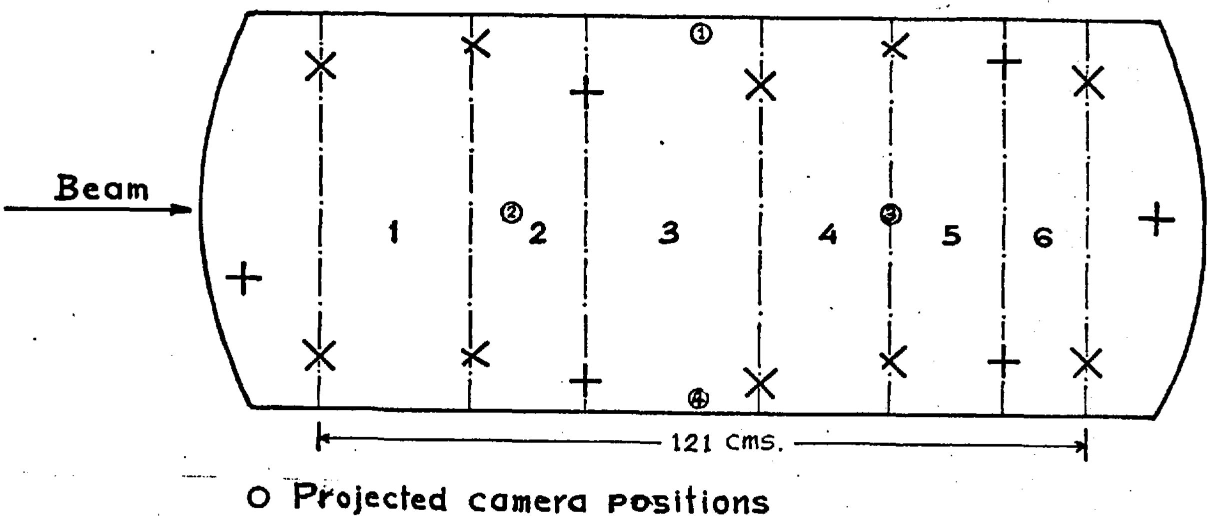

Fig. 2·3b

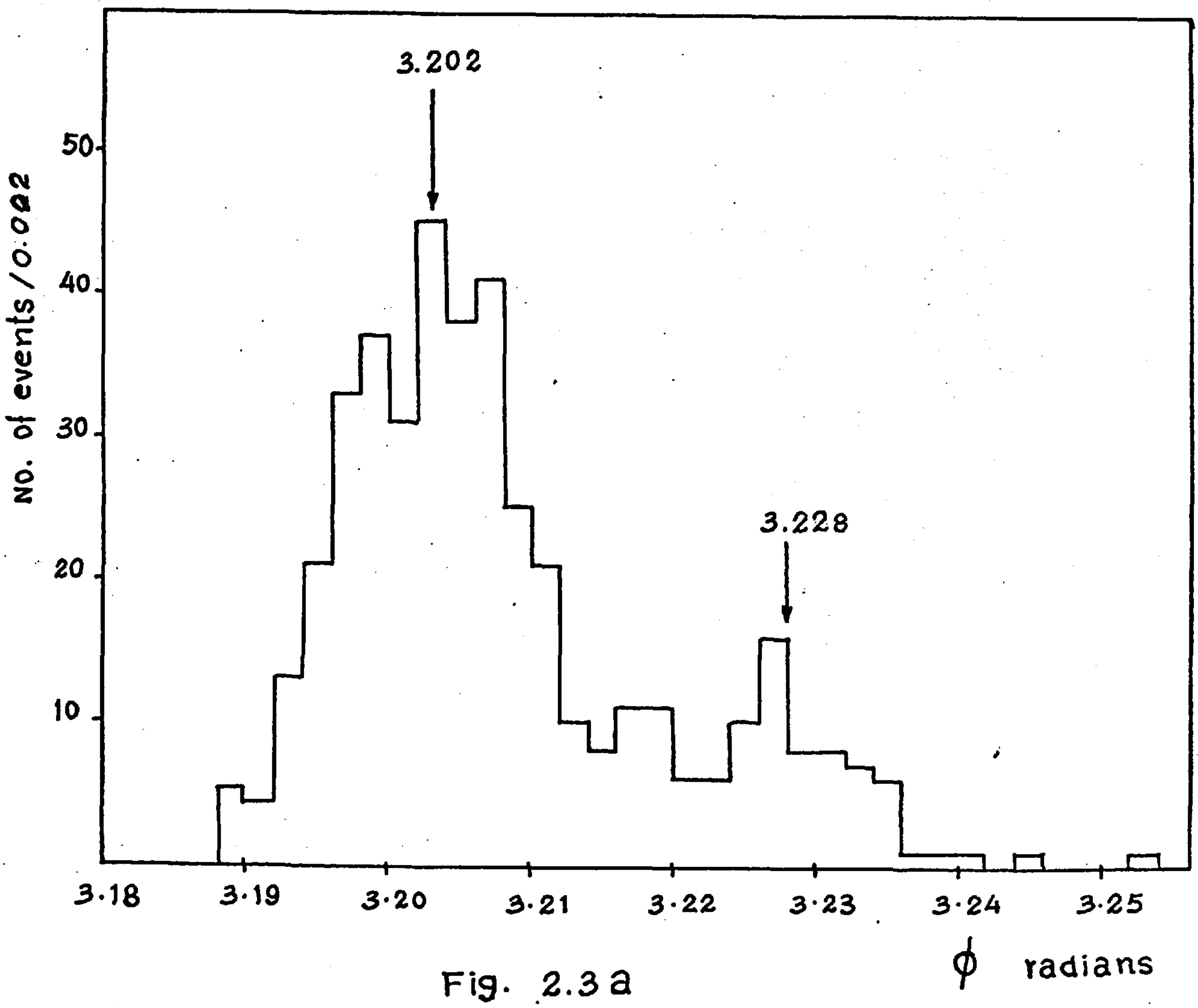

Fig. 2.3a

needed for the full kinematic fitting procedures (described in section 2.4.2). Figures 2.4a to 2.4c show the general distributions of curvature ($1/\rho$), dip angle (λ) and azimuthal angle (ϕ) for the beam tracks, where λ and ϕ are the two parameters defining a track direction in space.

λ is defined as the angle between the X - Y plane and the track tangent reckoned positive towards the z-axis.

ϕ is defined as the angle between the X-axis and the projection of the track tangent in the X - Y plane reckoned positive anti-clockwise.

As the beams at high energy are less curved and well confined within a spread of a few cms, dip angles are small and of the order of 4 - 5 m-radians. The azimuthal angle is close to π radians. By knowing the radius of curvature and the corresponding central value of magnetic field (H) perpendicular to the X - Y plane, the momentum of the beam particles can be calculated from the realtionship:-

$$P \cos\lambda = 0.3 \, H \rho$$

P = momentum (MeV)
ρ = radius (cm)
H = magnetic field (K gauss)

P = 0.3 H is a good approximation for small dip angles. The 16.08 GeV beam momentum value results in an average radius of curvature of about 31.05 metres calculated from the distribution of figure 2.4a. The corresponding measurement error distributions for these three quantities ($1/\rho, \lambda, \phi'$) are shown in figures 2.5a to 2.5c respectively whilst the distributions of X, Y and Z position of the events are illustrated in figure 2.6 a,b,c.

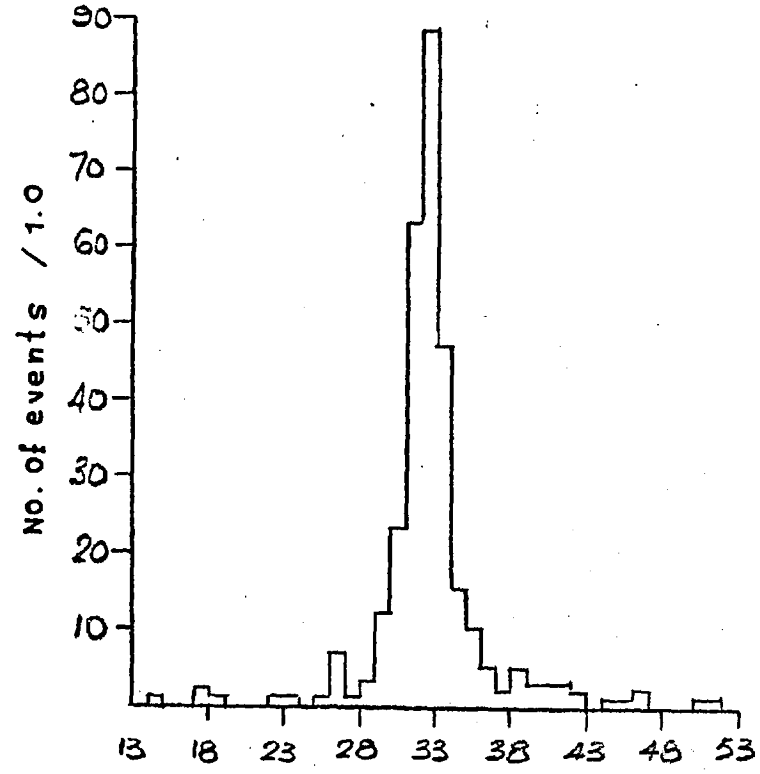

Fig 2.4a $1/\rho \times 10^{-5}$ (MICRONS)

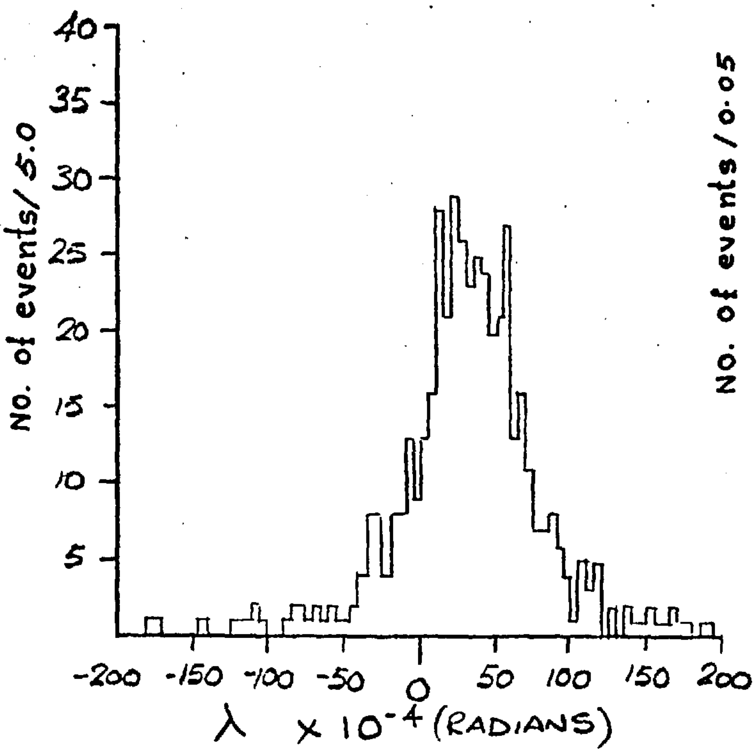

Fig. 2.4b

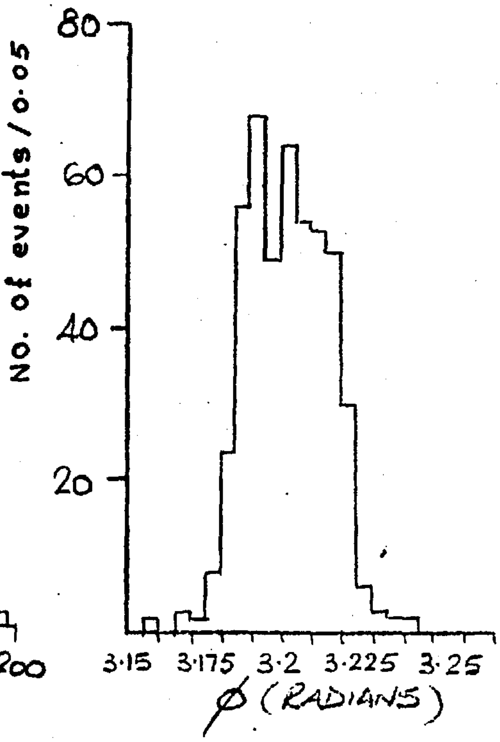

Fig. 2.4c

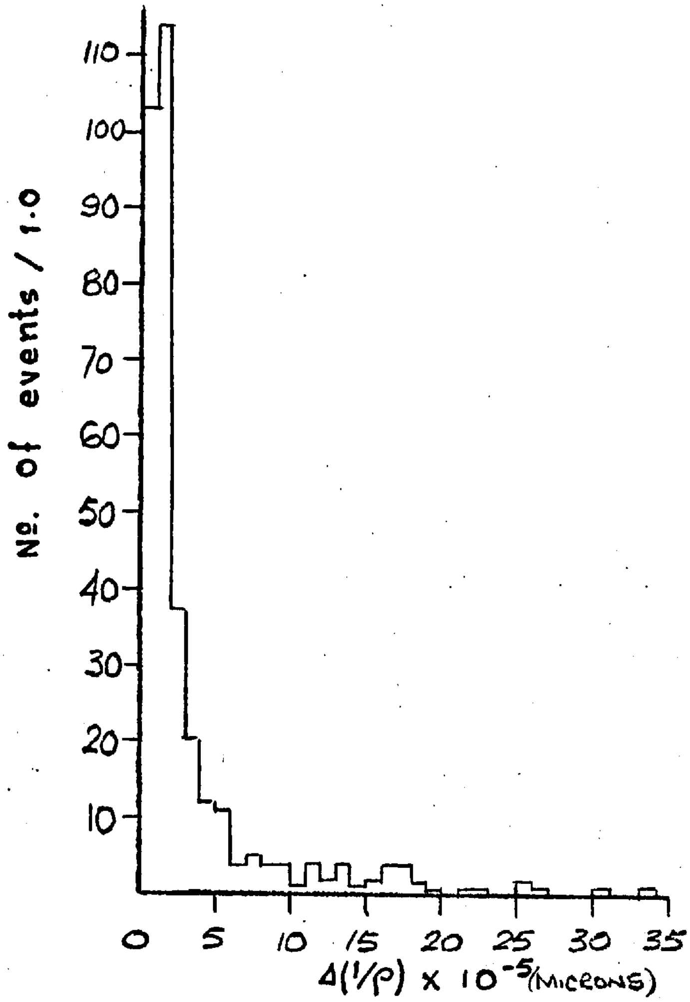

Fig. 2.5a

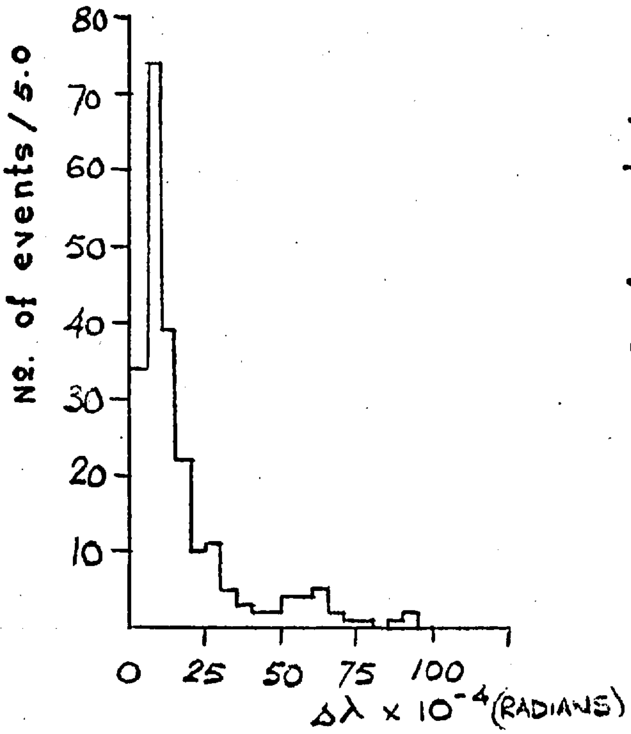

Fig. 2.5b

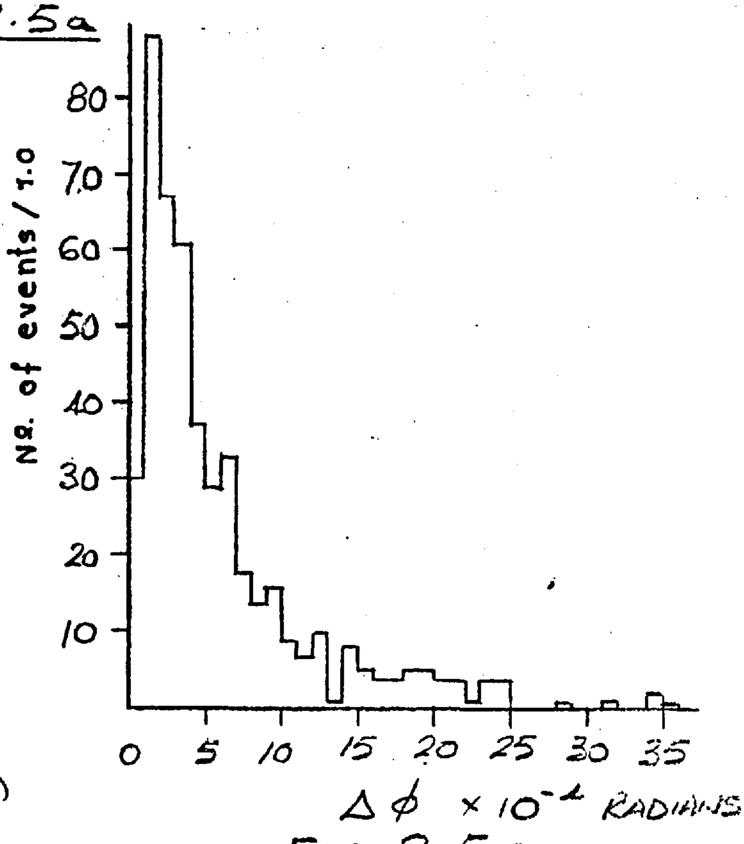

Fig. 2.5c.

Fig 2.6

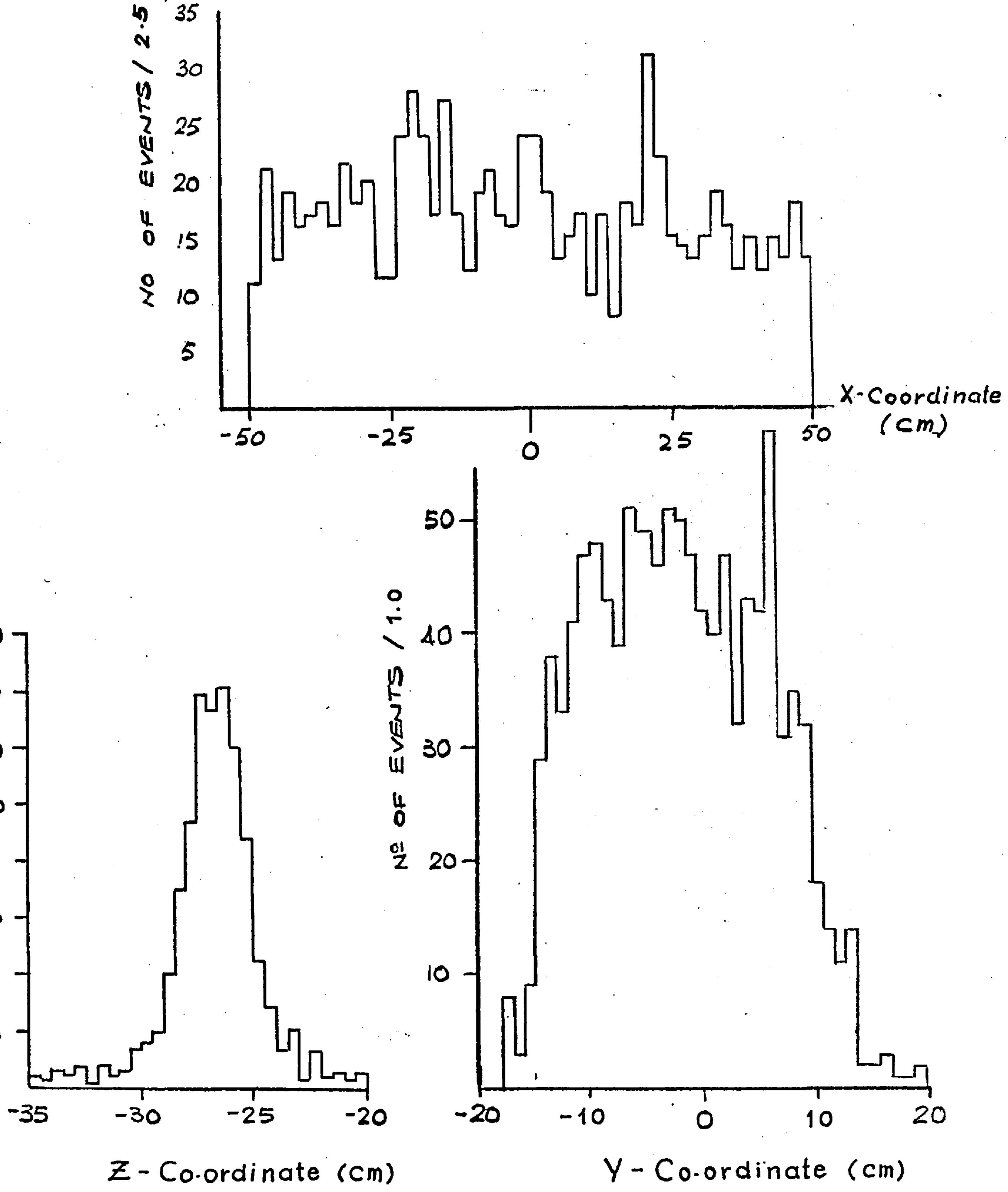

No OF EVENTS / 2.5
35
30
25
20
15
10
5
-50
-25
0
25
50
X-Coordinate (cm)
160
140
120
100
80
60
40
20
-35
-30
-25
-20
Z - Co-ordinate (cm)
No OF EVENTS / 1.0
50
40
30
20
10
-20
-10
0
10
20
Y - Co-ordinate (cm)

2.2.2 Scanning Criteria - The main objective was to scan for 4-prong events only, with no strange particles; nevertheless 3-prong events were also included in case one of the secondary particles had insufficient energy to produce a visible track. There are two cases to consider: first, one of the protons in the final state being produced close to the line of sight of a camera with small energy, alternatively a negative pion taking part in a charge-exchange interaction before leaving a visibly long track (i.e. $\pi^- p \longrightarrow \pi^0 n$).

View 1 (top) was used as the standard view for scanning because it had better optics; view 3 (exit) and view 4 (bottom) were used as references.

The number of 3-prong events was small and most of them fitted the invisible proton case (3-constraint fit). 3 or 4-prong events were recorded if they satisfied certain scanning criteria as described below:-

(1) An apex of an event had to be at least 12 cms from the entrance on view 1, or, on the other hand, any apex of an event was required to lie within the first pair of fiducial marks to be accepted, so long as the secondary tracks yielded a length of more than 10 cms for measurement.

(2) An incident beam track was accepted at the scanning table (viewed at about x10 magnification) if its displacement from the general beam direction was less than 3 mm over a 30 cm length.

(3) Events containing strange particle decays were rejected.

(4) Frames were rejected if:-

(i) they contained more than about 25 beam tracks.

(ii) a frame number or illumination flash was missing for any view.

(iii) they were too faint for all the tracks to be visible.

A predigitising machine called D-MAC provided the rough measurements for selecting the particular type of 4-prong event (described in 2.3) and was used during the first scan. By means of this facility, all the scanning information was recorded on 5-hole paper tape accompanied with a specific identification of an event in a form suitable for further calculation. Those frames that were rejected on the basis of the above criteria were also recorded on the scanning sheet to correct the determination of cross section.

The detailed first, second and check scans on a sub-sample of 10 half rolls of film were analysed independently later, then compared, frame by frame, with the digitized scan. This procedure showed that there was a 97% scanning efficiency.

2.2.3 <u>The Fiducial Volume</u> - In general the choice of dimensions of the bubble chamber is governed by the type of interaction and the nature of the particle under investigation.

A discussion of chamber design for strong interaction physics by C.M.Fisher(7) considers how the errors in momentum and angles are related to the chamber dimensions, field and spatial precision. The projected fiducial volume of view 1 of the 2-M HBC is illustrated together with the projected position of cameras, in figure 2.3b. The actual chamber dimensions of 150 x 50 cm^2, with a depth of 50 cms, is in fact extended in the length axis to be visible up to 160 cms.

The fiducial region for the events of the experiment were chosen bearing in mind that the conventional measuring machines were capable of a measurement accuracy of about 5 μ on film, and the way the CERN standard chain reconstruction and kinematic fitting programmes were written. The mass dependence, of the curvature of particle tracks, calculation was ignored in the geometrical reconstruction stage. However the chosen fiducial volume still gave acceptable results for beam or secondary tracks down to a minimum of 12 cm in length(36). This result was shown by testing the following various hypotheses for all possible permutations of particle tracks:-

$$p + p \longrightarrow p + p + \pi^+ + \pi^-$$

$$p + p \longrightarrow p + p + K^+ + K^-$$

$$p + p \longrightarrow p + p + p + \bar{p}$$

It was found that there was no significant reason to reject those events that were measured with short tracks provided they were found to be consistent with the ionization. This evidence justified the chosen fiducial region. The fiducial region was divided into smaller sections to avoid the confusion of identification of adjacent events. These sections (No's 1....6) are down-stream from the beam entry as shown in figure 2.3 and are constructed by taking lines joining each pair of fiducial marks on view 1, so approximately indicating the boundary. An arbitrary sub-division was introduced for the left and right of each section where more than one 3 or 4-prong events occurred.

The width of the fiducial region is difficult to define because of the bubble chamber optics and the difficulty in finding appropriate fiducial marks. However, with three chosen cameras, each seeing different regions of the chamber, the effective width required is where the apex of an event is just visible on two views.

2.3 D-MAC Selection and Measurements

It has been known for some time that the total proton-proton cross section remains essentially constant at high energies[37] (39.9 mb). However from recorded bubble chamber cross section data[38,40] on 4-prong events, it has been suggested that some 90% of them also produced neutral particles. Only the remaining 10% are of interest in the present experiment. Since a complete three view measurement of one 4-prong event would, on average, take about 25 minutes, it was considered time-wasting to analyse all the scanned events. Therefore it was proposed to employ a rough predigitization system, performed on the "D-MAC" scanning table, which allowed approximately 50% of the events produced with neutral particles to be distinguished and rejected before beginning measurement. This fraction was compatible with the rejection rate of the other half of the film analysed by the Template Method at Cambridge[39].

The nominal beam momentum in space was given by CERN as about 16 GeV and so the projected beam momentum on the X-Y plane for high energy particle tracks with small dip angles can be taken as 16 GeV. For the interesting events of type: $P + P \longrightarrow 1 + 2 + 3 + 4$

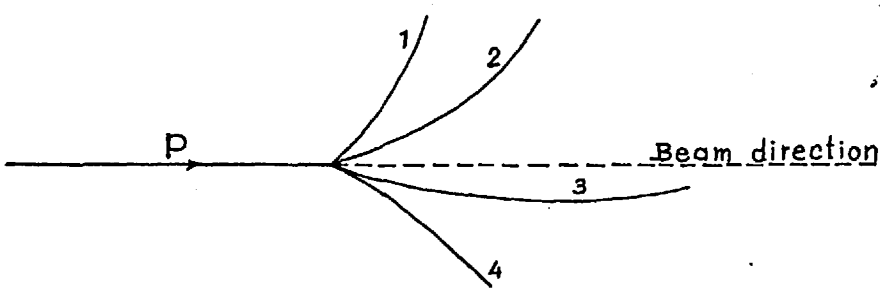

the vector sum of projected momenta (P_{sum}) for all outgoing particles of an event producing no netural particles can be defined as:-

$$P_{sum} = \sum_{i=1}^{4} P_{xy}^{(i)} \cos\beta_i = 16 \quad \text{GeV}$$

P_{xy} = the projected momentum on the X-Y plane

β_i = the angle between the tangent of i^{th} particle and the beam direction.

Since D-MAC selection was approached on the assumption that each projected track formed a segment of a circle of radius(R) in a uniform magnetic field, with no consideration of track directions, it follows that the algebraic sum of projected momenta can well be satisfied to the first approximation by the following equation:-

$$P_{sum} \approx \sum_{i=1}^{4} P_{xy}^{(i)} \geqslant 16 \quad \text{GeV}$$

Because of momentum conservation, rejected events are those that have large missing momentum which distinguishes them from the events of interest. The general features of the projected momentum sums are illustrated in figure 2.7a, hence it seems clear that the lower peak mainly represents those events produced with neutral particles. However, there is no doubt that the overlapping area contains contributions from both cases. A test was applied to five half-rolls by measuring every event (see appendix I for the D-MAC rough measurement procedure*) found in one scan, to determine an

* The writer wishes to thank Dr M.Mermikides for assistance in writing the D-MAC programme.

optimum value of the momentum sum such that events having a lower value could be rejected. Obviously, the value chosen must be a compromise between losing too many events of interest and including too many spurious ones produced with neutral particles. After fitting, the events were checked for consistency in ionization appropriate to the particle. Thus only 1% of well fitted events arose from interactions which contributed to the area in figure 2.7a where P_{sum} was less than 10 GeV; while figure 2.7b shows the distribution of this well fitted sample in term of P_{sum}. For this reason, the optimum value was set at 10 GeV, which leads to a good balance in computer time and analysis.

It was decided that those events which passed the D-MAC selection should be measured on all three consistent views (view 1, 3 and 4) using information from the D-MAC output. On each view a fixed fiducial was measured first as the datum, followed by the measurement of the other three in a given sequence (see fig. 2.3b). The rest of the event was then measured with identification labels for apex, beam, etc., in correct sequence for recognition by the next computer programme (BIND). This whole procedure was then repeated for all three views.

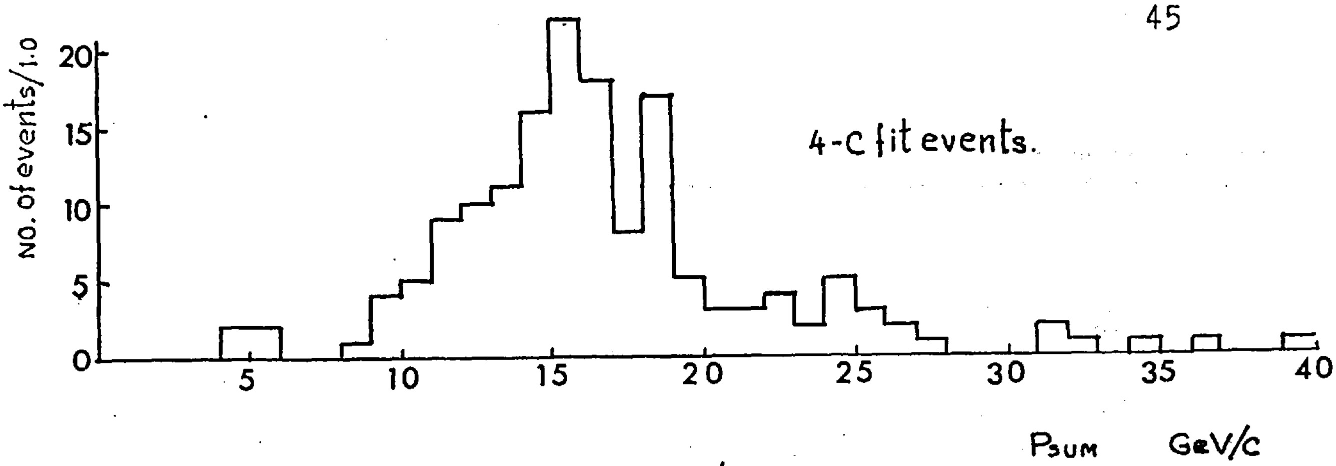

Fig. 2·7 b

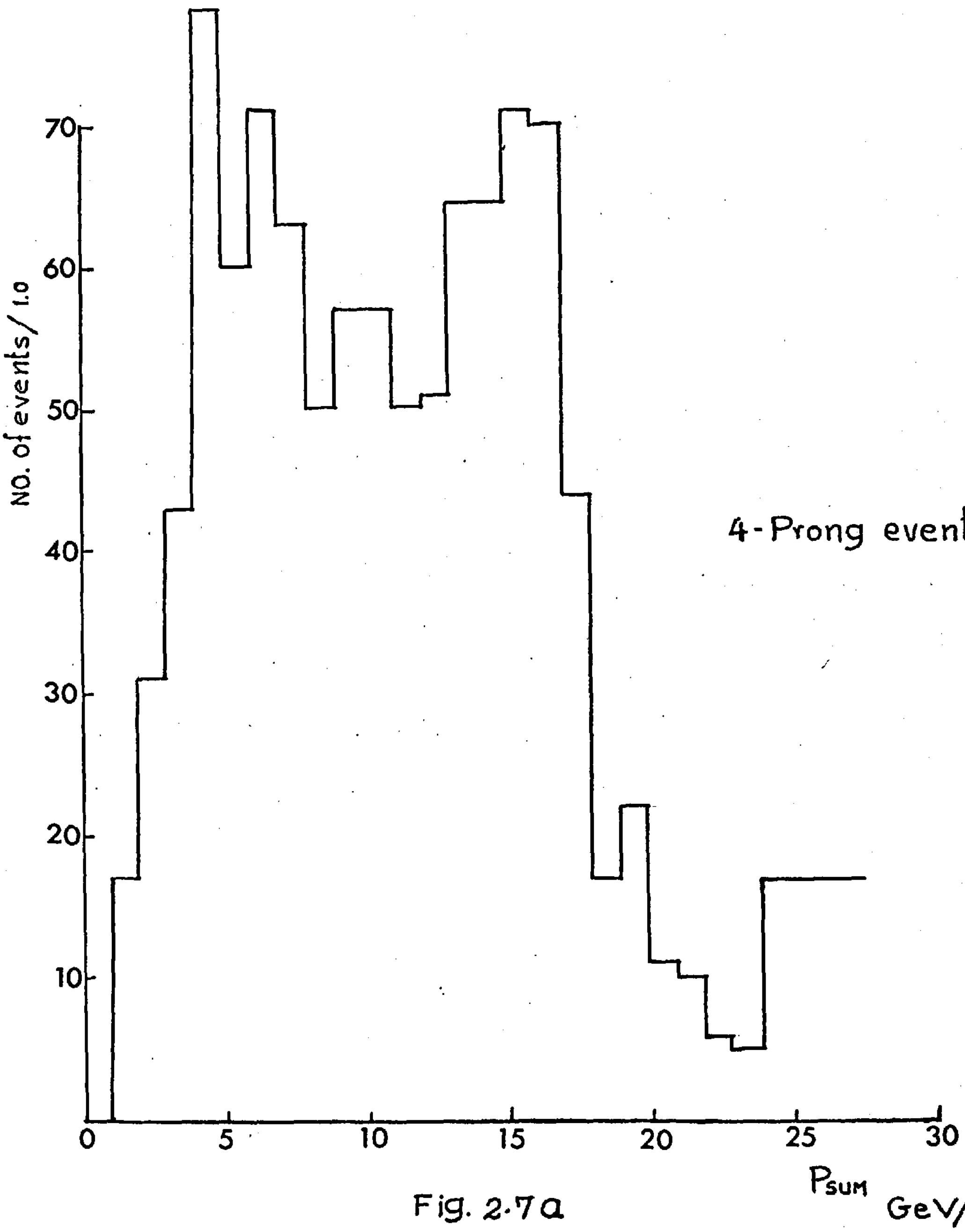

Fig. 2·7 a

2.4 The Reconstruction and Kinematic Computation[43,44]

The measurement of each bubble chamber track was taken serially for each stereoscopic view. It was not usually possible to establish directly the correspondence of these views with a single point in space. Naturally, the next essential aspect for further analysis and study would be the transformation from the local system of the measuring apparatus into the absolute system of the chamber where the interaction really occurred. The geometrical information necessary for the reconstruction is referred to as THRESH TITLE[43]. Examples are the fiducial marks, the cameras' positions, the refractive indices and the error tolerances of measurement.

The input part[44] is mainly raw data and is read by the programme BIND which checks for completeness, sorts the data associated with the event and decodes onto magnetic tape with the right format and relevant information. The rejected events are listed and sent back to be remeasured.

2.4.1 THRESH - The general flow diagram of the geometry programme, THRESH, for each event is shown in fig.2.8. The $z = 0$ plane is defined to be the inside of the front glass with the z-axis pointing toward the cameras. The optical axes of the apparent position of the fiducial marks (X_i, Y_i) in the $z = 0$ reference plane are found by substituting the corresponding measured point (X_i, Y_i) in the linear transformation

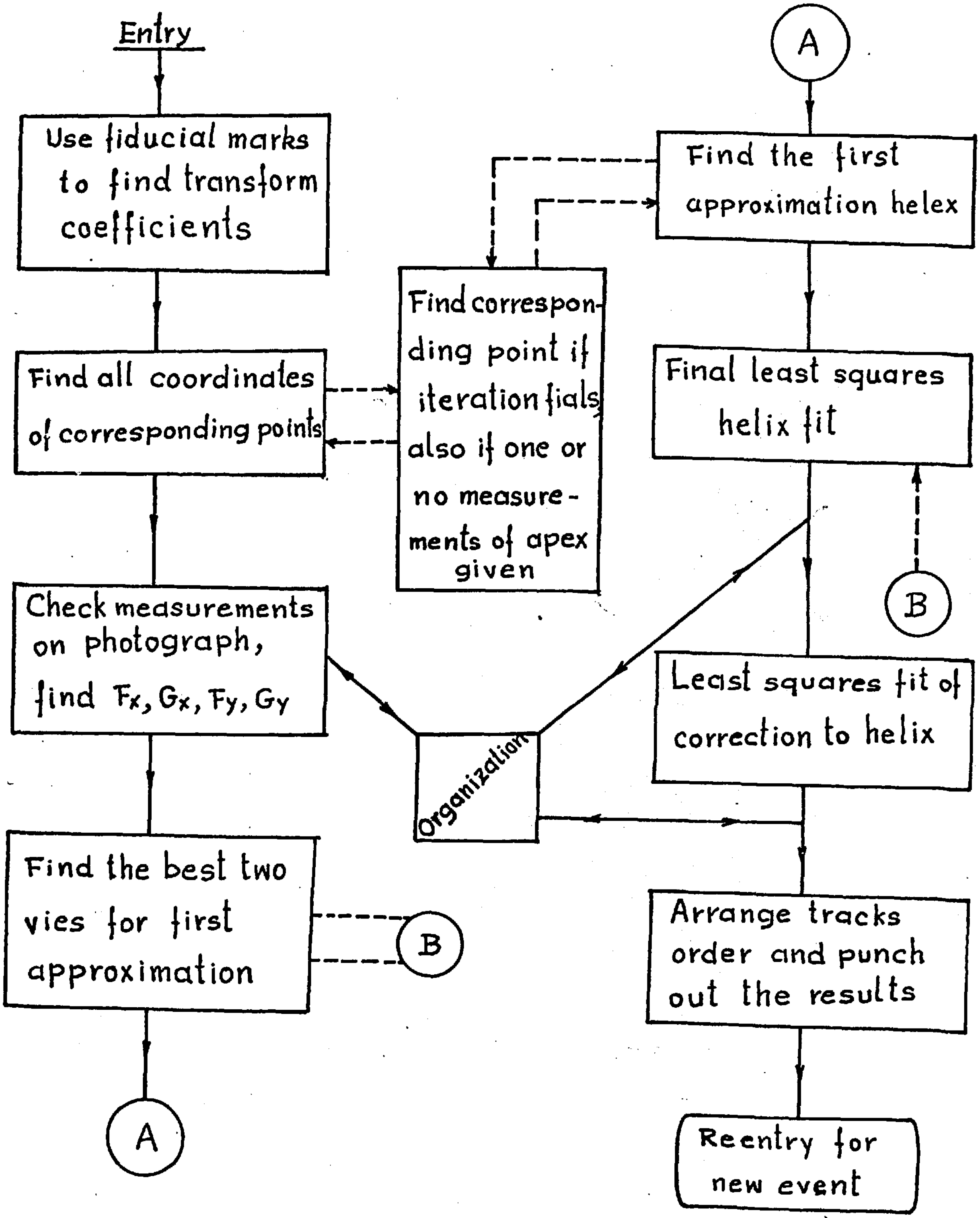

Fig. 2·8

Flow Chart of THRESH

relations:-

$$X_i' = \alpha_1 + \alpha_2 X_i + \alpha_3 Y_i$$

$$Y_i' = \alpha_4 + \alpha_5 X_i + \alpha_6 Y_i \qquad \ldots\ldots\ldots\ldots\ldots \text{(2.1)}$$

Measuring four fiducial marks on each view in turn enables the six coefficients (α_m; $m = 1\ldots6$) to be determined from a least squares fitting process. The new points (X_i', Y_i') are compared with the title values (given independently) to check that the accuracy of the measurements is within the set tolerances. They then serve as the reference frame for the reconstruction of each event.

A similar transformation is immediately applied to all the measurement of the view, points and tracks, and the coordinates (X', Y') are again transformed to remove any possible lens distortion and film tilt effects. Unfortunately the 2-M HBC showed certain inconsistencies due to non-parallel surfaces[26] during the experiment operating period, causing a great deal of difficulty in finding the best set of chamber constants. Especially for a four-constraint fit event at high energy (missing mass)^2 and missing energy about zero there may not be convergence because some missing momentum in the Z-direction (Pz) is introduced that may not be compensated for, and will thus be lost. An additional (empirical) parameter, proposed by D.Drijard[45] is indicated as β_7, in equation(2.2)and may take into account this deviation. The formula, corrected for distortion, therefore is as follows:-

$$X' = \left[1+\beta_1\frac{X}{D}+\beta_2\frac{Y}{D}+\beta_3\frac{XY}{D^2}+\beta_4\frac{X^2}{D^2}+\beta_5\frac{Y^2}{D^2}+\beta_6\frac{(X^2+Y^2)^2}{D^4}\right]X$$

$$Y' = \left[1+\beta_1\frac{X}{D}+\beta_2\frac{Y}{D}+\beta_3\frac{XY}{D^2}+\beta_4\frac{X^2}{D^2}+\beta_5\frac{Y^2}{D^2}+\beta_6\frac{(X^2+Y^2)^2}{D^4}\right]Y+\beta_7\frac{X}{D} \qquad \ldots\ldots\ldots(2.2)$$

where D is the camera Z coordinate. The set of β_i coefficients is determined separately by the CERN programme PYTHON.

(i) Reconstruction of Labelled Points - This section describes the calculation of space coordinates of the labelled points (apices, stopping points, etc).

The light ray joining any point of the Chamber to a given camera is shown as a broken line in figure 2.9 and the segment inside the sensitive part of the chamber is called the "Reconstruction line" and is described by the following equations:-

$$X = F_{xi}Z + G_{xi}$$

$$Y = F_{yi}Z + G_{yi} \qquad \ldots\ldots\ldots(2.3)$$

By the method of least squares one obtains the coordinates (X, Y, Z) of each point with their standard errors ΔX, ΔY, ΔZ, using all available views for the intersection of their reconstruction lines. These results are ignored if none of the possible combinations of views give ($\Delta X + \Delta Y + \Delta Z$) less than the tolerance constant given in the title. If a labelled point is measured on one view only, it will be used as a starting point for any track originating from it.

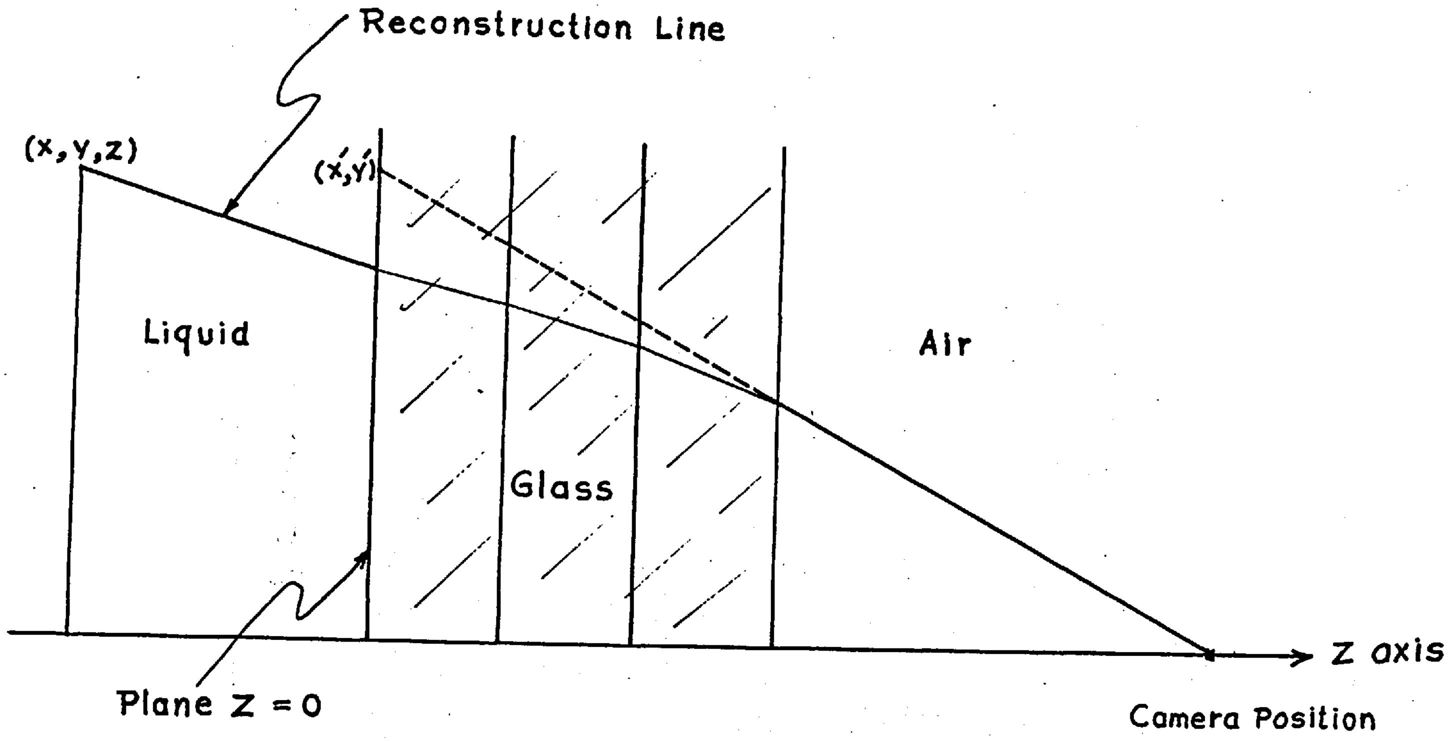

Fig. 2·9 Section Through a Light Ray and Optical Axis

(ii) Reconstruction of Tracks - The next problem is to obtain the reconstruction line for any point on the tracks. TRACK MATCH is a facility to check and correct the sequences of corresponding measured tracks on all views.

A preliminary check on the photograph is made; if more than two points are outside the fringe tolerance circle the event is rejected and sent back to be remeasured with a marker indicating the error. Apart from the labelled points, there are obviously no coresponding reconstruction lines for points measured on different views so that the X, Y, Z coordinates of equation (2.3) cannot be found directly. Instead, THRESH selects the two views α and β, such that the line joining these two corresponding cameras lenses is most nearly perpendicular to the track in the XY plane. This yields the best stereoscopic conditions. THRESH then reconstructs the points along the tracks by the method of Near Corresponding Points[44]. The reconstruction line associated with a given measurement on view α is thus described by:-

$$\begin{aligned} X &= F_x^{\alpha} Z + G_x^{\alpha} \\ Y &= F_y^{\alpha} Z + G_y^{\alpha} \end{aligned} \qquad \text{.......... (2.4}$$

A set of coefficients $(F_x^{\beta}, G_x^{\beta}, F_y^{\beta}, G_y^{\beta})$ for the spatial point image in view β is found by linear interpolation between the corresponding coefficients of the j^{th} and $(j+1)^{th}$ reconstruction lines with the added condition that the reconstruction line

$$\begin{aligned} X &= F_x^{\beta} Z + G_x^{\beta} \\ Y &= F_y^{\beta} Z + G_y^{\beta} \end{aligned} \qquad \text{........... (2.5}$$

intersects the reconstruction line of equation (2.4) in space. This point represents the actual position of the corresponding point on the track in the chamber.

After the approximate coordinates of the apex have been derived, the axis system (X' Y' Z') becomes the original system (X Y Z) rotated through an angle β about the Z-axis and translated to a new origin A, B, C (see figure 2.10). The first view chosen is that in which the track is viewed most nearly as an orthogonal projection, and thus all points in one view have been reconstructed with their corresponding points of intersection on the plane Z=C, where the best circle fit is made through (ABC). This has the equation in X and Y:-

$$(X - A)^2 + (Y - B)^2 + \lambda_1 (X - A) + \lambda_2 (Y - B) = 0 \quad ....(2.6)$$

and acts as the very first approximation to the helix. The radius is $\frac{1}{2}\sqrt{\lambda_1^2 + \lambda_2^2}$, and the centre is at $\frac{1}{2}(2A - \lambda_1)$, $\frac{1}{2}(2B - \lambda_2)$. λ_1 and λ_2 are found by least squares using equation (2.3) for X and Y coupled with their errors. The second view can be chosen at this stage.

In order to determine the points in terms of Z where the reconstruction lines intersect this cylinder (fig. 2.10), we substitute equation (2.3) in equation (2.6). The first approximation to the helix which is fitted to the data is described by:-

$$X' = \rho(\cos\theta - 1)$$
$$Y' = \rho \sin\theta$$
$$Z' = \rho\,\theta \tan\alpha \quad ....(2.7)$$

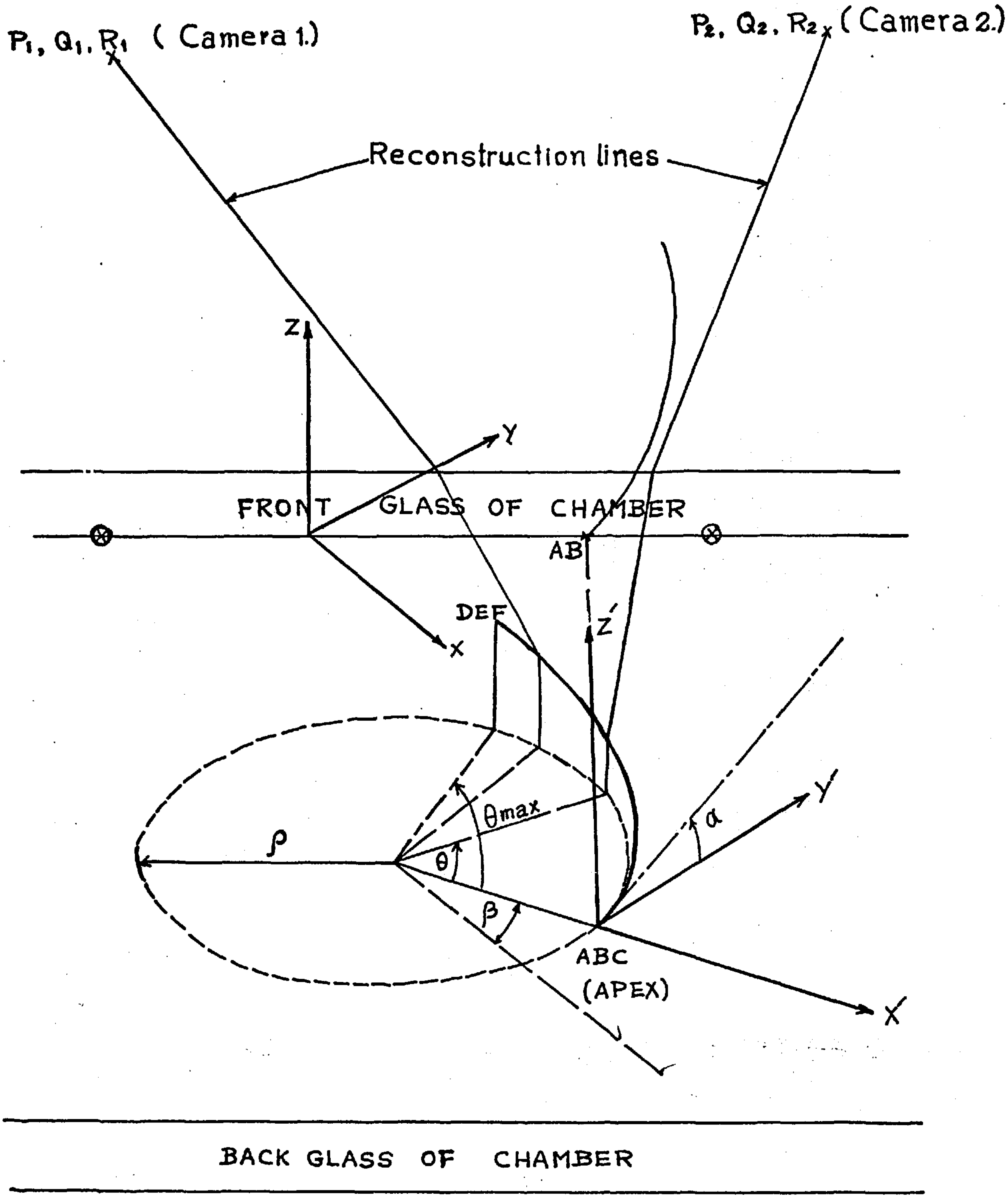
P1, Q1, R1 (Camera 1.)
P2, Q2, R2 (Camera 2.)
Reconstruction lines
Z
Y
X
FRONT GLASS OF CHAMBER
AB
DEF
Z′
θmax
θ
ρ
β
α
Y
ABC
(APEX)
X
BACK GLASS OF CHAMBER

Fig. 2.10

where ρ is the radius of the helix

α is the dip angle of track (small)

θ_i is the aximuthal angle of the i^{th} reconstructed point on the track, while

β is the aximuthal angle of the beginning point w.r.t. the X-axis.

These helix parameters are used as starting values in a final least squares fit, in which all views are averaged with the aim of finding small corrections to the parameters ρ, β, $\tan\alpha$, A (or B) and C so that the (X_i, Y_i Z_i) satisfy simultaneously equations (2.5) and (2.7) by iteration and converge to the best fit solution. The programme finally arranges the tracks in order, punches out the relevant information, gives the curvature for a mean point and states the dip and azimuthal angles for the beginning point with their errors. Since this version of THRESH is mass-independent, there is no consideration of uncertainties due to Coulomb scattering. To reduce this effect, an effort was made at the measurement stage to avoid the end of the track where rapid changes of curvature occur.

(43)

2.4.2 Kinematic Analysis of Bubble Chamber Events (GRIND)

The purpose of GRIND is to identify an interaction specified by a successful numerical evaluation by THRESH. This is done by assigning masses to the participating tracks of an interaction consistent with physical hypothesis specified by the user.

The first stage of GRIND is to convert the radius of curvature to momentum and extrapolate the values of p, λ and ϕ to the production vertex (originally specified at the middle of the track in THRESH) using range momentum tables supplied as data. This analysis of an event serves a double purpose:-

(i) to detect wrong interpretations

(ii) for a correct interpretation to impose the constraints of momentum vector and energy conservation at an interaction vertex.

There are four equations representing the conservation of the components of the momentum in a spatial Cartesian coordinate system and the conservation of the total energy. Each track is defined by three parameters (e.g. $1/p$, λ, ϕ) and has a normal distribution of error to fulfil the requirements of least squares fitting. The following four equations are formed:-

$$f_1 = \Sigma_i (P_x)_i = \Sigma_i c_i P_i \cos\lambda_i \cos\phi_i = f_1(\bar{X}_i) = 0 \quad \ldots\ldots\ldots (2.8)$$

$$f_2 = \Sigma_i (P_y)_i = \Sigma_i c_i P_i \cos\lambda_i \sin\phi_i = f_2(\bar{X}_i) = 0 \quad \ldots\ldots\ldots (2.9)$$

$$f_3 = \Sigma_i (P_z)_i = \Sigma_i c_i P_i \sin\lambda_i = f_3(\bar{X}_i) = 0 \quad \ldots\ldots\ldots (2.10)$$

$$f_4 = \Sigma_i E_i = \Sigma_i c_i \sqrt{P_i^2 + m_i^2} = f_4(\bar{X}_i) = 0 \quad \ldots\ldots\ldots (2.11)$$

At the production vertex $-M_T$ stands for the target energy.

c_i is +1 (-1) for an outgoing (incoming) track at the vertex.

m_i is the trial mass assigned to a track.

X_i are the values of momentum and angles corrected by fitting which fulfil the conservation equations (2.8) - (2.11).

The other information required by GRIND are the fixed data. These are referred to as the GRIND Title, and comprise the range momentum table to calculate momentum loss along tracks and possible particle masses (known as the hypothesis). The beam title is also stated along with its tolerances for fitting. The last item can be found independently of the experiment by reconstructing a reasonable number of beam tracks. The beam parameters P, λ_o, ϕ_o are obtained by extrapolation to a fixed point specified by coordinates (X_D, Y_D, Z_D) as follows:-

$$\lambda = \lambda_o + C_Z Z_D$$
$$\phi = \phi_o + C_Y(Y - Y_D) + C_X L_D \quad \dots\dots\dots \quad (2.12)$$

where the values of the C's for this experiment are

$$C_x = -0.00030 \text{ rad/cm}$$
$$C_y = 0.00020 \quad " \quad "$$
$$C_z = -0.00090 \quad " \quad "$$

In general ϕ can be measured very accurately, beam momentum is imposed by the title value as this parameter is often poorly measured. The general flowchart of fitting is shown in fig.2.11

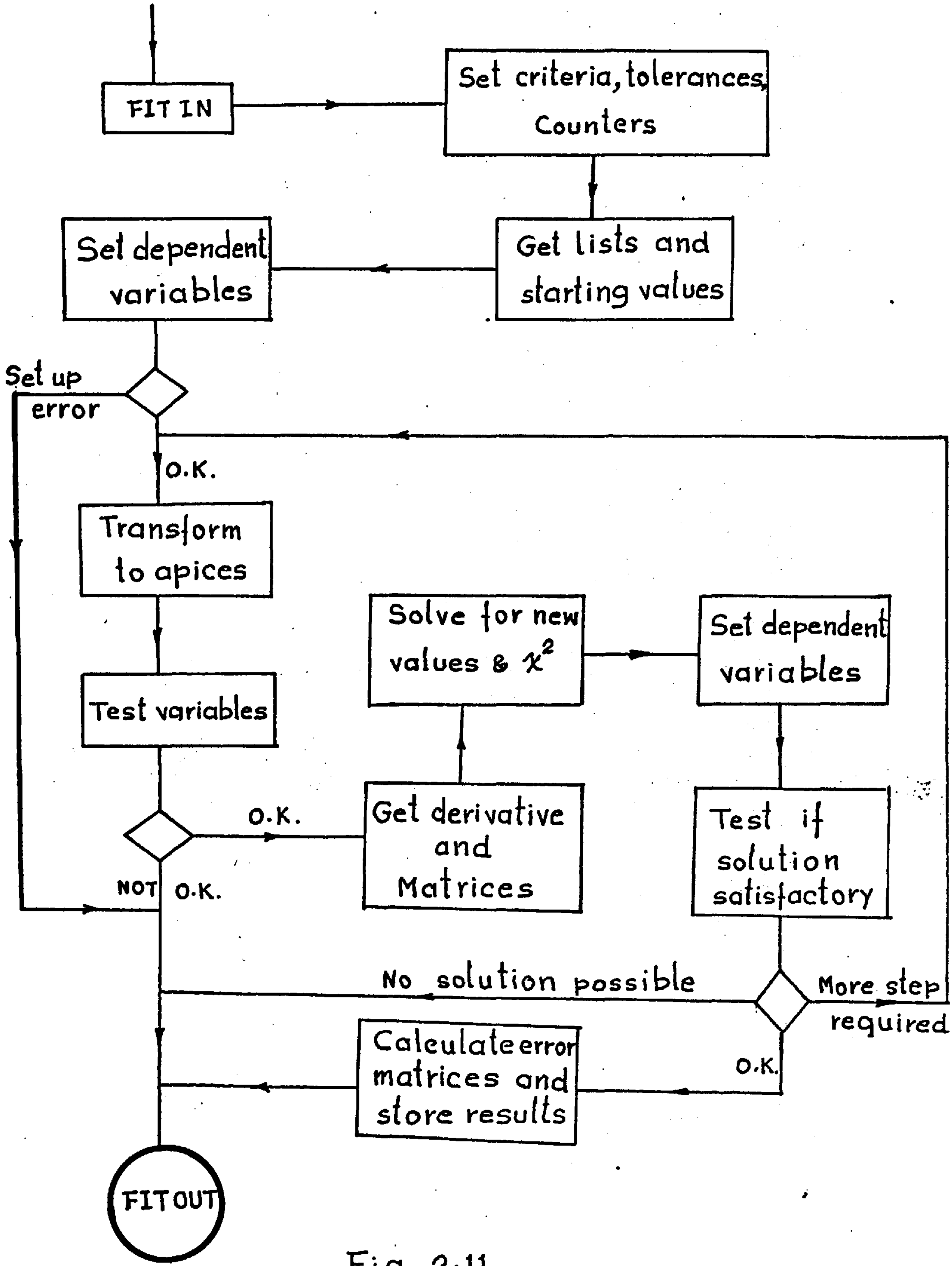

Fig. 2·11

Flow Chart of Fit

The best set of X_i can be reached by adjusting parameters in such a way that $f_1 = f_2 = f_3 = f_4 = 0$, with an additional condition of a minimum for the function χ^2 (chisquare) defined by:

$$\chi^2 = \sum_i \frac{\Delta X_i^2}{\sigma_{xi}^2} = \min \qquad \ldots\ldots\ldots (2.13)$$

$$\Delta X_i = \bar{X}_i - X_{io}$$

X_{io} are measured variables (P, λ, ϕ) and σ_{xi} are the standard deviations of error on X_{io}.

A description of different ways of using the method of least squares in kinematic analysis of bubble chamber events is given in ref.46. The method of Lagrangian multipliers is introduced as a conventional means of solving this problem. Thus the function to be minimized is rewritten as:-

$$M = \chi^2 + 2 \sum_j \alpha_j f_j = \min ; \quad j = 1, \ldots 4 \qquad \ldots\ldots\ldots (2.14)$$

we require $\frac{\partial M}{\partial X_i} = 0$; $i = 1, \ldots n$

α_j are Lagrangian multipliers which are eliminated during the calculations.

A linear approximation with iteration is used; thus each f_j is developed in a Taylor expansion to terms in the first order.

$$f_j(\bar{X}_i) = f_j(X_i) + \sum_i \frac{\partial f_j}{\partial X_i}(\bar{X}_i - X_i) \qquad \ldots\ldots\ldots (2.15)$$

X_i is a value which is changed during a calculation in order to arrive at the value $\bar{X}_i$ and $X_i = X_{io}$ for the first step of the iteration. The magnitude of χ^2 is dependent on how big are the differences between the fitted and measured values. To check for goodness of fit, χ^2 can be converted into a probability by taking the n degrees of freedom (n = no. of constraint equations = no. of unknown variables) into account thus[47]

$$f_n(\chi^2)d\chi^2 = \frac{(\chi^2)^{n/2-1}}{2^{n/2}\,\Gamma(n/2)}\, e^{-\chi^2/2} d\chi^2 \qquad \text{.........} \; (2.15)$$

where $\Gamma(n/2)$ is the Gamma function $\equiv (n/2 - 1)!$

This relation is used as one of the criteria for accepting the fit at the final stage.

2.5 D.S.T. and Statistics Programme

All the possible physical interpretations of the four-prong events which are convergent in the fitting procedure by GRIND are recorded in the GRIND library tape. Only the candidates for the reaction $pp \longrightarrow pp\pi^+\pi^-$ are of interest in the present experiment. Additional consistency criteria (as given in Chapter 3) are imposed in order to get as pure a sample as possible for the analysis. A Data Summary Tape (D.S.T.) is then produced by picking out all the relevant information from the GRIND library tape corresponding to the selected interpretations of the accepted fits as well as some computed quantities necessary for statistical analysis.

Examples of such quantities which must be written out in a suitable format are the combination of effective masses for the final state, the momentum transfer and the decay angle between pairs of particles, etc. Furthermore, in order to avoid the complication of misidentifying two identical particles (e.g. protons) in the final state, a separation between slow and fast protons in the Lab system (or backward, forward moving protons in the centre of mass system) is arranged before recording the event on the D.S.T.

The experiment dependent statistic programme to complete the chain of data processing is "POOR MAN'S SUMX"(34). Various histograms and two dimensional scatter plots, with or without conditional selections, may be produced by this programme with appropriate data instruction cards. The latter facility is an original programme from the standard NIRNS CHAIN-2 series. Facilities are also available for the connection of any user's routine to calculate other quantities which may not be presented on the D.S.T.

TABLE 2.1

The Breakdown of Events from a Test Strip and One Scan of 10 half rolls.

Data from	2-prong %	4-prong %	6-prong %	8-prong %	other type %
Test strip	29.05	42.1	15.1	1.09	1.05
One scan	35.0	40.5	17.3	3.11	3.12

CHAPTER 3

THE $pp \longrightarrow pp\pi^+\pi^-$ PRODUCTION CROSS SECTION

3.1 The Assignment of Events to the Final State

The kinematic fitting programme (GRIND) was used initially on the following three hypotheses. Each particle permutation was attempted and a fitting probability was derived:-

$$P + P \longrightarrow P + P + \pi^+ + \pi^- \quad \text{..........} \quad (1)$$

$$P + P \longrightarrow P + P + K^+ + K^- \quad \text{..........} \quad (2)$$

$$P + P \longrightarrow P + P + P + \bar{P} \quad \text{..........} \quad (3)$$

The occurrence of reactions (2) and (3) from a reasonable sample of film yielded a very small cross section, as expected[38,40]; and their inclusion in the programme merely produced ambiguities. Therefore they were neglected. Only the hypothesis of reaction (1) was then carried on for the present experiment, and since the measured events had already undergone a preliminary selection (see Chapter 2 - section 2.3), most of them were the 4-constraint candidates for this reaction with no neutral particles. Acceptable interpretations of fitted events were decided by the project physicist later. To be accepted, a fit had to satisfy certain criteria. These are described below:-

(i) Fitting Probability - The χ^2 value of the fit was calculated[47,52,53] in GRIND for the appropriate number of degrees of freedom. Its relation to the integral probability is calculated from eqs. (2.15) with a normalization;

$$\int^{\infty} f_n(\chi^2)\, d(\chi^2) = 1$$

After an event has passed through GRIND, one has to decide if the tested hypothesis is correct or not (detailed testing can be found in ref. 46 and 84). χ^2 is dependent on the magnitude of the differences between the fitted and the measured values. Frequently the deviation of the χ^2-distribution is known to belong to a certain family of distributions(84) which depend on the number of degrees of freedom. Figure 3.1a shows the distribution for 4-degrees of freedom, while figure 3.1b shows the corresponding χ^2-probability ($P(>\chi^2)$) distribution for events fitted to reaction (1).

In order to accept a reasonable physical hypothesis for a given event, one can introduce as a cut off limit a <u>maximum</u> value of χ^2 or a <u>minimum</u> value of probability. A check is made that the χ^2-distribution obtained from the fit procedure is the function of errors (Δp_i, $\Delta\lambda_i$ and $\Delta\phi_i$) introduced to the fit that agrees with the theoretically expected one. The peak at the low end of the $P(>\chi^2)$ shown in figure 3.1b could be due to the fact that the measurement errors occasionally result in a spurious missing particle with small momentum. Also, in the high energy range, secondary particles have a large momentum in the X-direction with a large error. Any variation in χ^2 would certainly depend upon the transverse momentum rather than the longitudinal momentum, and so it is more difficult to force an event to fit with 4-constrainst (4C) than with 1-constraint (1C). On this basis, the 4C fit will always be accepted when the event also fits with 1C.

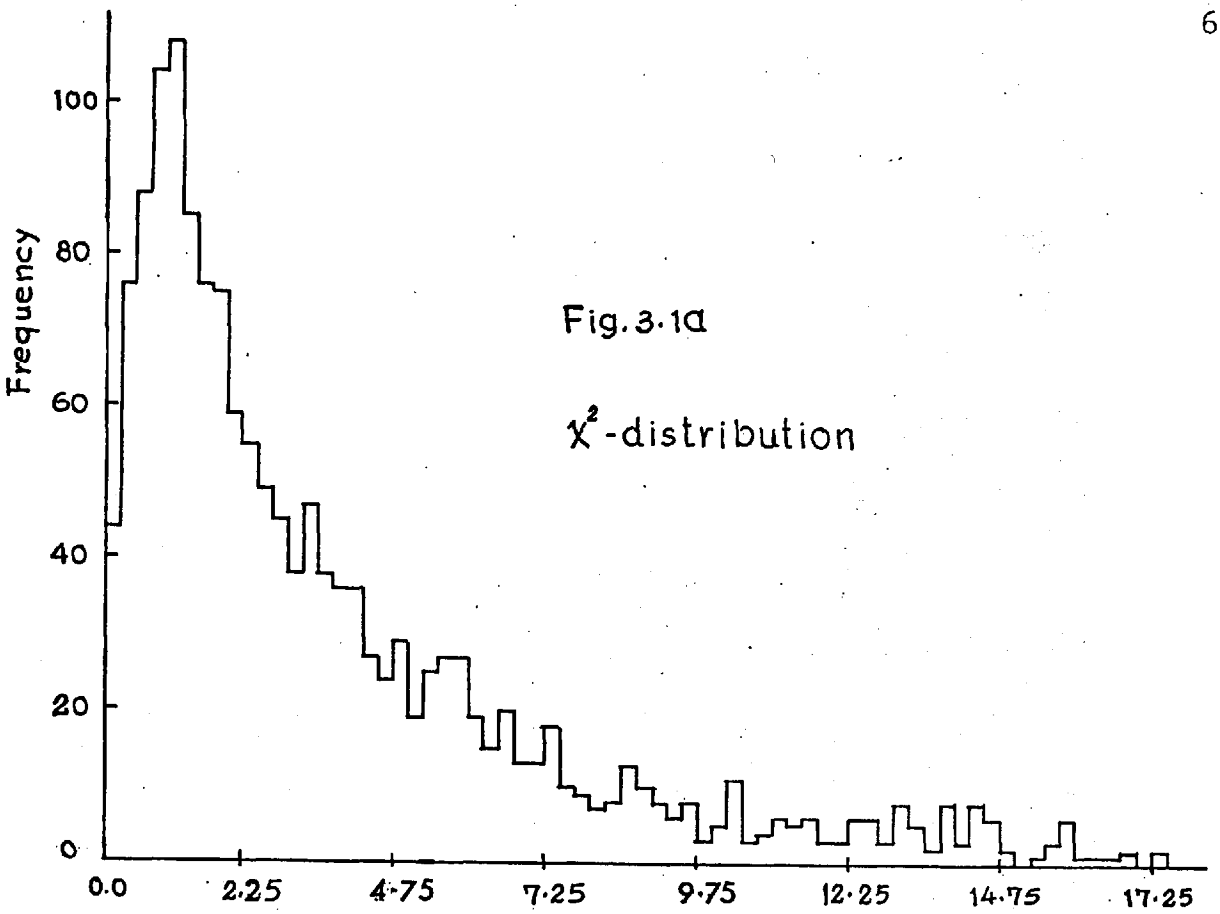

Fig. 3.1a

χ^2-distribution

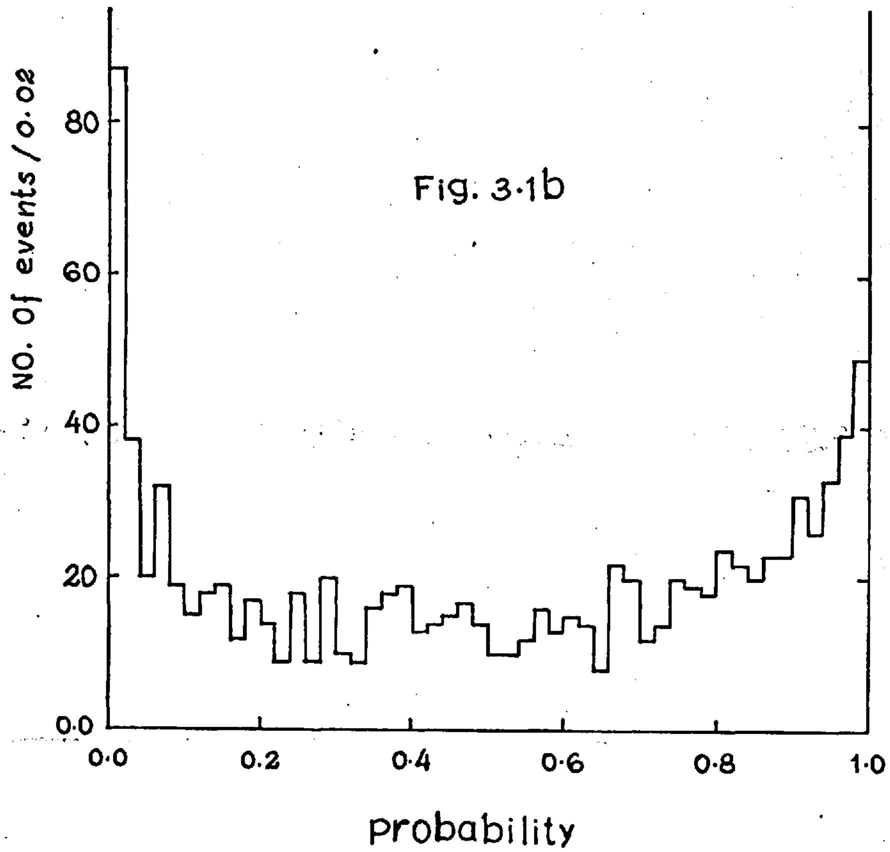

Fig. 3.1b

If two or more hypotheses gave 4C fits consistent with ionization, one hypothesis was accepted if its probability was three times greater than the alternatives, but otherwise these events are assigned to a "two-fold ambiguous" category for subsequent adjustment of cross section calculation. However those fits having a probability of less than 0.5% were rejected as incorrectly identified events.

(ii) Ionization - Every fitted event was checked on the scanning table for consistency of ionization of charged tracks. The predicted density of ionization for bubble chamber track is proportional to $1/\beta^2$ where

$$\beta = v/c = pc/E$$

For practical purposes, if we assume that the ionization density of infinitely fast tracks (beam tracks) I_0 (minimum), the density of ionization (I) for any track with momentum p, and assigned mass m is expected to be

$$I \propto I_0\left(1 + \frac{m^2c^2}{p^2}\right) \qquad \text{...........} \quad (3.1)$$

Typical curves of ionization versus momentum for protons and pions are shown in figure 3.1c. These values were calculated for a proton, kaon and a pion in each track and printed in the GRIND output. This had to agree with the estimated value of the ionization, obtained by inspection at the scanning table. A proton, kaon or pion could sometimes be distinguished, but in practice the usefulness of the check was severely limited at the present experimental level of energy because many of the tracks had high momentum and were of minimum ionization

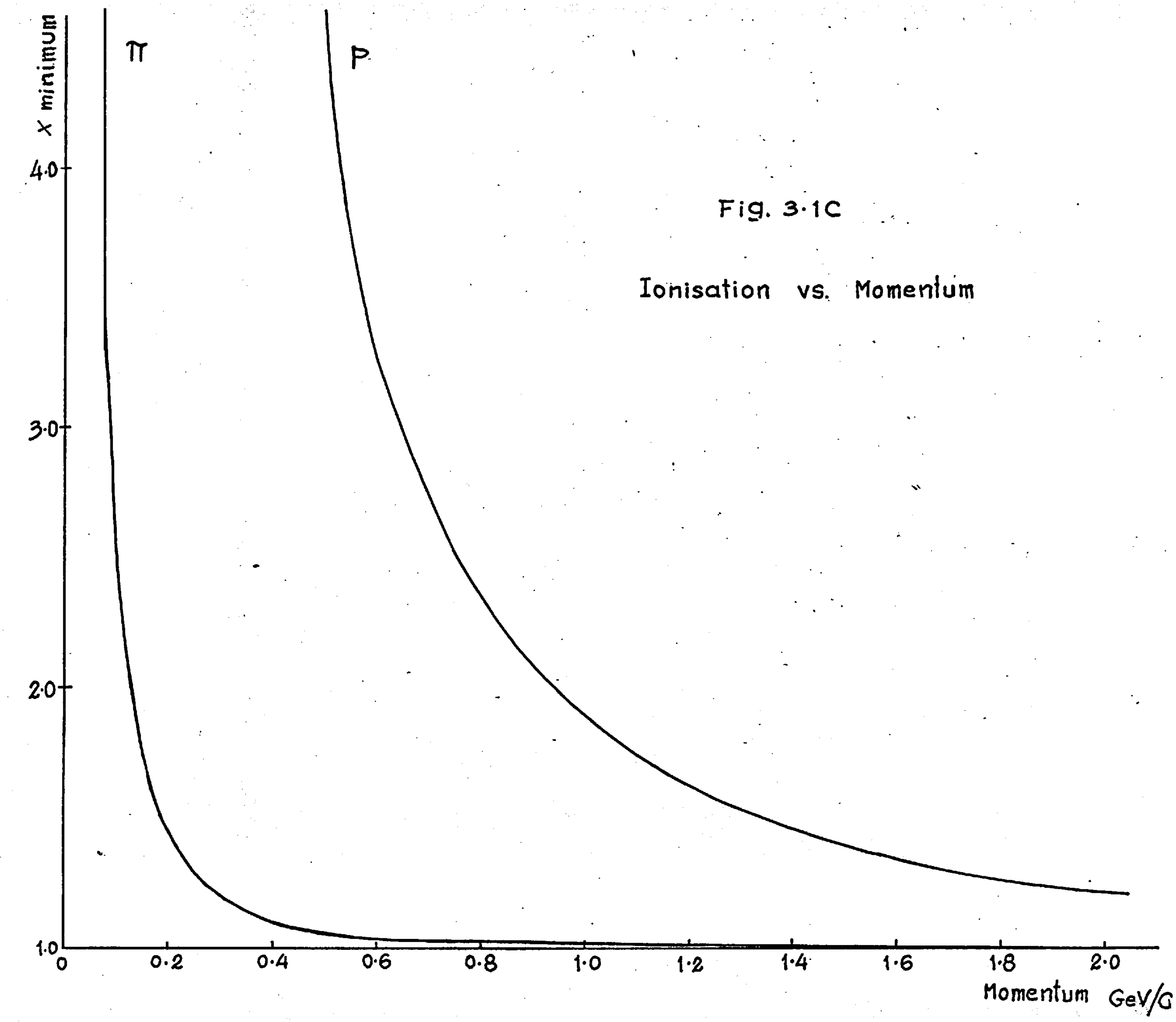

X minimum
4.0
3.0
2.0
1.0
π
P
Fig. 3·1C
Ionisation vs. Momentum
0
0·2
0·4
0·6
0·8
1·0
1·2
1·4
1·6
1·8
2·0
Momentum GeV/C

for all mass hypotheses. This situation gave rise to biased samples of events from the same reaction from a background of wrong identification.

It was found that by ionization checking one could resolve most of the ambiguous events, and the identification of a single heavy track as a proton could frequently eliminate all the low probability fits. At the same time, the beam track of each fitted event was also rechecked (see Chapter 2).

After such analysis more than 90% of the total samples were 4C fits, the rest being 3C. This left about 3% of the total as ambiguous events and this was considered a reasonably good identification rate at this energy.

3.2 Scanning Efficiency and Biases

With two independent scans and one check scan on the same amount of film, the "scanning efficiency" could be calculated as follows:-

let N_1 be the number of events found in the 1st scan.

N_2 be the number of events found in the 2nd scan.

N_{12} be the number of events found in both 1st & 2nd scan.

and let e_1 and e_2 be the corresponding scanning efficiencies.

Let N be the true number of events. Then if we assume that all events have an equal probability of registering :

then,
$$N_1 = Ne_1$$
$$N_2 = Ne_2$$
$$N_{12} = Ne_1 \; e_2$$
$$\therefore \quad N = \frac{N_1 \; N_2}{N_{12}}$$

The final scanning efficiency (ε) is then defined :

$$\varepsilon = \frac{N_1 + N_2 - N_{12}}{N}$$

$$\varepsilon = \frac{N_{12}}{N_1 \; N_2}\left(N_1 + N_2 - N_{12} \right) \quad \ldots\ldots\ldots (3.2)$$

The results were thus found to yield

$e_1 = 78\%$

$e_2 = 90\%$ and a final scanning efficiency of $\varepsilon = 97.09\%$ which is disappointingly low and probably due to poor film quality.

3.2.1 Scanning Biases - Scanning bias might arise in many ways:-

(i) Through poor frame quality and fluctuation in the number of beam tracks. An over or under-estimate in the number of beam tracks affects the calculation of the cross section.

(ii) Through a tendency to miss an event on a frame where there were more than two four-prong events. The ratio of the numbers of frames for various numbers of four-prong events found from the five roll sample was as follows:-

$$\frac{\text{No. of frames for one event}}{\text{No. of frames for two events}} = 2.72$$

$$\frac{\text{No. of frames for two events}}{\text{No. of frames for three events}} = 2.88$$

(iii) Through off-beam events, which mainly arise close to either side of the chamber window. A possible explanation is that the beam track is scattered at a small angle before entering the chamber. Some were fitted with 4-constraints (4C) but as the beam momentum was outside the limit they were rejected.

The interpretation of the experiment is not biased by (i) and (ii), which simply results in a loss of events. However this is not the case with (iii) where actual errors may be introduced, but fortunately, the number of these events was small. An estimate of the number was made from extrapolation of the four momentum transfer distribution (fig. 5.10c); 1.1% of the total data corresponds to missing events of this type.

3.2.2 Systematic Biases - Any systematic bias of the individual variables ($1/p$, λ, ϕ) for each track, can be revealed by plotting the normalised Stretch function of the production vertex, fitted for each variable. The special high constraint class of events fitted with no missing particles (4C) as shown in figure 3.2 will be particularly sensitive to any such biases. The Stretch function of a variable X is defined:-

$$F\ (X) = \frac{X_m - X_f}{\langle \sigma_m - \sigma_f \rangle} \quad \text{.........} \quad (3.3)$$

X_m is the measured variable

X_f is the fitted variable

and σ_m, σ_f are the correspdonding R.M.S. errors.

σ_f for variables $1/p$, λ, ϕ, were in this case calculated by the following relations with f_o as the initial value:-

$$\Delta(1/p) = \frac{8 f_o}{(L \cos\lambda)^2}$$

$$\Delta\lambda = \frac{f_o}{L \cos\lambda}$$

$$\Delta\phi = \frac{4 f_o}{L \cos\lambda}$$

where f_o = error of measurement multiplied by the demagnification of the chamber; usually f_o in GRIND is allowed to be larger than its true value (to allow for other uncertainties such as turbulence effect, etc).

L = length of the track.

The dotted lines in figure 3.2a show the normalised unbiased Stretch distributions for a sample of 4C fits in the variables $1/p$, λ, ϕ. For $1/p$ and ϕ, these were found to be normally

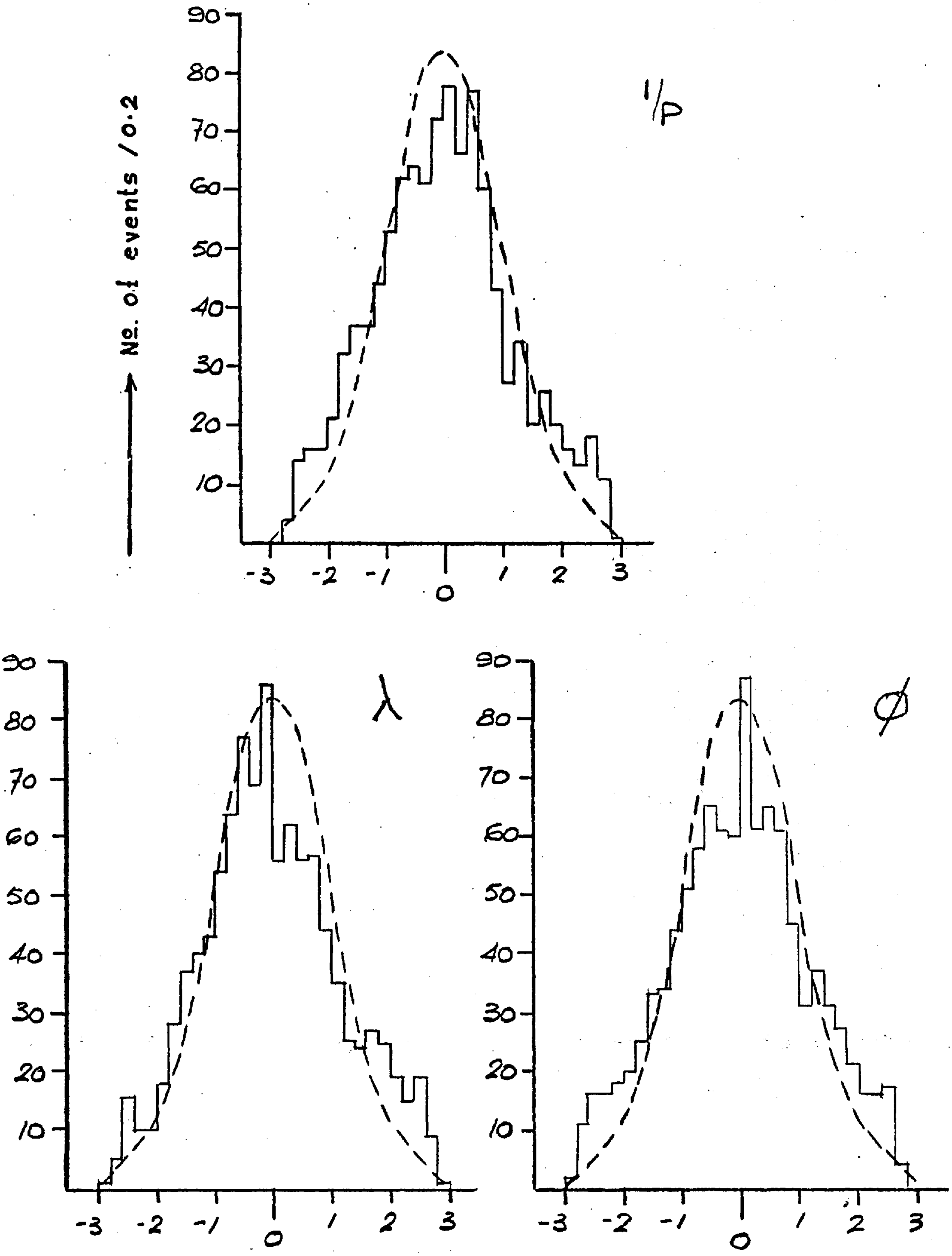

Fig. 3.2a

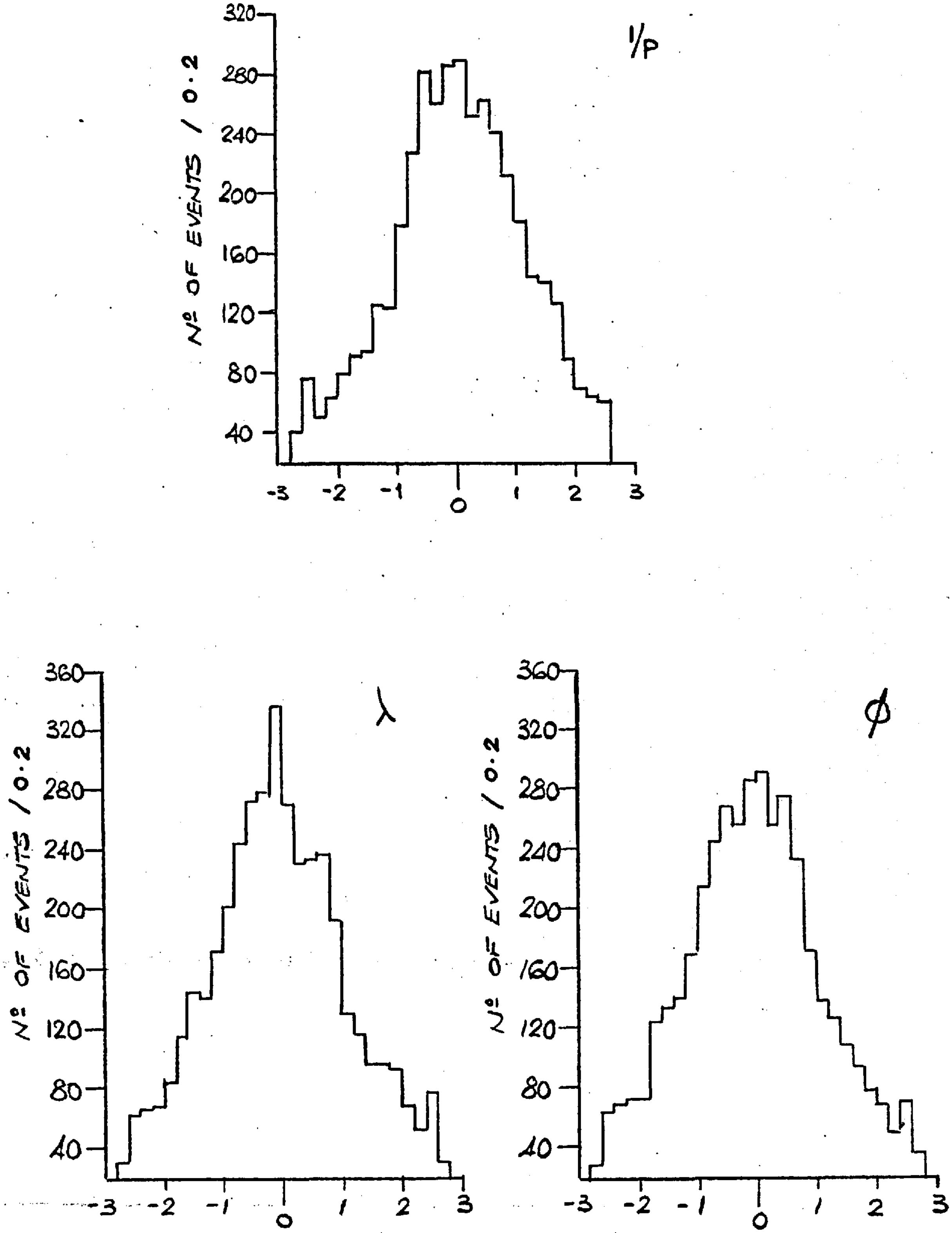

Fig. 3.2b

distributed with a peak at zero as expected. However, the dip (λ) angle was found to have a peak at a negative abscissa. This effect was subsequently investigated closely. Figure 3.2b shows the Stretch function of the other four tracks.

A very thorough investigation (see Chapter 4) was made of the problem of distortion[22,23] in the chamber. Such distortion could cause systematic bias in geometric and kinematic fitting particularly at high energies. The extra correction coefficient used in the reconstruction programme (see Chapter 2) was not of the correct form to overcome this effect. The following procedures were then carried out for examination:-

(i) Missing momenta - In high energy interactions momenta in the X-direction are always large and have large errors. In order to check the fit of high energy tracks, which are very sensitive to any kind of bias, a scatter plot of ΔP_Y versus ΔP_Z (where $\Delta P_Y, \Delta P_Z$ are missing momenta in the Y and Z-direction of the fitted events) was drawn and is reproduced in figure 3.3a. There is some indication of an assymmetric population of points which is related to an imbalance in the missing momentum. The projection of ΔP_Y and ΔP_Z are also shown in figure 3.3b.

(ii) The differences in the dip angles of the beam track

The evidence from the preliminary investigation and the chamber dependence described in Chapter 8, section 8.2, suggested that somehow the fast (high momentum) tracks were not

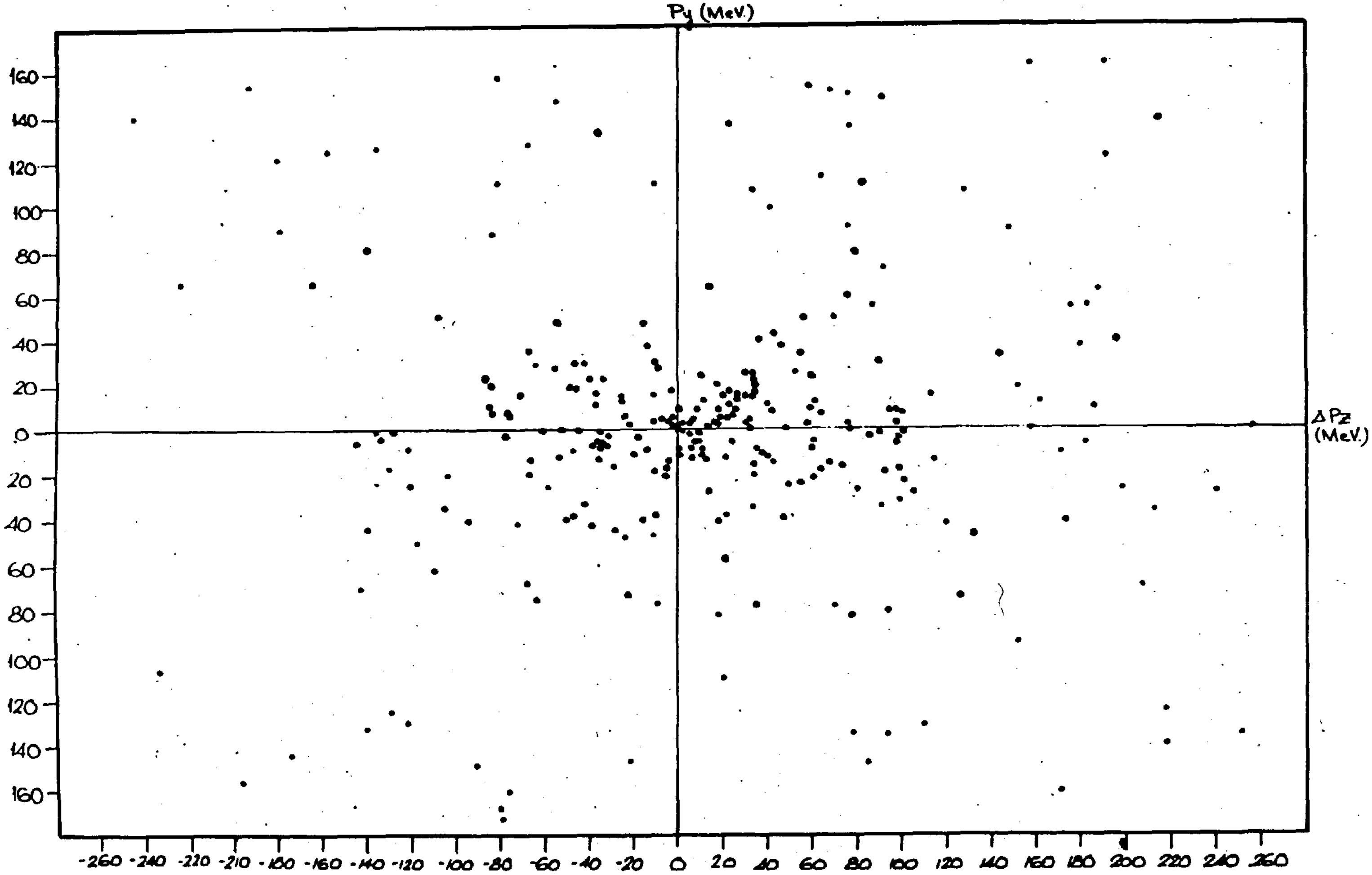

Missing Py Vs. Missing Pz

Fig 3.3a

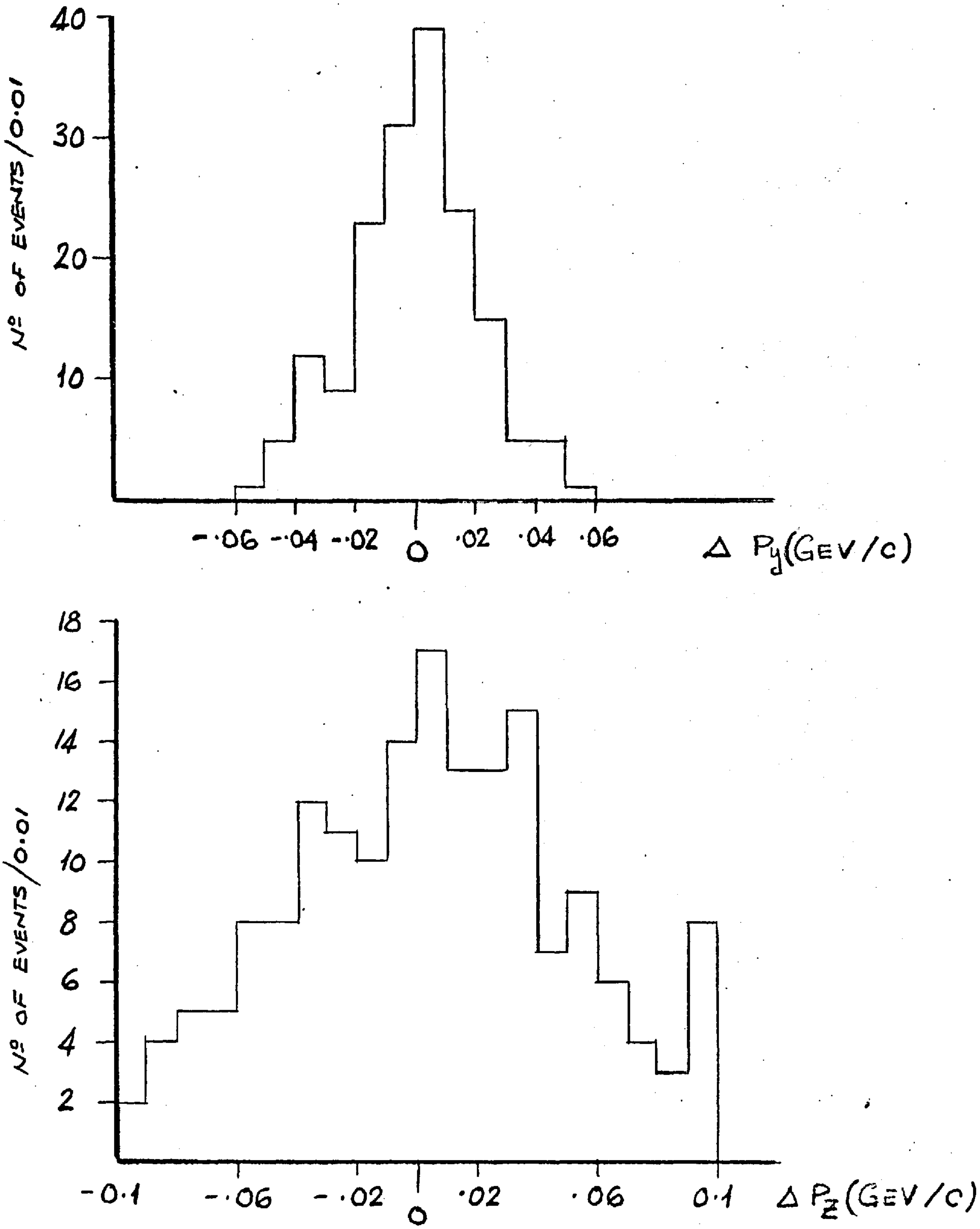
40
30
20
10
No. of EVENTS/0·01
-·06 -·04 -·02 0 ·02 ·04 ·06
Δ Py(GeV/c)
18
16
14
12
10
8
6
4
2
No. of EVENTS/0·01
-0·1 -·06 -·02 0 ·02 ·06 0·1
Δ Pz(GeV/c)

Fig. 3.3b

reconstructed properly on account of unknown distortions in the chamber. The effort expended in trying to find a solution to this problem has occupied the writer for 30% of the data reduction time, but, to this date, no reliable or reasonable correction has been achieved. The problem is discussed in greater detail in Chapter 4.

A second useful test for distortion can be made by artificially constructing a one prong event from the beam track, using a point as the apex of the event where a noticeable δ-ray (on all three views) is associated with the beam track. Alternatively one beam track is split into two parts. The first part is measured as a normal beam track, the second part as one secondary particle. Approximately three hundred such events were randomly selected and reconstructed by BIND and THRESH respectively. If there was no bias or the distortion of the chamber was corrected, one would expect the reconstruction of these two lines to join into the original track within the error limit.

Unfortunately, this procedure showed differences in dip angles for the two parts of the same beam track; this was considered significant evidence of the distortion, especially in the beam entry region. This effect was less pronounced toward the beam exist. Figure 3.4a shows the scatter-plot of the X-coordinate of the artificial apex versus the different value in dip angles of same beam track, while figure 3.4b shows the

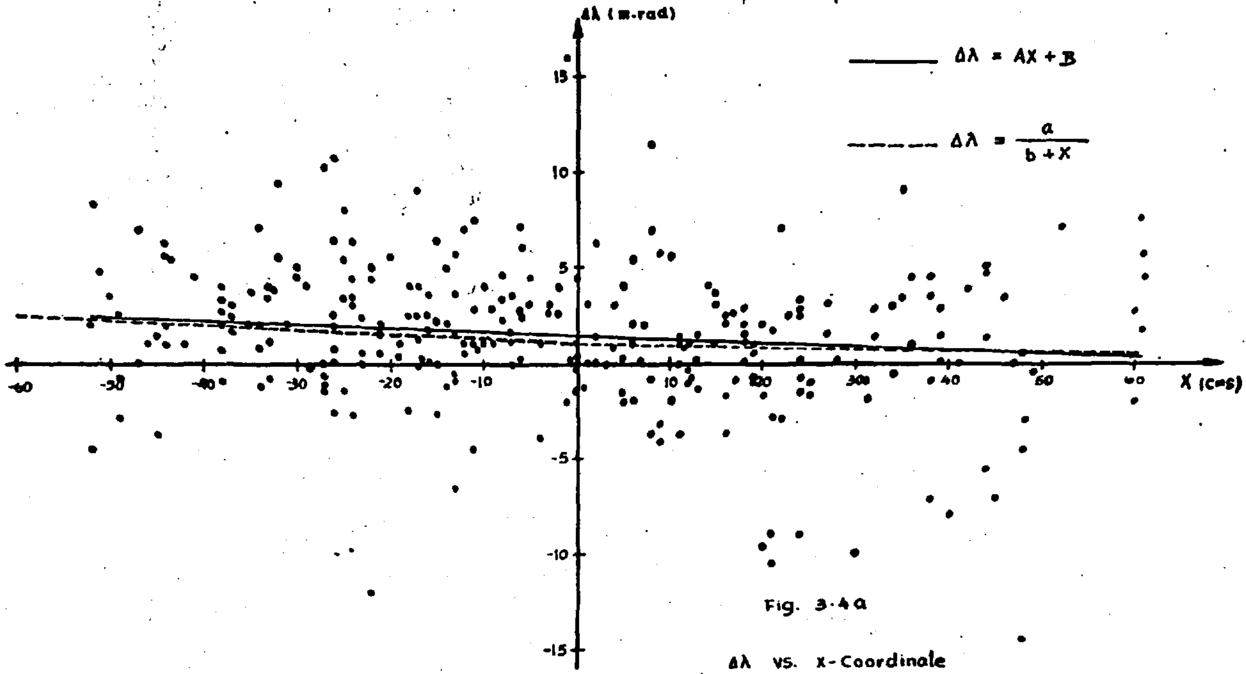

Fig. 3·4a

Δλ vs. X-Coordinate

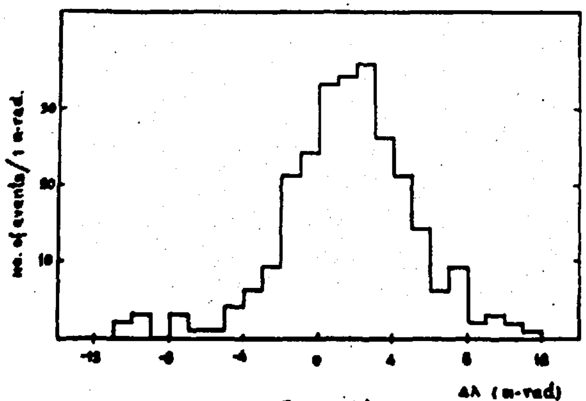

Fig. 3·4b

projection of these different values. This evidence was supported and confirmed by the Stockholm Group[51] on a similar experiment at 19 GeV, operating at the same period of time in the CERN 2M HBC. The alterations that have been attempted to correct this effect are discussed in detail in Chapter 4.

3.2.2 Remeasurement - Events judged to be incorrectly or poorly measured and thus unsatisfactory for reconstruction and kinematic fitting were sent back for measurement. After three consecutive attempts had been tried to measure an event, without success, it was classified as "unmeasurable".

On the first measurement, some 30% of the events required remeasurement, although the percentage varied greatly with the quality of the frame. Some errors were detected in BIND and found to be "measurer" dependent. Error flags were printed out when an event was badly measured in the reconstruction stage. For kinematic fitting, a remeasurement was only requested when there were more than two of the variables $1/\rho$, λ, ϕ failing to fit within their respective limits.

After a total of three measurements had been made, a residue of about 10% remained which were unmeasurable and had not been successfully analysed. These would be expected to contain at the maximum some 1.0% of the 4C fits, used in the cross section. A breakdown of scanned, measured, unmeasurable and fitted events is listed in table 3.1.

Another category of events was remeasured successfully and then reconstructed and fitted. These were events with one short and straight secondary track (non stopping) which could not yield a measurable momentum, thus giving rise to 3-constraint fits on a "two-point" measurement to obtain the direction. If such a track was a proton and was known to stop in the chamber, an additional label to the two-point measurement was required (TAG) and the energy and momentum was taken from the range.

TABLE 3.1

Scanned events	Measured events	Unmeasurable events	Fitted 4C events
16733	9013	973	1548 unique fit 69 amb. fit

3.3 Cross Section Calculation

Cross section calculations require a knowledge of the total number of beam tracks entering the fiducial volume. This was obtained by adding up the number of beam tracks on each half roll, as this varied widely from roll to roll (see fig. 2.2b) due to the very poor film quality. On the very worst rolls, the efficiency was only $\approx 80\%$. For this reason, the calculation was based on a sample of ten half rolls. These rolls were scanned carefully and rescanned by the writer. The total number of beam tracks (N_o) was calculated separately for each roll from the average number dervied from the good pictures on that roll. The results were then combined to give the number of total beam tracks for these ten half rolls:-

$$N_o = (6.971 \pm 0.026) \times 10^4$$

The total length (L) of beam tracks was calculated from a knowledge of fiducial length (l) and the direction which the tracks travelled through the chamber. No significant correction was necessary for the very high energy tracks of slight curvature.

Two methods were used to evaluate the cross section for the final state $PP\pi^+\pi^-$ from the sample of events processed at Imperial College. Both were based on the beam count procedure

(i) The Microbarn Equivalent - To a good approximation the microbarn equivalent of an interaction can be written as:-

$$\sigma = \frac{1}{nL}$$

where n is the number of protons per c.c.

$n = A\rho$

A = Avagadros number = 6.023×10^{23} mols/gms mol.

ρ = the density of hydrogen liquid at 26°K

= 0.0605 gms/c.c.

L = the total length of beam tracks

= $N_o l$

N_o = total number of beam tracks

l = the fiducial length (120 cms)

The calculated microbarn equivalent for an interaction after correction (section 3.2) was :-

$$\sigma = 1.02 \pm 0.04 \quad \mu b/\text{event}$$

In principle the microbarn equivalent can also be determined from a knowledge of the total cross section for the energy range in question and the total number of events observed. However, this analysis is outside the scope of the present experiment.

(ii) <u>The Total Cross Section Method</u> - One may calculate the cross section for the reaction

$$PP \longrightarrow PP\,\pi^+\pi^- \quad \ldots\ldots\ldots\ldots (1)$$

by using the most recent proton-proton total cross section at 16 GeV derived from counter experiments[37] which is equal to 39.9 mb. One must also know the total number of beam tracks entering the fiducial volume of this experiment:-

Let σ_T be the total proton cross section at 16 GeV.

N_0 is the number of beam tracks at x = 0,

and n is the number of protons per c.c. in hydrogen liquid of density .

If N = number of beam tracks after travelling a distance x without interaction.

$$N = N_0 e^{-n\sigma_T x}$$

Now let σ_1 be the cross section for reaction (1) and assume that in the distance interval dx;

$d\lambda_1$ interactions of type (1) occur

Then
$$\begin{aligned} d\lambda_1 &= Nn\,\sigma_1\,dx \\ &= N_0 n \sigma_1 e^{-n\sigma_T x}\,dx \end{aligned}$$

Therefore in the total fiducial (l) cms the total number λ_1 of these interactions is given by:-

$$\begin{aligned} \lambda_1 &= \int_0^l d\lambda_1 = \int_0^l N_0 n \sigma_1 e^{-n\sigma_T x}\,dx \\ &= N_0 n \sigma_1 \left(\frac{1 - e^{-n\sigma_T l}}{n}\right) \\ &= \frac{N_0 \sigma_1}{\sigma_T}\left(1 + 1 + n\sigma_T l - \frac{1}{2} n^2 \sigma_T^2 l^2 + \ldots\ldots\right) \end{aligned}$$

Since $n\sigma_T$ is small, of the order of 1.34×10^{-3}/cms., the higher terms are neglected. Thus

$$\lambda_1 = N_0 \sigma_1 n l \left(1 - \frac{1}{2} n l \sigma_T\right)$$

$$\sigma_1 = \frac{\lambda_1\left(1 + \frac{1}{2} n\sigma_T l\right)}{N_0 n l}$$

After being corrected for scanning losses, unmeasurable events and small t losses, cross section values were derived from both methods. The values obtained were 1.61 and 1.74 mb respectively which gives a final value of:

$$\sigma_1(PP \longrightarrow PP\pi^+\pi^-) = 1.67 \pm 0.10 \text{ mb.}$$

This value is consistent with results obtained in similar experiments at different energies as shown in fig.3.5.

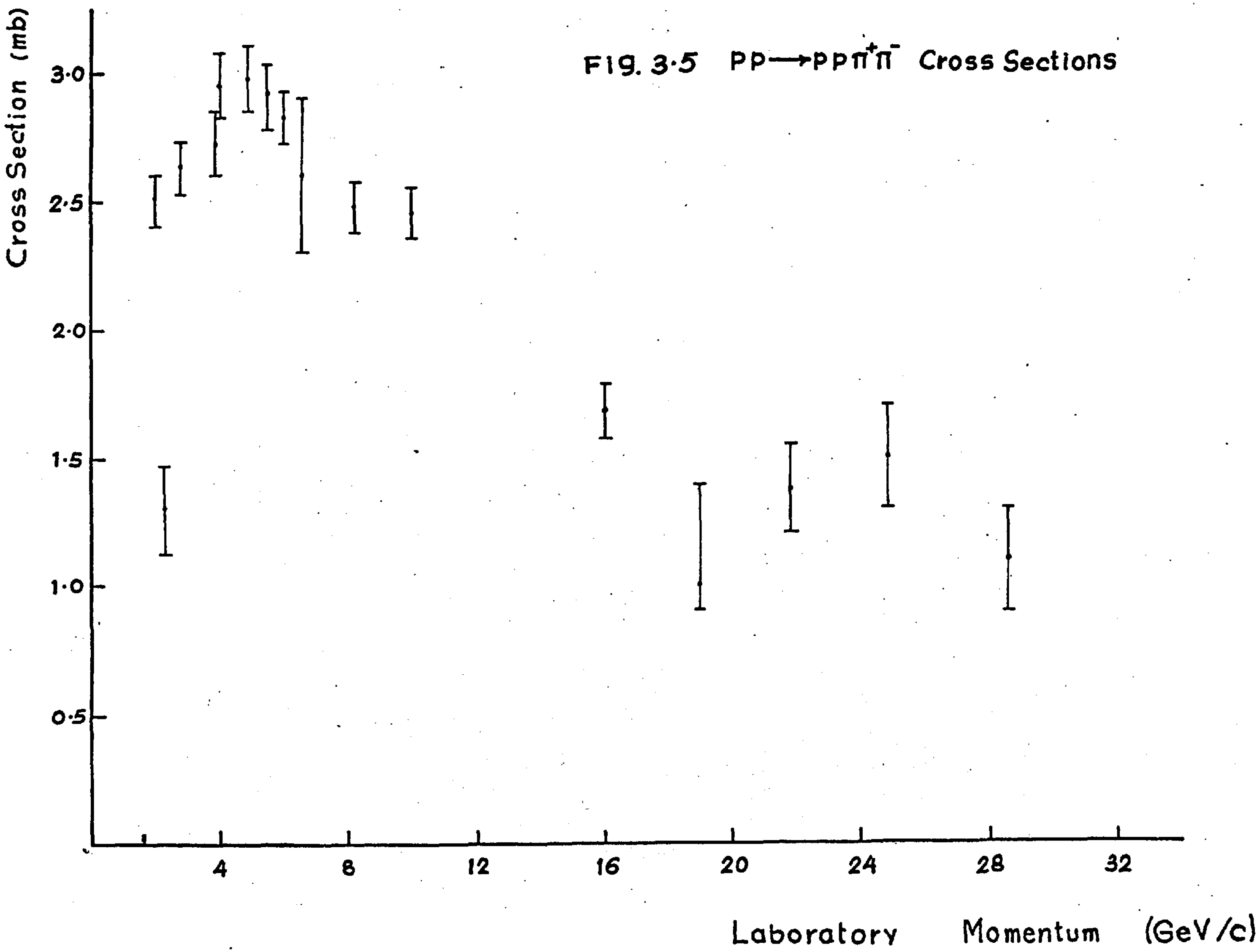

Fig. 3·5 $pp \longrightarrow pp\pi^+\pi^-$ Cross Sections

CHAPTER 4

OPTIMISATION OF THE OBSERVATIONS

4.1 Introduction

In general, PYTHON (see CERN Track chamber programme library)[44] is used to find the best possible set of parameters for the optical distortions of the chamber from accurate measurements of the fiducial marks. However, some special remarks apply to the operation period June 1966 to January 1967.[45] Data gathered from the 2-M HBC during this period has consistently given unsatisfactory results with larger residuals than expected for reconstructed tracks. This suggested a bending of the back of the glass window facing the cameras, for this surface is engraved with the fiducial marks and is thus the reference (Z=0) plane. There is however no known distortion which will account for these errors in a consistent way, but non-parallel windows, a wedge shape of the front window, or bending of the film gate are all possibilities.

As soon as this distortion became known in early 1967, an additional parameter (see 4.2 below) was added to the standard distortion formula (equation 2.2, page). The results of this procedure have, in general, not been satisfactory for high energy beam tracks ($\geq$ 15 GeV) and the remainder of this chapter discusses subsequent alternative procedures attempted independently by D. Drijard and the author.

4.2 The Empirical Parameter in THRESH

D.Drijard[45] (CERN) has suggested that only one additional parameter is necessary on the following grounds:-

(i) there are not enough fiducial marks available to fit more parameters without losing their significance.

(ii) most of the particles are travelling in the X-direction whic is four times as long as the Y-direction.

The procedure used to evaluate the parameters in the relevant equation (2.2) is as follows:-

(i) all fiducial marks are measured about ten times on five different pictures, approximately one hundred frames apart.

(ii) the camera position, vacuum path, film lens distance, and distortion are independently fitted for these five frames.

(iii) the weighted average of the resulting values are derived.

(iv) the corrected estimate of the positions of the fiducial marks on the rear of the front chamber window are used in all further calculations and are included, for example, in the THRESH Titles.

The five tests described below examined the improvement due to the 7-parameter fit ($\beta_1 \ldots \beta_7$) of equation (2.2) over the original 6-parameter fit ($\beta_1 \ldots \beta_6$).

(a) χ^2-Test - The improvement, as judged by the χ^2 test is shown in table 4.1 where the χ^2 value for the uncorrected data is also listed.

(b) Reconstruction of fiducial marks in space - The X and Y coordinates of the fiducial marks were obtained directly from the film and then the Z coordinates were reconstructed by using various combinations of two cameras on the plan Z = 0. The differences between the known Z-coordinates and the reconstructed ones (ΔZ) was plotted against the X coordinate of the fiducial marks in the chamber. Figure 4.1 shows the improvement of the plots for the 7-parameter fit compared to the 6-parameter fit. The reconstructed points lie away from Z = 0 plane in a C shape.

TABLE 4.1

	χ^2
Uncorrected data	31.13
6-parameter function	6.25
7-parameter function	6.00

(c) Reconstruction of the beam tracks - An automatic track following measuring machine has been employed at CERN to measure a few hundred beam tracks along their full length from three points of view (1, 3 & 4). Twenty-five points on each track were measured for each view. After reconstruction by THRESH they were projected back into the film, and the deviation δ (residuals) of a single measured point was found. Figure 4.2 compares the residuals plotted against the angle θ (the angle formed by the radius vector along the track) for 6 and 7-parameters. An improvement can again be seen in the 7-parameter fit.

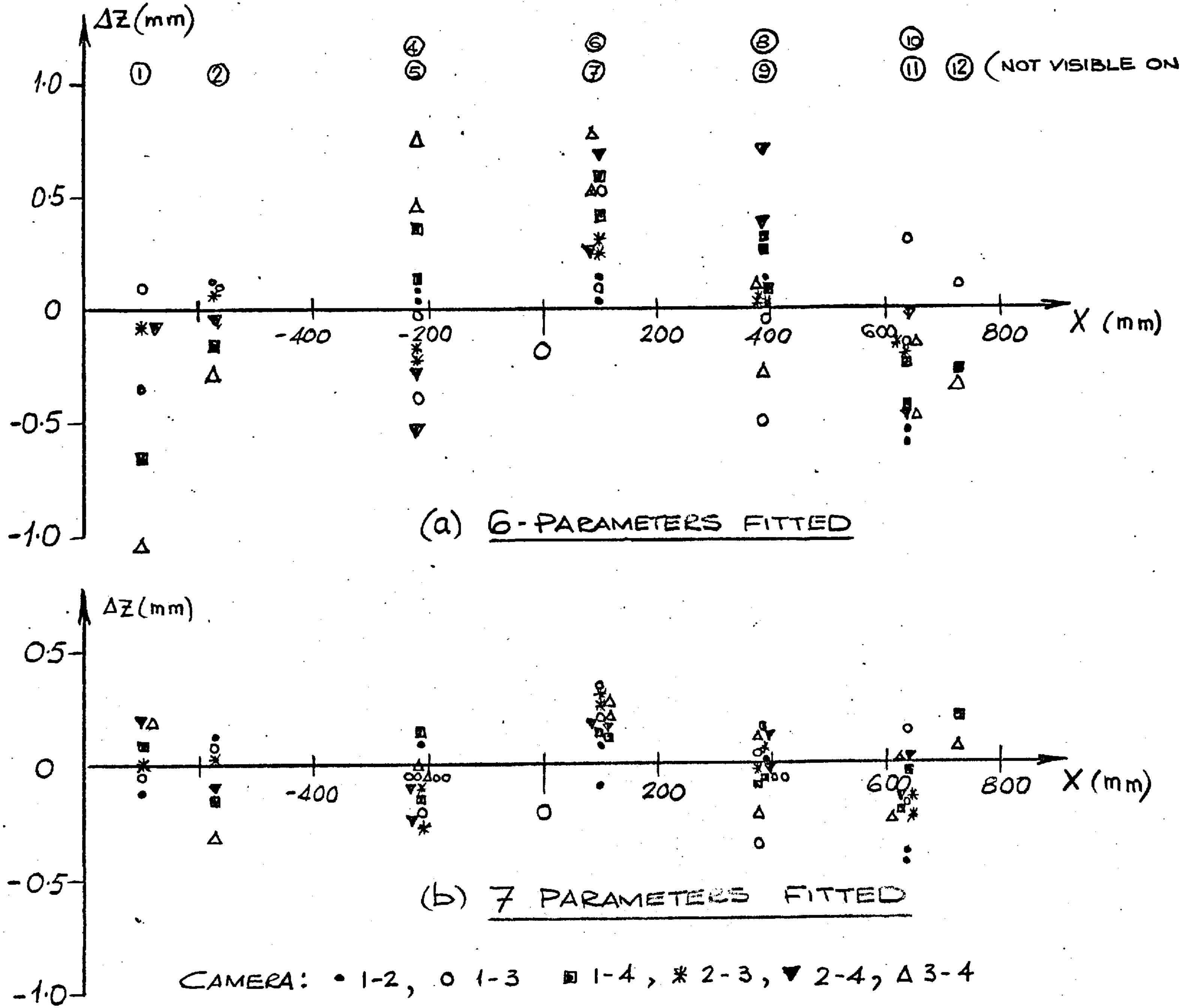
ΔZ (mm)
① ② ④ ⑤ ⑥ ⑦ ⑧ ⑨ ⑩ ⑪ ⑫ (NOT VISIBLE ON VIEW 2)
1.0
0.5
0
-0.5
-1.0
-400
-200
200
400
600
800
X (mm)
(a) 6-PARAMETERS FITTED
ΔZ (mm)
0.5
0
-0.5
-1.0
-400
200
600
800
X (mm)
(b) 7 PARAMETERS FITTED
CAMERA: • 1-2, o 1-3 ▣ 1-4, ✱ 2-3, ▼ 2-4, Δ 3-4

Fig. 4.1

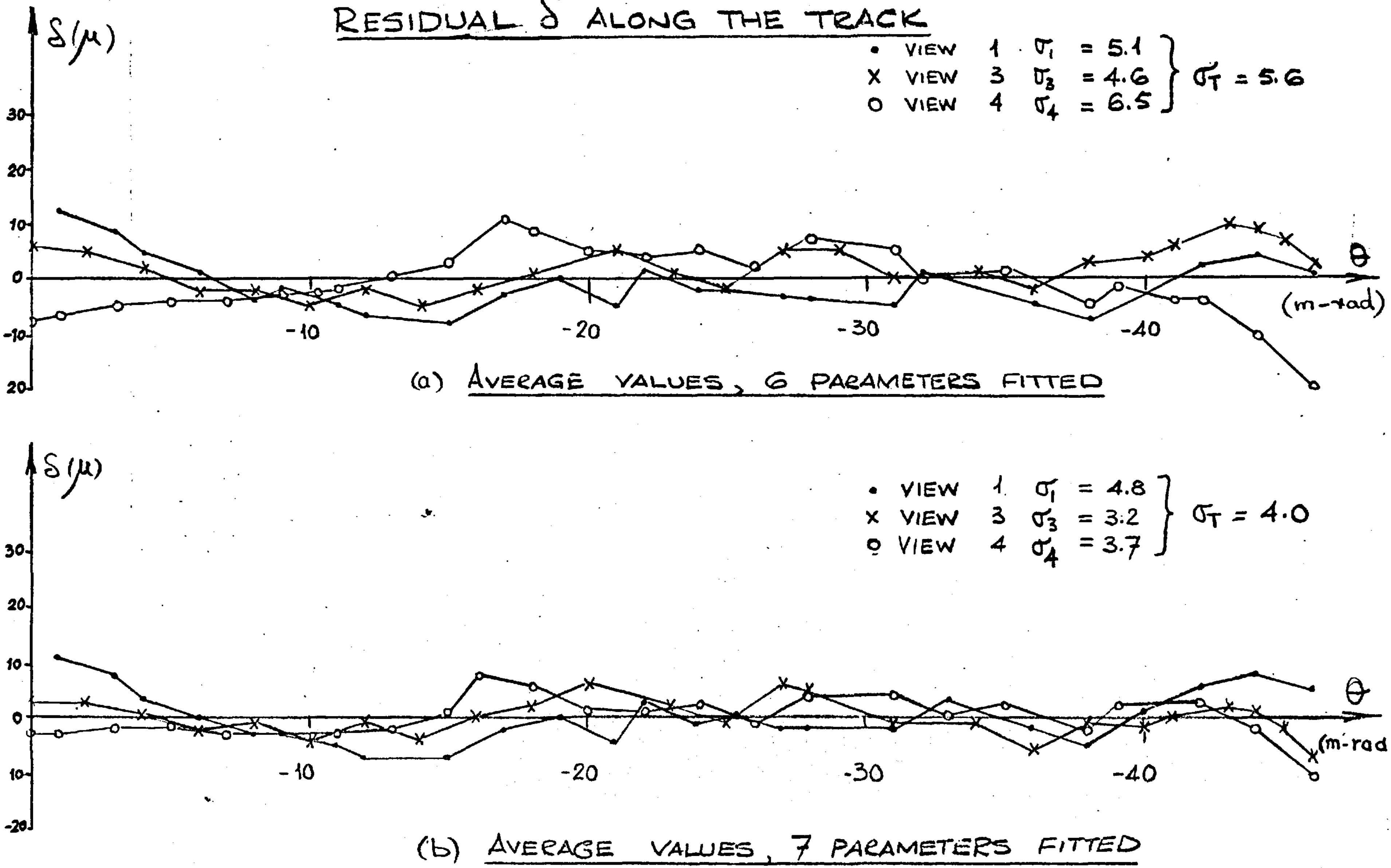
RESIDUAL δ ALONG THE TRACK
δ(μ)
• VIEW 1 σ1 = 5.1
X VIEW 3 σ3 = 4.6
O VIEW 4 σ4 = 6.5
σT = 5.6
30
20
10
0
-10
20
θ
(m-rad)
-10
-20
-30
-40
(a) AVERAGE VALUES, 6 PARAMETERS FITTED
δ(μ)
• VIEW 1 σ1 = 4.8
X VIEW 3 σ3 = 3.2
o VIEW 4 σ4 = 3.7
σT = 4.0
30
20
10
0
10
-20
θ
(m-rad
-10
-20
-30
-40
(b) AVERAGE VALUES, 7 PARAMETERS FITTED

Fig. 4.2

(d) Geometry and kinematic fitting - In this test a sample of events has been processed through THRESH and GRIND for geometric and kinematic fitting first with 6 and then with 7-parameters respectively. Only very small changes were detected. They are almost negligible, except for those events produced by small missing mass and energy, where the production vertex is near the entry of the chamber. Because of the distortion-induced curvature of the track in the X - Z plane for the 6 parameter fit (see figures 4.1 and 4.2), which possibly gives rise to the inbalance of the missing momentum in the Z component (fig. 4.3a), the fitting process may be non-convergent and the events would be lost.

(e) Investigation of missing momenta - Owing to the interesting nature of events which have small missing quantities and are thus sensitive to the distortion, further investigations were performed on missing momenta to check for anisotropy in missing momentum in the Y and Z plane. Figure 4.3 shows the distribution of these missing momenta where the missing component of the momentum in the x-direction is less than 1 GeV, whilst the scatter plot of these two quantities is illustrated in figure 4.3b. A 6-parameter function is fitted to these events. The slight improvement due to 7-parameters is seen in figures 3.3a and 3.3b. page 74/5.

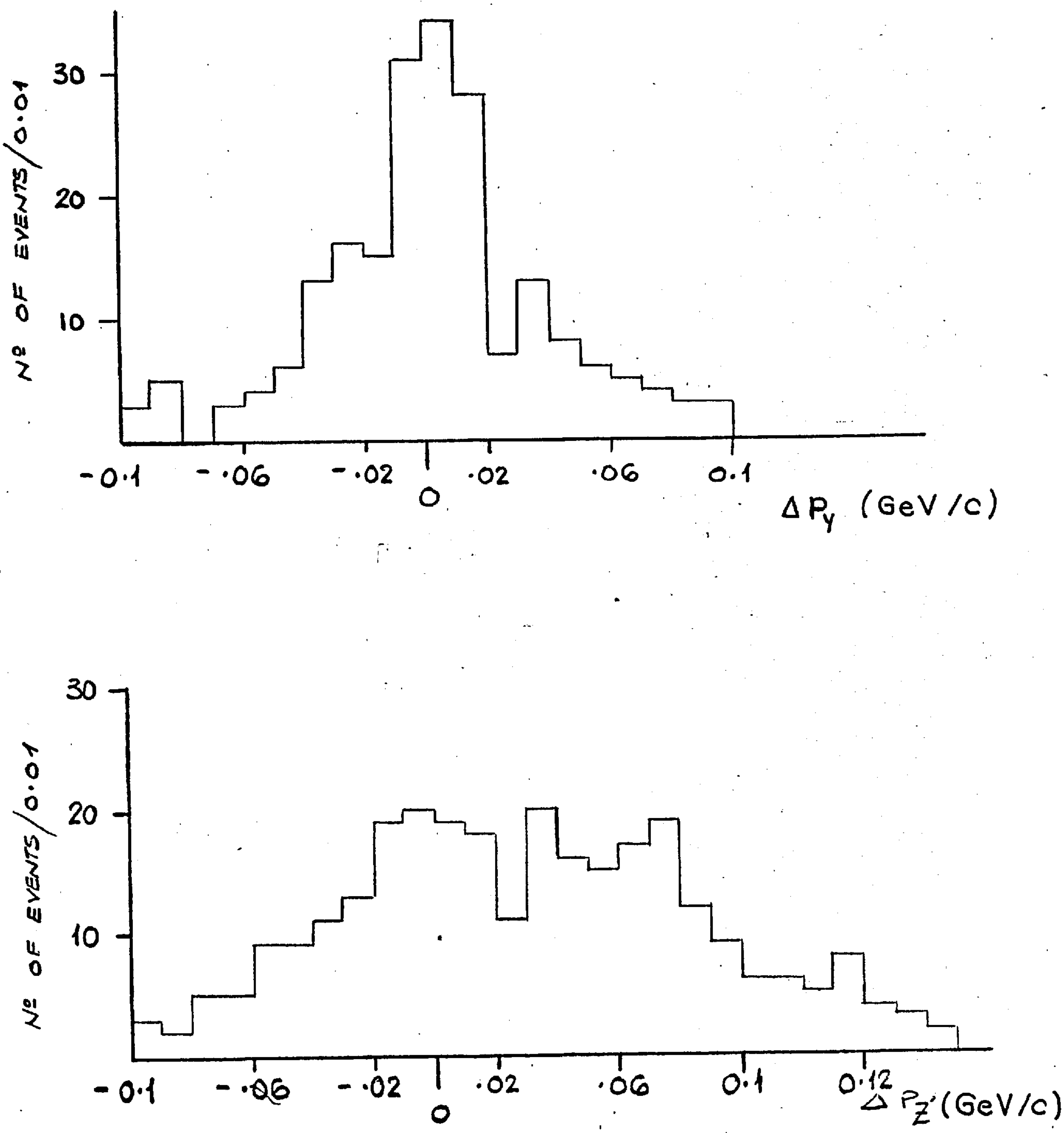

Nº OF EVENTS/0.01
30
20
10
-0.1
-.06
-.02
0
.02
.06
0.1
Δ P_y (GeV/c)
Nº OF EVENTS/0.01
30
20
10
-0.1
-.06
-.02
0
.02
.06
0.1
0.12
Δ $P_{Z'}$ (GeV/c)

Fig. 4.3 a

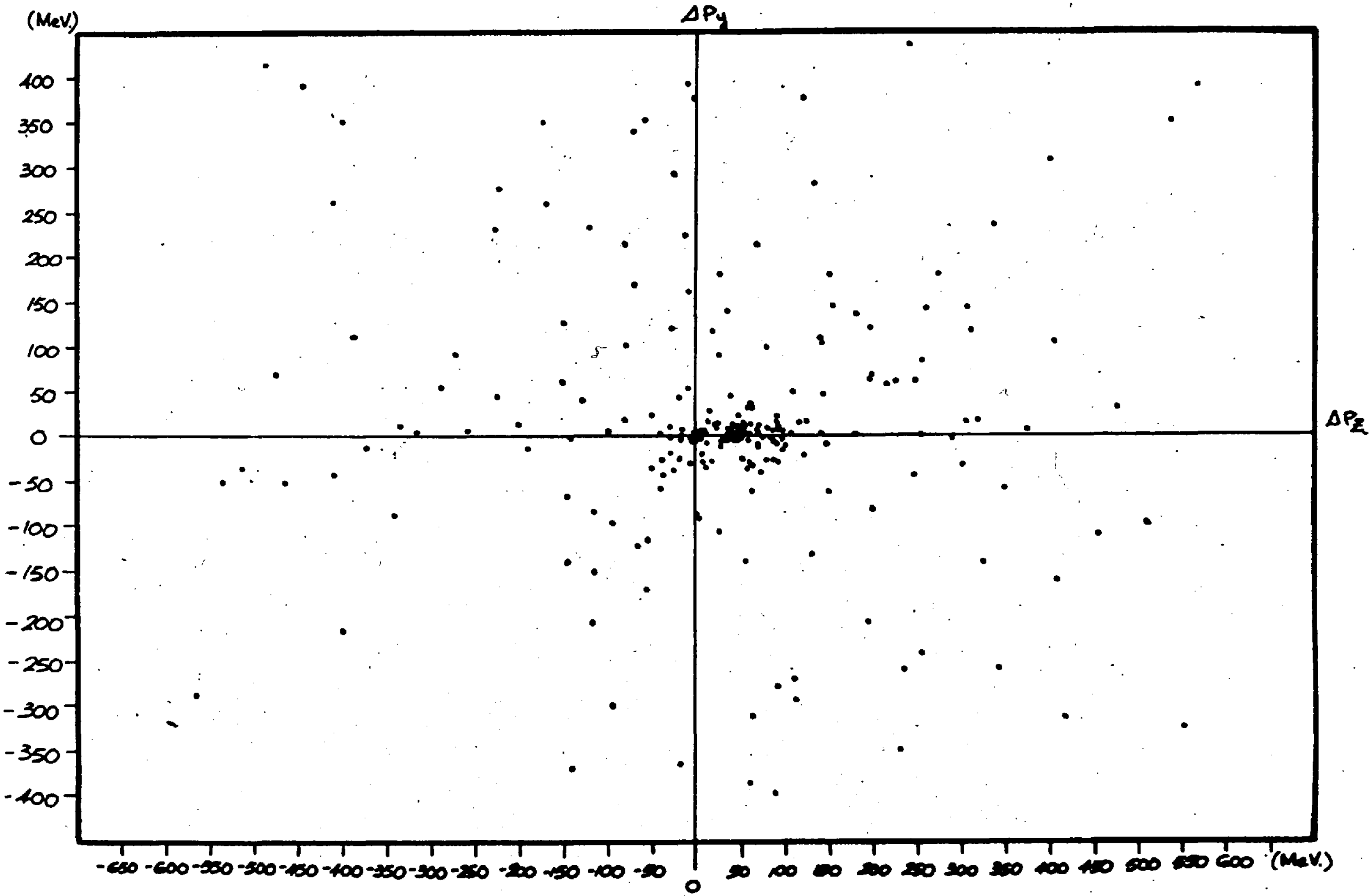

Fig. 4.3b Missing P_y Vs. Missing P_z where Missing $P_x < 1$ GeV/c

4.3 Attempts to correct the beam dip angle λ.

The introduction of an empirical distortion coefficient (β_7) only partly removes the trouble in the calculation of the CERN 2M-HBC optical distortion coefficients and reduces the reconstruction residuals for the points on film as shown.

Unfortunately, however, in the present experiment the beam dip stretch function distribution is shifted to the left in comparison with the normal distribution for the data (dotted curve in figure 3.2b) c.f. section 2, Chapter 3. This strong effect has caused the most severe difficulty in analysing the data, in particular a failure to arrive at consistent results for the high energy (fast) tracks. For this reason, in the construction of some histograms for data analysis, only the combination of slow protons in the final state has been used. A typical comparison of the mass combination of $p_s\pi^-$ and $p_f\pi^-$ (where p_s and p_f are the slow and fast protons respectively) is shown in figure 4.4. In the range 1400 - 1500 MeV, the $p_s\pi^-$ combination shows a peak whereas $p_f\pi^-$ shows a dip.

The author has paid considerable attention to this inconsistency problem, and the following attempts were carried out consecutively to obtain the optimum parameters for geometric reconstruction and kinematic fitting. The computer time (PDP6), required for any investigation with a reasonable number of events is eight to ten hours. Altogether, more than six months and more than sixty hours of computer time have been used in these analyses.

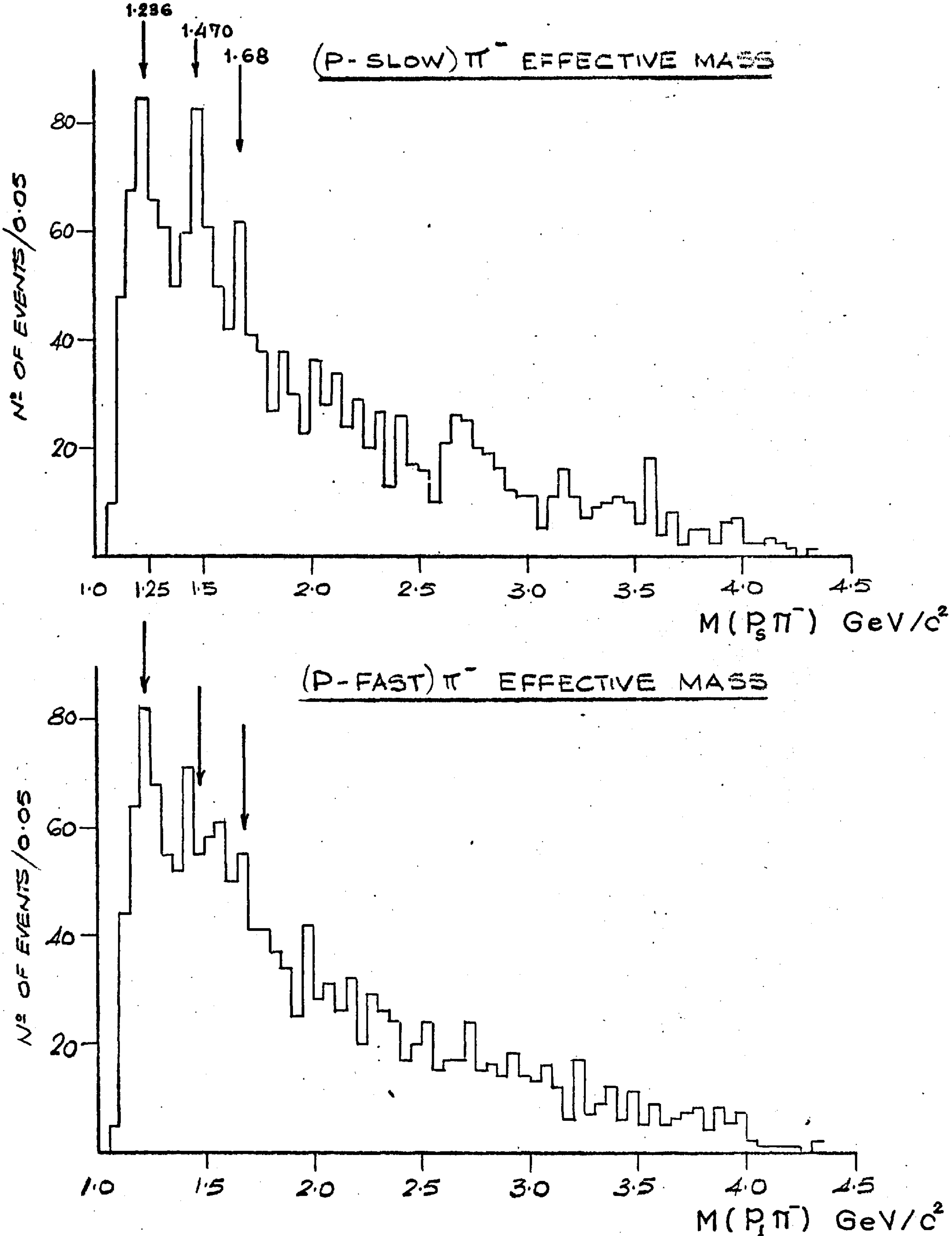
1·236
1·470
1·68
(P-SLOW) π⁻ EFFECTIVE MASS
Nº OF EVENTS/0·05
80
60
40
20
1·0
1·25
1·5
2·0
2·5
3·0
3·5
4·0
4·5
M(P_s π⁻) GeV/c²
(P-FAST) π⁻ EFFECTIVE MASS
Nº OF EVENTS/0·05
80
60
40
20
1·0
1·5
2·0
2·5
3·0
3·5
4·0
4·5
M(P_f π⁻) GeV/c²

Fig. 4.4

The basis of all these attempts has been the knowledge of certain differences in the dip angle along the same beam track. Therefore, from here onward the term "measured beam track" is taken to refer only to those beam tracks which were artificially measured as one-prong events (see 3.2.2, chapter 3) The significance of the beam dip angle correction will become apparent later. The correction is independent of the THRESH programme.

The following paragraphs outline the attempts at beam dip angle correction.

(i) Straight line fitting - The averaged values of dip angle residuals are listed in table 4.2. Some correlation between dip angle and the length of the track can be seen. A linear variation $\Delta\lambda = Ax + B$ was first chosen to fit the differences in dip angle. This yields the values:-

$$A = -0.20 \pm 0.005 \quad \text{m-rad/cm}$$
$$B = 1.39 \pm 0.12 \quad \text{m-rad}$$

TABLE 4.2

Length dependent beam dip angles for unweighted (λ_{uw}) and weighted ($\bar{\lambda}_w$)

Length (cm)	λ_{uw} (m-rad)	$\bar{\lambda}_w$(m-rad)
All length	1.39	1.43
< 120	1.07	1.60
120 - 140	2.20	1.46
> 140	1.39	1.42

The resulting line is drawn (solid line) in figure 3.4a. Hence the correction formula for the reconstructed beam track can be written as: $\lambda = \lambda_0 - (AX + B)$

where λ = new dip angle

λ_0 = original reconstructed dip angle

X = X-coordinate of the apex.

Although eight hundred 4C events have been processed thoroughly through the THRESH-GRIND statistic programme using this correction, only very small changes can be seen compared to the uncorrected data. The distribution of the stretch-function for beam tracks variables $1/p$, λ , ϕ, are shown in figure 4.5. For $1/p$ and ϕ there is good agreement with the normal distribution (dotted line), but in the case of the dip-angle, the peak of the distribution is still shifted in a negative sense.

(ii) Length dependent fitting - The evidence of figure 4.1 suggests that the distortions result in a curvature of the X - Z plane, coupled to the evidence of table 4.1, that the changes in dip-angle of the beam track are track-length dependent.

A new approach, discussed below, was proposed by Mr N.C. Barford[52] for correcting both parts of the measured beam tracks.

In the general case:-

$$\epsilon_1 = \alpha l_1 + \beta_1 l_1^2 \quad \text{..........} \quad (4.1)$$

$$\epsilon_2 = \alpha l_2 + \beta_2 l_2^2 \quad \text{..........} \quad (4.2)$$

where ϵ_1, ϵ_2 and l_1, l_2 are the errors and track lengths of tracks one and two respectively.

α, β_1 and β_2 are free parameters:-

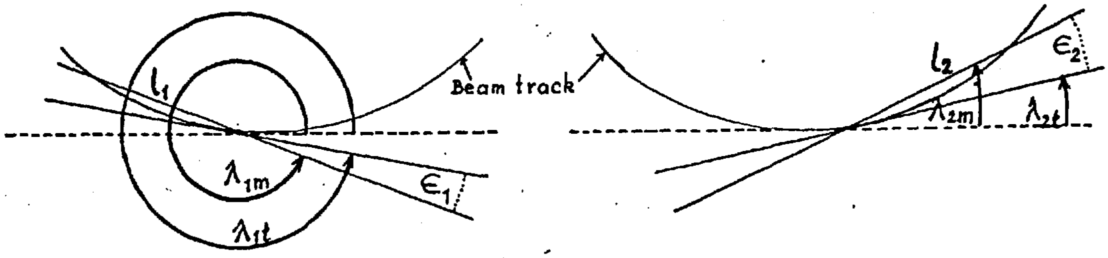

$\lambda_{1t} = \lambda_{1m} + \epsilon_1$ $\qquad\qquad$ $\lambda_{2t} = \lambda_{2m} - \epsilon_2$

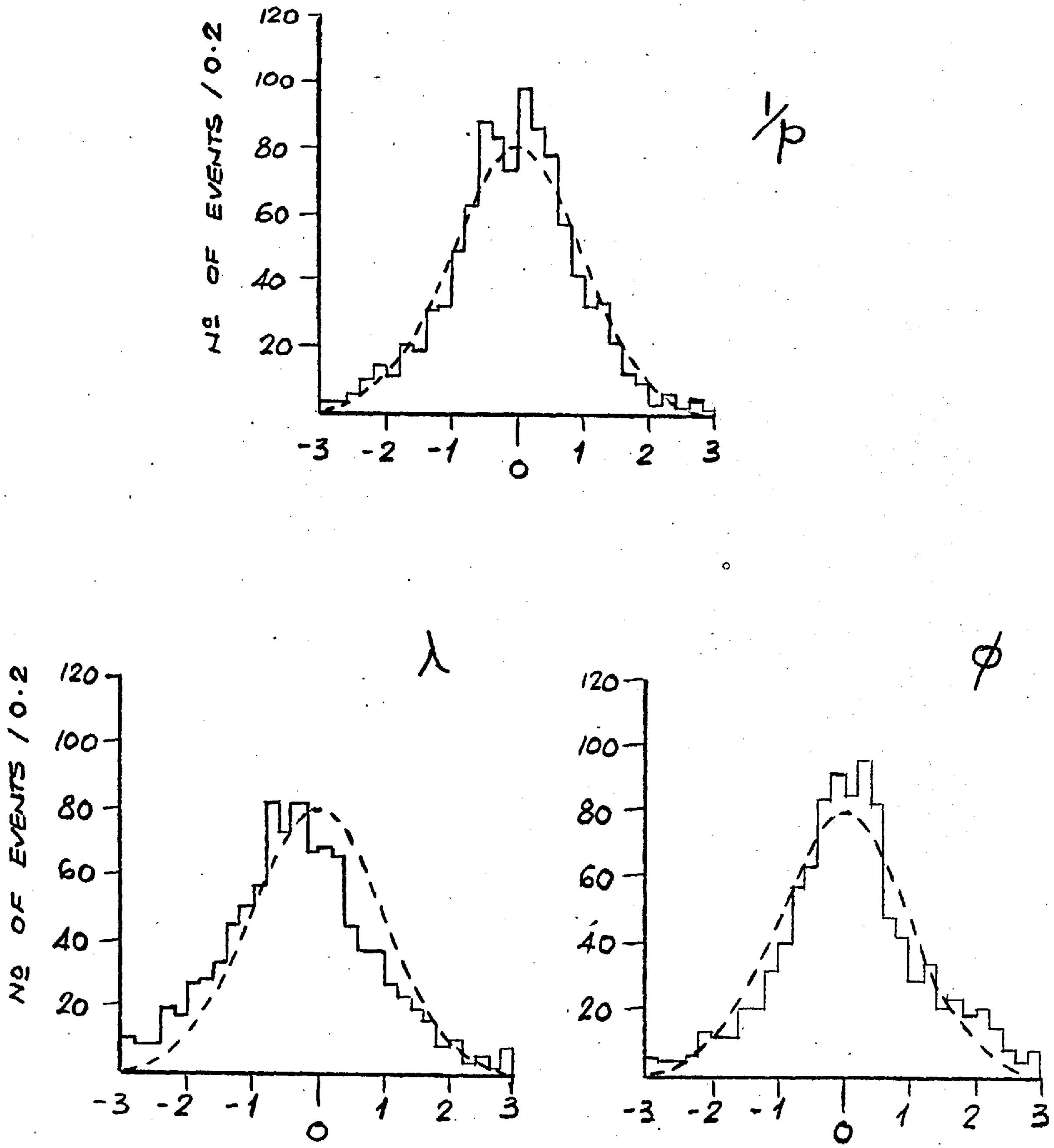

CORRECTED BEAM STRETCH FUNCTION DISTRIBUTION

Fig. 4.5

Referring to the figure above λ_{1t} , λ_{2t} are true dip angles while λ_{1m} , λ_{2m} are measured dip angles for the first and second part respectively of the same beam track.

$$\therefore \quad \lambda_{2m} - \lambda_{1m} = \lambda_{2t} - \lambda_{1t} + \epsilon_2 + \epsilon_1$$

Now λ_{1t} is equal to λ_{2t} because they are the <u>same</u> beam track and the convention in THRESH is to take small dip angles.

$\therefore \ \Delta\lambda = \epsilon_1 + \epsilon_2$ (from the plotted results of fig. 4.3)

In this case one assumes that the whole length of beam track has been measured, so $l_1 + l_2$ is constant (L). Thus

$$\Delta\lambda = (\alpha L + \beta_2 L^2) - 2\beta_2 L l_1 + (\beta_1 + \beta_2) \quad l_1^2$$

If this is to agree with $\epsilon_0 + \gamma l_1$ (appendix II) then

$$\epsilon_0 = \alpha L + \beta_2 L^2$$

$$\gamma = -2\beta_2 L$$

$$\text{and } \beta_1 = -\beta_2 = \beta \qquad \ldots\ldots\ldots\ldots \ (4.3)$$

Substituting (4.3) into (4.1) and (4.2) we find

$$\Delta\lambda = \alpha L - \beta L (L - 2l_1) \qquad \ldots\ldots\ldots\ldots \ (4.4)$$

The "maximum likelihood" method was employed to fit the difference in dip angle of the measured beam track. This yielded:-

$$\alpha = 0.908 \times 10^{-5} \quad \text{m-rad/cm}$$

$$\text{and} \quad \beta = -0.453 \times 10^{-7} \quad \text{m-rad/cm}^2$$

Therefore the corrected functions, before the kinematic fitting are:-

$$\Lambda_1 = \Lambda_{1m} + (\alpha l_1 + \beta l_1^2)$$

$$\Lambda_2 = \Lambda_{2m} - (\alpha l_1 - \beta l_2^2)$$

Λ_1, Λ_2 are the corrected dip angles and should be the same. A typical correction to any track having a length of the order of a hundred cm will be:-

1.35 m-rad for the first part of the chamber

and 0.45 m-rad for the second part of the chamber

This is further evidence indicating a strong distortion in the beam <u>entry</u> region that decreases toward the chamber exit. In conclusion the correction is not greatly different from results for the first (linear in X) attempt. The beam stretch function distributions show a similar structure to figure 4.4, in particular, for the variable Λ which is s till shifted to the left from zero value.

(iii) <u>Trial fitting of $\Delta\Lambda = a/(b+x)$</u>

This is an equivalent method to that employed by Cambridge[39]. The following different conditions are summarized:-

Cambridge (Cavendish) Laboratory	Imperial College
Only $\beta_1 \ldots \beta_6$ coefficients in optical distortion formula.	$\beta_1 \ldots \beta_6$ coefficients in optical distortion for X coordinate and one additional β_7 in Y coordinate.
Own geometric reconstruction and kinematic fitting programme.	CERN standard THRESH and GRIND programme.
Two point measurements were used to determine the beam dip angle.	Dip angle was obtained in THRESH as the angle between the tangent of the beam and the X-Y plane.
The correction relating to X and Z coordinates can be written as:- $Z = Z - \frac{(X + 57)}{100}$; $X \quad -57$ cms $Z = Z$ for $X \quad -57$ cms $Z = Z$ coordinate after correction.	Fitting formula:- $\Delta\Lambda = \frac{a}{b + x}$ The correction relation is $\Lambda = \Lambda_0 - \Delta\Lambda$ yielding the result $a = 0.131$ rad/cm and $b = 121.4$ cm
Z axis pointing away from camera position.	Z axis pointing towards camera position.

In both cases a small increase in the mean error in the geometrical programme was allowed for the uncertainty in each procedure.

The dashed line in figure 3.4a illustrates the curve $\Delta\lambda = 0.131/(121.4 + X)$ fitted to the measured beam tracks. Figure 4.6 shows the Stretch function distributions of the beam track variables ($1/p, \lambda, \phi$). A clear improvement can be seen particularly in the dip angle. The distributions are peaked at the right place, but their widths are narrower compared to the normal distribution curves (dashed lines) in figure 4.6. An incorrect estimate of fitting errors is a possible explanation.

In order to test the effectiveness of this optimisation, the statistic programme was run to produce from the D.S.T. a number of preliminary histograms (angular distribution, invariant mass distributions, etc.) for three regions of the fiducial volume extends over approximately equal length in the x-direction.

It is worth noting that, in general, one would expect to see better structure for events occurring in the first (entry) region compared to the other two regions, because these events have longer secondary particle tracks and would be measured relatively more accurately. Hence one would expect a better mass resolution.

However, it was concluded from a comparison of results that there was no indication of better structure in the first or entry region; on the contrary, it could be worse and probably shows a less impressive resonance when

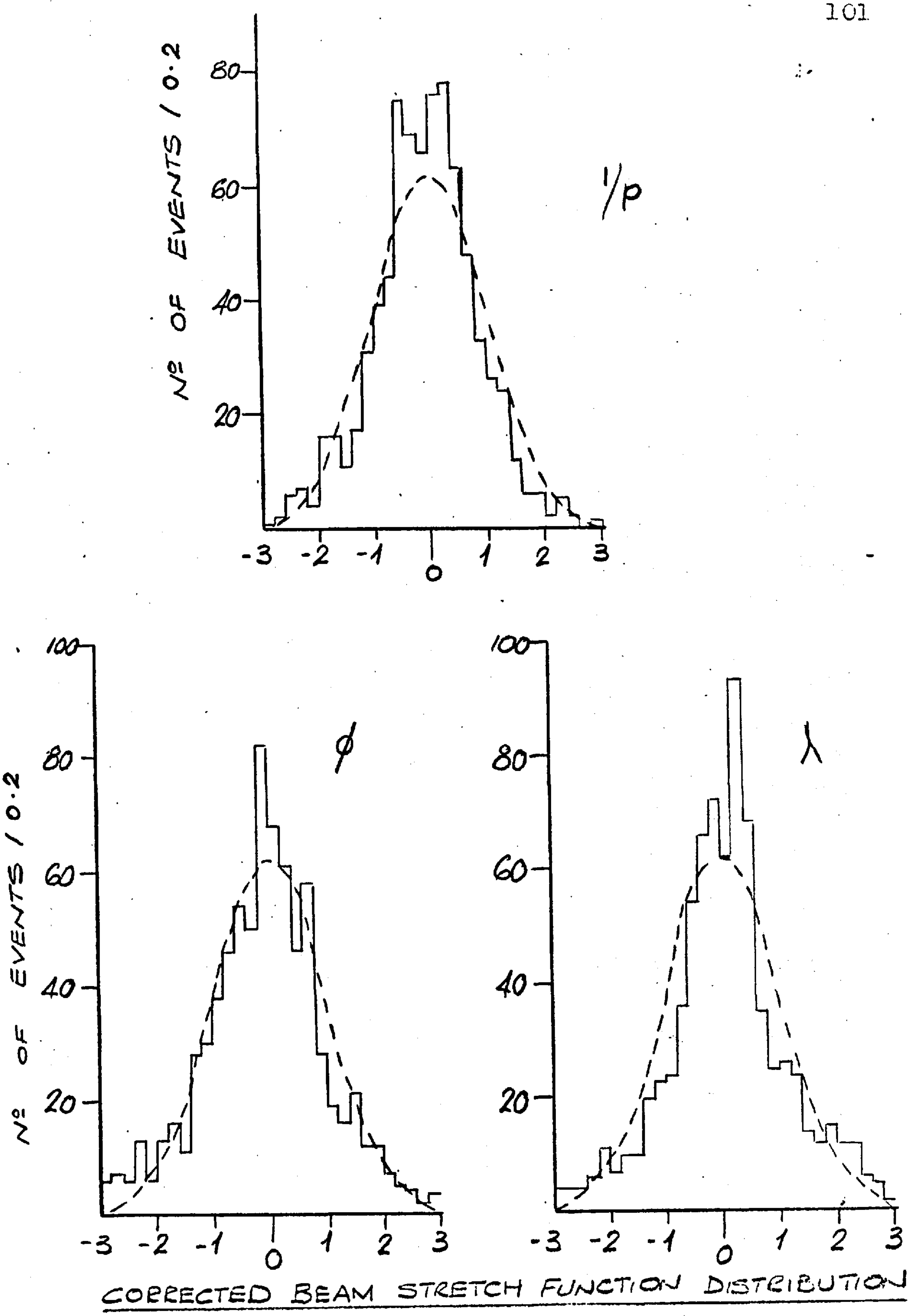
Nº OF EVENTS / 0·2
80
60
40
20
1/p
-3
-2
-1
0
1
2
3
100
80
60
40
20
φ
λ
CORRECTED BEAM STRETCH FUNCTION DISTRIBUTION

Fig. 4.6

there is an enhancement in the other two regions. One set of typical comparison histograms for proton-pion invariant mass combination is shown in figure 4.7. Thus no satisfactory conclusion can be drawn at this stage.

(iv) Exluding 10 cm of the beam entry region

In addition to the previous report(45) from CERN, some further information indicates that in the beam entry region, some events were reconstructed badly due to a distortion. A rejection of these events has been suggested, but, despite this, the β_7 coefficient is still required in THRESH.

Subsequently X = -65 cm was set as the minimum value for any measured point to be accepted by THRESH. Some of the events already measured would fail under this condition because the beam track has been cut shorter, resulting in tracks too short to be measured for curvature. An alternative method is to impose the beam variable from the title block for these events separately. Since only a few hundred 4C events have been reprocessed through THRESH for this test, the number of failed events was small and so they were neglected.

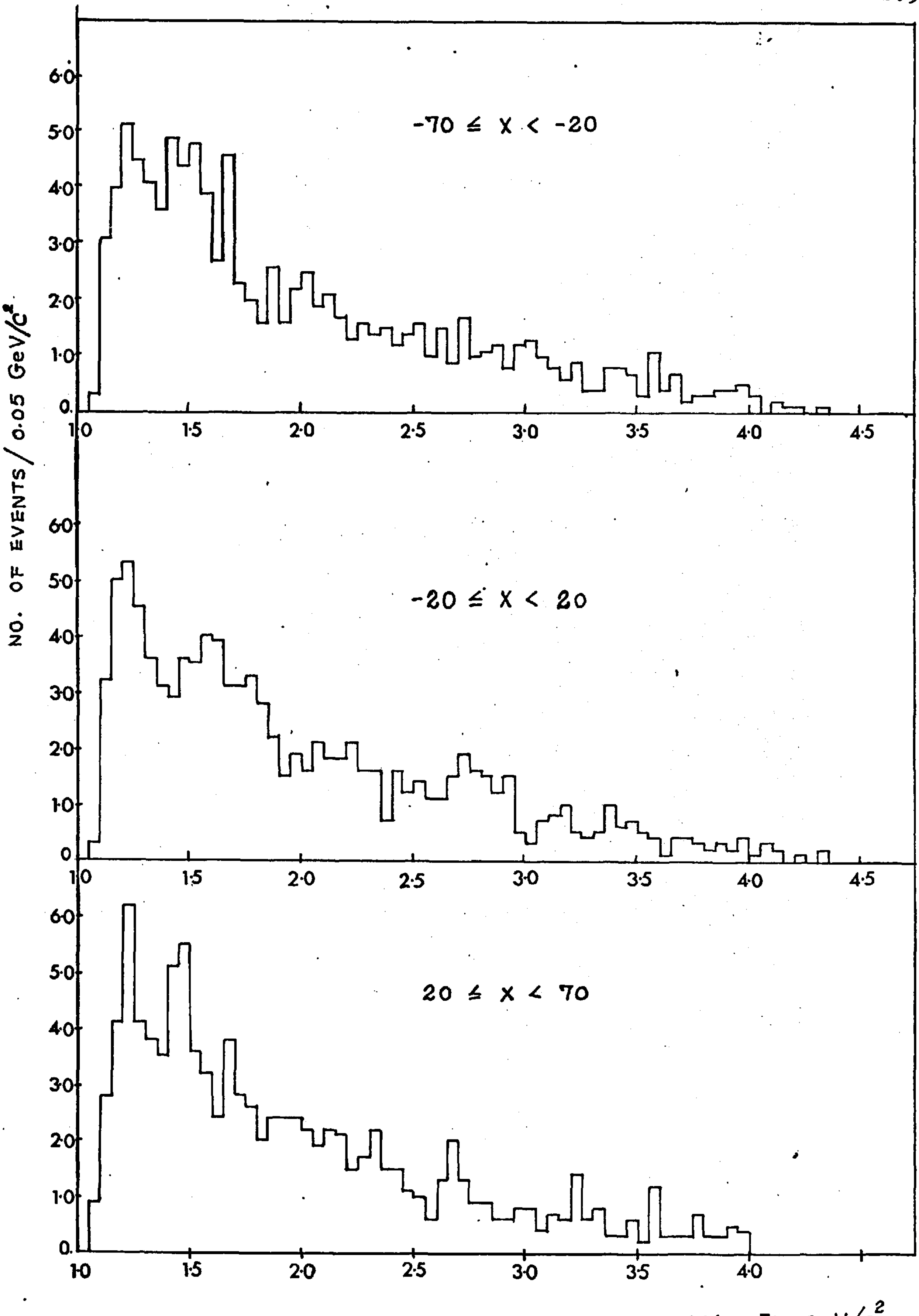
NO. OF EVENTS / 0·05 GeV/c²
-70 ≤ X < -20
-20 ≤ X < 20
20 ≤ X < 70
6·0
5·0
4·0
3·0
2·0
1·0
0.
1·0
1·5
2·0
2·5
3·0
3·5
4·0
4·5
M(pπ⁻) GeV/c²

Fig. 4.7

It is very important, before reconstructing the measured beam tracks under this new condition in THRESH and before any further decision is made, to see if the differences in dip angle for the same beam track were improved. The differences in dip angle are plotted versus the arificial apex (X-coordinate) together with its projection (figure 4.8 a - b). After fitting to $\Delta\lambda = \dfrac{a}{b + X}$ one obtains the result:-

$$a = C.120 \text{ rad cm}; \; b = 95.4 \text{ cm}.$$

This is similar to (iii).

It is interesting to note that the beam stretch function distribution (in particular the invariant mass distribution) are very similar to those obta ined by method (iii). This is considered sufficient to justify the correction.

(v) <u>The transformation of the Rutherford Laboratory's constants</u>

Rutherford Laboratory has developed an alternative optimisation programme for finding a set of constants for CERN 2M HBC. Some better results have been claimed, especially when applied to their own geometric reconstruction programme. Their set has been changed by an I.C. transformation programme* into an appropriate format for use in THRESH.

* The writer wishes to thank Mr M.Losty for assistance in writing the transformation programme.

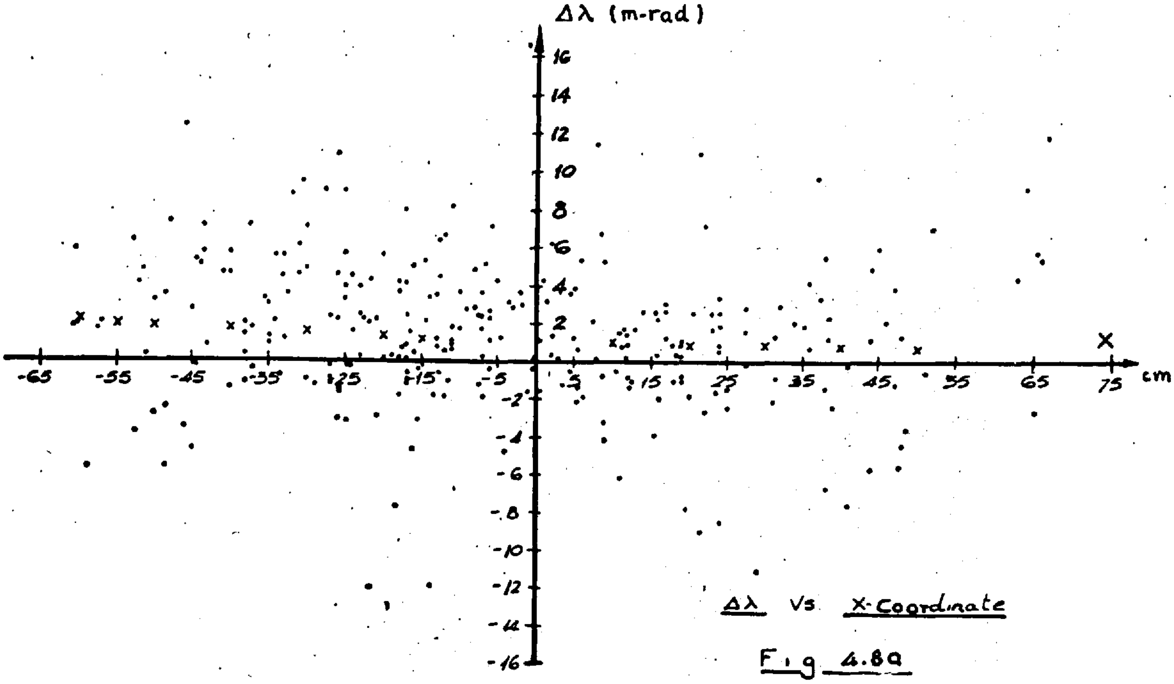

Δλ Vs X-Coordinate

Fig 4.8a

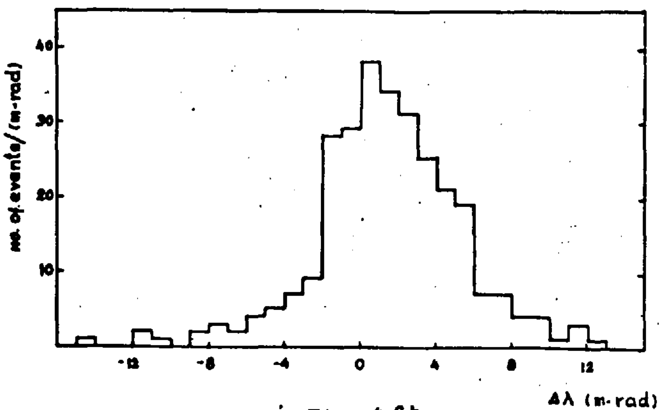

Fig. 4.8b

In general, if the best set of constant has been obtained for any geometric reconstruction programme of a bubble chamber experiment, then only the standard optical distortion coefficients ($\beta_1 \dots \beta_6$) are required. The reconstruction of the measured beam tracks is a sufficient and powerful test of this new reconstruction constant set. Figure 4.9 shows the scatter plot of $\Delta\lambda$ for the beam track versus the X coordinate of the artificial apex. No fitting of these points has been attempted because of the wider spread of the points than previous cases (see figure 3.4a). It appears that the new set of constants has probably resulted in an increase in the differences in the dip angle of the beam tracks. It does appear that the individual method of obtaining each constant set results in it being only suitable for its own geometric reconstruction procedure.

(vi) The two-view Procedure - For a long time the three-view geometric reconstruction programme (THRESH) has been used successfully for bubble chamber analysis. Up to now for the present experiment we have not yet obtained any satisfactory set of constants for reconstruction (in particular the optical distortion coefficients) despite repeated efforts. The use of only two-views for geometric reconstruction is permissible provided the best two-views (the line joining these two appropriate camera lenses is most nearly perpendicular to the track in the X Y plane) are chosen. The two appropriate cameras for

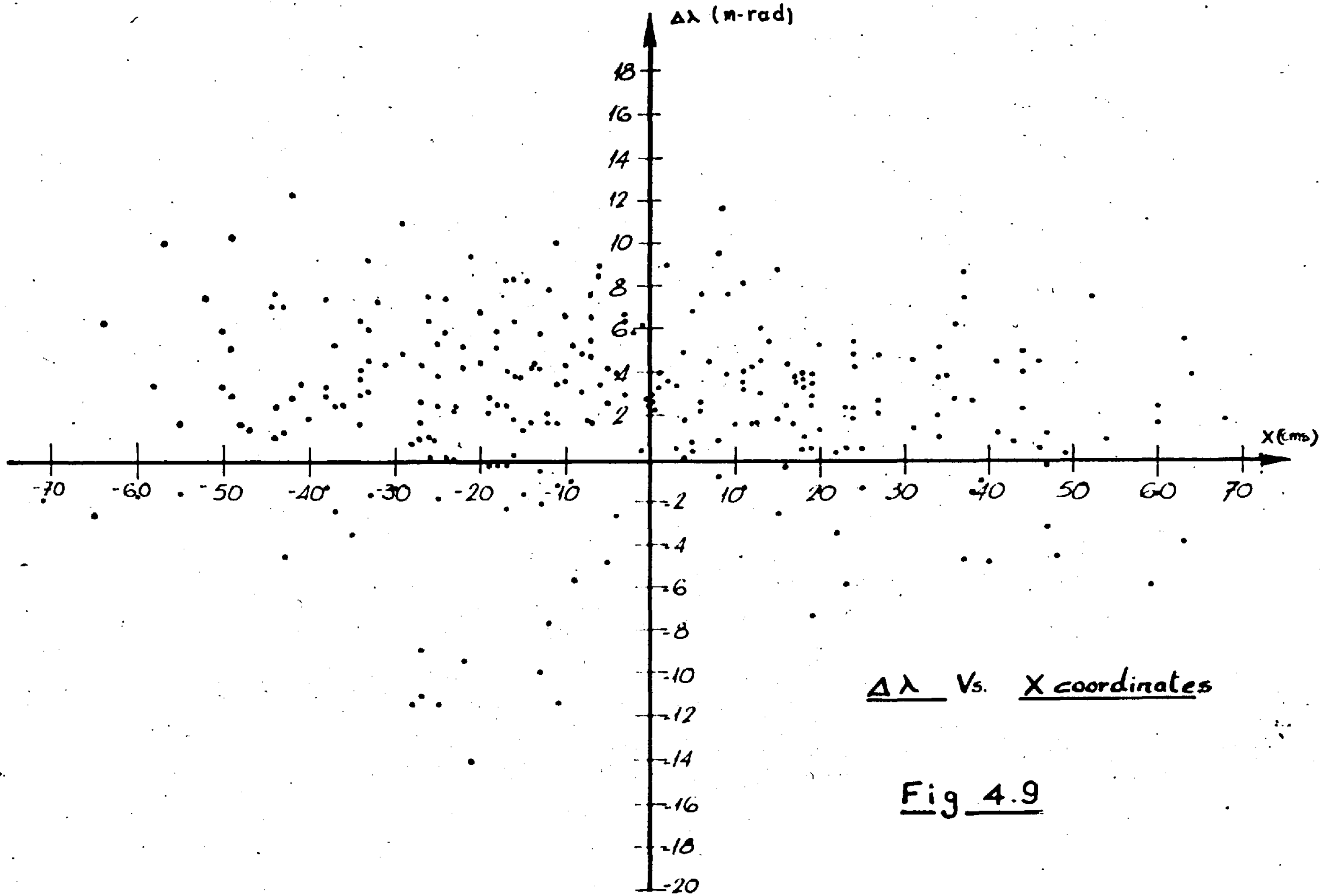

Δλ Vs. X coordinates

Fig 4.9

the present experiment are camera 1 and 4 (see figure 2.3) because most of the particles having a high energy especially the beam track would travel very fast in a forward direction in the chamber, thus yielding the best stereoscopic condition. For camera 3, the view is more tangental to the tracks, and thus would not give a very good result as it would broaden the average values for reconstructed points and tracks.

As a check the measured beam tracks were thoroughly processed through BIND and THRESH to ensure that the two data yielding views for reconstructing points and tracks were adequat and reliable enough for data analysis. The observation of the $\Delta\Lambda$ distribution and the scatter plot of $\Delta\Lambda$ against the artificial X coordinate of the apex in figure 4.10 (a - b), suggests that on average the differences in dip angle consistently lie about 2.5 m-rad away from the zero axis through the chamber. This correction has therefore been applied on a sample of 4C events before GRIND and the resultant beam stretch function distribution as shown in figure 4.11. The uncorrected distribution curves normalised to the data are also illustrated in figure 4.11 and show that the beam dip angle stretch function distribution is still pecked at a negative value.

Furthermore, the author has tried to run GRIND on these events with an increase in the control errors for momentum instead of correcting the beam dip angle. This allows a larger adjustment in momentum range during fitting. This leads in turn

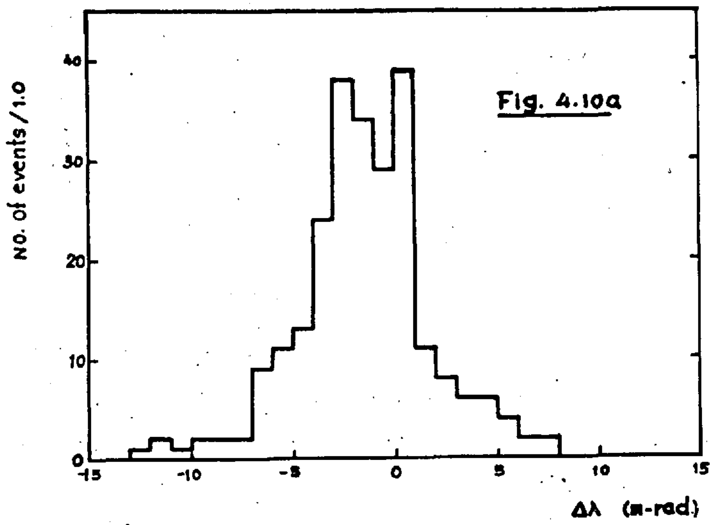

Fig. 4.10a

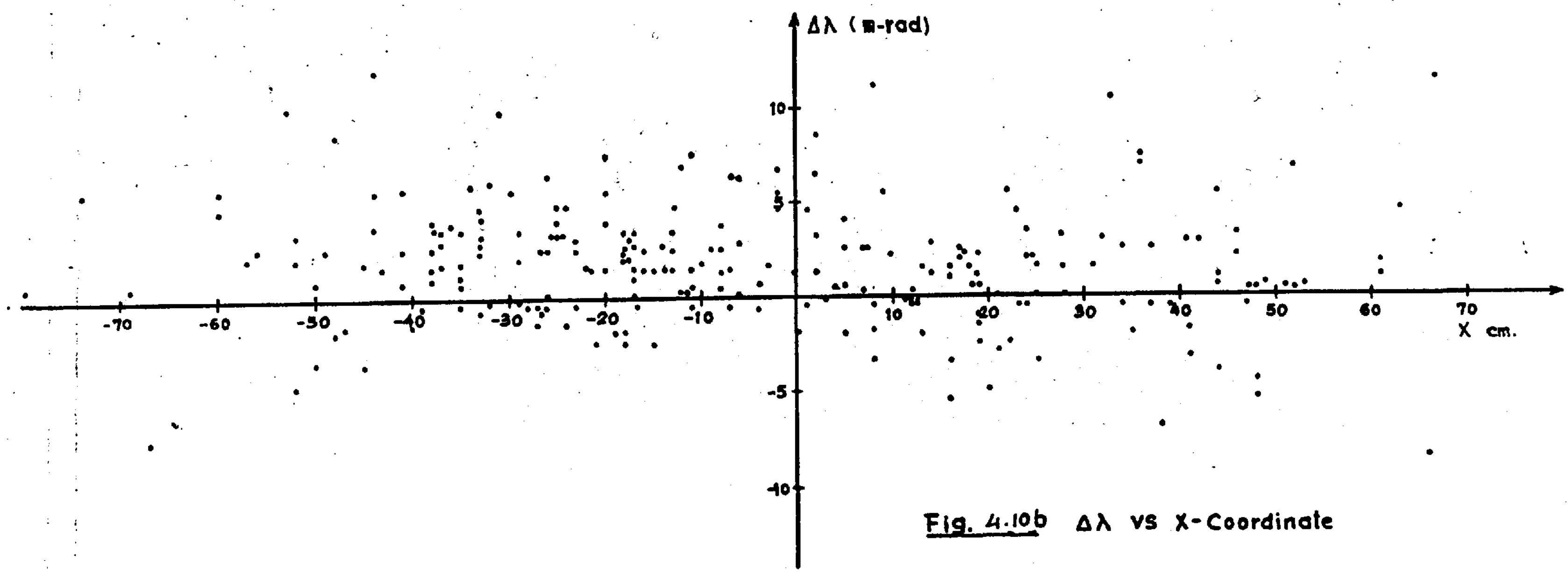

Fig. 4.10b Δλ vs X-Coordinate

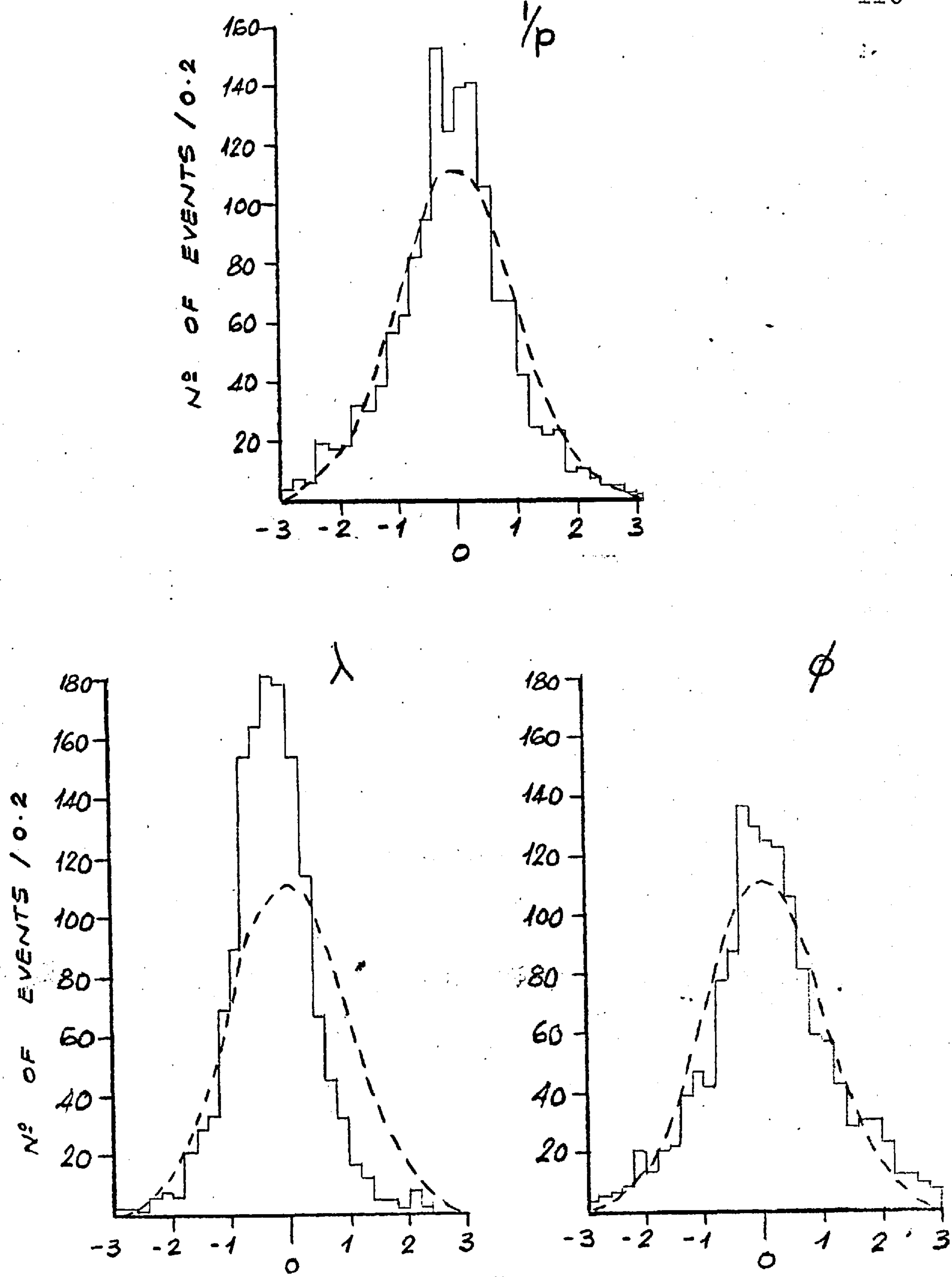

CORRECTED BEAM STRETCH FUNCTION DISTRIBUTION

Fig. 4. 11

to an improvement in the dip angle stretch function distribution (figure 4.12) and gives the peak at the right position as expected, but the width is narrower than it should be. Although the method described gives a satisfactory result as far as systematic errors are concerned, it is not justified due to the fast proton inconsistency at high energy.

4.4 Summary

In conclusion, the author found that after all possible attempts to eliminate the differences in beam dip angle were completed and tested, it was not possible to correct the remaining distortion in the chamber perfectly. The slow/fast proton inconsistency is partly due to the distortion of the chamber and partly due to an inability to measure the different curvature tracks to the same degree of accuracy (see section 2, Chapter 8). Despite this, in order to obtain the best beam stretch function distributions and the best invariant mass distributions, it had been decided to use the three-view geometrical programme (THRESH) with a 7-parameter fit for the optical distortion coefficient. In addition to this, the length dependent correction (method (ii)) for the beam dip angle is considered to be necessary because most of the tests described have shown that somehow the distortion varied along the chamber. An appropriate increase in fitted errors for the uncertainty in the procedure was also taken into account.

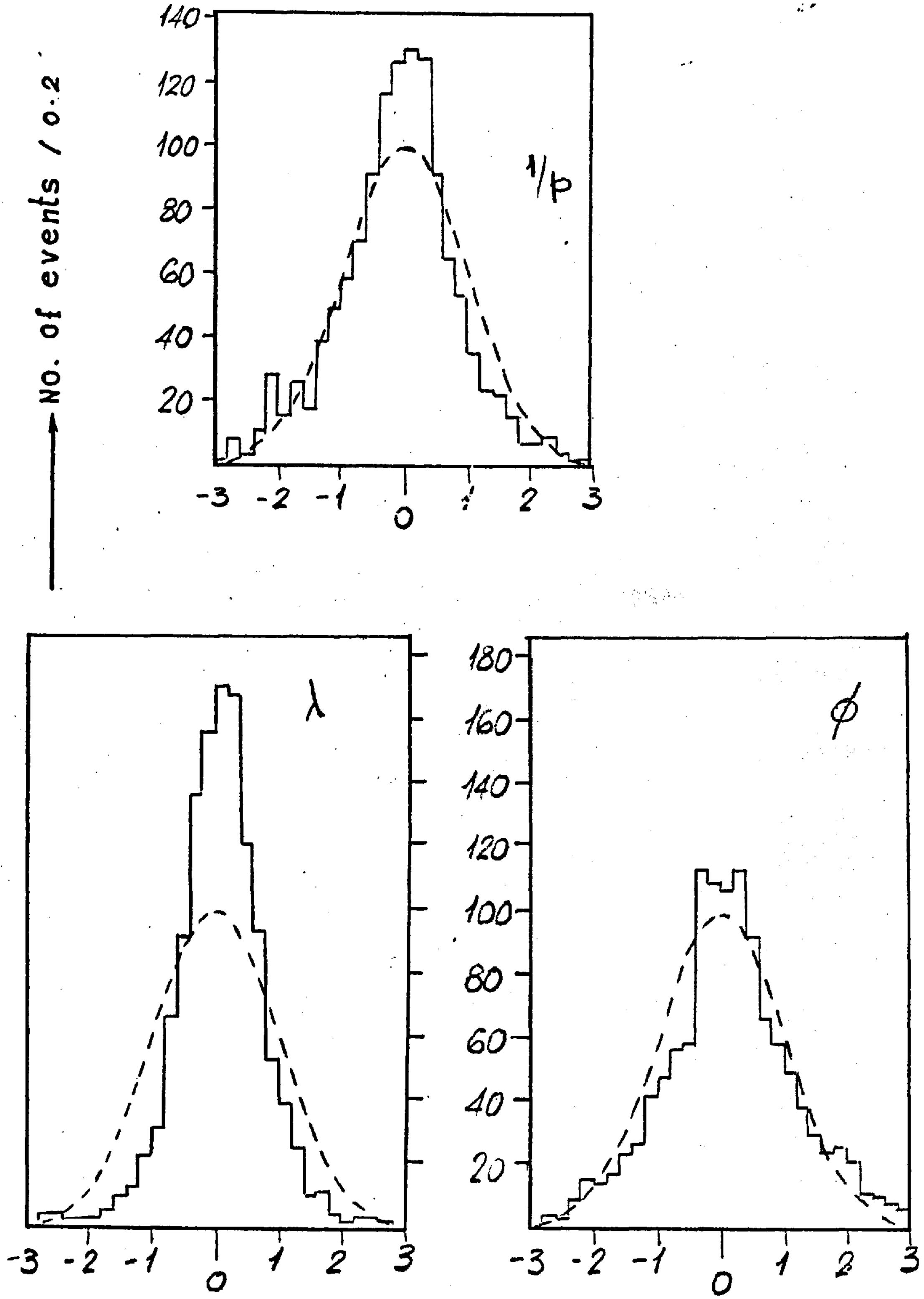

CORRECTED BEAM STRETCH FUNCTION DISTRIBUTION

Fig 4.12

CHAPTER 5

GENERAL KINEMATIC PROPERTIES OF PARTICLE PRODUCTION

5.1 INTRODUCTION

The three most important kinematic features of high energy nucleon-nucleon collisions are:-

(i) Nature of the number of secondary particles and the energy partition amongst these.

(ii) The distribution in angle, energy and transverse momentum of the created particles.

(iii) Correlation between properties of the secondary particles.

These are all accessible for investigation.

The inherent symmetry of the proton-proton collision in the initial state, and the fact that these particles are charged, makes this interaction easier to investigate than the neutron-proton collision. At low multiplicity the baryons are strongly collimated in the forward and backward direction while the mesons are less well collimated. Such collimation decreases with the increase in multiplicity up to a six body final state[54]. The meson angular distributions are found to be isotropic (in this case the baryons are also distributed nearly isotropically). As more pions are produced more resonances are likely to occur, or conversely, the increase of pions may be due to the baryon resonance production. Thus the decay distribution of such resonances results in a decrease in the forward backward peaking of the individual particles. Furthermore, the tendency towards greater isotropy at high multiplicity is consistent with the idea that the more complex, highly inelastic, reactions occur in the low partial wave.

The general features of transverse and longitudinal momenta in terms of the final state multiplicity can be briefly described[56]:-

(i) The transverse momentum distribution P_t^* of each individual particle in the final state is independent of particle type but the averaged transverse momentum shows a slight tendency to move to higher values for heavier particles.

(ii) As the shape of the P_t^* distribution is particle independent, $\sum_i |P_t^*|$ the sum of the magnetudes of P_t^* for all final state particles has a similar shape for the full range of multiplicities. The peak of this distribution however narrows with increasing multiplicity.

(iii) In the C.M.S. P_l^* the longitudinal momentum of each particle is, in general, randomly distributed in the forward and backward direction, but, the peak of the distribution of the sum of the magnitudes of P_l^* for all particles $\left(\sum_i | P_l^* | \right)$ shows a characteristic shift to lower values with increasing multiplicity.

Missing mass distribution - For a given mass assignment to each track of an event, the quantities missing mass, missing energy and missing momentum, are calculable from the measured and fitted values and the experimental errors, as described in Chapter 2.

Thus, if $E_m = \sum_i E_i$ is the missing energy

and $P_{mx} = \sum_i P_{ix}$ is the missing momentum in the x-direction

then M_m the missing mass is given by:-

$$M_m^2 = (\textstyle\sum_i E_i)^2 - ((\sum P_{ix})^2 + (\sum_i P_{iy})^2 + (\sum_i P_{iz})^2) \quad \ldots\ldots\ldots (5.1$$

In the case where all the particles produced are observed, and therefore the missing quantities are almost zero, the distribution of the squares of the missing mass(M_m^2) is not centred around zero, but shifted to a negative value. This striking feature of the distribution of this quantity is shown in figure 5.1a for the 16 GeV $pp \longrightarrow pp\,\pi^+\pi^-$ reaction and is accompanied by the distribution of the squares of the corresponding errors in figure 5.1b. The scatter plot of these quantities is also shown in figure 5.1c.

A possible mathematical explanation of this shift[55] is as follows:-

Consider a Taylor expansion of equation (5.1), keeping terms up to the second order in P_i, with the following two assumptions:-

(i) only the error in the momentum (Δp) is considered since $\Delta\lambda$ and $\Delta\phi$ are small and can be ignored.

(ii) Δp is normally distributed about zero.

Now $E_o = \sum_i E_{oi}$ the true missing energy = 0

and $P_o = \sum_i P_{oi}\,\nu_i$ the true missing momentum = 0

where $\nu_i = l_i, m_i, n_i$ are the direction cosines for the i^{th} particle

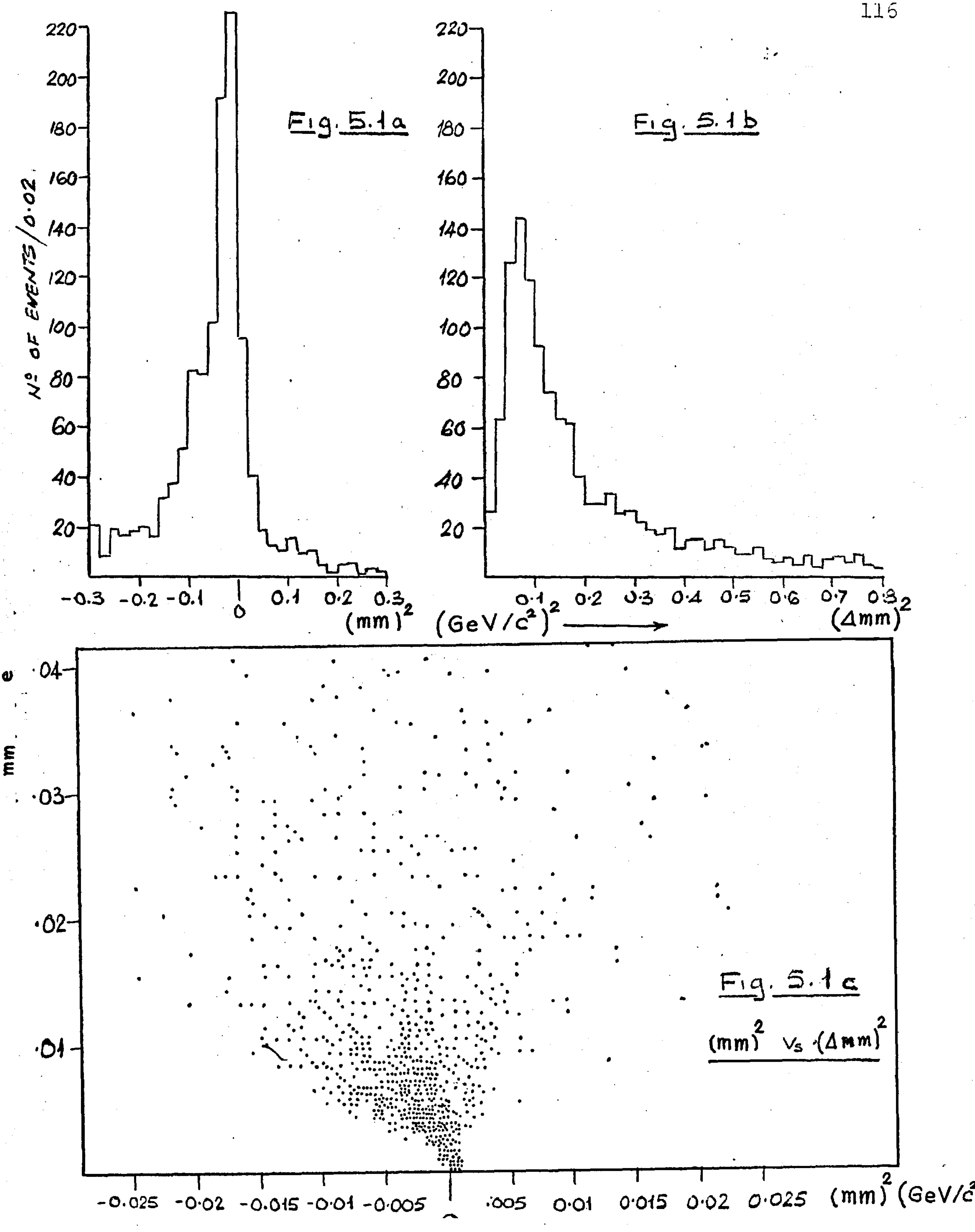

Fig. 5.1a

Fig. 5.1b

Fig. 5.1c

(mm)² Vs (Δmm)²

The expansion of equation (5.1) can be written:-

$$M_m^2 = \left\{\left[\Sigma_i E_{oi} + \frac{\partial E_i}{\partial P_i}\Delta P_i + \tfrac{1}{2}\Sigma_i \frac{\partial}{\partial P_i}\Sigma_j \frac{\partial \Sigma E_k}{\partial P_j}\Delta P_i \Delta P_j\right]\right\}$$

$$- \Sigma_{\nu = l,m,n}\left\{\Sigma_i (P_{oi}\nu_i) + \Sigma_i \frac{\partial}{\partial P_i}(\Sigma_j P_j \nu_j)\Delta P_i + \tfrac{1}{2}\Sigma_i \frac{\partial}{\partial P_i}\Sigma_j \frac{\partial \Sigma P_k \nu_k}{\partial P_j}\Delta P_i \Delta P_j\right\}^2 \quad \ldots\ldots\ldots\ldots (5.2)$$

From the assumptions described we obtain:-

$$\Delta P_i \Delta P_j = 0 \quad \text{where} \quad i \neq j$$

$$\text{and} \quad \Sigma E_{oi} = \Sigma_i P_{oi}\nu_i = 0$$

Thus the missing mass formula becomes:-

$$M_m^2 = \left\{\Sigma_i \frac{\partial \Sigma E_j}{\partial P_i}\Delta P_i\right\}^2 - \left\{\Sigma_\nu \Sigma_i \frac{\partial}{\partial P_i}(\Sigma P_j \nu_j)\Delta P_i\right\}^2 \ldots\ldots\ldots (5.3)$$

Let $\frac{\partial \Sigma E_j}{\partial P_i} = \beta_i = v/c$ (the velocity of particle/velocity of light)

$$\frac{\partial}{\partial P_i}\Sigma P_j \nu_j = \nu_i$$

$$l^2 + m^2 + n^2 = 1 \quad \text{then,}$$

$$M_m^2 = \Sigma(\beta_i^2 - 1)\Delta P_i^2 \quad \ldots\ldots\ldots (5.4)$$

Thus the calculated value for the square of the missing mass eqn (5.4) is always negative because

$$\beta_i \leq 1$$

5.2 The Single Particle Distribution for the Centre of Mass System (C.M.S.)

The general kinematic properties for the individual particles in the final state:

$$pp \longrightarrow pp\pi^+\pi^- \qquad \ldots\ldots\ldots (1)$$

are discussed and an attempt has been made to fit some statistical models to the experimental data.

5.2.1 Angular Distributions - A scattering or production angle (θ^*) is used to describe the configuration of a particle, or combination of particles, in the final state. This angle is defined by :-

$$\mathrm{Cos}\theta^* = \vec{P}_f \cdot \vec{P}_i \qquad \ldots\ldots\ldots (5.5)$$

where $\vec{P}_f$ and $\vec{P}_i$ are unit vectors in the direction of the final particle (or combination of particles) and the incident particle (proton) respectively in the overall centre of mass system.

Figures 5.2a - 5.2c show the actual C.M. angular distribution of the protons and the pions for reaction (1). The forward/backward peaking of the protons along the incident particle direction suggests that some peripheral mechanism is important in this reaction. The pion C.M. angular distributions are less sharply peaked than those derived for the protons One of the main difficulties in the quantitative analysis of high energy proton-proton interactions is distinguishing between two protons and other high energy particles in the final state. On account of the inherent symmetry of this reaction in the

* An asterisk denotes the quantity in the C.M.S.

Fig. 5·2

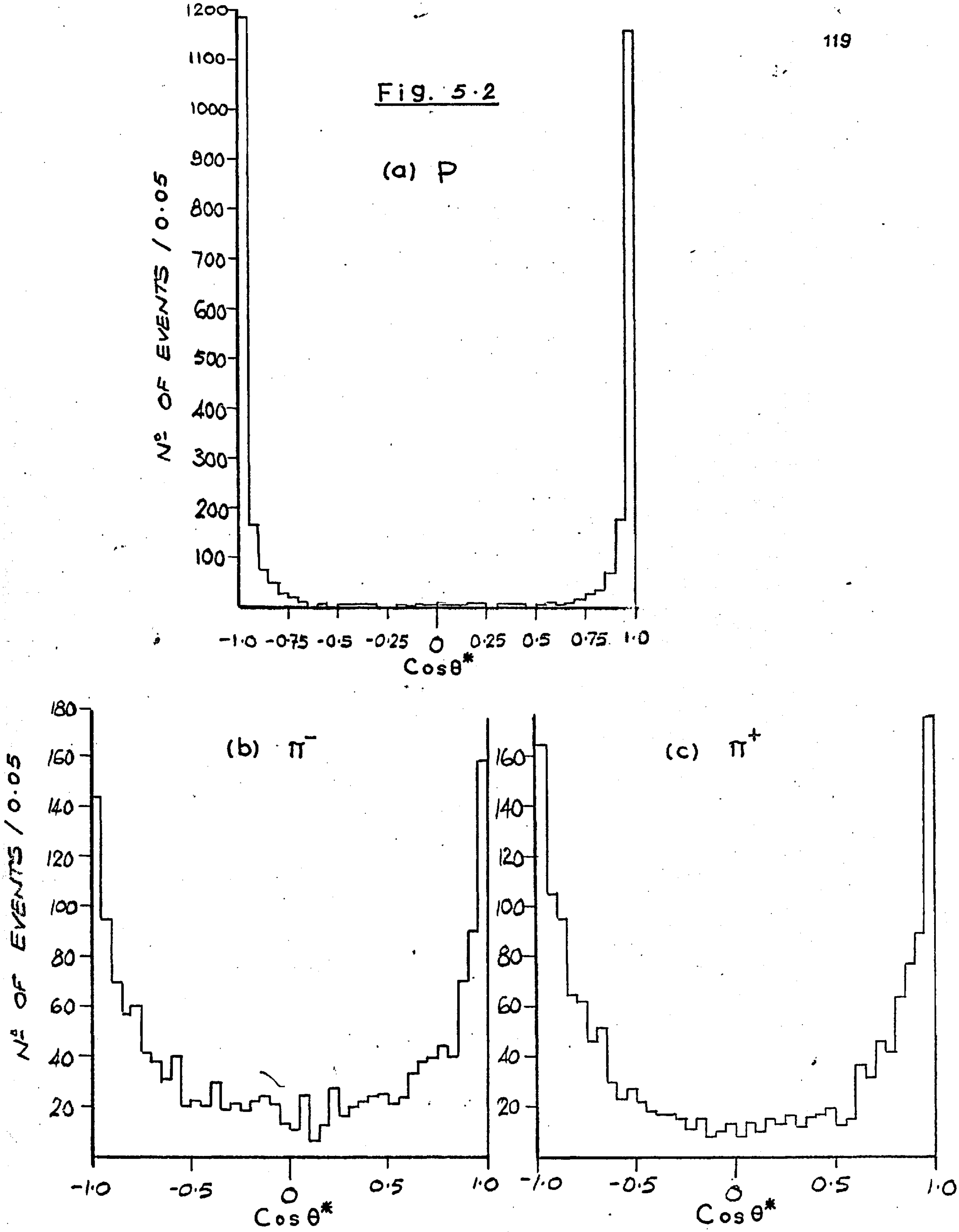
(a) P
Nº OF EVENTS / 0·05
1200
1100
1000
900
800
700
600
500
400
300
200
100
-1·0
-0·75
-0·5
-0·25
0
0·25
0·5
0·75
1·0
Cos θ*
(b) π⁻
(c) π⁺
Nº OF EVENTS / 0·05
180
160
140
120
100
80
60
40
20
-1·0
-0·5
0
0·5
1·0
Cos θ*

C.M.S., one would expect the forward to backward scattering ratio to be zero for any particle. In practice this is not so. Several selections have been made, in order to eliminate two protons produced in the same hemisphere, and so reduce the number of the misidentified fast particles. The ratio (forward - backward)/(forward + backward) for protons and pions for various cases are listed in table 5.1. A small excess of backward pions indicated that some misidentification has occurred.

Figure 5.3 (scatter plot of $\cos\theta^*_{\pi^+}$ versus $\cos\theta^*_{\pi^-}$) shows further evidence of peripheral collisions. One can see a clear depopulation in the central region. This correlation suggests that about 2/3 of the events involve two pions travelling into the same hemisphere, or away from the same vertex. This corresponds to neutral exchange which could well be associated with the enhancement of the low ($p\pi^+\pi^-$) mass. The remaining 1/3rd of the events (where the pions travel into opposite hemispheres or away from different vertices) correspond to charge exchange.

5.2.2 <u>Transverse and Longitudinal Momentum</u> - Very early workers[56,57] drew attention to the fact that the mean value of the transverse momentum component $\langle P^*_t \rangle$ for secondaries always was approximately 0.4 GeV even though they are produced from the nuclear collisions of primaries with widely varying energies. Furthermore the shape of the P^*_t-distribution is always the same. Therefore it has become

TABLE 5.1

Backward-forward asymmetries for protons and

f = no forward b = no backward

The excluded events	(Proton) $\frac{f-b}{f+b}$	(π^+) $\frac{f-b}{f+b}$	(π^-) $\frac{f-b}{f+b}$
-	-44/3096	-82/1548	-60/1548
where two protons travel into the same hemisphere	0/1312	-106/1506	-56/1506
$-t(p - p) < 0.05 (GeV)^2$	-44/2444	-58/1222	+10/1222
where the quality of film is bad	-38/2538	-47/1269	--21/1269

TABLE 5.2

Particle	$\langle p_t^* \rangle$ (MeV)
p	403
π^+	259
π^-	357

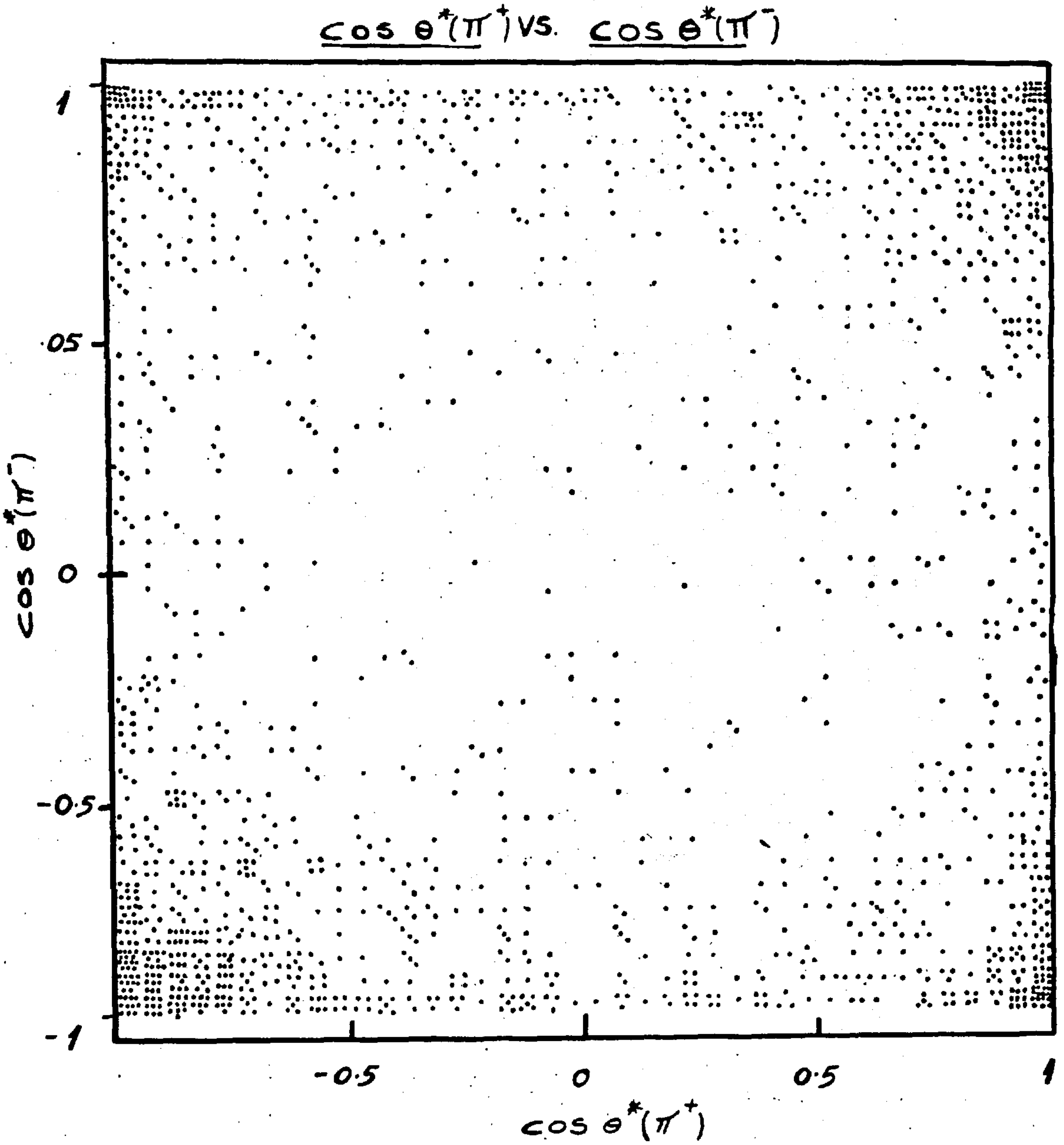

Fig 5.3

common practice to assume that the distributions may be represented by the relation:-

$$N\,(P_t^*)dP_t^* = \frac{\pi}{2\sigma^2}\,P_t^*\,\exp\left(\frac{-P_t^{*2}\pi}{4\sigma^2}\right)dP_t^* \quad \ldots\ldots\ldots \quad (5.6)$$

where P_t^* = the transverse momentum in c.m.s

σ = standard deviation (this implies that P_y and P_z are both normally distributed; $P_t^* = \sqrt{P_y^2 + P_z^2}$).

and that the distribution P_t^* is in insensitive to the physical characteristics of the interaction. For proton-proton collisions of fixed energy, the transverse momentum distributions of the secondary particles fit, with reasonable accuracy, the simple exponential expression:-

$$dN/dP_t^* \propto \exp(-P_t^*/A)$$

where $A \approx$ 165 MeV. This value is found from 10 - 30 GeV pion production work as well as cosmic rays data up to 10^5 GeV[58].

Recently, however, with somewhat better statistics, several attempts[54,57,59] have been made to fit the observed distribution of P_t^* with various analytical expressions. Satisfactory fits have been claimed proving consistency of the P_t^* distribution law in all physical situations so far investigated. However, other authors[59] have obtained contradictory results in which the form of the P_t^* distribution is sensitive to the various physical parameters of the interaction (e.g. primary energy, nature of the secondary particle, etc.) In particular it has been claimed that the P_t^*-distribution for baryons obeys a Boltzmann-type law, while the law for pions is a superposition of two such distributions with widely different numerical parameters. For the pion case the mean value of P_t^* is almost constant and independent of the details of the meson production process.

For the interaction of interest with four particles in the final state : $1 + 2 \longrightarrow 3 + 4 + 5 + 6$

Wu and Yang[57] suggested that the "fall off factor" for the sum of the magnitudes of P_t $\left(\sum_{i=1}^{4} |P_t^*|\right)$ should vary as $\exp\left(-\sum_{i=1}^{4}|P_t^*|/0.3\right)$.

The actual transverse momentum distributions for the protons and pions produced in reaction (1) are shown, with fitted curves, in figures 5.4a - 5.4b respectively. The mean transverse momentum $\langle P_t^* \rangle$ for each final particle is listed in table 5.2 and the distributions have been fitted to the function:-

$$N(P_t^*) \propto P_t^* \exp(-P_t^*/A) \qquad \text{........ (5.7)}$$

This is the simples model which can give a reasonable description of the experimental results. The fitted value from this experiment is in good agreement with the early work as described, yielding:-

$A = 165.9 \pm 2.1$ (MeV) for pions

and $A = 198.8 \pm 2.2$ " for protons

The distribution of the sum of the magnitudes of the transverse momenta for all particles in the final state of the reaction $pp \longrightarrow pp\,\pi^+\pi^-$ is shown in figure 5.5.

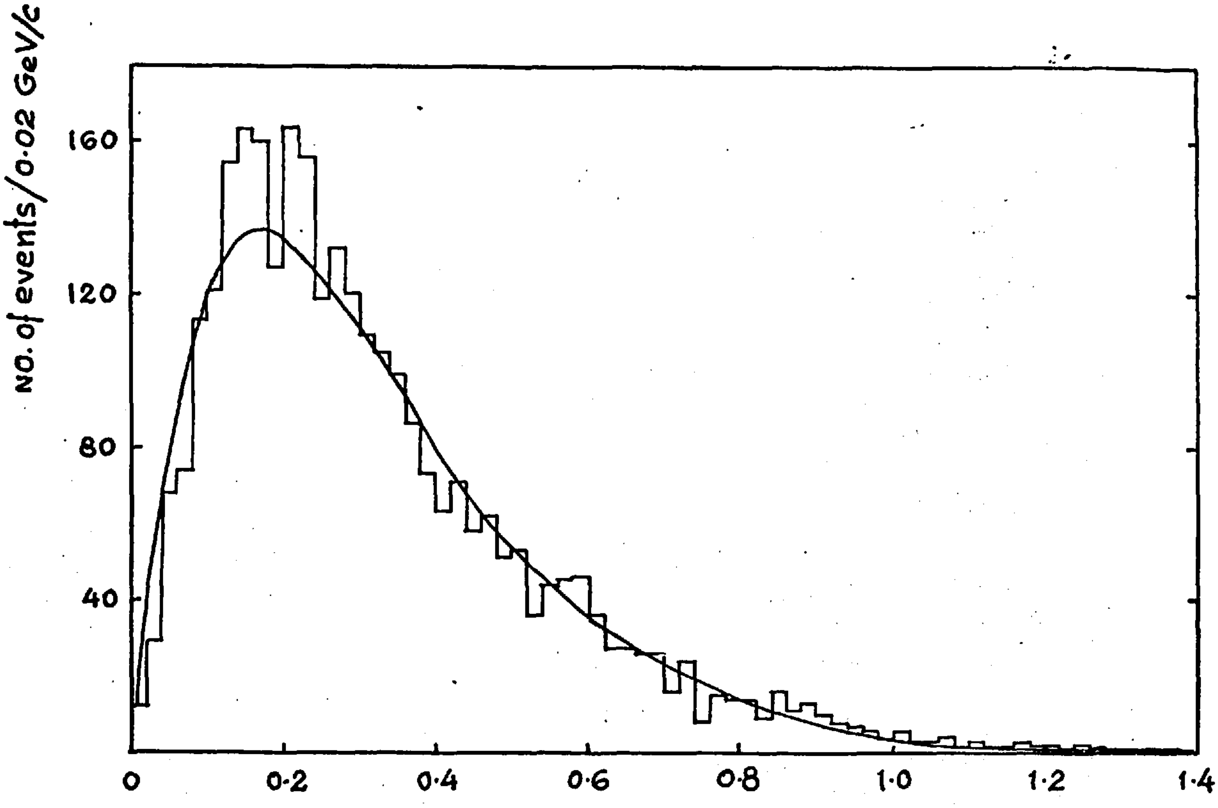

Fig. 5·4a $P_t^*(\pi)$ GeV/c

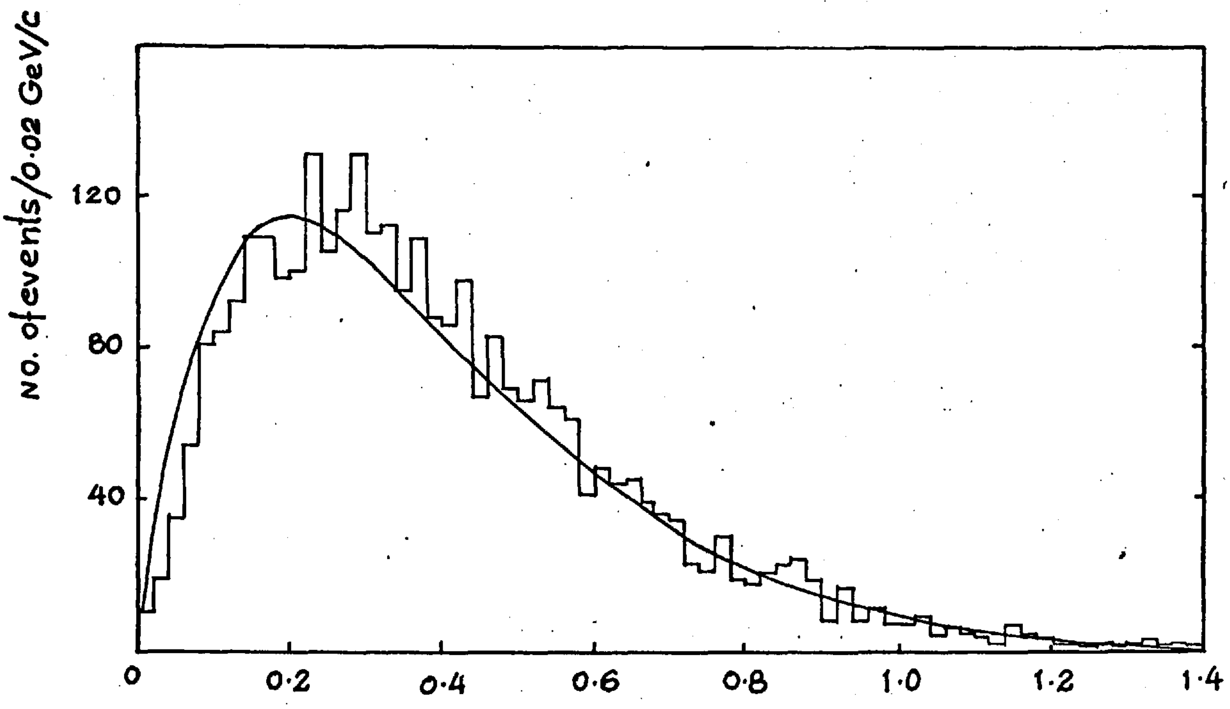

Fig. 5.4 b $P_t^*(P)$ GeV/c

TRANSVERSE MOMENTUM OF π^-

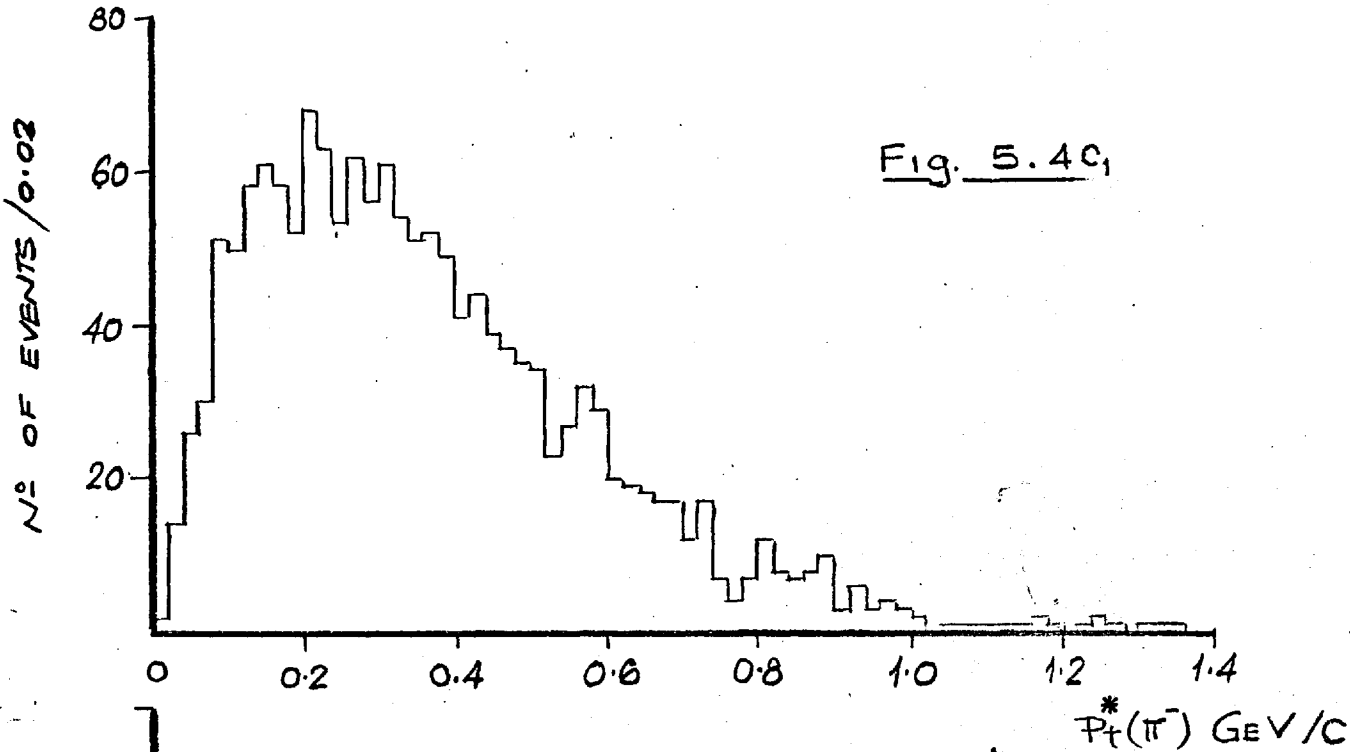

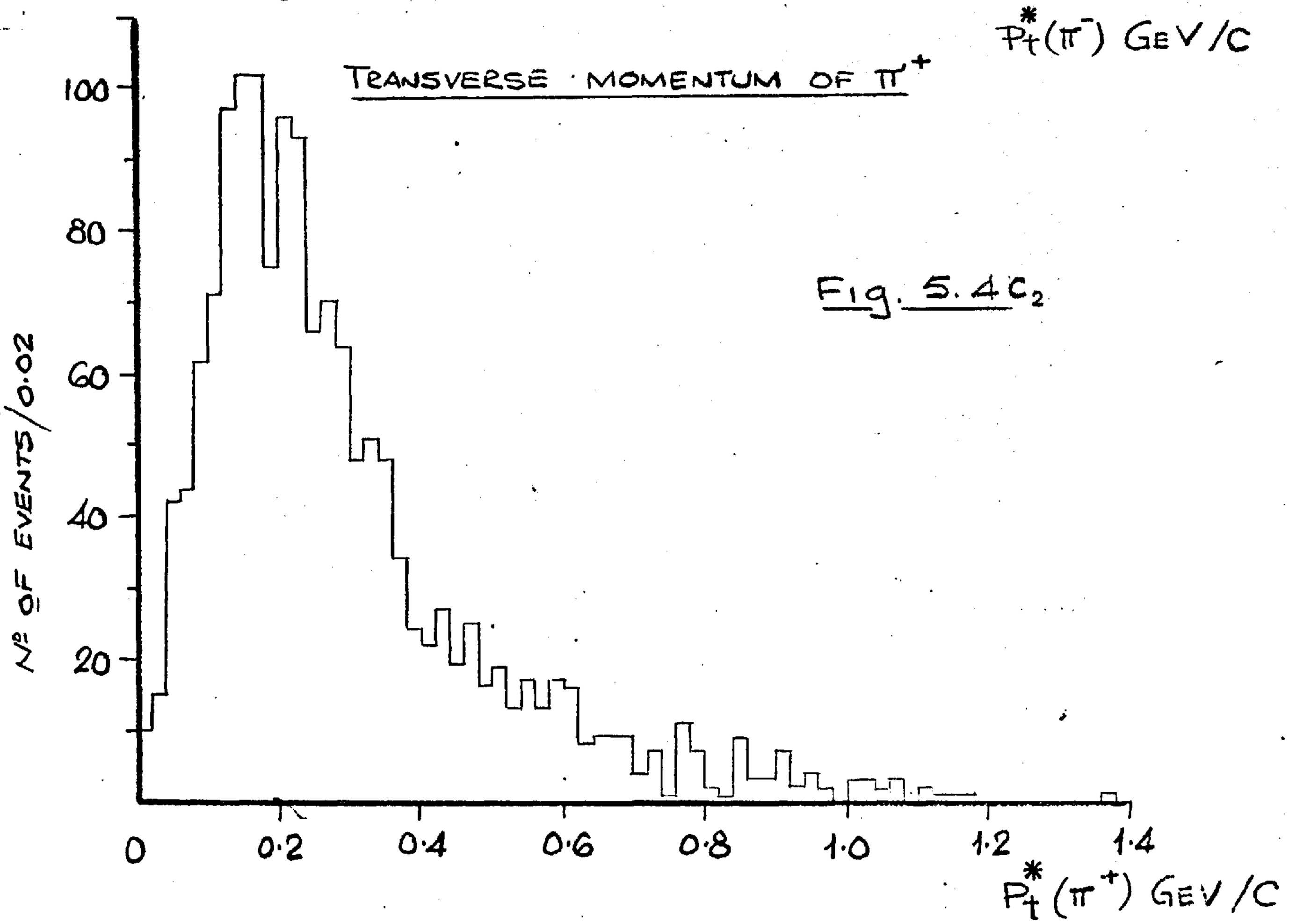

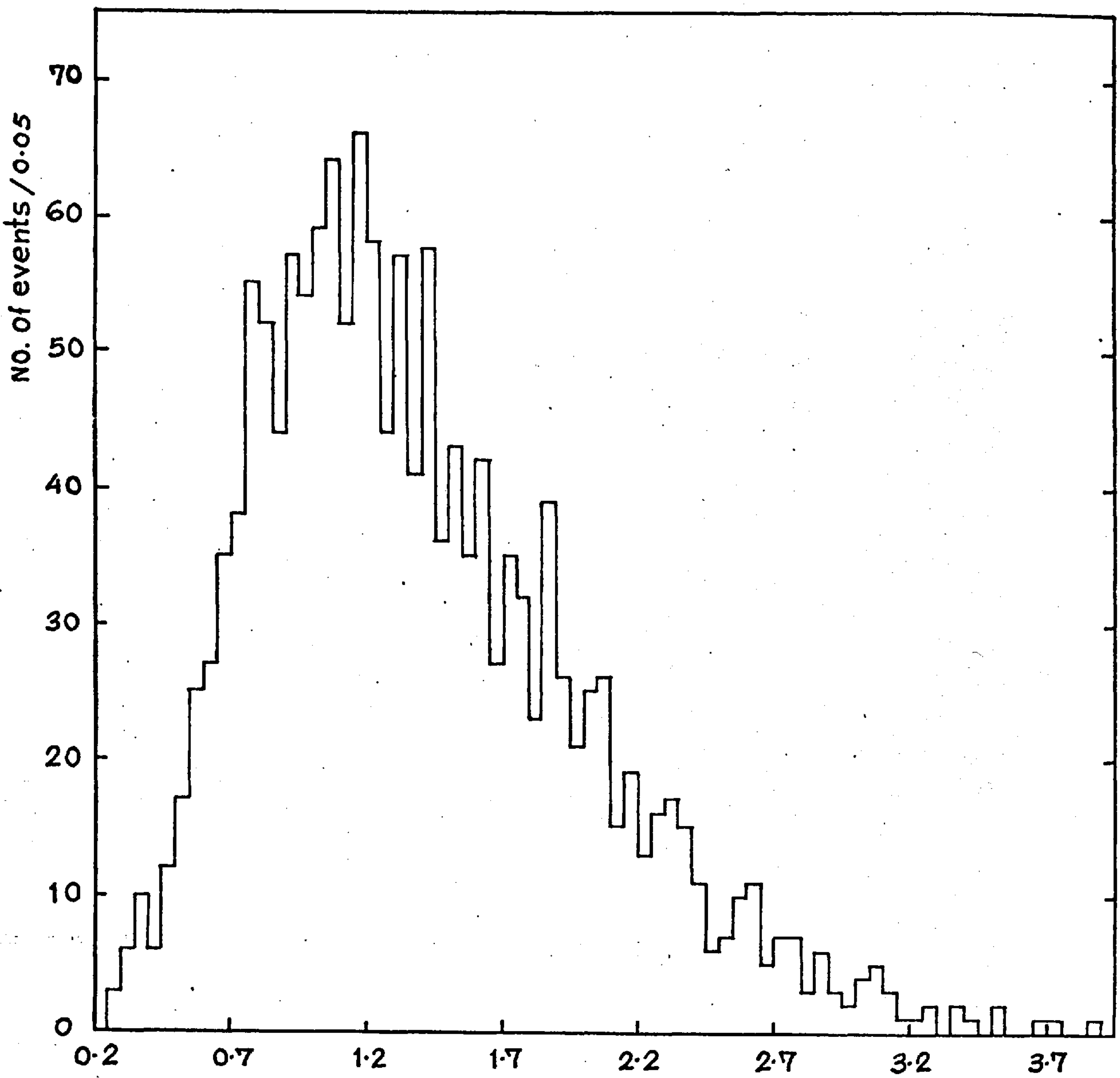

Fig. 5·5

$\sum_{i=1}^{4} |P_t^*|$ GeV/c

The most remarkable features of the longitudinal momentum in the C.M.S. (P^*_l) of the proton at high energy in figure 5.6a are the maxima (in the forward and backward direction) where the Lorentz invariant phase space prediction (dash curve) does not agree with the experiment data. This result is to be compared with the distribution in P^*_l for pions, which are distributed in a small interval around zero as shown in figure 5.6(b,c). The curve shows the characteristic normal distribution.

5.3 Correlation Between the Particles in the Final State

A number of kinematic variables are computed from the vector momenta of all tracks as evaluated by the fitting programme (GRIND). These variables each possess certain distinct properties which may be used to study the behaviour and the correlation between particles produced in an interaction.

5.3.1 The Invariant Mass - The variable used in the investigation of mass correlation between particles (in particular resonances) and a combination of particles in a given final state, is the "effective mass". This variable is Lorentz invariant and is usually plotted as a histogram or ideogram. The invariant masses (or effective masses) of any group of particles in the interaction is defined by:-

$$M^2_{eff} = (\Sigma_i e_i)^2 - \left\{ (\Sigma_i P_{1i})^2 + (\Sigma P_{2i})^2 + (\Sigma_i P_{3i})^2 \right\} \quad \ldots\ldots\ldots (5.9)$$

where Σ_i denotes a summation over the chosen group of particles, ($e_i, P_{1i}, P_{2i}, P_{3i}$) is the energy momentum four-vector of particle "i".

Fig 5.6 LONGITUDINAL MOMENTUM DISTRIBUTIONS

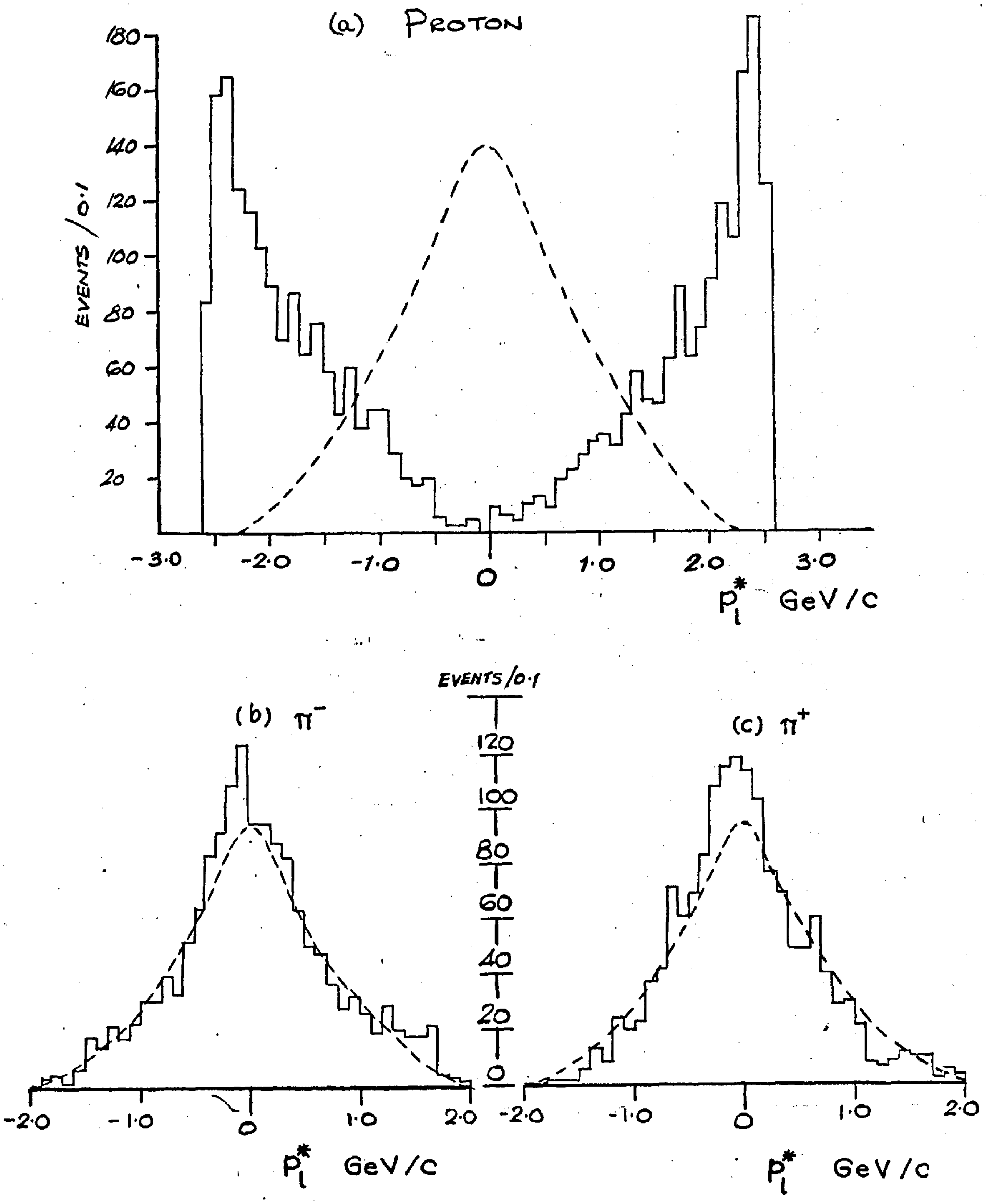

The phase space prediction disagrees violently with all experimentally observed distributions and is not suitable for describing the non-resonant background. The deviations from such a phase space distribution indicate the existence of some form of interaction between the particles concerned. This may be due to the formation of a single short lived state (a resonance) decaying into the observed particles, or the deviation may merely be due to kinematic effects.

These distributions are generally plotted according to their frequencies
Three and four body final state problems, however, may usefully be displayed in the form of "Dalitz" or Triangle" plots respectively. Their significance in relation to physical representations will be discussed in Chapter 7, fig. 5.7 (a-g) show the general invariant mass distributions for all combinations of the particles produced in reaction (1). Note that in fig. 5.7 b,c and d each event is plotted twice. Δ^{++} (1236) is a dominant feature of the $P\pi^+$ mass distribution, indicating that a large fraction of the events proceed through a $\Delta^{++}\pi^-$ process. The major peaks present in the $p\pi^+\pi^-$ mass distribution are at about 1.5 and 1.7 GeV. A minor peak is also present at about 2.0 GeV. There is some indication of Δ^0(1236), N^{*0} (1470) and N^{*0} (1688) in the $p\pi^-$ mass distribution, and very weak evidence for f^0 production in the $\pi^+\pi^-$ mass distribution. No indications of resonances in the pp and $pp\pi^\pm$ distributions are to be seen at all.

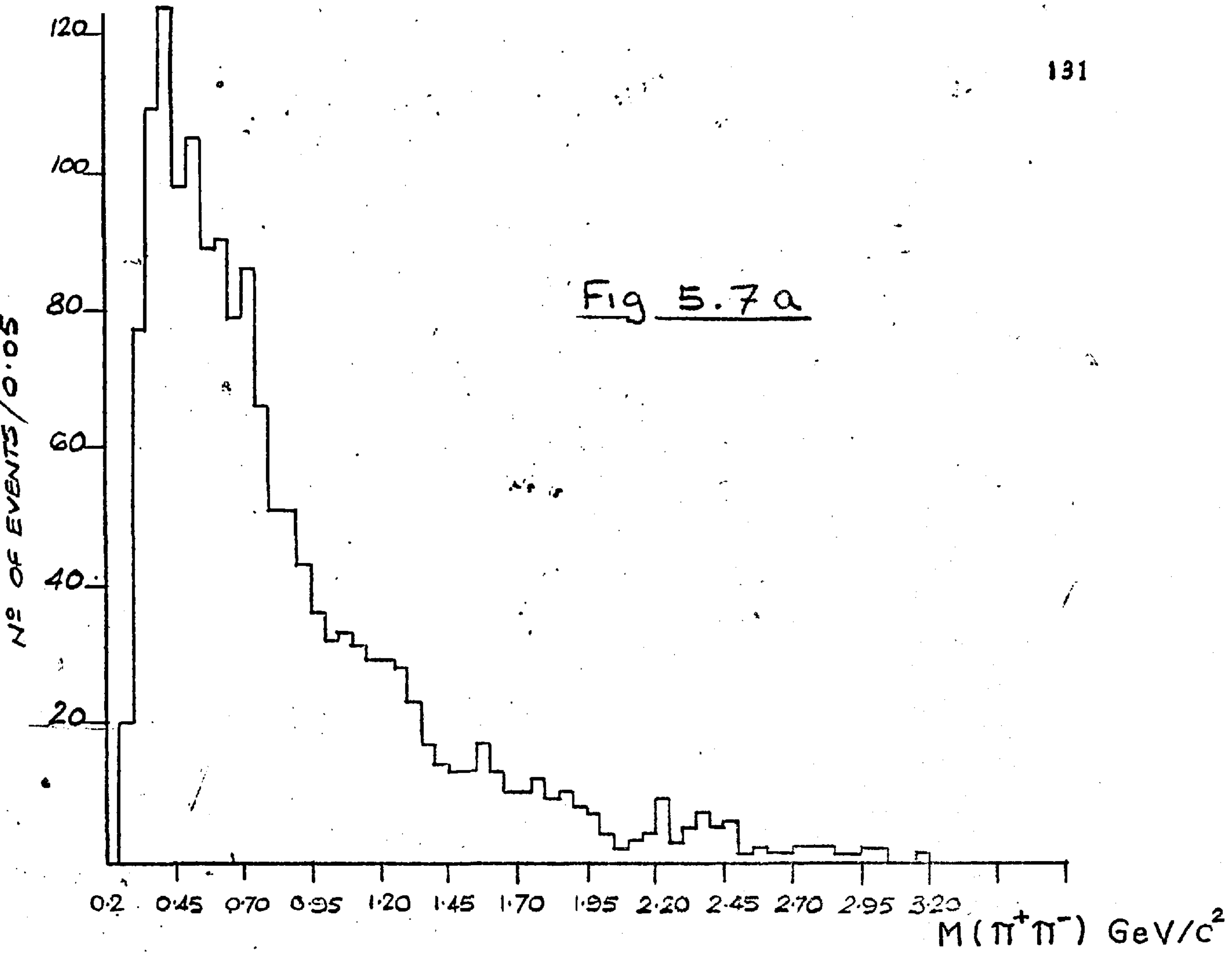

Fig 5.7a

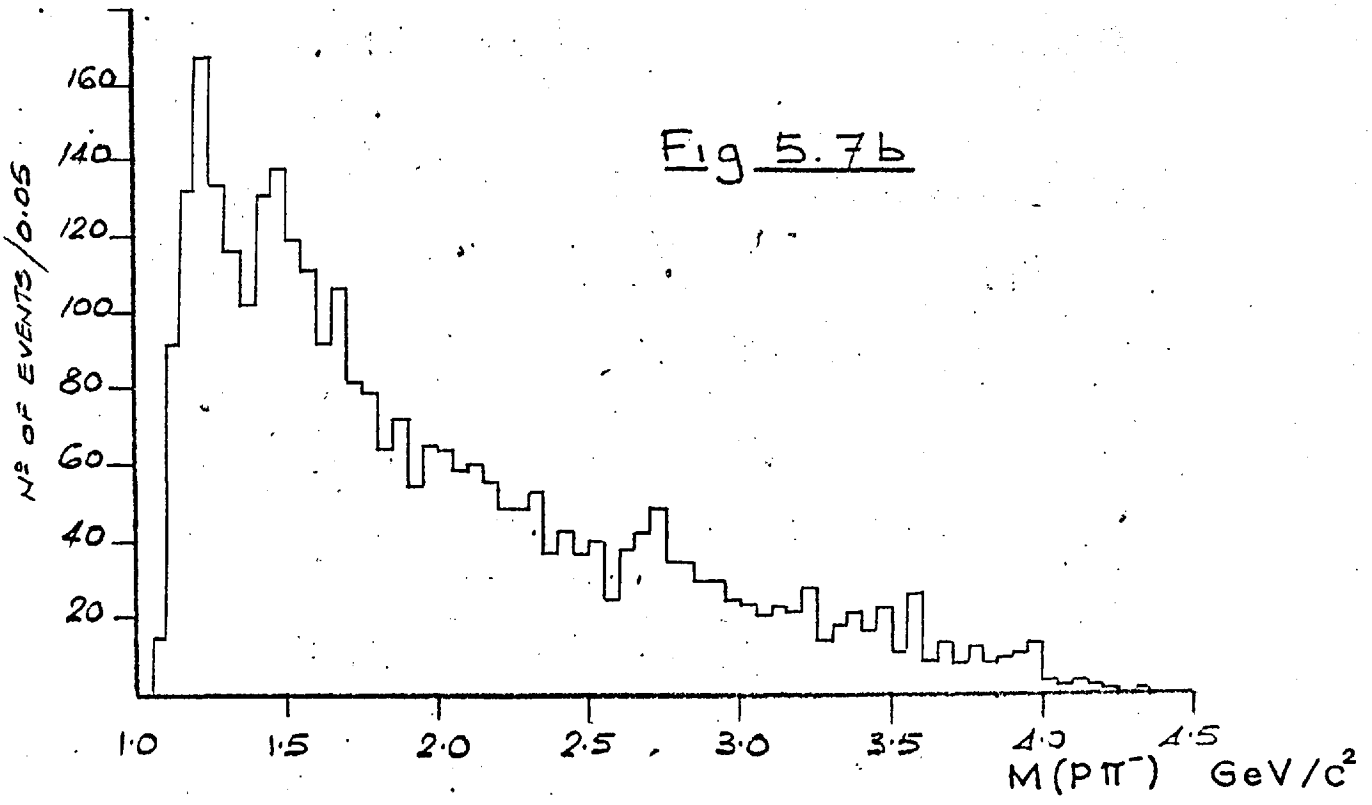

Fig 5.7b

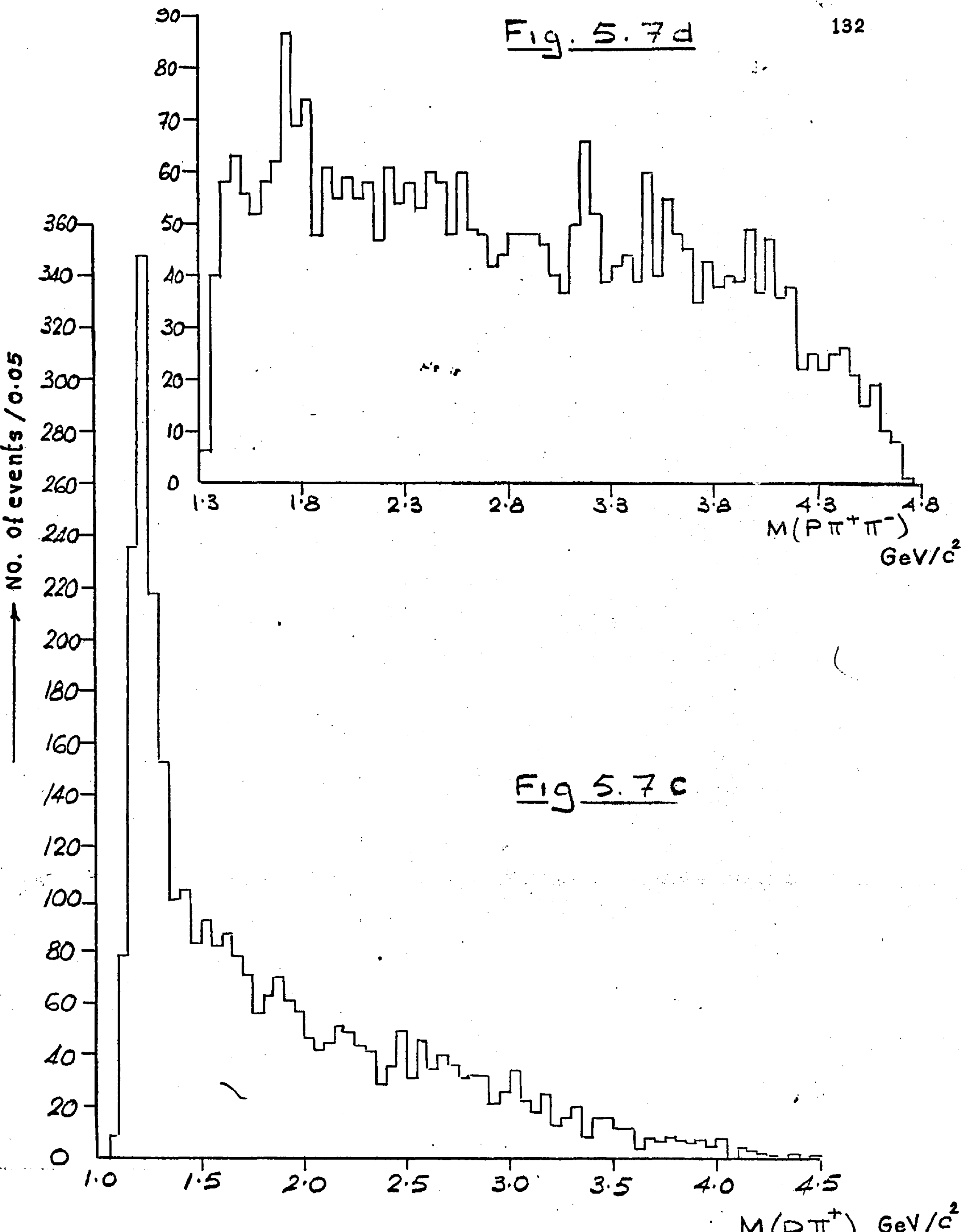

Fig. 5.7d

Fig 5.7c

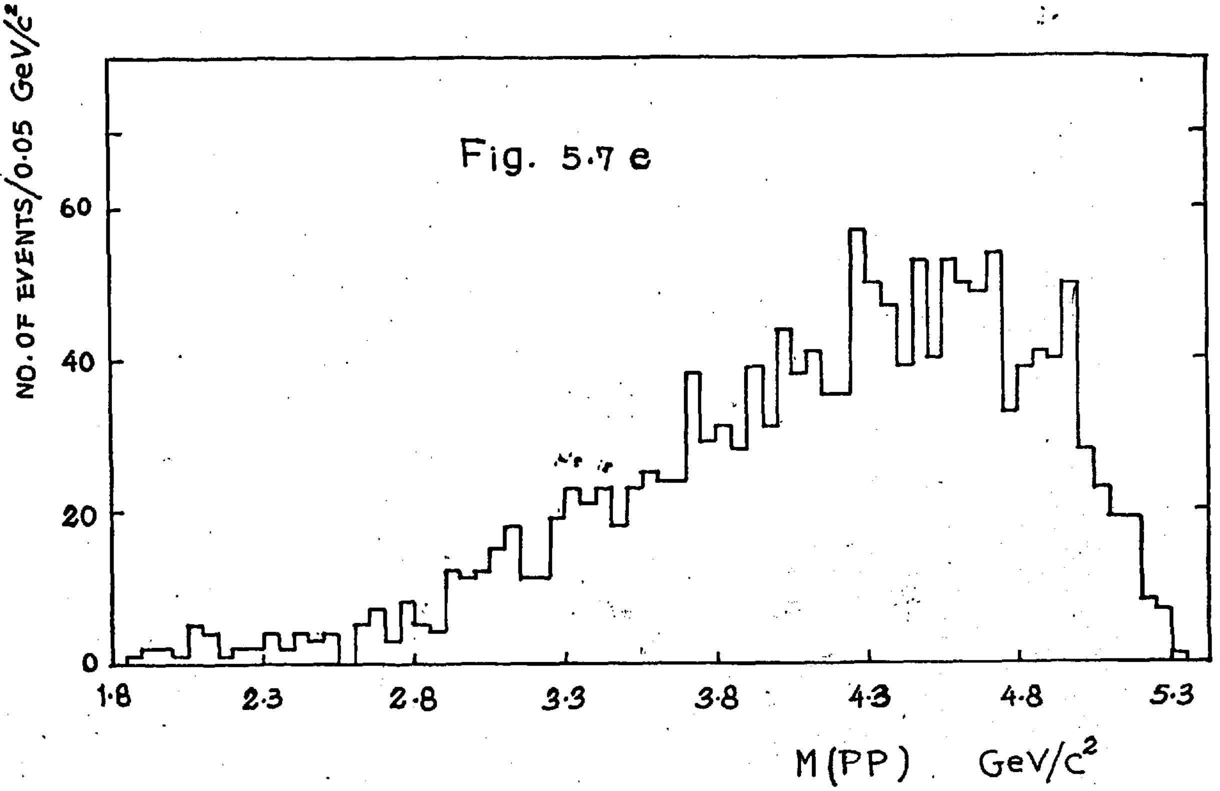
NO. OF EVENTS/0.05 GeV/c²
Fig. 5.7 e
0
20
40
60
1·8
2·3
2·8
3·3
3·8
4·3
4·8
5·3
M(PP) GeV/c²

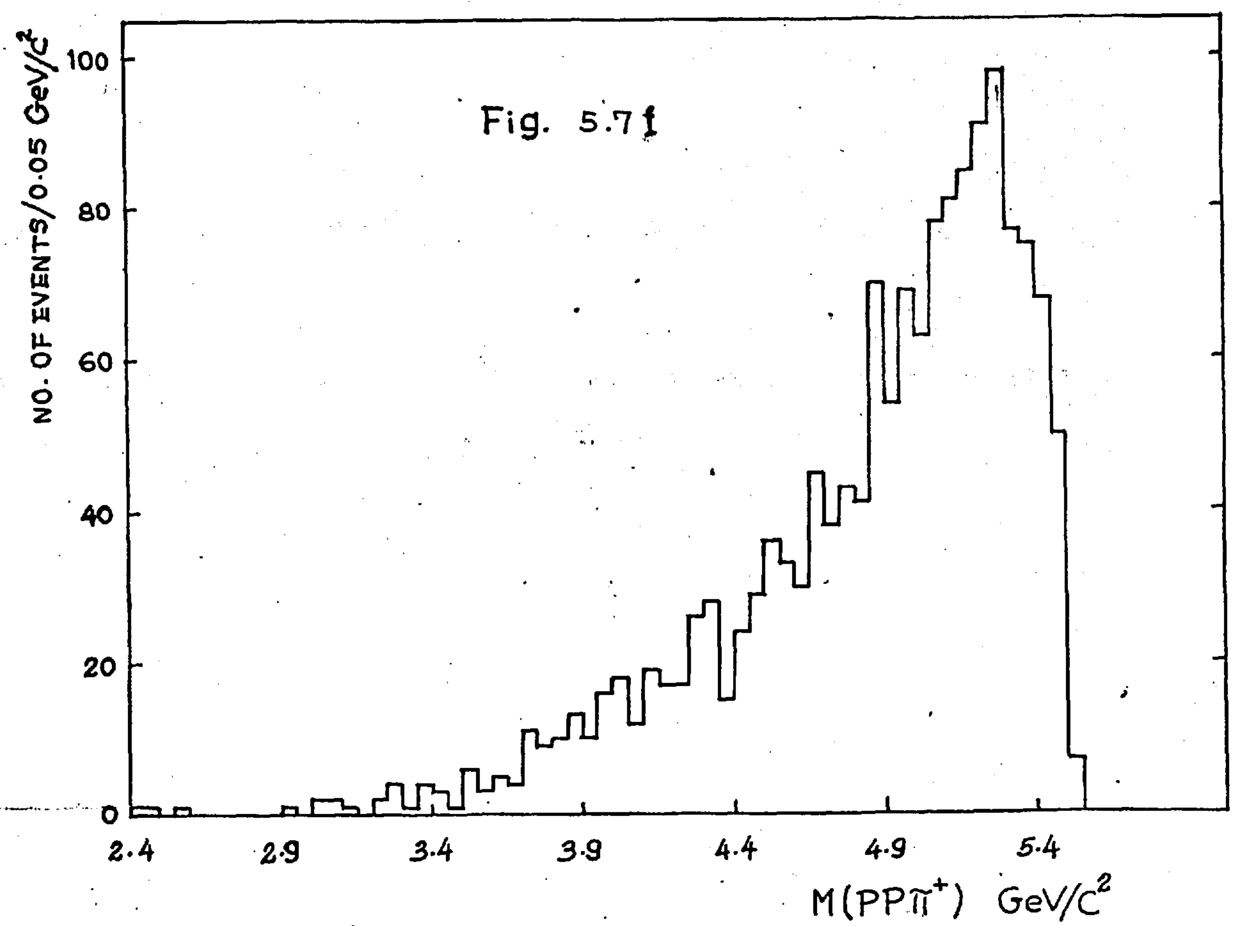
NO. OF EVENTS/0.05 GeV/c²
Fig. 5.7 f
0
20
40
60
80
100
2·4
2·9
3·4
3·9
4·4
4·9
5·4
M(PPπ⁺) GeV/c²

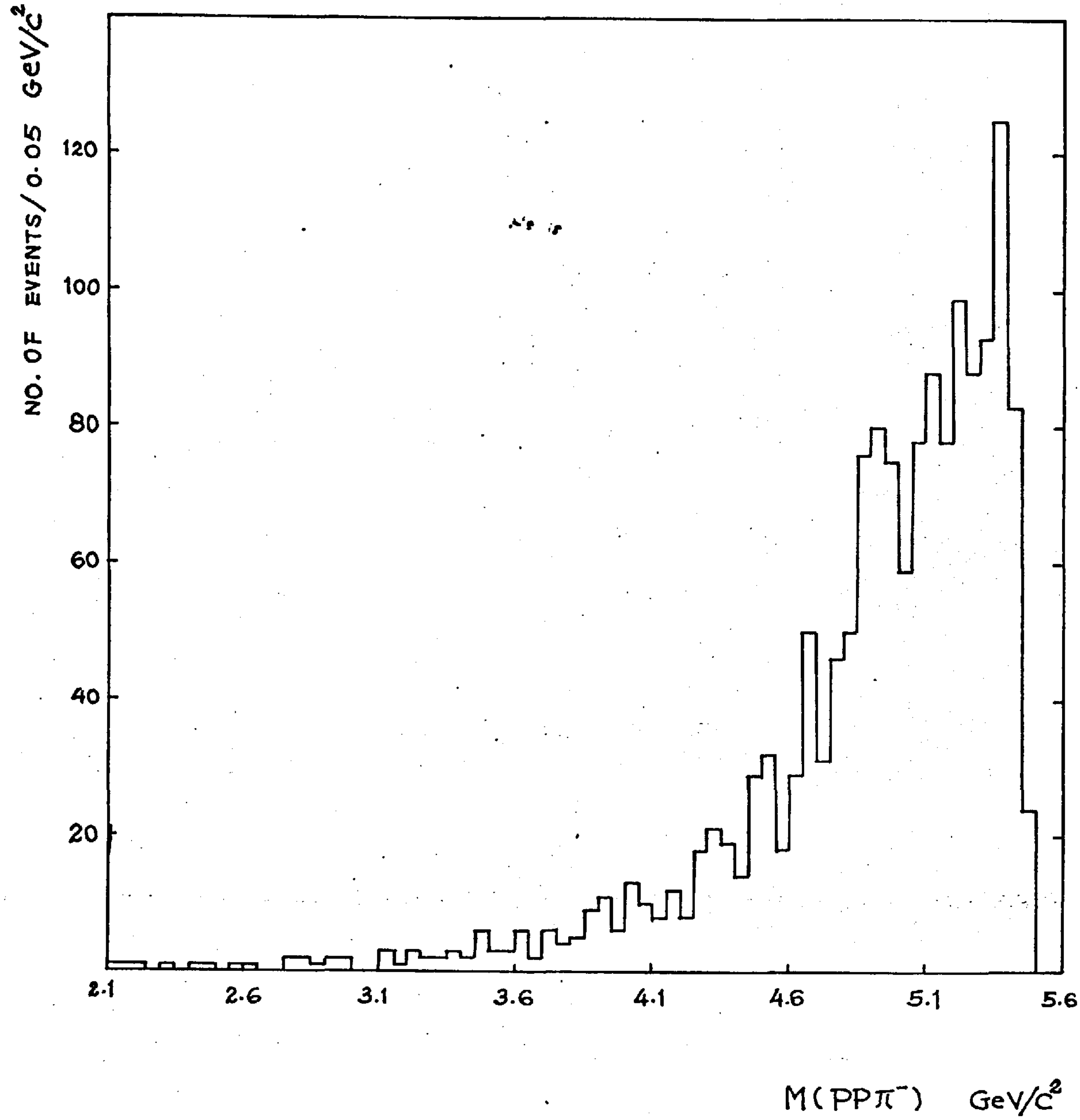
NO. OF EVENTS/0.05 GeV/c²
120
100
80
60
40
20
2.1
2.6
3.1
3.6
4.1
4.6
5.1
5.6
M(PPπ⁻) GeV/c²

Fig. 5.79

5.3.2 Angular and Four Momentum Transfer. – The production angles for a given particle combination, in its rest frame, are a guide to the type of interaction taking place. They are particularly useful when the particle combination forms a resonance.

The production angles are linearly related to other kinematic variables as follows:-

(i) Decay angles θ and ϕ – These two angles are known as Gottfrid-Jackson and Trieman-Yang angles respectively. They are usually meaningful only with interactions involving resonances. Distributions of these angles are used to test the production mechanism in operation, since these angles are determined by the spin and parity of the resonance.

The choice of the cartesian coordinate reference system is arbitrary. The axes are chosen, in this case, to be orthogonal in the resonance rest frame of the production process in the following manner. Consider figure 5.8a which illustrates the reaction:-

$$a + b \longrightarrow c + d \quad \text{(resonance)}$$

where "d" decays according to the relation

$$d \longrightarrow \alpha + \beta$$

We will here denote the momenta in the C.M.S. by $\underset{\sim}{a}^*$, $\underset{\sim}{b}^*$, $\underset{\sim}{c}^*$, $\underset{\sim}{d}^*$, $\underset{\sim}{\alpha}^*$ and $\underset{\sim}{\beta}^*$ and used $\underset{\sim}{a}$, $\underset{\sim}{b}$, $\underset{\sim}{c}$, and $\underset{\sim}{\alpha}$ for the $\underset{\sim}{\beta}$ corresponding momenta after the transformation into the d-resonance rest-frame.

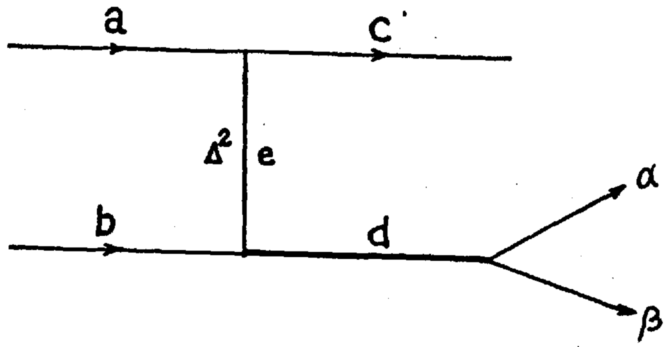

Fig. 5.8a

(i)

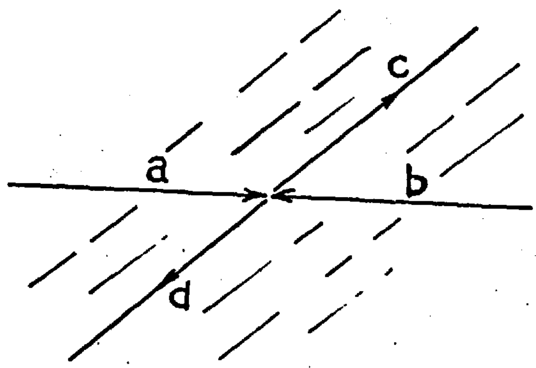

Fig. 5.8b

(ii)

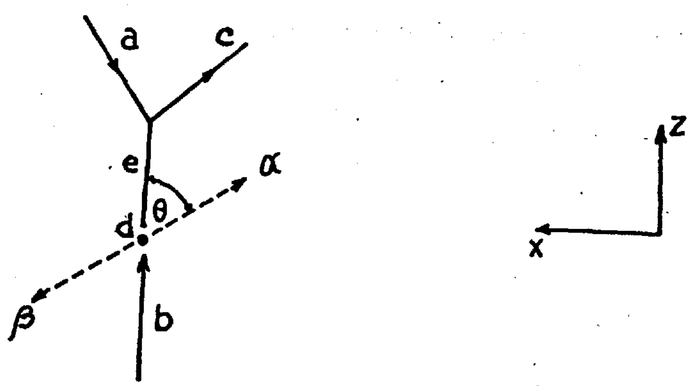

Fig. 5.8c

In the overall centre of mass system (see fig.5.8b) $\underset{\sim}{a}^*$ and $\underset{\sim}{b}^*$ are one straight line while $\underset{\sim}{c}^*$ and $\underset{\sim}{d}^*$ form another line. These two lines define the production plane (i) and can be taken as the plane of the paper. $\underset{\sim}{d}^*$, $\underset{\sim}{\alpha}^*$ and $\underset{\sim}{\beta}^*$ define a second plane called the decay plane which intersects with the prodution plane at an angle ϕ. By choosing a transformation into the rest-frame of the d-resonance, we are able to reduce the number of variables which define the direction of the decay particles. The production and decay planes remain unchanged with $\underset{\sim}{a}^*$, $\underset{\sim}{b}^*$ and $\underset{\sim}{c}^*$ changing to $\underset{\sim}{a}$, $\underset{\sim}{b}$ and $\underset{\sim}{c}$ as shown in figure 5.8c(ii). The most significant consequence of this procedure is that $\underset{\sim}{\alpha}$ and $\underset{\sim}{\beta}$ are equal in magnitude and opposite in direction.

The Y-axis is chosen along the direction of the normal to the production plane and +z is the direction of the incident particle.

We define $\hat{n} \equiv \dfrac{\underset{\sim}{a} \wedge \underset{\sim}{c}}{|\underset{\sim}{a} \wedge \underset{\sim}{c}|}$

The X-axis lies in the production plane. The unit vector in this direction is then given by $\hat{n} \wedge \dfrac{\underset{\sim}{b}}{|\underset{\sim}{b}|}$ where particle "e" is exchanged in the mechanism producing the d-resonance.

The decay angles θ and ϕ are the polar and azimuthal angles respectively, of the decay particle α (or β) in that system, and they are given by the following formulae:-

$$\cos\theta = \frac{\underset{\sim}{b}\cdot\underset{\sim}{\alpha}}{|\underset{\sim}{b}||\underset{\sim}{\alpha}|} \qquad \text{.........} \quad (5.10)$$

$$\cos\phi = \frac{\underset{\sim}{a}\wedge\underset{\sim}{c}}{|\underset{\sim}{a}\wedge\underset{\sim}{c}|}\cdot\frac{\underset{\sim}{b}\wedge\underset{\sim}{\alpha}}{|\underset{\sim}{b}\wedge\underset{\sim}{\alpha}|} \qquad \text{..........} \quad (5.11)$$

$$\sin\phi = \frac{\underset{\sim}{b}\wedge(\underset{\sim}{a}\wedge\underset{\sim}{c})}{|\underset{\sim}{b}\wedge(\underset{\sim}{a}\wedge\underset{\sim}{c})|}\cdot\frac{\underset{\sim}{b}\wedge\underset{\sim}{\alpha}}{|\underset{\sim}{b}\wedge\underset{\sim}{\alpha}|} \qquad \text{...........} \quad (5.12)$$

ϕ is generally defined so that $\phi = 0$ in the production plane.

(ii) <u>The Four Momentum Transfer</u> - The square of the momentum transfer is another useful kinematic variable for studying the kinematics of scattering with greater precision. Theoretical predictions may often be written more simply for scalar particles (without both spin and isospin) in terms of this variable.

The field theoretical treatment based on the "Feynman diagram" and the formalism developed by Mandelstam[61] introduces three Lorentz invariant scalar variables, s, t and u. They are defined as follows (see fig. 5.9) :-

(1) The "s" variable

$$S = (P_1 + P_2)^2 = (P_3 + P_4)^2$$

$$= (e_1 + e_2)^2 - (\vec{P}_1 + \vec{P}_2)^2$$

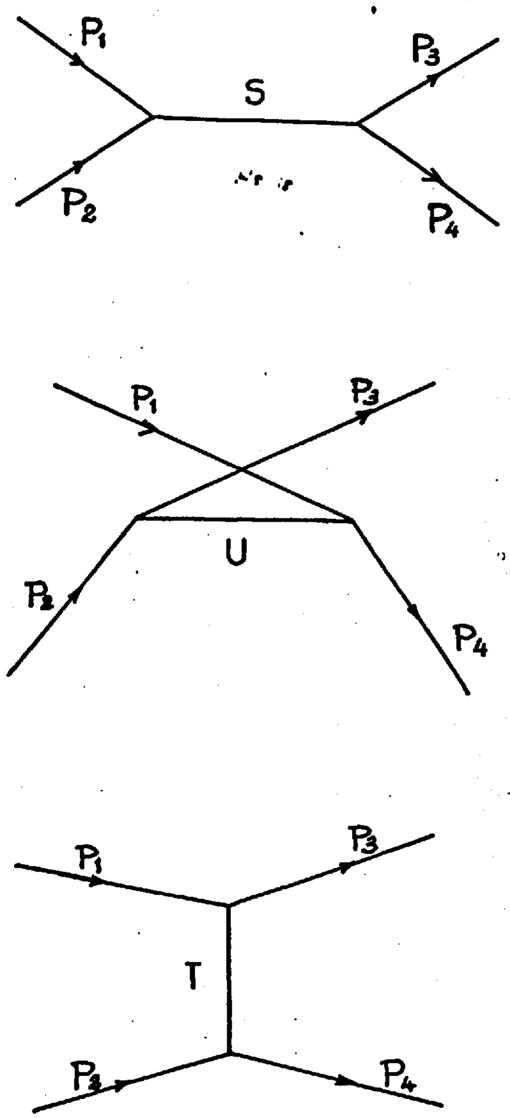

Fig. 5.9

(2) The "t" variable

$$t = (P_1 - P_3)^2 = (P_2 - P_4)^2$$

$$= (e_1 - e_3)^2 - (\bar{p}_1 - \bar{p}_3)^2$$

(3) The "u" variable

$$u = (P_1 - P_4)^2 = (P_2 - P_3)^2$$

$$= (e_1 - e_4)^2 - (\bar{p}_1 - \bar{p}_4)^2$$

where P_i = the four momentum of the i^{th} particle

e_i = the energy of the i^{th} particle

$\bar{p}_i$ = the three momentum of the i^{th} particle

m_i = the i^{th} particle rest mass

and $i = 1, \dots 4$.

From the conservation of energy and momentum in the C.M.S.

$P_3 = -P_3$, $P_4 = -P_4$

$$\therefore \quad P_1 + P_2 + P_3 + P_4 = 0$$

and

$$\bar{P}_i = -m_i^2 \quad ; \quad (i = 1, \cdots 4)$$

This results in the relation:-

$$s + t + u = m_1^2 + m_2^2 + m_3^2 + m_4^2 = \sum_i m_i^2 \qquad \text{........ (5.13)}$$

Due to the dominance of the peripheral production mechanism at high energy, the "t" variable is the most widely used and can be written precisely as:-

$$t = (e_1 - e_3)^2 - (\vec{p}_1 - \vec{p}_3)^2$$

$$= (e_1^2 + e_3^2 - 2e_1e_3 - \vec{p}_1^2 - \vec{p}_3^2 + 2\vec{p}_1\cdot\vec{p}_3)$$

$$= (m_1^2 + m_3^2 - 2(e_1e_3 - p_1p_3\cos\theta) \quad \text{.........} \quad (5.14)$$

The physical region of "t" is usually negative, and θ is the angle between vector P and P .

The experimental t_1 and t_2 distributions for slow proton, t_1 (target-p_s), and for fast proton, t_2(beam-p_f), in the final state:

$$p + p \longrightarrow p_s + p_f + \pi^+ + \pi^- \quad \text{.........} \quad (1)$$

are separately plotted in figure 5.10a and b respectively. It is found that for small values of $|t|$ the $d\sigma/dt$ distribution can be reasonably fitted by the formula

$$d\sigma/dt = e^{-At} \quad \text{..........} \quad (5.15)$$

Where A is called the slope, since the logarith of is usually plotted against a linear scale of t. The more elaborate formulation

$$d\sigma/dt = e^{-bt + ct^2} \quad \text{..........} \quad (5.16)$$

gives a better fit to the data and extends over a large range of t-values. Both fitted curves are also shown in figure 5.10a,b for t_1 and t_2 respectively). In addition, extrapolation of the fitted curve to formula 5.15 for $t \longrightarrow o$ yielded an estimate of the number of missing events due to slow protons of inadequate energy to produce clear tracks.

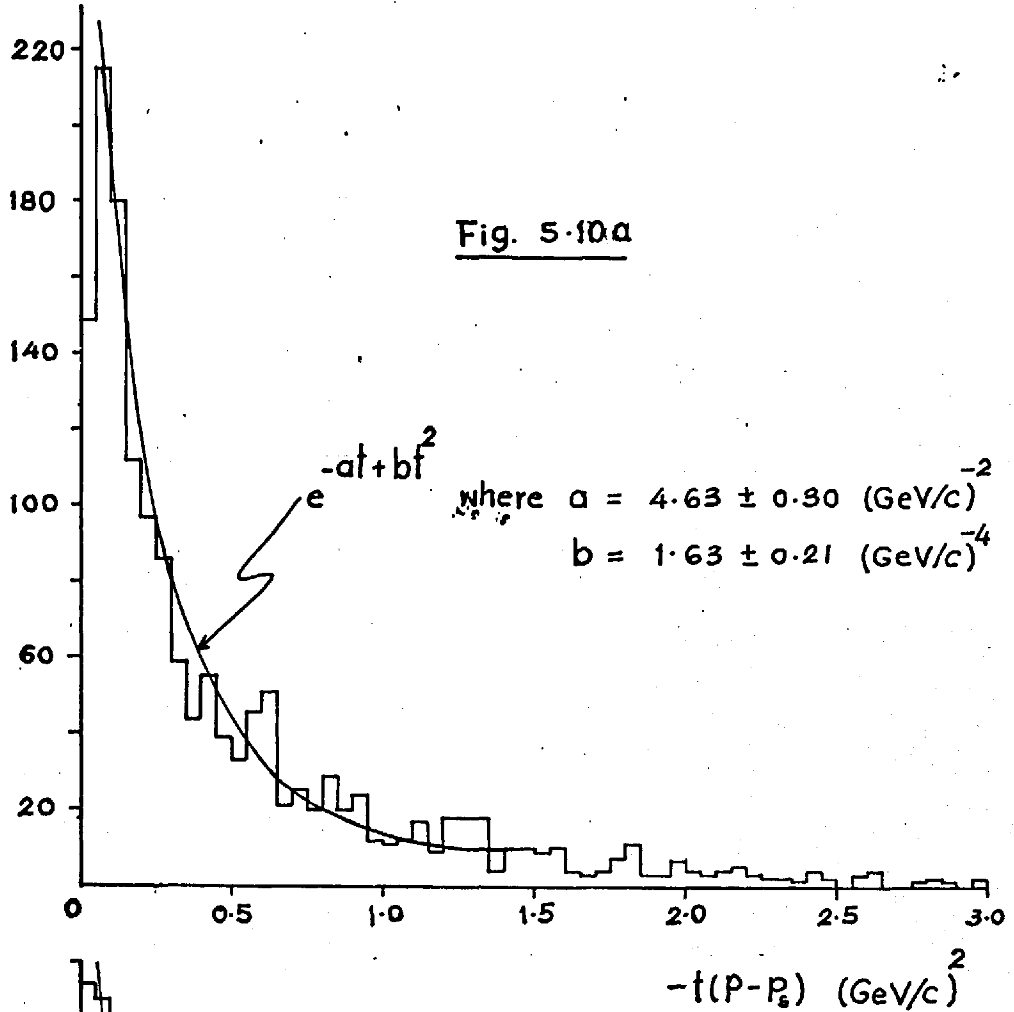

Fig. 5·10a

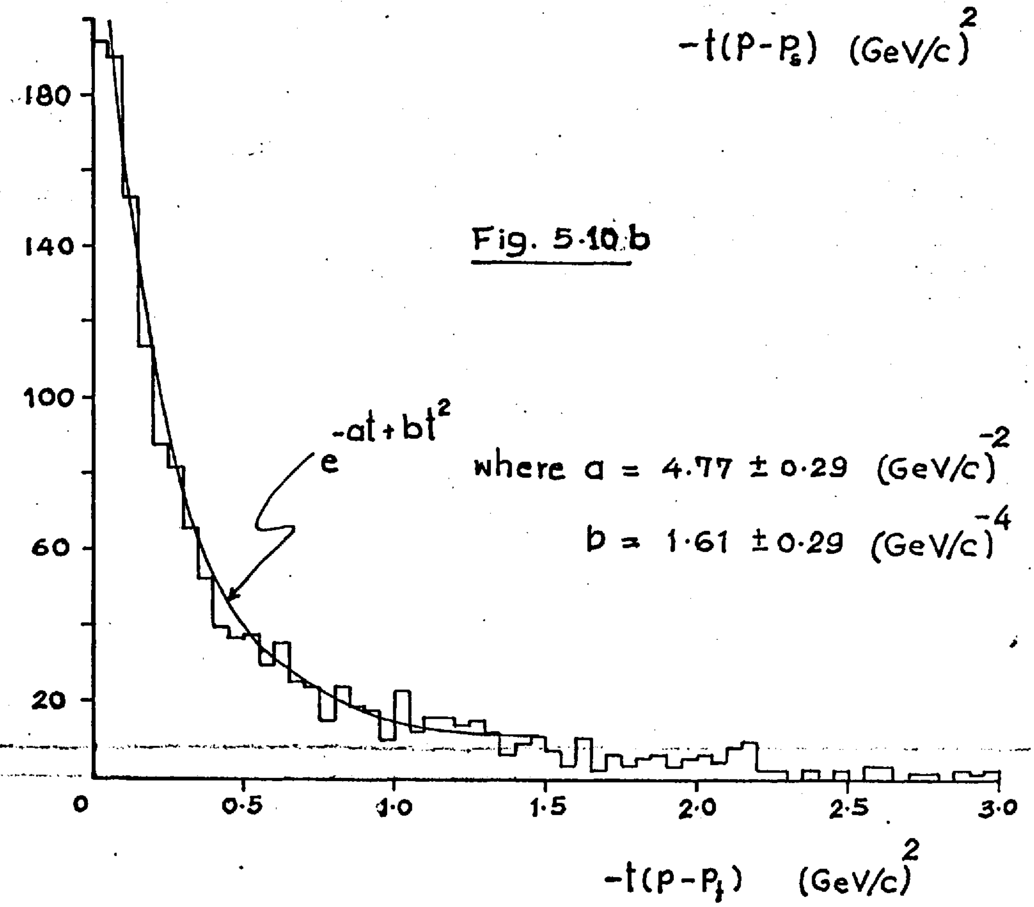

Fig. 5·10 b

Table 5.3 lists typical values for expected track lengths of protons produced when the four momentum transfer has the values tabulated in the t-column.

The logarithm of t distribution is displayed in figure 5.10c; missing 4-constraint fit candidates were estimated by extrapolation of the fitting line for t_1 and t_2, with $A = 3.84 \pm 0.21 (GeV)^{-2}$, down to the lowest t-value. This value was taken into account for the correction of cross section calculation (Chapter 3, section 3).

The significance of the angular distribution in relation to the physical mechanism is discussed in Chapter 7.

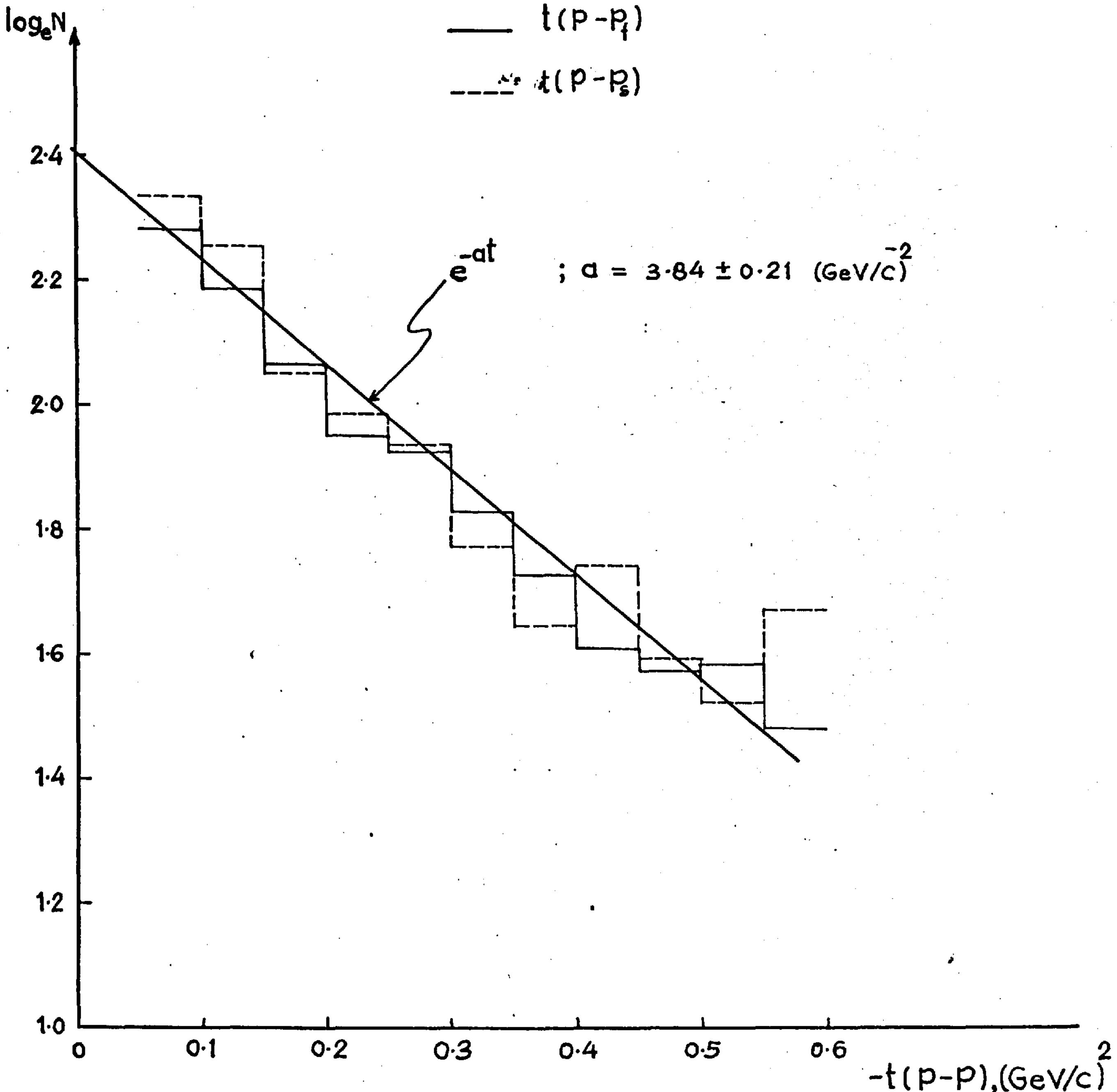

$\log_e N$
$t(p-p_f)$
$t(p-p_s)$
e^{-at}
; $a = 3{\cdot}84 \pm 0{\cdot}21\ (GeV/c)^{-2}$
2·4
2·2
2·0
1·8
1·6
1·4
1·2
1·0
0
0·1
0·2
0·3
0·4
0·5
0·6
$-t(p-p),(GeV/c)^2$

Fig. 5·10 c

TABLE 5.3

-t (GeV)^2	Kinetic Energy (GeV)	Length (cm)
0.005	0.00275	0.083
0.01	0.00533	0.27
0.02	0.0106	0.91
0.03	0.0212	3.215
0.05	0.0275	5.62

CHAPTER 6

THE THEORETICAL SITUATION AND MODELS

The popular and fundamental field of high energy physics has a certain duality which is, at present, apparent in the use of an alternative name: "Elementary particle physics". One of its main tasks is the study of all properties of elementary particles: mass, spin, isospin, parity, electo-magnetic properties, decay properties and the existence of excited states, etc. The high energy collisions which have been studied up to now mainly include the most common among the strongly interacting particles; viz: nucleons and pions. Data for kaons and anti-protons is relatively scarce. The best known type of collision is the proton-proton encounter, and the limited evidence available points towards the fact that all strongly interacting particle collisions have similar qualitative properties.

It is impossible to present, or interpret, experimental results without an appropriate set of concepts and models of the interaction. Such models are especially necessary for the discussion of strong interactions, but in this case there is the further difficulty that the nature of the forces with strong coupling constant ($G^2 \approx 14$) is not completely known. Weak interactions, in comparison, ($g^2 \approx 10^{-15}$) can be more rigorously analysed.

This chapter is devoted to a brief review of the various theoretical situations and models available for Nucleon-Nucleon (N-N) interactions. The main emphasis is placed on the treatment relevant to the analysis of high energy inelastic scattering.

6.1 The One Particle Exchange Models (OPEM)

An approximation, which introduces an intermediate resonance state in the s-channel, is very useful in certain physical situations such as π-N scattering, but it has little application in N-N scattering because no bound state with baryon №. = 2 exists at high energy. Therefore the concept of exchange in the t-channel, which has already been introduced in electron proton scattering[66], has been developed and now plays an important role in the description of peripheral phenomena at high energy.

Many inelastic reactions are characterised by the forward-backward peaking of the production angular distribution in the C.M.S. which corresponds to small four momentum transfer. This distinct feature suggests a peripheral interaction. For instance, in the case of inelastic N-N scattering, one would say that the interaction takes place in the virtual pion cloud of the nucleon and not with the nucleon itself.

The "Peripheral Model" or "One Particle Exchange Model"[64] can be represented by a Feynman diagram. Figure 6.1a shows a generalized inelastic process of the type:-

$$a + b \longrightarrow c + d \qquad \ldots\ldots\ldots\ldots (6.1)$$

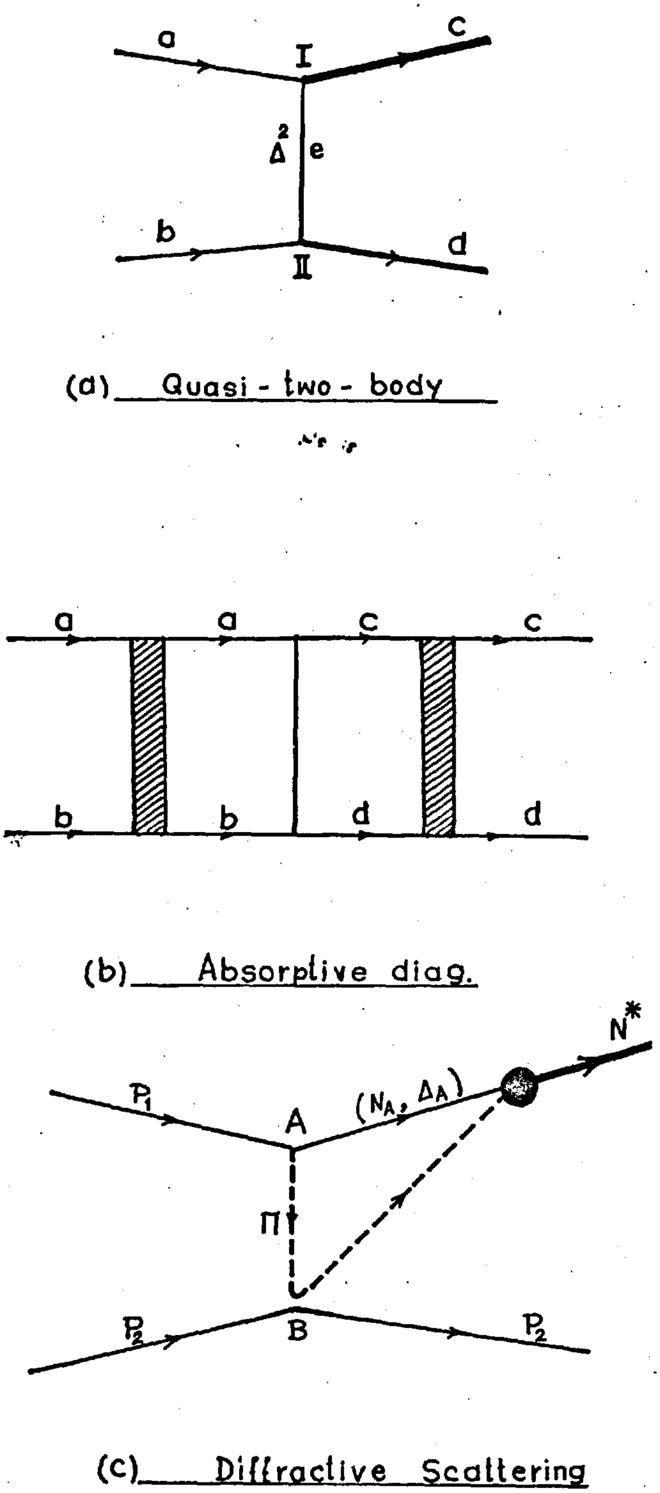
a
c
I
Δ^2
e
b
d
II
(a) Quasi - two - body
a
a
c
c
b
b
d
d
(b) Absorptive diag.
N^*
P_1
A
(N_A, Δ_A)
π
P_2
B
P_2
(c) Diffractive Scattering

Fig. 6·1

The incident particle 'a' interacts with 'b' by the exchange of particle "e". c and/or d can be either single particles or resonances with definite spin, parity and isospin quantum numbers. In the latter case these are called "Quasi-two-body" reactions.

Chew and Low[62] were the first to consider the theory of peripheral inelastic processes. They considered extrapolation from a physical to an unphysical region. One considers that any diagram with a One Particle Exchange (OPE) contributes a pole to the scattering amplitude of a physical process. This pole is assumed to arise from a singularity in the relativistically invariant square of the four momentum transfer (Δ^2) of the exchange particle. The exchange of the lightest particle (pion), which has the longest effective range, gives the nearest singularity to the physical region.

The central physical principle employed in this model is the existence of poles in the matrix element M_{fi} of the figure as shown in diagram 6.1a. This corresponds to single particle exchange and has the following general structure:-

$$M_{fi} = M_I(\Delta^2, m_c)\frac{1}{\Delta^2 + m_e^2} M_{II}(\Delta^2, m_d) \quad \dots\dots\dots\dots (6.2)$$

where m_e is the mass of the exchange particle

$\Delta^2 = -t =$ the four-momentum transfer, taken as positive in the physical region.

$$\begin{aligned} \Delta^2 &= -(P_c - P_a)^2 = -(P_d - P_b)^2 \\ &= -\left\{(e_c - e_a)^2 - (\bar{P}_c - \bar{P}_a)^2\right\} \\ &= -\left\{(m_c^2 + m_a)^2 - 2(e_c e_a - \bar{P}_c \cdot P_a)\right\} \quad \dots\dots\dots\dots (6.3) \end{aligned}$$

$(\Delta^2 + m_e^2)^{-1}$ = the propagator of the exchange particle, and

M_I, M_{II} = the appropriate function for the vertices I and II in figure 6.1a.

Scattering appears to proceed by pion exchange for N-N interactions. Here, for instance, the vertex factors squared and summed over initial and final spins are given in Born approximation(66) by:-

$$\Sigma \left| M_{p\pi N} \right|^2 = G^2_{p\pi N} \left(\sqrt{-t} \right)^2 \qquad ; \quad N = p \text{ or } n$$

$$\Sigma \left| M_{p\pi\Delta} \right|^2 = \frac{2}{3} \frac{1}{m_\pi^2} G^2_{p\pi\Delta} \frac{1}{4 m_\Delta^2} \left[(m_\Delta + m_p)^2 - t \right]^2 \left[(m_\Delta - m_p)^2 - t \right]^2 \quad \text{..........} \quad (6.4)$$

$$\Delta = \Delta^{++}(1236)$$

The coupling constants are given by $G^2_{p\pi N}/4\pi = 15$ and $G^2_{p\pi\Delta}/4\pi = 2.5$.

Due to four-momentum conservation at the vertex I of figure 6.1a, the Δ^2 value is equal to the four momentum of the exchange particle "e" (the pion). From equation (6.3) it can accordingly be interpreted as the negative square of the virtual mass of e.

The peak in the differential cross-section for the distribution is due to the propagator $(\Delta^2 + m_e^2)^{-1}$ and to the vertex function. One can see clearly that the cross-section has a pole at the unphysical point ($\Delta^2 = -m_e^2$), when the exchange particle "e" is sufficiently near to the (real) mass-shell for any vertex to be approximated by the lowest order term in the perturbation expansion.

A vertex is then approximately equal to the matrix elements for the physical processes:-

$$\begin{aligned} a + e &\longrightarrow c \\ b + e &\longrightarrow d \end{aligned} \qquad \text{.........} \ (6.5$$

These matrix elements are proportional to the coupling constants for the two vertices. The exchange particle must conserve all relevant quantum numbers at each vertex.

Qualitatively this simple model describes the gross features of reaction (6.1). In general, however, the model is quite inadequate to reproduce the observed differential cross-section ($d\sigma/d\Delta^2$), for the experimental results are more peripheral than that predicted; i.e. the observed distribution falls off quicker than the predicted values.

6.1.1 <u>OPEM with Form Factor</u> - The model discussed above was soon modified to improve the agreement with the experimental results. An empirical t-dependent Form Factor[(65)] was introduced to account for the off-the-mass-shell correction due to the virtual nature of the exchange particle.

A discussion by Ferrari & Selleri[(65)] for processes in which virtual $\pi + N \longrightarrow \pi + N$ shows that the amplitude for such a vertex is given by a known function of the energy and momentum transfer multiplied by a "pionic form factor" F (Δ^2) for the nucleon. Thus F (Δ^2) is an empirical form factor in the perturbation theory formula and requires normalization at the pion pole, $\Delta^2 = -m_\pi^2$ ($F(-m_\pi^2) = 1$). The coupling constants are defined in terms of a pion on the mass shell. This form factor, when fitted to an experiment, rapidly decreases with increasing $|t|$, and should be valid at any energy for One Pion Exchange reactions.

At high energy F(Δ^2) does not cause the cross-section to fall sufficienty rapidly, particularly for vector meson exchange processes. To obtain a reasonable agreement with the experimental distributions, the form factor can be readjusted. However, this procedure is not satisfactory as it reduces the model to mere curve fitting.

6.1.2 Absorption Model - Another possible improvement to the peripheral model for high energy is Gottfried & Jackson's[(67)] absorptive peripheral model. The idea is to modify the One Meson Exchange model to include absorptive effects. These are considered as due to competition from the various inelastic channels by elastic scattering in the initial and final states. This is shown in figure 6.1b.

It is assumed that, at higher energy, more complex reactions are favoured and that these are less peripheral and characterised by small impact parameters with large momentum transfer. They may be allowed for by absorbing or suppressing the low partial waves in the amplitude of the corresponding quasi-two-body reaction. The absorption thus produces an appreciable reduction in cross-section and a pronounced collimation of the angular distribution. Hence the peripheral interactions with higher impact parameters are relatively unaffected. Thus the model provides a natural explanation for the highly peaked angular distributions previously described by ad hoc form factors, but, because of the importance of the decay correlations of resonances, the spins of the particles have to be properly treated in a consistent way (viz. example in ref. 67).

The amplitude is written using the Distorted Wave Born approximation. Necessary information concerning the absorption is obtained from the on-mass shell elastic diffraction scattering at high energy. In the initial state, this may be taken directly from experiment, however, the final state scattering of the resonance is unknown. This scattering is usually assumed to be stronger than the final absorption. The best agreement with the model is expected at small Δ^2 and large s, where many channels are opened. However, the model has mainly been formulated for a quasi-two-body final state.

Further modifications can be made by using vertex form factors. With these two corrections the model gives a slightly better account of the decay distribution of resonances, essentially by introducing more parameters. The model is in best agreement with experiment at low Δ^2; this is not greatly different from the distribution predicted by single particle exchange. The model has little success in the case of the vector meson and for high spin particle exchange[79]. Under the absorption model, only the Δ^2-dependence of the amplitude is modified but not the s. The same problem of an increasing cross-section is encountered for $J > 1$ due to the form of the amplitude.

6.1.3 <u>Diffractive Scattering</u> - Drell and Hiida[68] pointed out another important consequence of the peripheral effect in N-N scattering; namely the diffractive scattering of the virtual exchanged particle at the baryon vertex (Nucleon cloud). M.L.Good and W.D.Walker[68] predicted that these diffraction-produced systems should have an extremely narrow distribution in transverse momentum that is characteristic and, furthermore, that the final particle or resonance should have the same quantum numbers as the initial particle in spin, isotopic spin and parity.

Consider a proton-proton interaction of the same type as reaction (6.1) :

i.e. $$p + p \longrightarrow p + N^{*+} \qquad \text{.........} (6.6$$

The predicted cross section for N^* by the Absorption of Form Factor Peripheral Model decreases strongly with energy, whereas the experimental values are nearly constant[87] (the N^* cross sections of ref.87 are reproduced in figure 6.2). In this case the predictions of the Diffraction Dissociation Model probably give the best agreement[79].

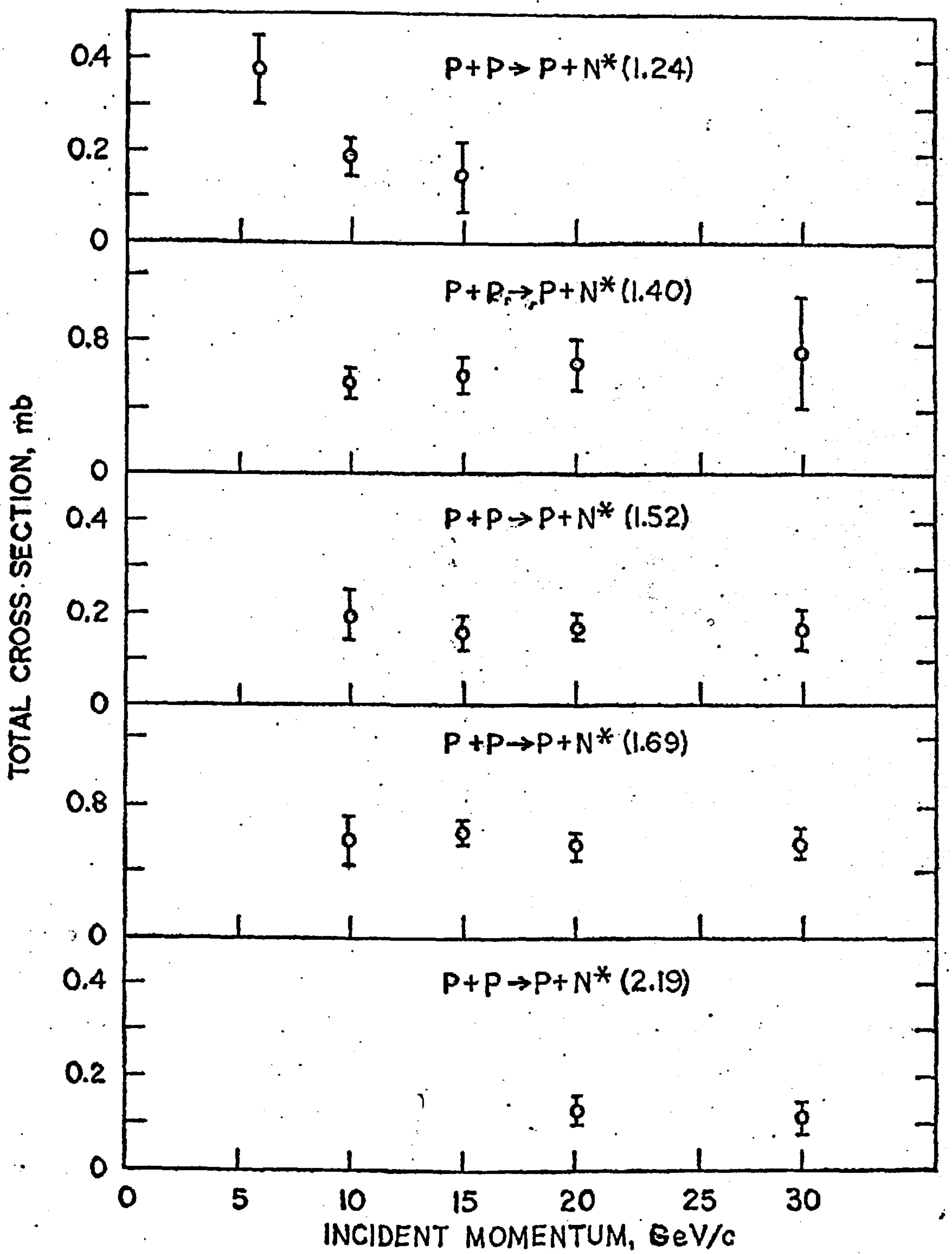
P+P → P+N* (1.24)
P+P → P+N* (1.40)
P+P → P+N* (1.52)
P+P → P+N* (1.69)
P+P → P+N* (2.19)
TOTAL CROSS SECTION, mb
0.4
0.2
0
0.8
0
0.4
0.2
0
0.8
0
0.4
0.2
0
0
5
10
15
20
25
30
INCIDENT MOMENTUM, GeV/c

Fig. 6.2

Figure 6.1c shows a Feynman diagram for the scattering, in the cloud of the target nucleon, of a pion from the incident projectile nucleon (i.e. p_1 dissociates at A into a virtual pion (shown dotted) and a nucleon N_A or Δ_A). The reaction is of type (6.6) where N^{*+} may decay into an $\Delta_A + \pi^-$ or $N_A + \pi^-$. The elastic (πp_2) scattering of the virtual pion from the vertex A at vertex B is a diffractive dissociation high energy process, so that the outgoing π and proton will have almost the same momentum as before, which is independent of the momentum of p_2. The pion leaving vertex B with high momentum then takes part in the final reaction with N_A or Δ_A to form the N^{*+} resonance.

The most important points of this mechanism can be summarized as:-

(i) The differential cross section for the dissociation $p_1 \longrightarrow N_A + \pi$ may be taken as independent of the momentum of p_2.

(ii) N_A and the pion leaving B have approximately the same velocity and therefore the cross section for them to combine together to form an isobar will be large. This is a low energy effect, and will be approximately independent of the momentum of p_2.

(iii) For a high energy elastic reaction at B, the cross section is approximately independent of energy.

Since the three cross sections described above, for A, B and the final interaction, are all independent of p_1, then the overall cross section for the reaction (6.6) may be expected to be approximately constant.

(iv) The relevant quantum number of N^{*+} will be the same as that of a proton with an isospin of $I = \frac{1}{2}$ (as a consequence of vacuum exchange).

(v) In contrast the well known production of $\Delta^{++}(1236)$ requires an exchange particle with I = 1. This is apparent from the corresponding decrease in the cross section with increasing incident energy. Thus this process cannot be explained by a diffraction dissociation mechanism.

6.2 The Regge Pole Models(61,63)

In general the exchange of a spin J particle gives rise to a term proportional to S^J in the cross section. This strong energy dependence on spin is the most serious difficulty with peripheral models.

The "Regge pole model", which originates in potential theory, offers some hope to suppress this violent energy dependence at high energy. Regge(69) opened new possibilities in discussing the connection between the non-relativistic potential scattering amplitude and the scattering of the two particle amplitude into the complex angular momentum plane (ℓ-plane). It was shown later by the Sommerfeld-Watson(66) transformation that, under reasonable assumptions, fulfilled by most field theoretical potentials, the scattering amplitude at some fixed energy determines the potential uniquely when it exists. Moreover, for special classes of potential, the spatial wave amplitude $f(\ell, E)$ is analytically continuous into the complex ℓ-values, except for cuts and possible poles which may correspond to bound states and resonances. These, so called "Regge Poles" correspond to the poles of the scattering amplitude f (l , s) that move in the complex angular momentum plane as the energy varies. The position of a Regge pole as a function of energy $\alpha(s)$ is called a "Regge Trajectory", where s is the square of the c.m. energy.

The Regge trajectory correlates particles (bound states of different angular momenta and resonances) having the same internal quantum numbers (i.e. baryon number, isospin, G-parity, etc) and the same parity. The spin however may differ by units of two. The set of resonances associated with a trajectory are called "Regge recurrences". A sample of a set of pictures (known as a Chew-Frautschi diagram) are illustrated in figure 6.3.

In Regge theory applied to high energy reactions, the concept of one particle exchange is replaced by the exchange of a whole Regge trajectory in the t-channel. The asymptotic scattering amplitude (A) for the exchange of a Regge trajectory α (t) may be approximated by the expression:-

$$A \approx \beta(t) \; \varphi(t) \left(\frac{S}{S_0}\right)^{\alpha(t)} \quad \ldots\ldots\ldots\ldots\ldots \; (6.7a)$$

$$\varphi(t) = \frac{1 + \tau \exp(-i\pi\alpha(t))}{\sin\alpha(t)} \quad \ldots\ldots\ldots \; (6.7b)$$

and $$\varphi(t) = \frac{\exp\left(\frac{-i\pi}{2}\alpha(t)\right)}{\sin\frac{\pi}{2}\alpha(t)} \quad \text{for} \; = \tau = +1$$

or $$= \frac{\exp\left(\frac{-i\pi}{2}\alpha(t)\right)}{\cos\frac{\pi}{2}\alpha(t)} \quad \text{for} \; = \tau = -1$$

where τ = trajectory signature

$\alpha(t)$ = " parameter: real for $t < 0$
ima. for $t > 0$

$\beta(t)$ = residue function.

S_0 = scaling factor.

FIG. 6·3

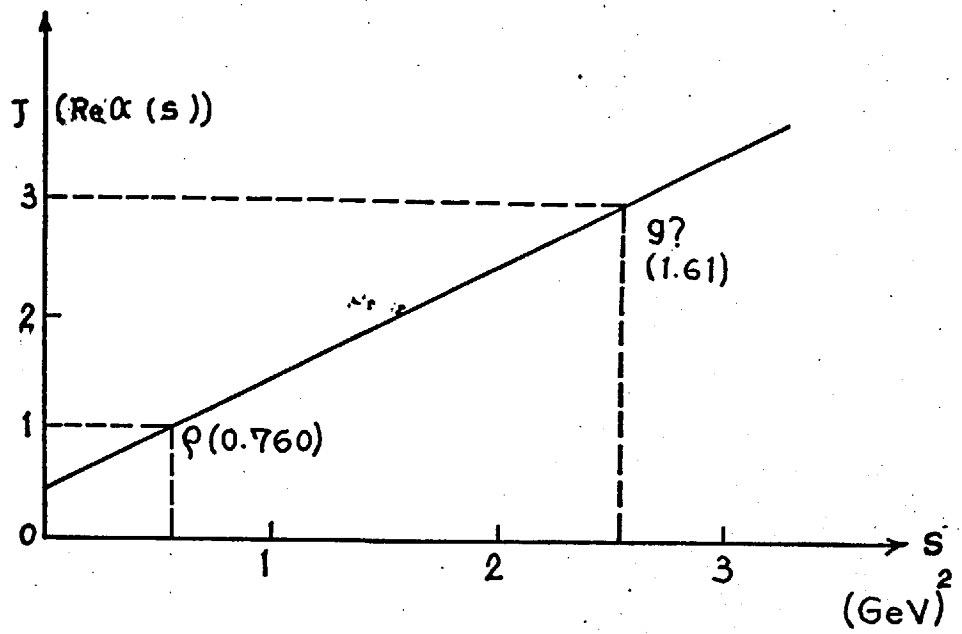

The Chew Frautschi Diag. for the ρ - Trajectory
Assuming a Constant Slope of 1 $(\text{GeV})^{-2}$

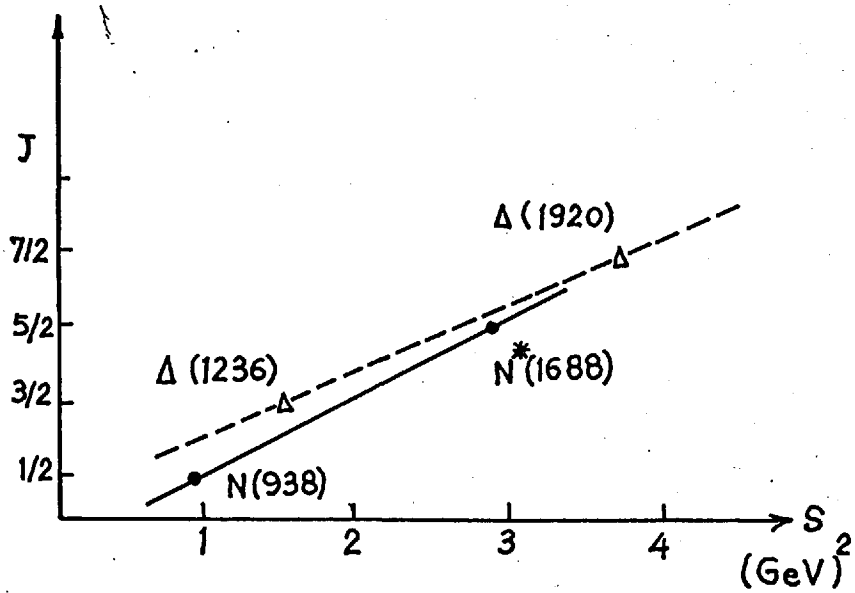

The Chew Frautschi Diag. for the N- and Δ - Trajectories

The results of Regge on the behaviour of A for $S \longrightarrow \infty$, predict some effect on the exchanged particle. Using the relation between total cross-section (σ_T) and the imaginary part of the amplitude in the forward (t=o) direction, the total cross-section can be written in the asymtotic limit form as:-

$$\sigma_T \sim \left(\frac{S}{S_o}\right)^{\alpha_1(o)-1} \qquad \text{.........} \quad (6.8a)$$

The characteristic Regge-energy dependent differential cross-section is then written :-

$$\frac{d(S,t)}{dt} \sim \left(\frac{S}{S_o}\right)^{2(\alpha_1(t)-1)} \qquad \text{.........} \quad (6.8b)$$

where α_1 (t) is the leading trajectory.

The Regge theory in addition predicts that (a) the diffraction peak should shrink with increasing energy, and (b) that the dips occur in $d\sigma/dt$ distribution correspond to the vanishing of the spin-flip amplitude. This is illustrated in the case of the charge exchange process $\pi^- p \longrightarrow \pi^o n$ where only ρ-exchange can occur. The extrapolation of the ρ-trajectory on the Chew-Frautschi plot (fig. 6.3) intercepts the s axis at $R_e\alpha(s) = 0$ at a value ≈ 0.6 $(GeV)^2$ corresponding to the point in the $d\sigma/dt$ distribution where a dip is seen experimentally. Furthermore experimental data from πN scattering suggest that as $S \longrightarrow \infty, \sigma_T \longrightarrow$ constant which requires that α (o) = 1 for the leading trajectory. This phenomenon is known as the Pomeranchuk(P trajectory[67] and is assigned a positive signature with $\alpha_1(o) = 1$. A purely imaginary forward amplitude is implied, and zero isospin (I = 0) is necessary for it to couple in a $\pi\pi$ resonance with $l = 2$. Good qualitative agreement with experiment is thus obtained (see application in reference 67 for example). It should be noted that P has all the quantum numbers of the vacuum, except spin, and so it is an example of a "Vacuum trajectory". This property allows it to be exchanged in all elastic reactions and is supposed to dominate all high energy scattering processes.

6.2.1 Double Regge Pole Model (DRPM)[70,80] - Unfortunately, due to the complexity of the problem, both our experimental knowledge and theoretical understanding of multi-particle production have remained at a considerably lower level than that for Quasi-two-body inelastic reactions, for which we can make remarkable predictions on the constant total cross-section, the imaginar scattering amplitude and the shrinkage in the diffraction peak. Nevertheless, some progress has been made over the last few years using the "Multi-Regge Pole Model" which covers reactions in which more than two particles (or resonances) are produced in the final state.

The Double Regge Pole Model of Chang-Hong-Mo, K.Kajantie and G.Ränft[70] is a special case concerning hadron production processes in which three final particles are produced at high energy as depicted in figure 6.4a for the reaction:-

$$1 + 2 \longrightarrow 3 + 4 + 5 \qquad \text{.........} \quad (6.9)$$

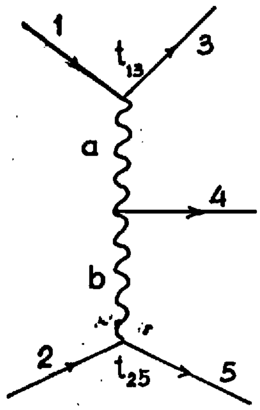

Fig. 6·4a

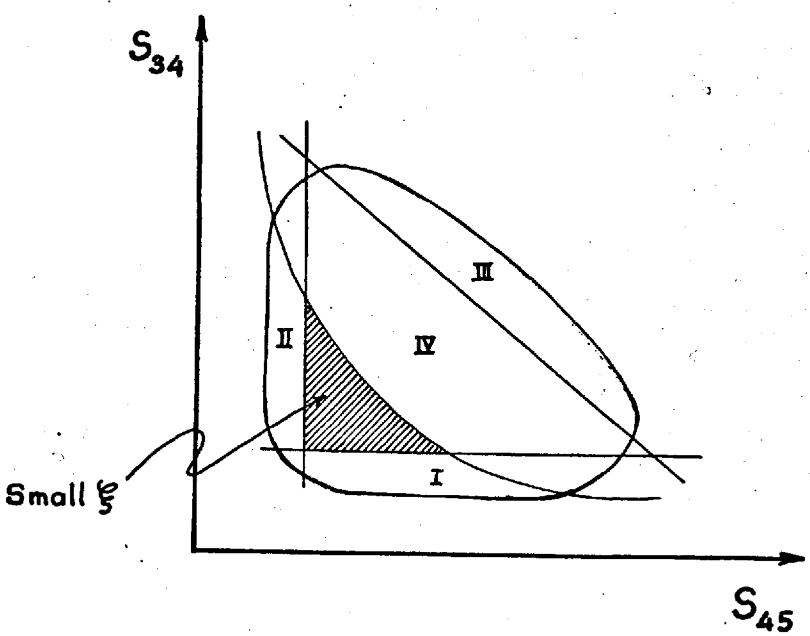

I Small S_{34}

II Small S_{45}

III Small S_{35}

Fig. 6·4 b

In fact, the exchange particles a and b can be either physical particles (double peripheral picture) or Regge trajectories (double Regge pole picture). As the model is obtained from an extension to the Regge pole model for quasi-two-body reactions at high energy, various relevant conservation laws at each of the three vertices are still needed; furthermore because of the peripheral nature of the reactions the four-momenta at vertex I and II (t_{13} , t_{25}) should, in practice, have low values. Some important properties of the Double Regge graph are proposed by the authors of reference 70. These are expected to be valid only for non-resonant events which correspond to the centre of the Dalitz plot (region IV of figure 6.4b) where all two-body effective mass is large.

Here, $S_{34} = (P_3 + P_4)^2$ and similarly for S_{45} and S_{35}

$$S = \text{the total energy squared} \qquad \text{.........(6.10}$$

$$S = (P_1 + P_2)^2 = S_{34} + S_{45} + S_{35} - m_3^2 - m_4^2 - m_5^2 \qquad \text{.........(6.11}$$

where P_i = the four-momenta of i^{th} particle.

Several important kinematical consequences of reaction (6.9) can be summarised:-

(i) In C.M.S. particle 3 and particle 5 will be peaked forward and backward respectively, while particle 4 will be more isotropically distributed.

(ii) The C.M.S. longitudinal momentum P^*_{Li} of the final particles (i = 3, ...5) measured in the direction of beam particle 1, tend to be ordered algebraically as follows:

$$P^*_{13} > P^*_{14} > P^*_{15}$$

(iii) For any permutation of the Regge graph satisfying (ii), the events of that graph will be populated only at one corner of the Dalitz plot, when

$$\mathcal{G} = \frac{S_{34}\,S_{45}}{S} \quad \text{is small.}$$

(iv) The final particles of low mass cluster are connected by the exchange a, b which is taken to be Reggeised. (Figure 6.4a).

The amplitude for the graph in figure 6.4a is intuitively suggested as:-

$$|A|^2 = \gamma_a(t_{13})\,\gamma_b(t_{25})\,\gamma(t_{13}, t_{25}, \phi)\,\mathcal{S}_a(t_{13})\,S_{34}^{2\alpha_a(t)}\,\mathcal{S}_b(t_{25})\,S_{45}^{2\alpha_b(t)} \quad \ldots\ldots\ (6.12)$$

where γ_a or γ_b = the coupling for the Regge pole a or b to particle 1, 3 or 2, 5.

$$\left.\begin{array}{lcl} \text{and } \mathcal{S}_a, \mathcal{S}_b & = & \text{signature factors} \\ \alpha_a, \alpha_b & = & \text{trajector parameters} \end{array}\right\} \text{see eqn 6.7}$$

The only new factor in addition to quasi-two-body reactions is:-

$\gamma(t_{13}, t_{25}, \phi)$ = the coupling of the two Regge poles a and b to the particle 4.

By analogy with the two-particle Regge pole model, one also expects an approximately exponential dependence on t_{13} and

t_{25} . This has led to the following approximate formula:-

$$|A|^2 \approx B_0 \exp\left[2(\Omega_a t_{13} + \Omega_b t_{25})\right] S_{34}^{2\alpha_a} \; S_{45}^{2\alpha_b} \qquad \ldots\ldots\ldots(6.13$$

with nearly straight Regge trajectories

where $\quad \Omega_a = a + \alpha_a' \log S_{34}$

and $\quad \Omega_b = b + \alpha_b' \log S_{45} \qquad \ldots\ldots\ldots (6.14)$

α' is taken to be approximately 1 $(\text{GeV})^{-2}$. The diffractive parameters a and b for each graph can be chosen as the constant parameters.

In the case of Ø-dependence (ref. 70) has shown that an amplitude strongly favours the value $\phi = \pi$ and that it decays exponentially from this value.

Ø is defined as some azimuthal angle in the rest frame of particle 4 by

$$\cos\phi = \frac{(\bar{p}_1 \wedge \bar{p}_3)\cdot(\bar{p}_2 \wedge \bar{p}_5)}{|\bar{p}_1 \wedge \bar{p}_3| \; |\bar{p}_2 \wedge \bar{p}_5|} \qquad \ldots\ldots\ldots (6.15$$

This procedure is compared to the predictions of the Double Regge Pole Model for three experiments at CERN: viz.

$\pi^+ p \longrightarrow \pi^+ \pi^0 p$ at 8 GeV

$\longrightarrow \pi^+ \pi^- n$

$\pi^- p \longrightarrow K_1^0 K_1^0 n$ at 7 and 12 GeV

and is described in detail as the example in reference 70.

The results are encouraging. The model also makes, in addition, several clear predictions subject to experimental test, and is sufficiently general to form the basis of a systematic analysis of three particle data. Reasonable fits are obtained[70] from a double Regge pole model with pion exchange for invariant mass and momentum transfer, etc., for the reaction $pp \longrightarrow \Delta^{++} p \pi^-$ at 6.6 GeV as well as for some higher energy experiments for the same reaction.

Figure 6.5a illustrates a special non-resonant case first explained by R.T. Deck[71]. The reaction is similar to reaction (6.9) where exchange particle a $\equiv$ particle 3 and particle 2 $\equiv$ particle 5. It indicates an obvious Pomeranchuk particle (P) exchange at the lower vertex. It can be shown that such a process will produce an enhancement at the low mass region in the mass spectrum of particles 3 and 4. This mechanism is called the "Deck effect" and was later modified by Moar and O'Halloran[71] to deal with kinematic enhancements in the final state for peripheral processes.

6.2.2 A Reggeised Multi-peripheral Model[72]

A phenomenological model for the inelastic process at high energy ($\gtrsim$ 5 GeV) is a natural extension of the Double Regge Pole Model (DRPM) and applied to production processes of the type:

$$A + B \longrightarrow 1 + 2 + 3 + \ldots \qquad \ldots\ldots\ldots \; (6.16)$$

The DRPM was formerly thought to apply only to the high energy domain in the asymtotic limit (large S_{ij} , region IV of fig.6.4b)

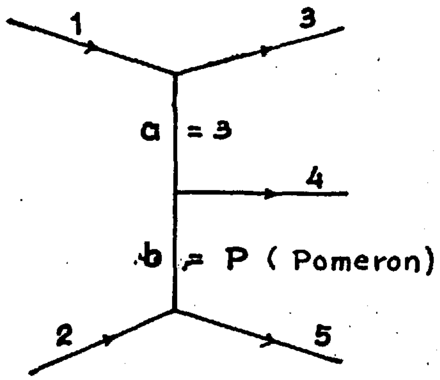

Fig. 6·5a Deck Diag. for 3-body Final State.

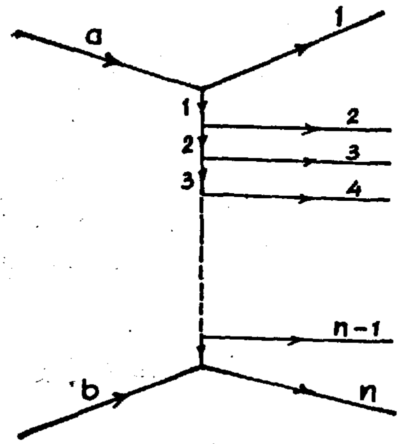

Fig. 6·5b Multi-Particle Final State

of the special case of a three-body final state. In practice, only a small fraction of production events satisfy such a criterion.

It has been discovered that one can include all events, where the final particles are clusters with low effective mass, provided the structure of such non-resonant clusters is assumed to be governed only by phase space. This part of the amplitude is replaced by an effective constant which corresponds to interactions within the cluster.

Let S be the incoming energy of reaction (6.16) defined as:

$$S = \sum_{i>j} S_{ij} - (n-2)\sum_{j} m_j^2 \qquad \text{........ (6.17)}$$

where $S_{ij} = (P_i + P_j)^2$

n = the multiplicity.

There are two alternative ways of considering the amplitude of the interaction:-

1) If S is fixed when n is small, all S_{ij} have a tendency to be large and the amplitude becomes fully Reggeised. If n increases, S_{ij} become smaller and form a single cluster yielding a picture close to "statistical equilibrium".

2) If n is fixed and we allow S to increase, the converse situation will arise.

However from the model the amplitude of reaction (6.16), as shown in figure 6.5b, can be parametrized in such a way that a smooth transition from the constant phase-space to the Reggeised picture is obtained as energy or multiplicity varies. The suggested amplitude is :-

$$|A| \sim \prod_{i=1}^{n-1} \left(\frac{g_i S_i + ca}{S_i + a}\right)\left(\frac{S_i + a}{a}\right)^{\alpha_i}\left(\frac{S_i + b}{b_i}\right)^{t_i} \qquad \text{........ (6.18)}$$

where a, b_i, c and g_i are constant parameters, obtained

(a) from well known values from other experiments

or (b) by fitting with the data.

and α_i is the intercept of the i^{th} Regge pole.

Variables S_i and t_i are defined as:-

$$S_i = (P_i + P_{i+1})^2 - (m_i + m_{i+1})^2$$

$$t_i = (P_A - \sum_{r=1}^{i} P_r)^2 \qquad \text{......... (6.19)}$$

Equation (6.18) reduces to:-

$$|A| \sim \prod_{i=1}^{n-1} g_i\left(\frac{S_i}{a}\right)^{\alpha_i} \exp\left[B_i + \log S_i\right] t_i \qquad \text{......... (6.20)}$$

when $S_i \gg a$ and b_i

and $B_i = -\log b_i$

We see that equation (6.20) is a fully Reggeised multi-particle amplitude with approximations to the vertices for coupling constant g_i and linear approximations to the trajectory of slope 1 $(\mathrm{GeV})^{-2}$.

In practice, one obtains the amplitude of a given reaction by the incoherent addition of all the permutation pictures of the final particles, providing the quantum selection rule is conserved. It is accepted that the "a" of equation (6.16) is taken to be fixed at 1 $(\mathrm{GeV})^2$ for Regge phenomenology and is reckoned as the boundary between the low energy phase-space and the high energy Regge type events. Some implications of this model are relevant to the present experiment and these will be discussed in Chapter 7.

This model is justifiable since its resulting amplitudes have been used as a weight in all the calculations in the Monte Carlo phase space programme FOWL(60). Comparison with experiment has been made for reactions(72).

(i) $\pi^{\pm} p \longrightarrow p + (n-1)\pi$

(ii) $K^{-} p \longrightarrow \Delta + (n-1)\pi$

where n = 3 ..... 9 and the energy range is from 5 to 16 GeV. The results are claimed to be encouraging.

CHAPTER 7

RESONANCE PRODUCTION

The cross sections for the resonances obtained in the present experiment are presented below. The main part of the chapter is concerned with a discussion of their experimental observation. Some implications of the models described in chapter 6, relevant to the $pp \longrightarrow pp\pi^+\pi^-$ reaction, are also discussed.

7.1 The Observation of Resonances

Final state interactions can be seen when the differential cross section is plotted with respect to the invariant mass, for two or more final state particles. Any resonance production is indicated by an enhancement in the differential cross section for a particular invariant mass value. Greater insight is offered by a suitable choice of scatter plot. The most useful forms for these plots are described below.

7.1.1 Phase space and the Dalitz plot - The "Statistical Model" was introduced first by Fermi[75] in his theory for pion production. His calculation of transition rate (W) between an initial state (i) and the final state (f) was based on the concept and use of Phase Space; so that the probability per unit for the reaction can be written as an expansion in perturbation theory. Thus,

$$W = \frac{2\pi}{\hbar}\left|M_{if}\right|^2 \rho_n(E) \qquad \text{.......... (7.1)}$$

where

M_{if} = the matrix element for the transition. Perturbation theory then gives $M_{if} \left(\approx \langle f | M | i \rangle\right)$

$\rho_n(E)$ = the density of final states (or phase space factor).

The expression (7.1) is invariant under Lorentz transformation and generally "M" is a function of the energy of the system and of the momenta of the particles in the final state. However, it is interesting to see whether or not a process is produced as a random fluctuation (or as the background) of an interaction. For the simplest possible physical state it has been assumed that $\langle f \,|M|\, i \rangle$ is unity and that the M values, for all final states, are essentially constant or the same. Thus, the phase space factor $\rho n(E)$ determines the final configuration completely. The Lorentz invariant phase space can be explicitly defined(76) by using the properties of the δ-function:

$$n(E) = \int \prod_{i=1}^{n} \left[d^4 q_n \; \delta(q_i^2 - m_i^2) \right] \delta^4\left(\sum_{i=1}^{n} q_i - Q\right) \quad \ldots\ldots\ldots \; (7.2)$$

n = total number of final state particles

$q_i = (E_i, \bar{p}_i)$ = the four-vector notation (p_x, p_y, P_z, E)

$Q = (E, \bar{p})$ = the total available energy momentum four-vector.

The statistical significance of any experimental enhancements or resonances in the mass (m_{r6}) distributions is then determined by comparison with the predicted frequency distribution obtained by differentiating equation (7.2) w.r.t. m_{rs}. Resonances are observed as departures from the phase space contribution. The shape of a resonance may be parameterised in the relativistic Breit Wigner form[42] :-

$$f\,(m_{rs}) = \frac{\Gamma/2}{(m_{rs} - m^*)^2 + \Gamma^2/4} \qquad \text{..........} \quad (7.3)$$

Γ = half-height full-width of the resonance
m_{rs} = effective mass of final state particles r and s.
m^* = central resonant mass.

The phase space and resonant phase space contributions are usually generated by Monte Carlo methods[60]. The shape of the phase space distribution depends on the value of the interaction energy as well as the masses of the particles. Details can be seen in reference 76.

However some further analysis of a significant enhancement has to be done (e.g. study of the spin&parity of the resonance, its decay correlations and/or the observation of a similar enhancement in other experiments at different energies) in order to show conclusively that the enhancement is not purely a kinematic effect (e.g. $N^* \longrightarrow \Delta^{++}\pi^-$ is observed and is probably the result of the diffraction scattering of the π^- from the lower vertex) and can be claimed as a "Resonance" (see example in ref.77).

More detailed information about resonances and the influence of one on another may be obtained from the study of a two dimensional plot of events in the reaction. The Dalitz plot[78] is a useful way of presenting results for a three-body final state and figure 7.1 shows such a diagram for the following reaction:-

$$1 + 2 \longrightarrow 3 + 4 + 5$$

Each event is plotted, in practice, as a point on a diagram in which the coordinates are the invariant masses S_{35} and S_{34} (one could also use the kinetic energies calculated in the C.M.S. of particles 4 and 3 respectively). Total energy and momentum conservation in the C.M.S. imposes a certain boundary for the plot as shown in figure 7.8a. It may be shown[63,76] that the density of points in the boundary area should be uniformly populated if the reaction proceeds in accordance with the prediction of Lorentz invariant phase space But if any two of these particles resonate and form a unique mass (i.e. $S_{34} = m_{34}$) the particle distribution in the Dalitz plot will cluster along a fixed value of S_{34} (see figure 7.8a for instance). The density of points is proportional to the square of the invariant matrix element for the reactions in question.

7.1.2 Triangle Plot - Another useful scatter plot can be used for investigating the four-body final state[64,76]

$$1 + 2 \longrightarrow 3 + 4 + 5 + 6$$

The chosen axes/are x and y the effective mass combinations of selected pairs taken from the four-body final state. In this representation the kinematic limits for a pair of "two-particle composites" having invariant masses m_x and m_y (in the overall C.M.S.) define a triangular allowed region. This region is a right angle isosceles triangle and the length of each leg is given by

$$Q_L = W - \sum_{i=1}^{4} m_i \qquad \text{.........} (7.4)$$

where W is the total energy in the C.M.S. and

m_i, = are the masses of the four outgoing particles.

The phase space distribution[35] is given by:-

$$\phi \propto \frac{1}{W} \int k_x \, k_y \, p_o \, dm_x dm_y \qquad \text{..........}(7.5)$$

k_x and k_y are the momenta in the C.M. of the x and y components respectively. p_o is their momentum in the C.M.S. It is worth noting that the distribution of points for phase space is no longer uniform, rendering interpretation rather difficult However, since there are three ways (channels) in which the final state particles can be "paired" off into two particle composites, inspection of the three possible triangle plots will show direct evidence of a double resonance (if it is present) by a clustering on one of the plots (see example in reference 35).

7.1.3 Decay correlations - At high energy if the differential cross sections are the only available data, it is often impossible to discriminate between the different models when accounting for the connection between the production mechanism and the angular correlation in the decay of resonances. It has been shown(74) that the OME model can be generalised by means of Regge pole exchange in a way which gives a natural explanation of the very peripheral nature of the production process, while maintaining agreement with the decay data.

Provided there are reasonable statistics, the spin and parity of a newly discovered resonance can be established from the decay angular distribution. $\cos\theta$ and ϕ defined in the Gottfried-Jackson frame are the most convenient and popular variables used to study this decay correlation and they have bee described in Chapter 5. The general expressions for the decay distribution for any spin can be found in ref. 64 and 74.

The decay angular distributions may be written down in terms of the density matrix element $\rho_{2m,2m'}$, where m and m' are the magnetic quantum numbers relative to the beam direction, this is taken as Z-axis in the resonance rest frame. Two parameters are necessary to define the as they are complex elements. From the probability density concept of quantum states we have the following properties:-

(i) $\rho^{+}_{m,m'} = \rho_{m,m'}$ i.e. $\rho_{m,m'} = \rho^{*}_{m,m'}$ and is hermitian

(ii) Trace $(\rho) = 1$, $\Sigma\rho_{m,m} = 1$ from unitarity

(iii) $\rho_{-m,-m'} = (-1)^{m-m'}\rho_{m,m'}$ by parity conservation.

This reduces the number necessary to specify the $\rho_{2m,2m'}$ from $2(2J+1)^2$ to $2J(J+1)$ for integral J, and to $2J(J+1)-\frac{1}{2}$ for half integral J.

As $\Delta^{++} \longrightarrow p\pi^{+}$ is the dominant resonance for proton-proton reactions we will briefly recall the properties of the hermitian density matrix element for a spin $J = 3/2$ baryon resonance decaying into a spin $J_\alpha = \frac{1}{2}$ fermion and a spinless boson ($J_\beta = 0$). The decay distribution is given(64) by:-

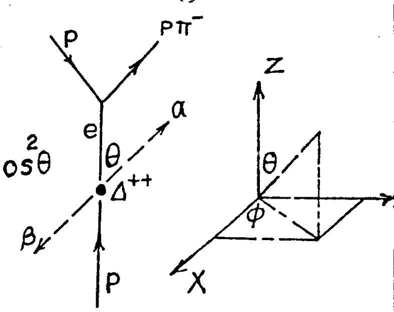

$$W(\cos\theta, \phi) = 3/4\pi\Big[1/6(1+4\rho_{3,3}) + 1/2(1-4\rho_{3,3})\cos^2\theta$$

$$- 2/3\,\mathrm{Re}\,\rho_{3,-1}\sin^2\theta\cos$$

$$- 2/3\,\mathrm{Re}\,\rho_{3,1}\sin 2\theta\cos^2\phi\Big] \qquad \ldots\ldots\ldots (7.6)$$

with Trace condition $2\rho_{3,3} + 2\rho_{1,1} = 1$

Integrating (7.6) over ϕ or $\cos\theta$ yields the following distributions:-

$$\int_0^{2\pi} W(\cos\theta,\phi)\,d\phi = 1/4\left[(1+4\rho_{3,3}) + (3-12\rho_{3,3})\cos^2\theta\right] \ldots\ldots (7.7)$$

$$\int_1^{-1} W(\cos\theta,\phi)\,d(\cos\theta) = 1/2\pi\left[(1+4/\sqrt{3}\,\mathrm{Re}\,\rho_{3,-1}) - 8/\sqrt{3}\,\mathrm{Re}\,\rho_{3,-1}\cos^2\phi\right] \ldots (7.8)$$

If the exchange particle is a pion the decay distributions (7.6), (7.7) and (7.8) can be simplified to:-

$$W(\cos\theta, \phi) = \frac{1}{8\pi}(1 + 3\cos^2\theta)$$

$$W(\cos\theta) = \frac{1}{4}(1 + 3\cos^2\theta)$$

$$W(\phi) = \frac{1}{2\pi} = \text{constant}$$

The above results are applied to the decay of the Δ^{++} in section 7.2.1.

There are three main methods of determining the density matrix elements experimentally[64].

(i) Method of maximum likelihood.

(ii) Method of moments.

and (iii) Method of least squares fit.

Method (i) is generally considered to be the most satisfactory and so was employed for the present experiment, viz:-

Let n = number of events which produce a Δ^{++}

θ_i, ϕ_i = the experimental values of the decay angles for the i^{th} event.

Let x_1, x_2, x_3 denote the three density matrix elements $\rho_{3,3}$, $\mathrm{Re}\,\rho_{3,-1}$ and $\mathrm{Re}\,\rho_{3,1}$ that occur in the decay distribution equation (7.4). The likelihood function for the experiment is defined by

$$\mathcal{L}(x_1, x_2, x_3) = \prod_{i=1}^{n} W(\cos\theta_i, \phi_i, x_1, x_2, x_3) \quad ....(7.9$$

Using a starting set (x_1, x_2, x_3) that is then varied, one finds the optimum set (x_1^*, x_2^*, x_3^*) that gives the maximum valu of $\mathcal{L}(x_1, x_2, x_3)$. This set is then the best estimate for the matrix elements.

Finally, it is worth mentioning that it is not possible experimentally to obtain a pure sample of the Δ^{++} resonance. One should take the background into account to determine the matrix elements. Background subtraction is usually performed[64] by determining the "density matrix elements" corresponding to adjacent regions to the Δ^{++} peak.

The x_i^* of the Δ^{++} can then be calculated:-

$$x_i^* = \frac{x_{ia}^* \; N_a \; - \; N_b \; x_{ib}^*}{N_a - N_b} \qquad \text{.........} \; (7.10)$$

where x_{ia}^* = matrix elements for all N_a events in the Δ^{++} mass region (defined as 1.15 - 1.30 GeV)

x_{ib}^* = matrix elements for events in the adjacent region.

N_b = background events (estimate from effective mass distribution within the Δ^{++} mass range).

7.2 The $\Delta^{++}\pi^-$ Final State

For the present experiment some 10.7% of four-prong events uniquely fit

$$pp \longrightarrow pp\pi^+\pi^- \qquad \text{..........} \; (1)$$

0.45% were ambiguous fits which could not be resolved by ionization. Since the latter number is small, they have not been included in the data analysis.

The $p\pi^+$ mass distribution (figure 7.5c) shows that of the 1,548 events of reaction (1), 802 proceed through reaction

$$pp \longrightarrow \Delta^{++}\, p\pi^- \qquad \text{..........} \; (1a)$$

Both protons in the final state contribute to the Δ^{++} mass range (1.15 - 1.30 GeV) for 20 events of reaction (1a).

A study of reaction (1a) on the basis of the $p\pi^+$ mass distribution alone cannot take into account the influence of $p\pi^+\pi^-$ resonances. For kinematical reasons, resonances at low $p\pi^+\pi^-$ mass give rise to enhancements at low $p\pi^+$ mass. Also, if higher isobars in $p\pi^+\pi^-$ decay via $\Delta^{++}\pi^-$:-

$$pp \longrightarrow N^*p \longrightarrow (\Delta^{++}\pi^-)\,p \longrightarrow (p\pi^+\pi^-) \qquad \ldots\ldots\ldots (1b$$

these cannot be separated from reaction (1a).

For high energy experiments, in general, the conventional Lorentz invariant phase space multiplied by the Breit-Wigner form[42] of resonance, yield an unsatisfactory cross section for resonances; in some cases the Lorentz invariant phase space cannot be used because of the violent disagreement with the experimental data. However, a peripheral phase space (weighted according to the dependence of experimental momentum transfer, i.e. Lorentz phase space multiplied by a simple exponentially falling form factor in the invariant four momentum transfer) is commonly used to describe a background of the resonance. In the case where the statistics are poor or the peaks are not significant or where there is lack of a reliable description of the non-resonant background, fits are difficult and generally impracticable. Therefore a visual estimate is usually made to obtain the cross section for resonances.

In addition, the writer found that the CLA* prediction (section 6.4, Chapter 6; and see application in section 7.4 for instance) of effective mass distributions for reaction (1)

* A Reggeized Multiperipheral Model for Inelastic Processes at High Energy By Chan-Hong.Mo, Loskiewiez and Allison.

and (1a) gave a satisfactory agreement with the experimental distributions, in particular for the non-resonant channels (e.g.). Hence the CLA prediction was taken as a description of the non-resonant background in fitting to determine the differential cross section for the resonances observed.

7.2.1 <u>The $\Delta^{++}(1236)$</u> - A reasonably pure sample of can often be selected, because it is dominantly produced at all energies. If the Δ^{++} is produced at one vertex, further information about the exchange can be obtained by studying the decay angular distribution (chapter 5, section 3).

One way to obtain further insight in the characteristics of the angular distribution, CosΘ was determined and plotted for 50 MeV intervals of the $p\pi^{+}$ effective mass distribution. It was found from the above examination that a useful parameter was given by dividing the distribution at CosΘ = 0.5 and the defined $A_i - B_i$.

where A_i is the number of events distributed between CosΘ = -1 and CosΘ = 0.5 for the i^{th} mass interval

B_i is the number of events distributed between CosΘ = 0.5 and CosΘ = 1 for the same mass interval

and $C_i = (A_i - B_i)$

It can be clearly seen from a plot of C_i as a function of $M(p\pi^{+})$ as shown in figure 72., that in the Δ^{++} mass region, C_i has positive values that decrease toward negative

Fig. 7.1

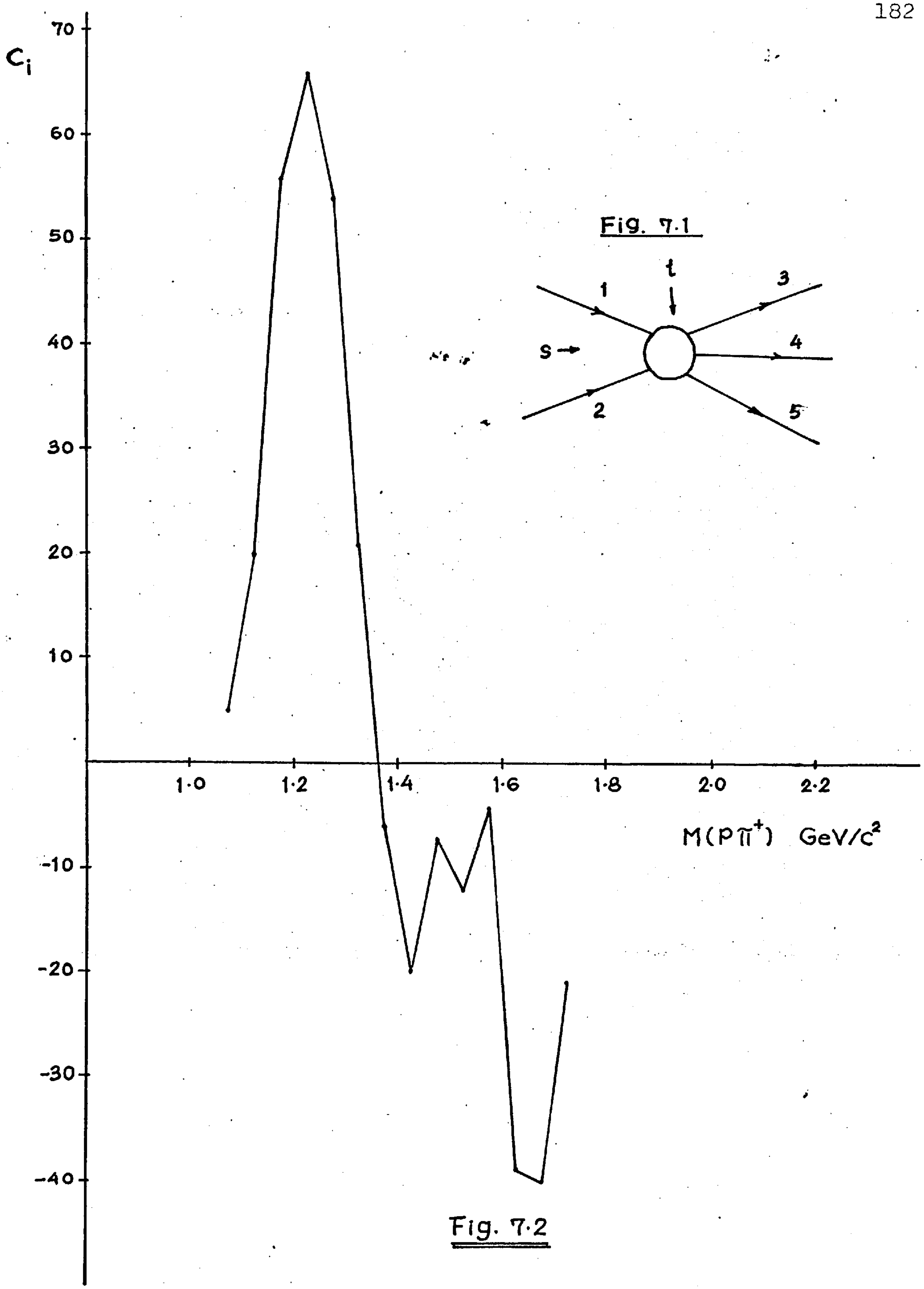
t
1
3
4
s
2
5
C_i
70
60
50
40
30
20
10
-10
-20
-30
-40
1·0
1·2
1·4
1·6
1·8
2·0
2·2
$M(p\pi^+)$ GeV/c^2

Fig. 7·2

values with higher mass. This indicates that when a resonance is formed, its angular distribution has certain characteristics different from the adjacent mass region and so is distinguishable.

We shall now consider correlations of the spin density matrix elements in the decay of $\Delta^{++} \longrightarrow p\pi^+$ (section 7.1.3). A maximum likelihood method was employed (programme MALIK)[83] to determine the experimental density matrix elements of the Δ^{++} and its adjacent region by using equation (7.4) for fitting. Equation (7.8) was used for background subtraction. The results are:-

$$\rho_{3,3} = 0.114 \pm 0.03$$

$$Re\,\rho_{3,-1} = 0.015 \pm 0.03$$

$$Re\,\rho_{3,1} = -0.008 \pm 0.03$$

While $Re\,\rho_{3,-1}$ is consistent with zero, $\rho_{3,3}$ appears to be inconsistent with the OPE prediction ($\rho_{3,3} = Re\,\rho_{3,-1} = 0$). The decay distribution should then have the form $\frac{1}{4}$ (1 + 3 Cosθ) and this is drawn (dotted line) and compared to the fitted curve (solid line) in figure 7.3. Since the two curves are very similar we can assume that one pion exchange dominates the Δ^{++} vertex.

Furthermore, detailed analysis of $\rho_{3,3}$, $Re\,\rho_{3,-1}$ and $Re\,\rho_{3,1}$ as a function of momentum transfer ($\Delta^2(p - \Delta^{++})$) yields the results shown in figure 7.4 (solid line). The dotted lines compare the results from ref.64 ($\pi^+ p \rightarrow \Delta^{++} \rho^0$ at 8 GeV). Once again, this plot shows that the values of $Re\,\rho_{3,-1}$ and $Re\,\rho_{3,1}$

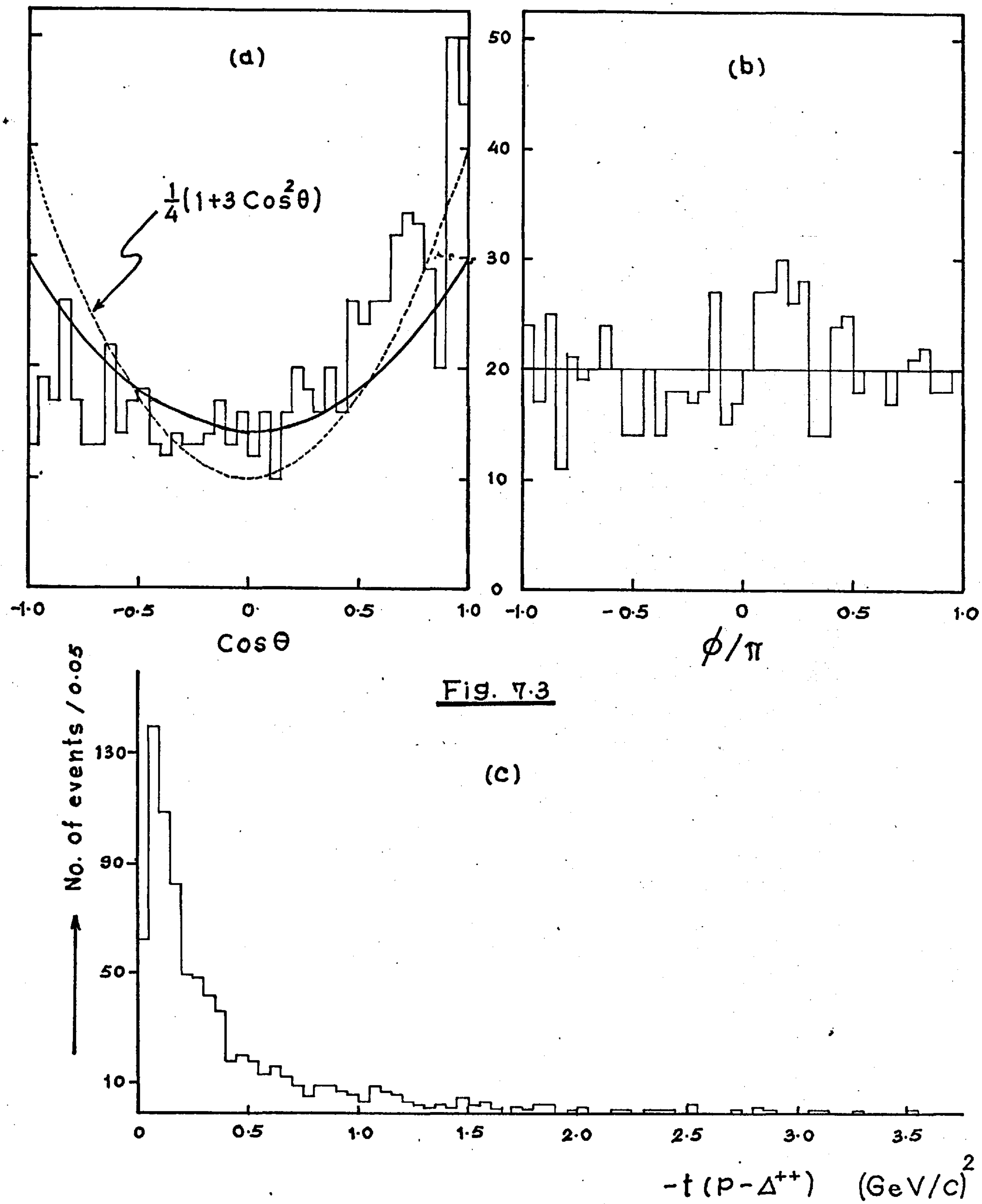
(a)
$\frac{1}{4}(1+3\cos^2\theta)$
50
40
30
20
10
0
-1·0
-0·5
0·
0·5
1·0
Cos θ
(b)
-1·0
-0·5
0
0·5
1·0
ϕ/π
No. of events / 0.05
130
90
50
10
(c)
0
0·5
1·0
1·5
2·0
2·5
3·0
3·5
$-t\,(p-\Delta^{++})$ $(GeV/c)^2$

Fig. 7·3

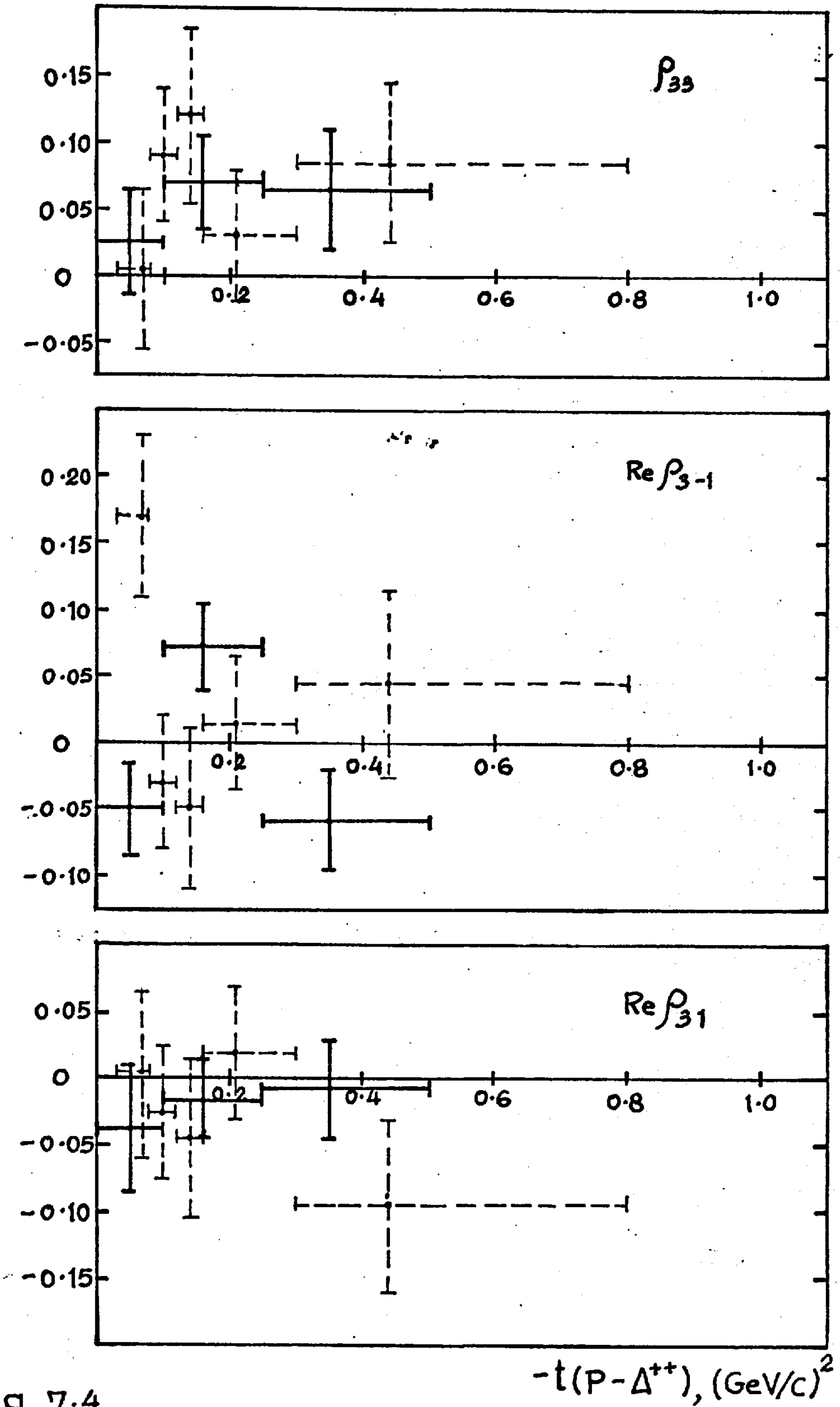

Fig. 7.4

——— $PP \longrightarrow \Delta^{++} P \pi^-$ at 16 GeV/c

- - - - - $\pi^+ P \longrightarrow \Delta^{++} \rho^0$ at 4 GeV/c are compatible with zero, but $\rho_{3,3}$ has a tendency to increase with momentum transfer. On comparison of these results with other experiments (table 7.1) one concludes that at the Δ^{++} vertex the process is dominated by pion exchange. Independent evidence for π-exchange dominance in the reaction

$$pp \longrightarrow \Delta^{++} p \pi^- \quad \text{at } 6.6 \text{ GeV}$$

can be seen in ref.38 in the text by E.Gellert et al.

Table 7.1 shows a list of density matrix elements for Δ^{++} (1236) produced in quasi two body reactions[83] and in $pp \longrightarrow \Delta^{++} p \pi^-$. The results for the reaction $\pi^+ p \longrightarrow \Delta^{++} \rho^o$ at 8 GeV, were found by the ABC collaboration[20] to be about the same as those derived by the ABBBHLM collaboration[64] at 4 GeV. It can also be seen that the results found by the CERN-Brussels collaboration[41] for reaction $K^+ p \longrightarrow \Delta^{++} K^{*o}$ are similar to the reaction $\pi^+ p \longrightarrow \Delta^{++} \rho^o$ which also proceeds by pion exchange. Finally, the density matrix elements found in $pp \longrightarrow \Delta^{++} p \pi^-$ at 8.1 and at 16 GeV are also listed for comparison in table 7.1. Because the values of the density matrix elements for all listed reactions are compatible within the errors, it may be concluded that they are essentially independent of the nature of the incident particle and incident energy

The Δ^{++} cross sections were determined by a chi-squared fit using the programme MINUIT[84] for various types of background estimate tabulated in table 7.2. The mass and width of the Δ^{++} was fixed at 1.236 and .120 GeV respectively. A visual estimate is also given using a smooth hand-drawn background.

TABLE 7.1

Density Matrix Elements for $\Delta^{++}(1236)$

Experimental Reaction	ρ_{33}	$\mathrm{Re}\,\rho_{3,-1}$	$\mathrm{Re}\,\rho_{3,1}$
5 GeV, $K^+p \rightarrow \Delta^{++}K^{*0}$	0.18 ± 0.04	0.01 ± 0.02	0.08 ± 0.02
4 GeV, $\pi^+p \rightarrow \Delta^{++}\rho^0$	0.08 ± 0.03	0.01 ± 0.03	-0.01 ± 0.03
8 GeV, $\pi^+p \rightarrow \Delta^{++}\rho^0$	0.05 ± 0.03	0.015 ± 0.03	-0.076 ± 0.03
8.1 GeV, $pp \rightarrow \Delta^{++}p\pi^-$	0.16 ± 0.02	-0.01 ± 0.02	-0.04 ± 0.02
16 GeV, $pp \rightarrow \Delta^{++}p\pi^-$	0.114 ± 0.03	0.015 ± 0.03	-0.008 ± 0.03

TABLE 7.2

The Cross Section for $pp \longrightarrow \Delta^{++} p \pi^-$

Background	Cross Section (mb)
Smooth hand drawn	0.76 ± 0.01
Peripheral	0.48 ± 0.02
CLA prediction	0.29 ± 0.02

7.2.2 Double Isobar Production

The reaction

$$pp \longrightarrow pp\pi^+\pi^- \qquad \ldots\ldots\ldots\ldots (1)$$

is strongly dominated by $\Delta^{++}(1236)$, the possible double isobar production will be in the following forms:-

$$pp \longrightarrow \Delta^{++}_{3,3} + \Delta^{o}_{3,3}$$

$$pp \longrightarrow \Delta^{++}_{3,3} + N^{*}_{3,j}$$

and $$pp \longrightarrow \Delta^{++}_{3,3} + N^{*}_{1,j}$$

where j/2 is the spin of the isobar.

Figure 7.5a is a plot of the $M(p_1\pi^+)$ versus $M(P_2\pi^-)$ for events of reaction (1) produced at 16 GeV. The $M(p\pi^+)$ projection given in figure 7.5b shows the strong presence of the $\Delta^{++}(1236)$; the curves were fitted as described in section 7.2.1. The projection of $M(p\pi^-)$ given in figure 7.5c reveals the presence of some $\Delta^{o}(1236)$, $N^*(1470/1520)$ and $N^*(1688)$.

The evidence shown in figure 8.3 suggests that the $p_s\pi^-$ mass resolution is considerably better than that for the $p_f\pi^-$ combination. Hence, an attempt was made to estimate the cross section for $p\pi^-$ resonance by using the $M(p_s\pi^-)$ alone (see figure 7.5d); these were simply fitted to three Breit Wigner resonances with no background consideration :-

$$f(p_s\pi^-) = \alpha_1 B_1(m_1,\Gamma_1) + \alpha_2 B_2(m_2,\Gamma_2) + \alpha_3 B_3(m_3,\Gamma_3)$$

Where p_s and p_f define the slow and fast protons in the final state (Lab. system).

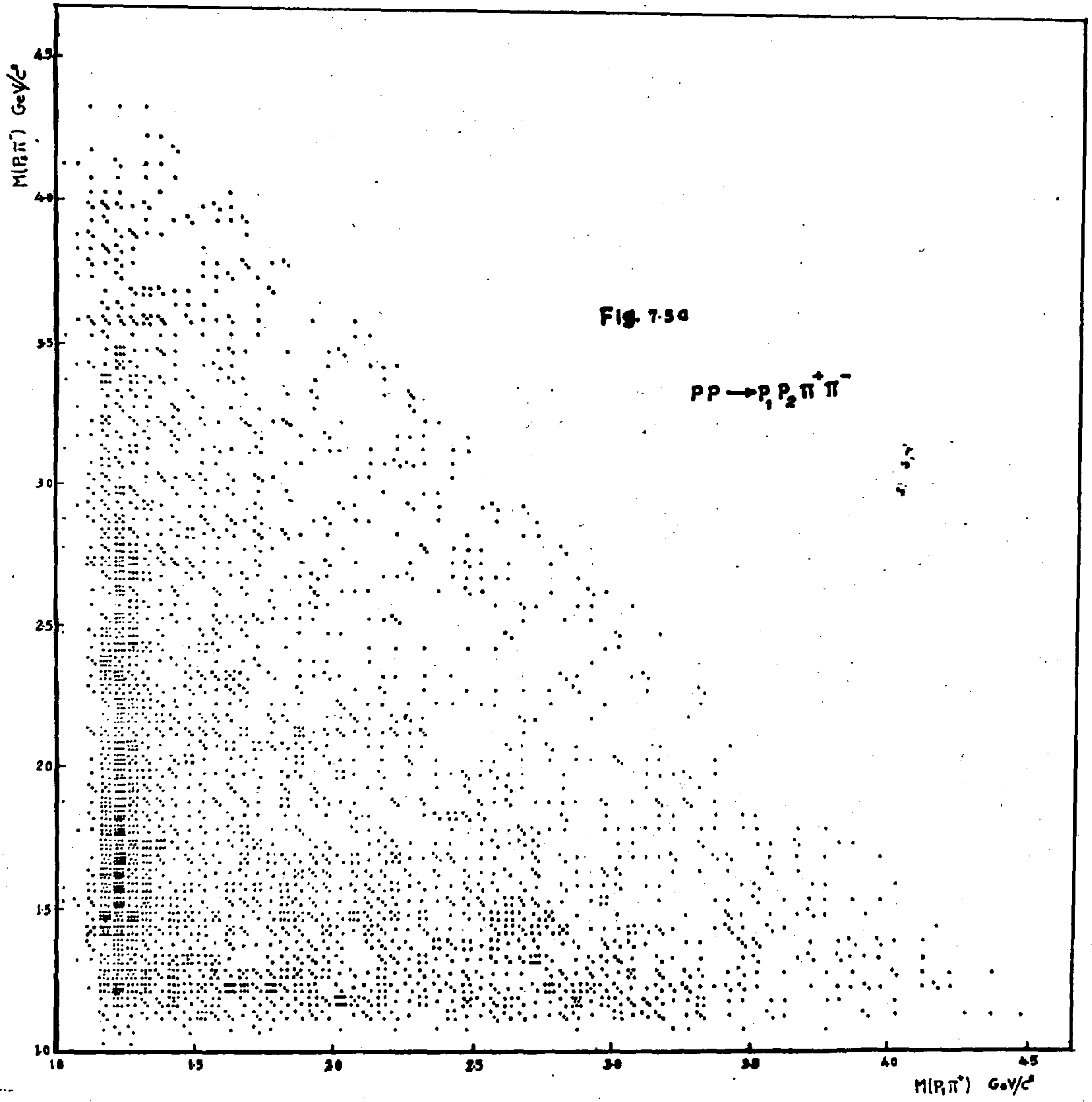

Fig. 7.5a

$pp \rightarrow p_1 p_2 \pi^+ \pi^-$

Fig. 7.5 b

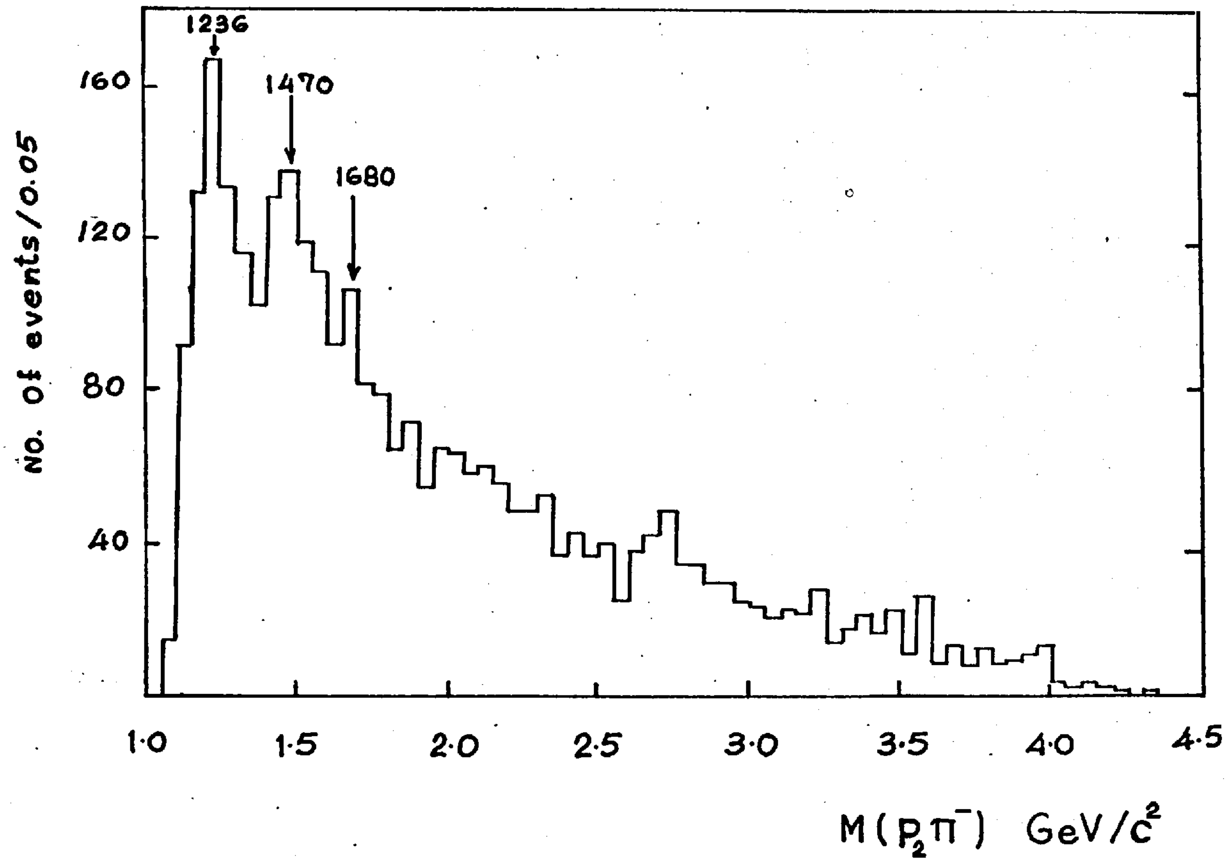

1236
1470
1680
No. of events/0.05
160
120
80
40
1·0
1·5
2·0
2·5
3·0
3·5
4·0
4·5
M(p₂π⁻) GeV/c²

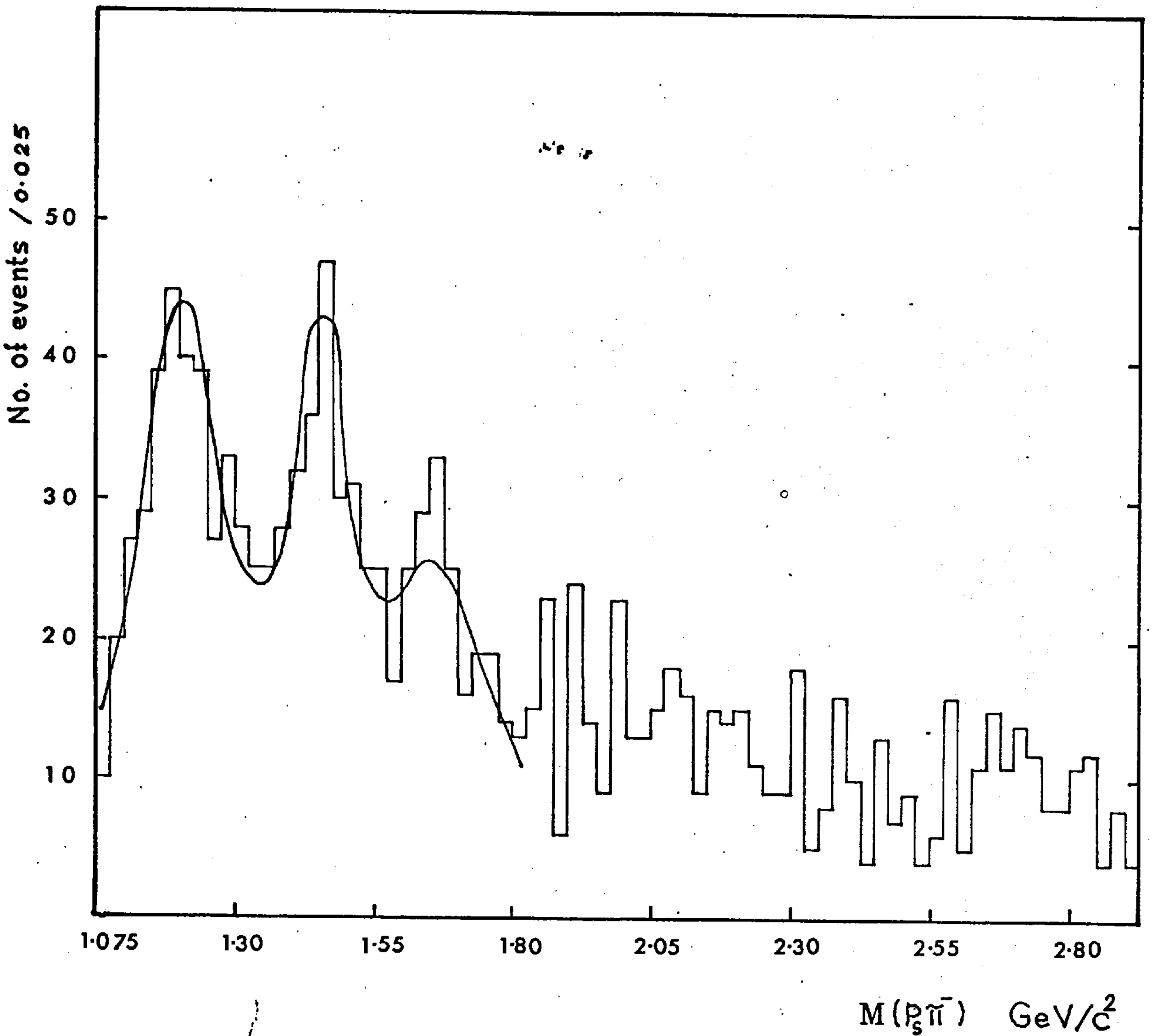
No. of events /0·025
50
40
30
20
10
1·075
1·30
1·55
1·80
2·05
2·30
2·55
2·80
M(p̄sπ⁻) GeV/c²

Fig 7·5d

where B_i (m_i , Γ_i) is the Breit-Wigner function for the i^{th} resonance,

and α_1 , α_2, α_3 are the relative fractions of each resonance respectively ($\alpha_1 + \alpha_2 + \alpha_3 = 1$).

The fitted results are illustrated in table 7.3.

TABLE 7.3

$p\pi^-$ Cross Section

Resonance	Mass (MeV)	Width (MeV)	α_i	Cross Section (mb)
$\Delta^o(1236)$	1222 ± 10	177 ± 34	0.41 ± .06	0.37 ± 0.05
$N^{*o}(1470)$	1475 ± 11	161 ± 64	0.32 ± 0.10	0.29 ± 0.09
$N^{*o}(1688/1750)$	1699 ± 18	237 ± 67	0.27 ± 0.16	0.25 ± 0.15

By the symmetrical nature of this collision, the maximum partial cross sections for $p\pi^-$ resonances can be estimated by multiplying the above results by two. The fitted curves are in reasonably good agreement with th experimental distribution, over the invariant mass range 1.075 - 1.825 GeV. The fit using the full range of $M(p\pi^-)$ will be discussed later.

In order to show the evidence for double isobar production, those events containing a $M(p\pi^+)$ falling in the $\Delta^{++}(1236)$ band were selected. The associated $M(p\pi^-)$ distribution was then plotted in figure 7.5e. The following double isobars are apparent:-

$$\text{(i)} \quad pp \longrightarrow \Delta^{++} + \Delta^{o}(1236)$$

$$\text{(ii)} \quad pp \longrightarrow \Delta^{++} + N^{*}(1470)$$

and

$$\text{(iii)} \quad pp \longrightarrow \Delta^{++} + N^{*}(1688)$$

The $N^{*}(1688)$ is relatively broad and is probably due to a mixture of different states. $pp \longrightarrow \Delta^{++}\ \Delta^{o}\ (1640)$ is excluded as no evidence is found for the charge symmetrical final state Δ^{o} (1236) Δ^{++} (1640). The remaining well established resonances in the region all have isotopic spin of one half. Figure 7.6 (a,b,c) shows the momentum transfer distributions for reactions (i), (ii) and (iii) respectively.

It has been observed that the cross sections for most of the inelastic two-body reactions tend to fall off rapidly with increasing beam momentum[79], the actual rate of decrease being a function of the nature of the particle exchanged. It is suggested by D.R.O.Morrison[79] that, for incident momenta well above threshold, the relationship between the total cross section (σ_T) and the incident momentum (P_{in}) can be expressed in the form: $\sigma_T = K(P_{in}/P_o)^{-n}$ where P_o is a constant which can be conveniently taken to be 1 GeV. K is also a constant and is thus the cross section extrapolated to 1 GeV. The value of the exponent n is determined by the production mechanism, e.g. $n \approx 1.5$ for a reaction governed by single meson exchange. In the framework of the Regge Pole Model,

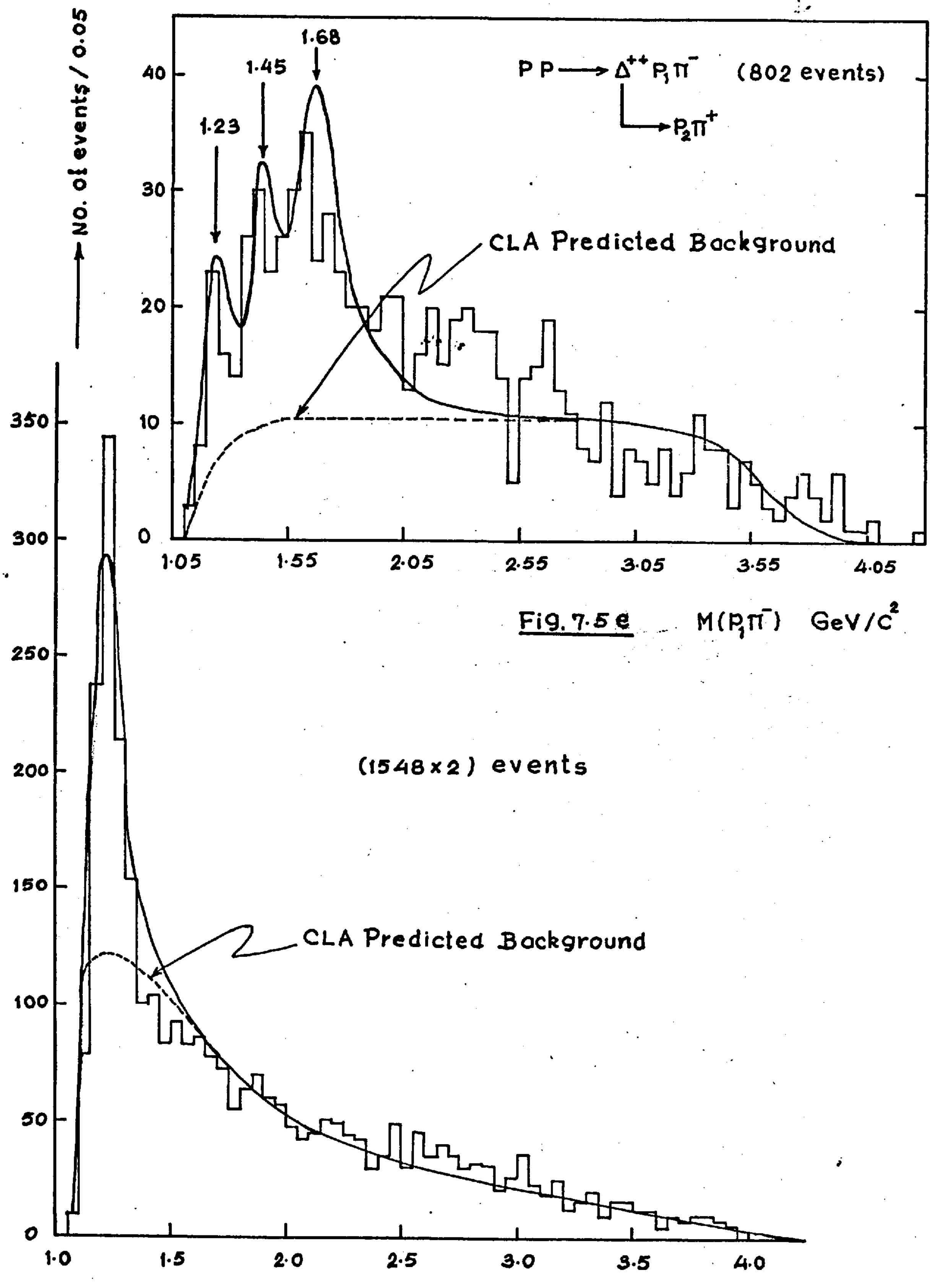

Fig. 7.5e $M(P_1\pi^-)$ GeV/c^2

Fig. 7.5c $M(P\pi^+)$ GeV/c^2

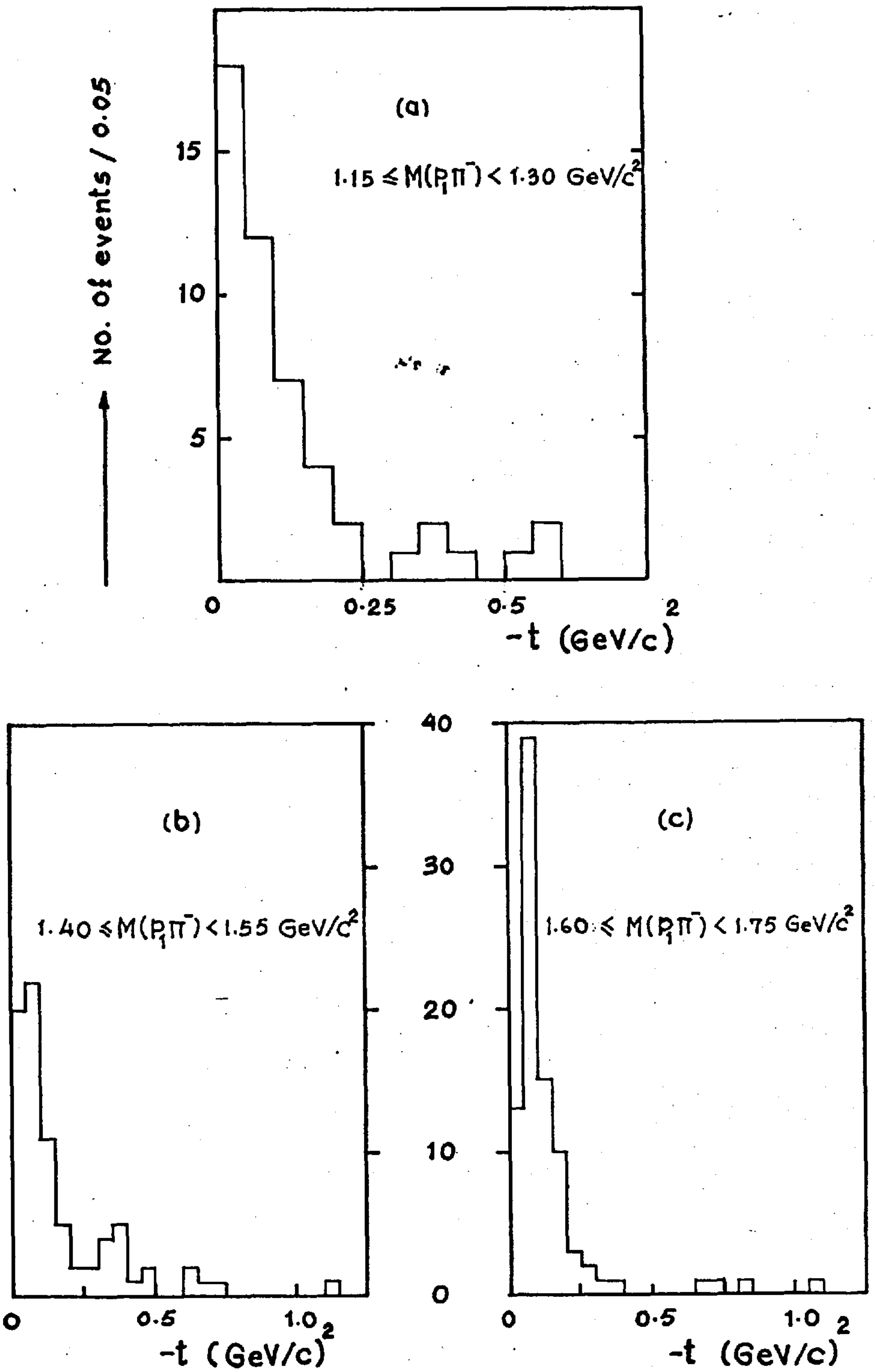

Fig. 7·6 $-t(P-P_1\pi^-)$ Where $M(P_2\pi^+)$ in Δ^{++} mass range this is explained in terms of the different intercepts $\alpha(o)$ of the trajectories exchanged in different types of reaction.

The cross sections for the double nucleon isobars produced in the present experiment were estimated by fitting the data using the CLA prediction as a background. The results are tabulated in table 7.4 with fixed masses and width of the resonances.

TABLE 7.4

Double-Isobar Cross Section($pp \rightarrow \Delta^{++}\Delta^{o}/N^{*o}$)

Resonance	Mass (MeV)	Width (MeV)	Cross Section (mb)
$\Delta^{o}(1236)$	1230	125	0.06 ± 0.01
$N^{*o}(1470/1520)$	1450	100	0.04 ± 0.01
$N^{*o}(1688/1750)$	1678	250	0.20 ± 0.02

7.2.3 ($\Delta^{++}\pi^{-}$) Enhancements - We shall conclude this section with a brief discussion of nucleon resonances decaying into Δ^{++}, principally:-

$$pp \longrightarrow N^{*}(1470) + P \quad \text{.........} \quad (i)$$

$$N^{*}(1750) + P \quad \text{.........} \quad (ii)$$

$$N^{*}(2030) + P$$

$$\quad \hookrightarrow \Delta^{++}\pi^{-} \longrightarrow p\pi^{+}\pi^{-} \quad \text{.........} \quad (iii)$$

The first evidence for a baryon resonance with a mass near 1400 MeV was in a pion-proton phase shift analysis[94] which assigned the state to a P_{11} resonance, $N^{*}_{1/2}(1400)$[78,82]. More recently, a number of experiments studying reactions of the type:

$$pp \longrightarrow pp\pi^+\pi^- \quad (38,86,88) \qquad \ldots\ldots\ldots\ldots (1)$$

as well as

$$\pi(\text{or } K) + p \longrightarrow \pi(\text{or } K)\, p\pi^+\pi^- \quad (81)$$

have reported enhancements in the final state $p\pi^+\pi^-$ invariant mass spectrum. The actual number of low mass enhancements and their interpretation as either resonance or kinematic effects[88] are all uncertain; as is their connection with the peaks seen in earlier missing mass experiments[87].

In addition, several of these studies indicate a more complicated structure in the $p\pi^+\pi^-$ invariant mass spectra, in particular higher mass enhancements at 1700 MeV and at 2057 MeV[82]. From a study of reaction (1) (page) in the present experiment copious Δ^{++} production in the quasi three body final state $\Delta^{++}p\pi^-$ is observed. There is some evidence that the above two resonances are present. The well established 1470 MeV resonance is clearly seen. However, their percentage cannot be accurately determined on account of the strong enhancement of the low mass $p\pi^+\pi^-$ spectrum. Figure 7.7a shows a distribution of $M(\Delta^{++}\pi^-)$ for :-

(i) all events

(ii) those having $\Delta^2 > 0.1$ $(\text{GeV})^2$

(Δ^2 defined by fig.7.7b)

and (iii) those having $\Delta^2 > 0.3$ $(\text{GeV})^2$

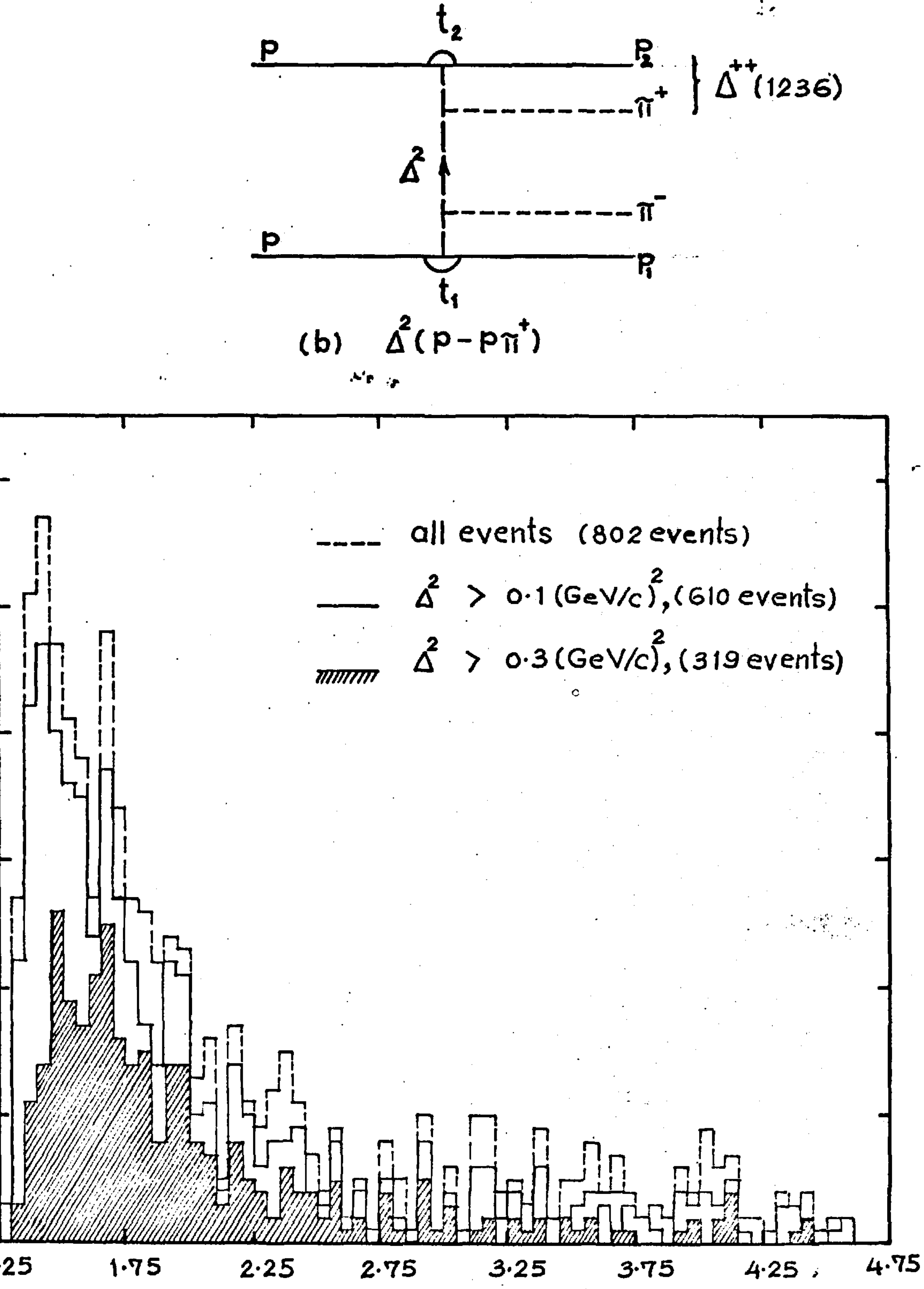

(b) $\Delta^2(p-p\pi^+)$

Fig. 7·7 (a) $M(p_2\pi^+\pi^-)$ GeV/c^2

This selection of Δ^2 is chosen to reduce the "Deck effect" background in the higher mass region, and serves to isolate the structure of the $N^*(2030)$ in particular. The enhancement observed between 1450 MeV and 1500 MeV is probably associated with the $N^*(1470)$, for it is narrower and of lower mass than that indicated by Deck's calculation (around 1500 MeV). Figure 7.8 shows the Dalitz plot (M^2 ($\Delta^{++}\pi^-$) VS. M^2 (P_1 π^-) where M (P_1 π^+) is not in the Δ^{++} mass range). There is no indication that the events contributing to the 1450 - 1500 MeV peak are concentrated at high $P_1\pi^-$ masses, where diffractive π^-p scattering should be dominant. In figure 7.9 the "Chew Low plot" shows the t-dependence of the $\Delta^{++}\pi^-$ events. Those having mass lower than 1500 MeV are more concentrated at low t-value than for events with higher masses. In the intermediate region, the peak attributable to a $N^*(1750)$ possibly includes some $N^*(1688)$.

It should be noted that both the phase shift resonance ($N^*(2050)$ D_{13}) together with $N^*(1470)$ P_{11} have natural parity, and may be produced by diffractive dissociation(68) or Pomeranchuk exchange. The cross section for such processes only slightly depend upon the incident momentum and so they become increasingly favoured at high energy. If $N^*(2030)$ has isospin 3/2 it cannot be produced in this way and its cross section would be expected to fall with increasing energy similar to the case of Δ^{++}. It is worth noticing

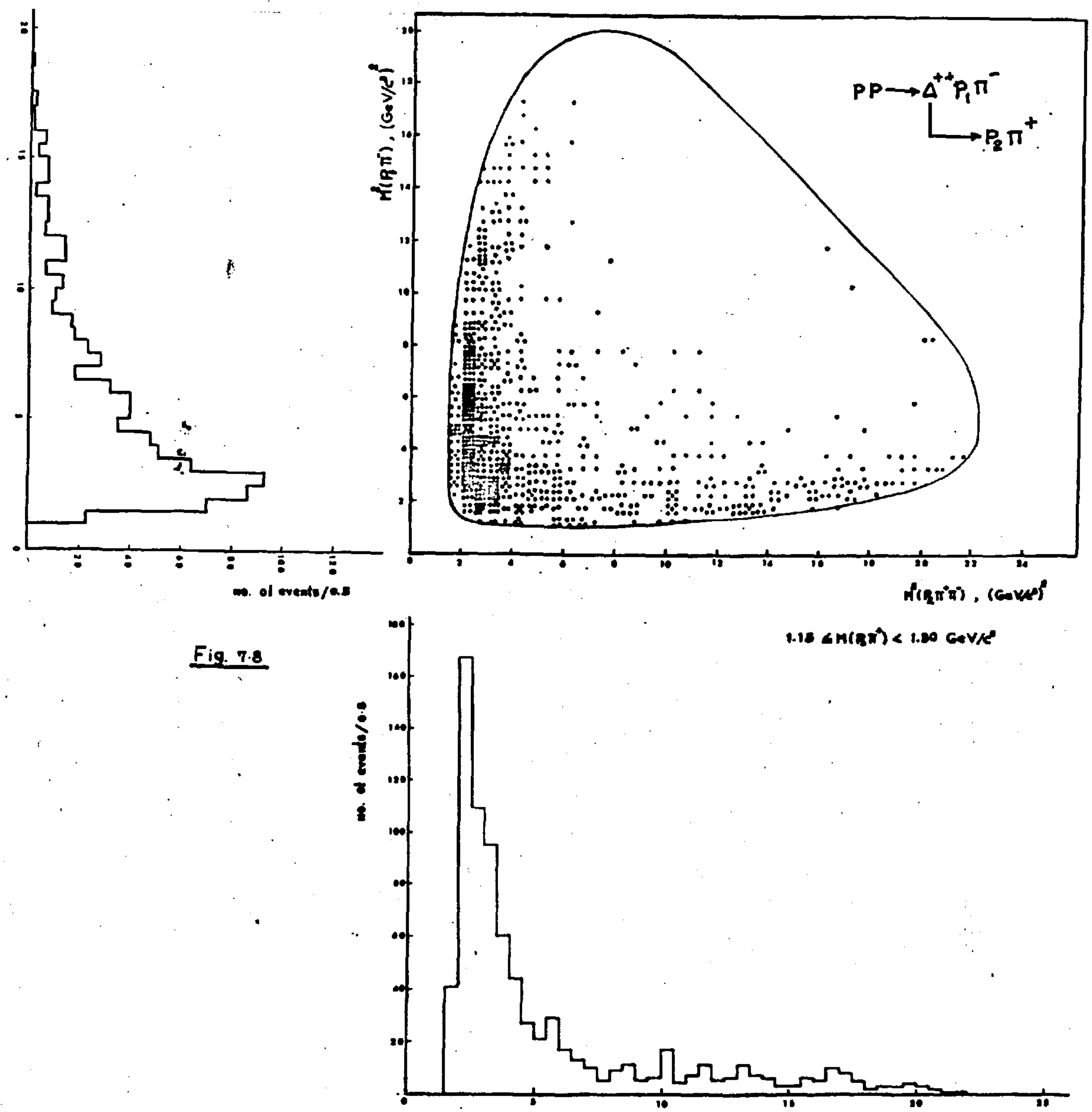

PP → Δ++ P1 π−
→ P2 π+
M²(P1π⁻) , (GeV/c²)²
M²(P2π⁺π⁻) , (GeV/c²)²
no. of events/0.5
1.15 ≤ M(P2π⁺) < 1.30 GeV/c²
no. of events/0.5

Fig. 7·8

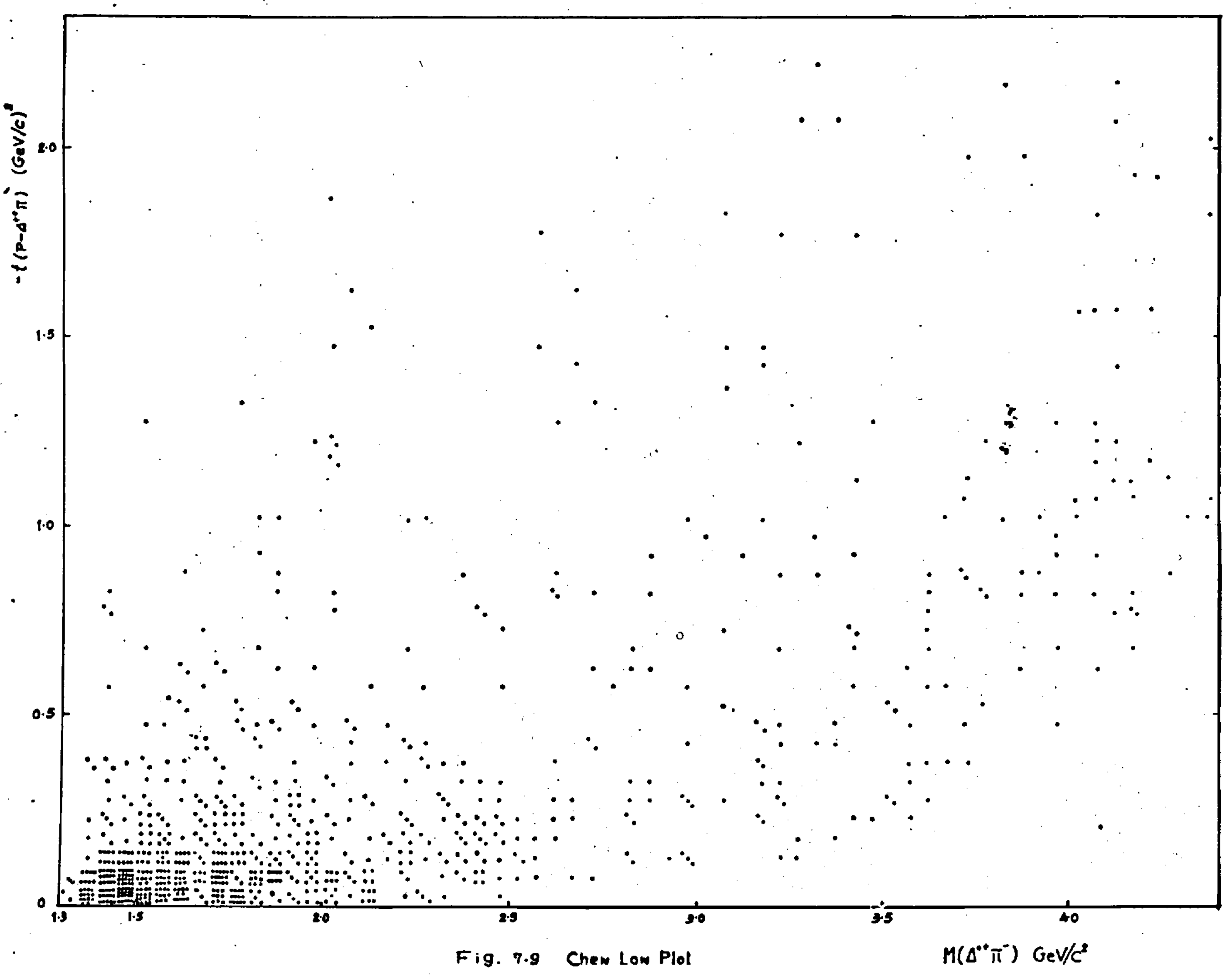

Fig. 7·9 Chew Low Plot

that this resonance has not appeared in any of the studies of the same reaction at energies lower than 16 GeV.

However, the situation is extremely complex and the $N^*(1520)$ and $N^*(1688)$ both having natural parity are not apparent in the present experiment, unless they are associated with the enhancements observed at 1470 and 1750 MeV respectively.

Because of these difficulties together with the lack of a good description of the peripheral background, the possibility of obtaining an accurate cross section for the resonance production is severely limited. From the CLA model a more peripheral non-resonant background can be obtained for inelastic processes at high energy. An estimate for the cross sections has been made by using Lorentz phase space multiplied by $\exp(-4.8(t_1+t_2))$ and the CLA prediction as a background for fitting. Both results are listed in table 7.5.

TABLE 7.5

$\Delta^{++}\pi^-$ Cross Section

Background	$N^*(1470)$ (mb)	$N^*(1750)$ (mb)	$N^*(2030)$ (mb)
CLA prediction	$0.294 \pm .03$	$0.052 \pm .01$	$0.086 \pm .01$
Peripheral phase space	$0.670 \pm .05$	$0.095 \pm .03$	$0.089 \pm .03$

The relevant t-distributions for these resonances are shown in figure 7.10 (a,b,c) respectively. Figure 7.11 shows the angular distributions for the decay of three-body resonances into Δ^{++} and π^- for the mass region pertaining to the $N^*(1470)$ and $N^*(1750)$ decay and the control region $1800 < M\ (\Delta^{++}\pi^-) > 1900$ MeV. These are given in a, b and c respectively. The $N^*(1470)$ distribution is roughly symmetrical whereas the $N^*(1750)$ case shows some excess events contributing to the peaking in the forward direction. A non-symmetric distribution should be produced at low values of $\Delta^2(P - \Delta^{++})$ and so the forward peak in $N^*(1750)$ case can be removed by a cut at $\Delta^2 > 0.1\ (\mathrm{GeV})^2$ (dotted lines), leaving a symmetrical distribution. The highly peripheral, $\Delta^2 < 0.1\ (\mathrm{GeV})^2$, events of the Deck type are exemplified in the control region.

7.3 Events with no Δ^{++} – There are 766 events of $pp \longrightarrow pp\pi^+\pi^-$ with no Δ^{++}. $p\pi^+\pi^-$ resonances were detected by choosing the less diffractive proton as being more likely to form a resonances. Figure 7.12 (a,b) shows the $M(p_1\pi^+\pi^-)$ and $M\ (p_2\pi^+\pi^-)$ distributions (i.e. $t_1(p - p_1)$ $t_2(p - p_2)$, p_1 and p_2 are final state protons defined by this criteria and by figure 7.12c). The former has the more promising structure to look for any resonance while the latter has no significant structure. This evidence lends support to this selection and it would be justified to use only the $M\ (p_1\pi^+\pi^-)$. It is worth noting that the same selection (less diffractive proton) is also applied in the case of $p\pi^-$ invariant mass distribution at Cambridge and gave the satisfactory result while it is not well justified to apply in the data derived at Imperial College. Figure 7.13 (a, b) show both distributions have some resonance structure although it is less well pronounced.

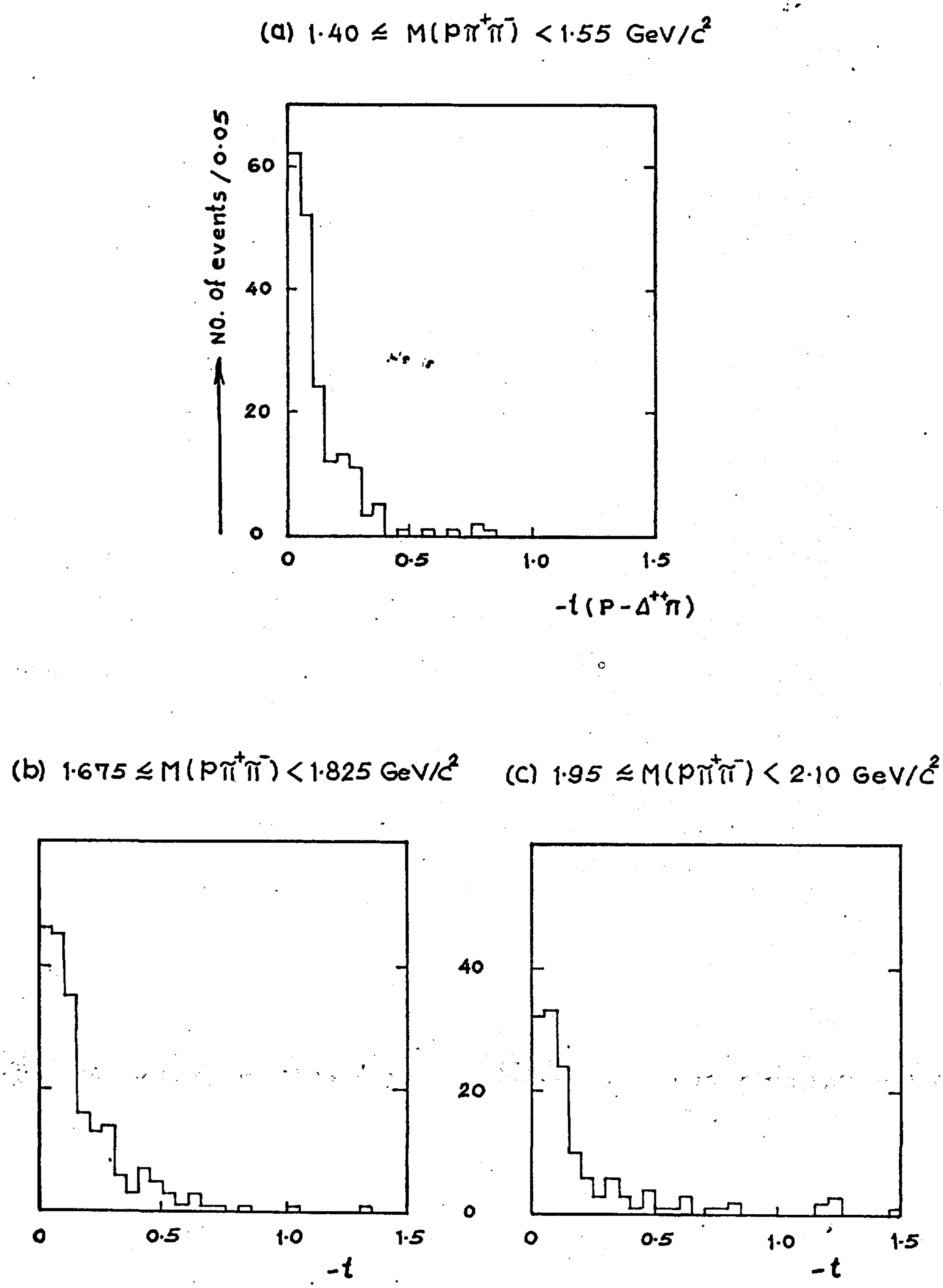

Fig. 7·10 $t(p-\Delta^{++}\pi^{-})$, $(GeV/c)^2$

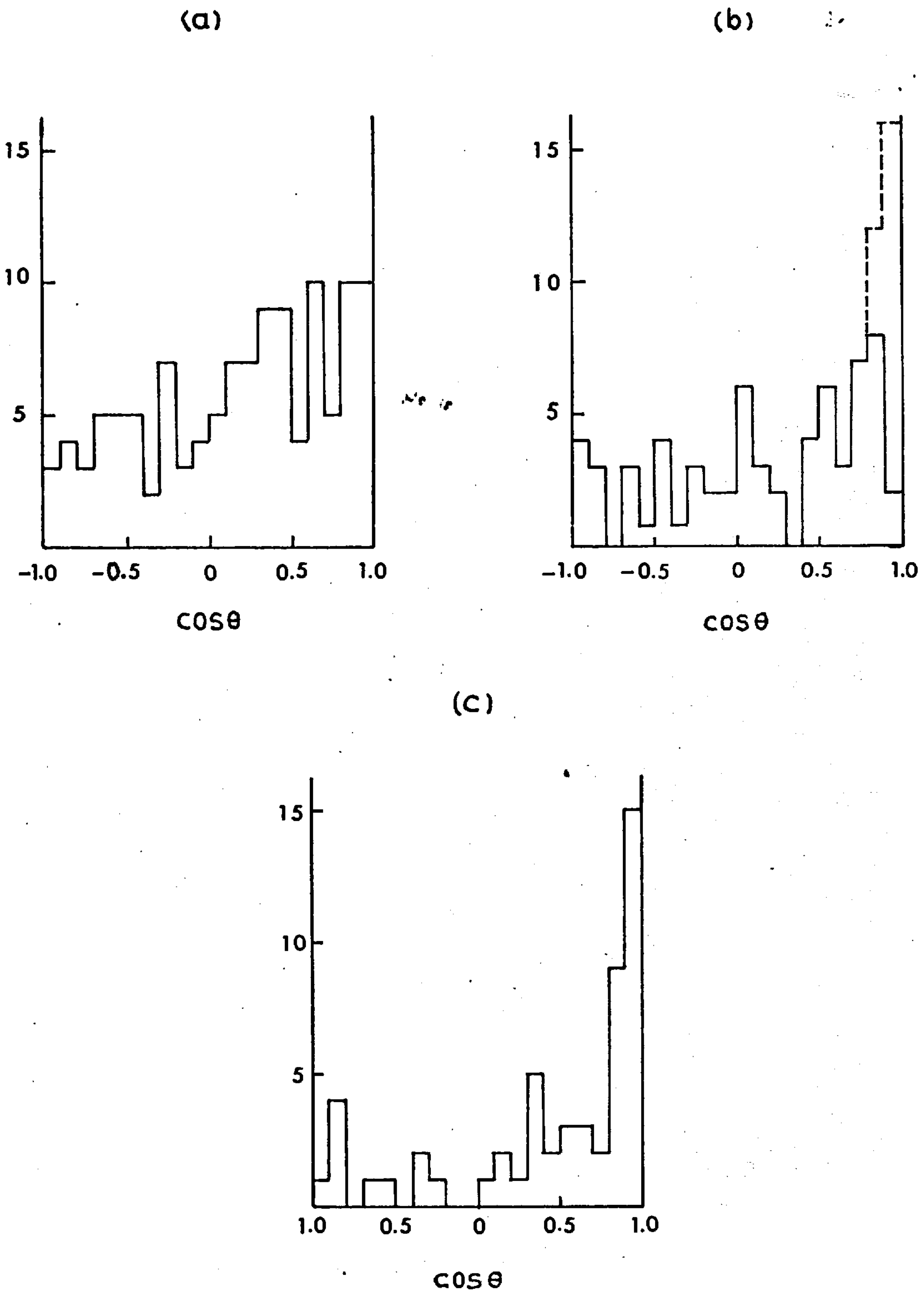
(a)
15
10
5
-1.0
-0.5
0
0.5
1.0
cosθ
(b)
15
10
5
-1.0
-0.5
0
0.5
1.0
cosθ
(c)
15
10
5
1.0
0.5
0
0.5
1.0
cosθ

Fig. 7·11

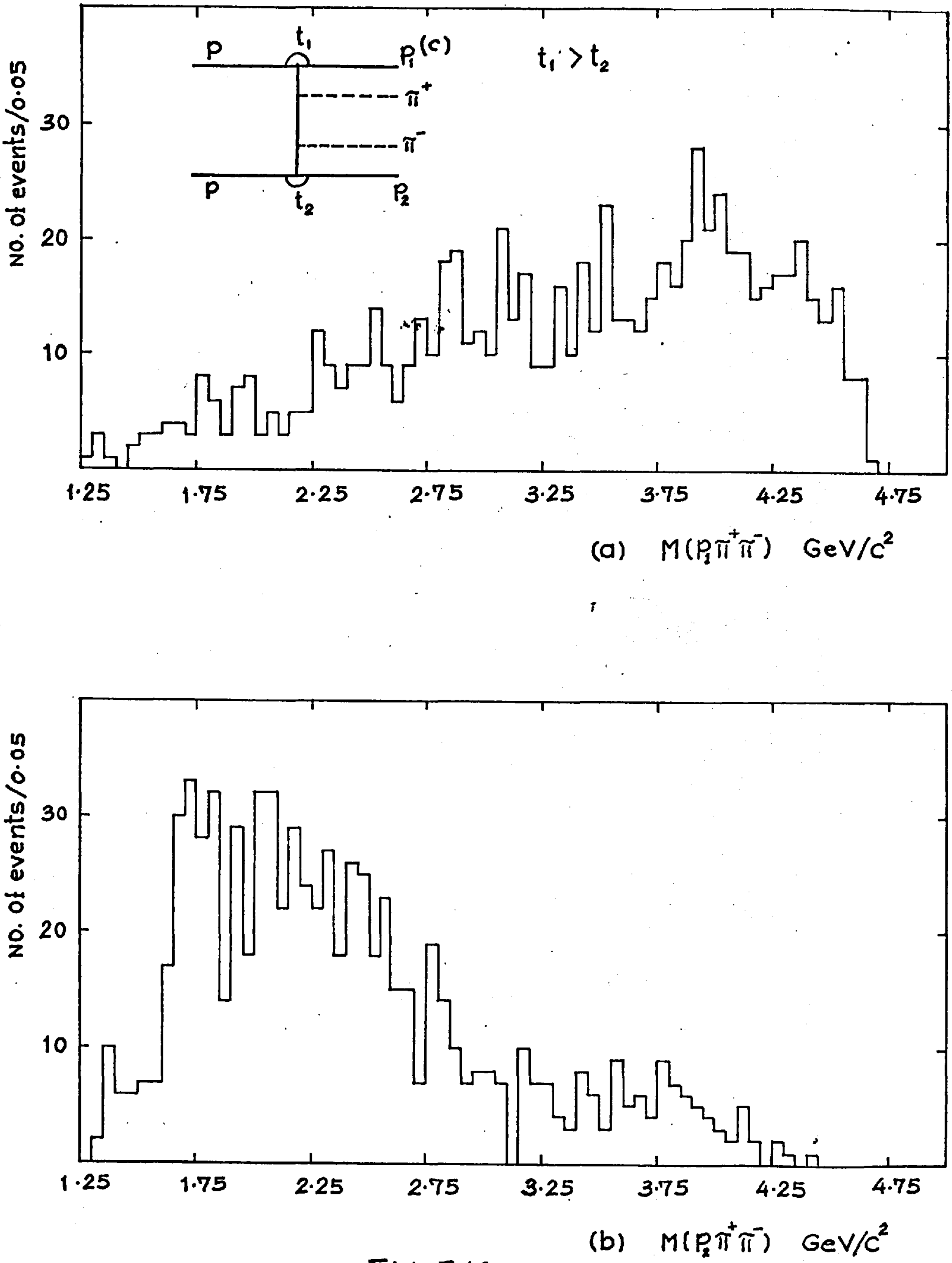

No. of events/0·05
10
20
30
p
p
t_1
t_2
$p_1^{(c)}$
π^+
π^-
p_2
$t_1 > t_2$
1·25
1·75
2·25
2·75
3·25
3·75
4·25
4·75
(a) $M(p_1\pi^+\pi^-)$ GeV/c^2
No. of events/0·05
10
20
30
1·25
1·75
2·25
2·75
3·25
3·75
4·25
4·75
(b) $M(p_2\pi^+\pi^-)$ GeV/c^2

Fig. 7·12

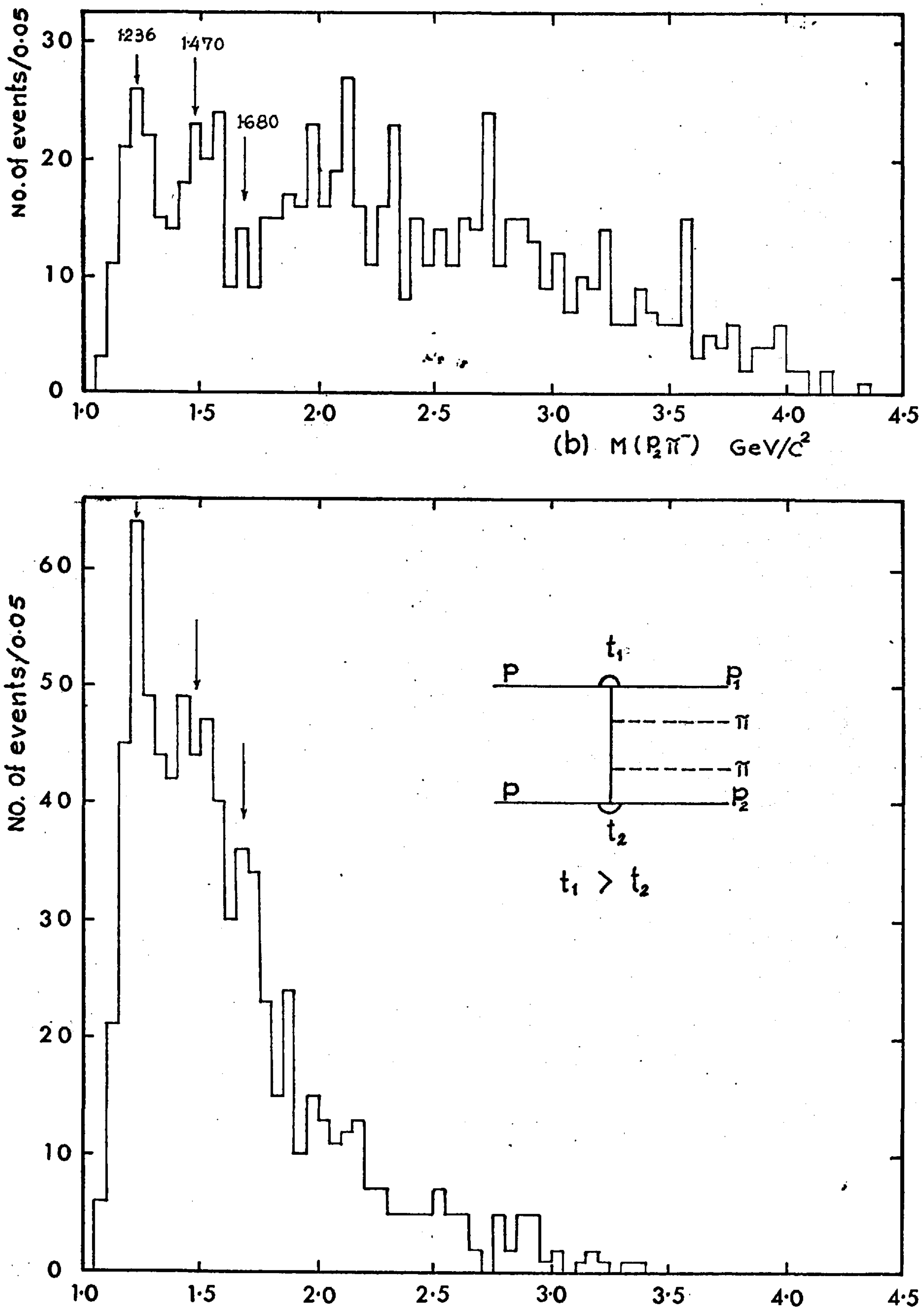

Fig. 7·13 (a) $M(P_1\pi^-)$ GeV/c^2

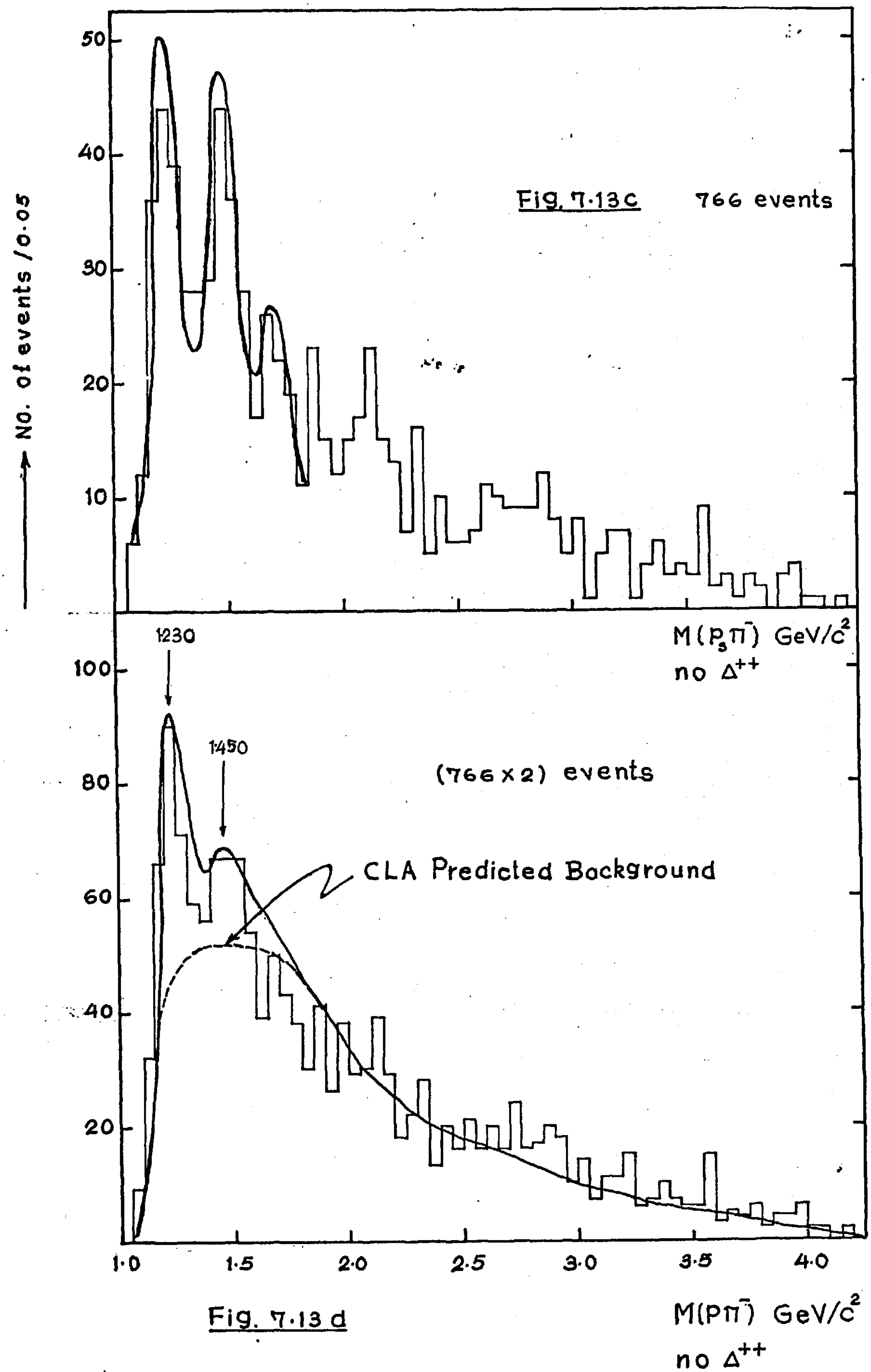

50
40
30
20
10
No. of events /0.05
Fig. 7.13c
766 events
M(P$_3$π$^-$) GeV/c^2
no Δ^{++}
1230
1450
100
80
60
40
20
(766 x 2) events
CLA Predicted Background
1.0
1.5
2.0
2.5
3.0
3.5
4.0
M(Pπ$^-$) GeV/c^2
no Δ^{++}

Fig. 7.13 d

A striking feature in the case of M $(P_1\pi^+\pi^-)$ is the fact that $N^*(1470)$ which has been seen for M$(\Delta^{++}\pi^-)$ has almost disappeared. There is also very little indication for $N^*(1688/1750)$ and even more doubt in the case of $N^*(2030)$. A reasonable conclusion is that most of the higher mass resonances are strongly correlated with the Δ^{++} and that the decay proceeds via

$$pp \longrightarrow N^* p$$
$$\quad\quad\quad \lfloor\!\!\longrightarrow \Delta^{++}\pi^-$$
$$\quad\quad\quad\quad\quad \lfloor\!\!\longrightarrow p\pi^+$$

The estimate for each cross section for the resonances in M$(\Delta^{++}\pi^-)$ and M$(p\pi^+\pi^-)$ does not differ significantly from those obtained from the M$(\Delta^{++}\pi^-)$ distribution alone. Thus the data are consistent with almost 100% decay of the three-body resonances into the $\Delta^{++}\pi^-$. Furthermore, if the $p\pi^+\pi^-$ resonance is in an $I = \frac{1}{2}$ state then one would expect any $\Delta\pi$ decay to have a branching ratio $\Delta^{++}\pi^- / \Delta^0\pi^+ = 9/1$ (40,86), a value that is consistent with the evidence observed in the present experiment (see table 8.1).

The estimated cross sections for $p\pi^-$ resonances observed in the absence of Δ^{++} is listed in table 7.6. In addition, the estimated cross sections for $P_s\pi^-$ was obtained by simply fitting into three Breit Wigner resonances with no background consideration. The fitted cruves are shown in figure 7.13c and the results are also listed in table 7.6.

TABLE 7.6

In the absence of $\Delta^{++}(1236)$

1) $p_s\pi^-$ Cross section

Resonance	Mass (MeV)	Width (MeV)	Fraction	Cross Section (mb)
$\Delta^0(1236)$	1243 ± 7	100 ± 15	0.34 ± 0.04	0.16 ± 0.03
$N^*(1470/1520)$	1483 ± 11	160 ± 35	0.46 ± 0.07	0.21 ± 0.03
$N^*(1688/1750)$	1720 ± 20	173 ± 48	0.20 ± 0.12	0.09 ± 0.05

2) $p\pi^-$ Cross Section

Resonance	Cross Section (mb)
$\Delta^0(1236)$	0.15 ± 0.02
$N^*(1470)$	0.07 ± 0.03

7.4 Production Mechanisms for Three and Four Body Processes

The Double Regge Pole[70] and a Reggeized Multi-peripheral model[72] for inelastic reactions (as described in Chapter 6) were used to account for the observed features of particles in three and four body final states. For reactions of low multiplicity, one expects a peripheral behaviour to dominate which inhibits the exchange of strangeness, charge or baryon number. The paragraphs below discuss these factors in greater detail.

7.4.1 Double Regge Pole Model (D.R.P.M.)

– The only three body final state reaction considered is:-

$$pp \longrightarrow \Delta^{++}\pi^{-}p \qquad \ldots\ldots\ldots\ldots \text{(1a)}$$

the other possible reactions involving meson resonances are neglected as there is no evidence for their production.

The data consist of 802 events belonging to reaction (1a). The cornering effect in the Dalitz plot (figure 7.15) is considered by the model only for the region where the energies of all particle pairs are large. This region is defined by

$$S_{\Delta^{++}\pi^{-}},\ S_{\pi^{-}p} > 3 \quad (\text{GeV})^2 \qquad \ldots\ldots\ldots\ldots (7.11)$$

These limits have reduced the number of events down to 187. In principle six possible double peripheral graphs (fig.7.14) contribute to the three corners of the Dalitz plots but since the graphs with the same middle particle will contribute to the same corner, only the first three graphs remain. The

Double Regge Graphs for the Reaction: $pp \rightarrow \Delta^{++}\pi^{-}p$

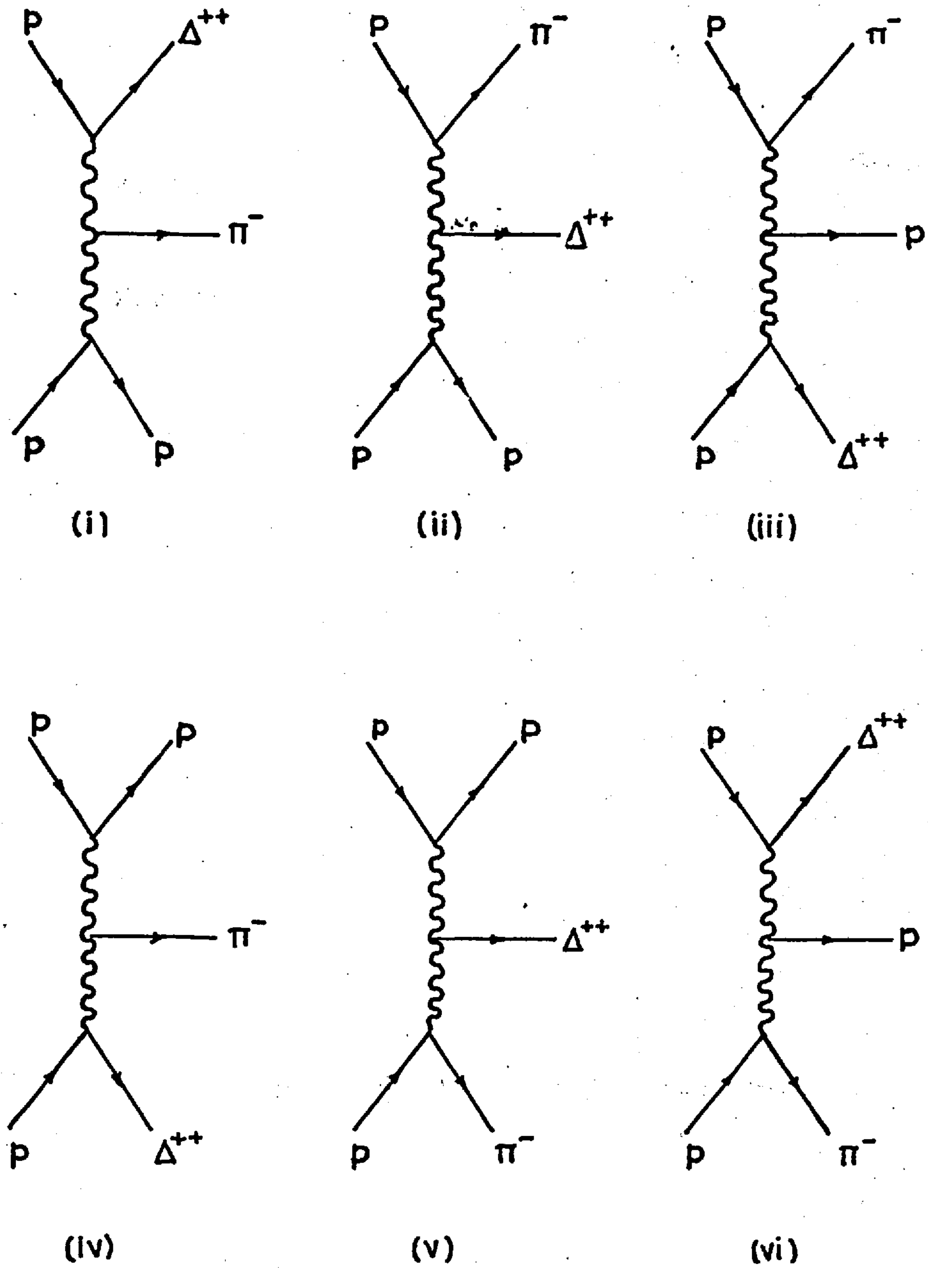

Fig. 7·14

requirement in case (ii), figure 7.14 , for a doubly charged charged exchange is not allowed, and the N -trajectory in case (iii) is known from backward $\pi^{\pm}p$ scattering to be very weakly coupled to the πN system. Furthermore, there is a tendency for the lightest particle permitted by the ordering of the P_l^* (section 6.3) to be produced in the centre of the Dalitz graph. This effect can be seen in figure 7.15. Therefore graphs (ii) and (iii) have been neglected in the analysis.

Figure 7.16 (a,b,c) shows the longitudinal momentum distribution in the C.M.S. (P_l^*) for particles involved in reaction (1a) within the limits specified in 7.11. The model also suggests that the parameters used in equations (6.13 and 6.14) (page 165) especially a and b of the D.R.P.M. should be energy independent.[80] The analysis method consists of generating a large number of "events" by a Monte Carlo method[60] and these were weighted by the amplitude function of equation (6.14) with a = 1.8 $(\text{GeV})^{-2}$, b = 3.1 $(\text{GeV})^{-2}$ and the following known constants from two particles reaction[70,52] were used:-

$$\alpha_a = 0.5 \qquad \alpha_b = 1$$

$$\alpha'_a = 1.0 \qquad \alpha'_b = 0$$

Figure 7.17 (a,b,c and d) shows the experimental results of θ_{14}, ϕ, t_{13} and t_{25} (Chapter 6, section 3) compared to their normalized predicted distributions except for ϕ. It is apparent that these features are in qualitative agreement with the predictions. However, it should be noted that the behaviour of ϕ favours $\phi = \pi$ and is not conclusive evidence for this

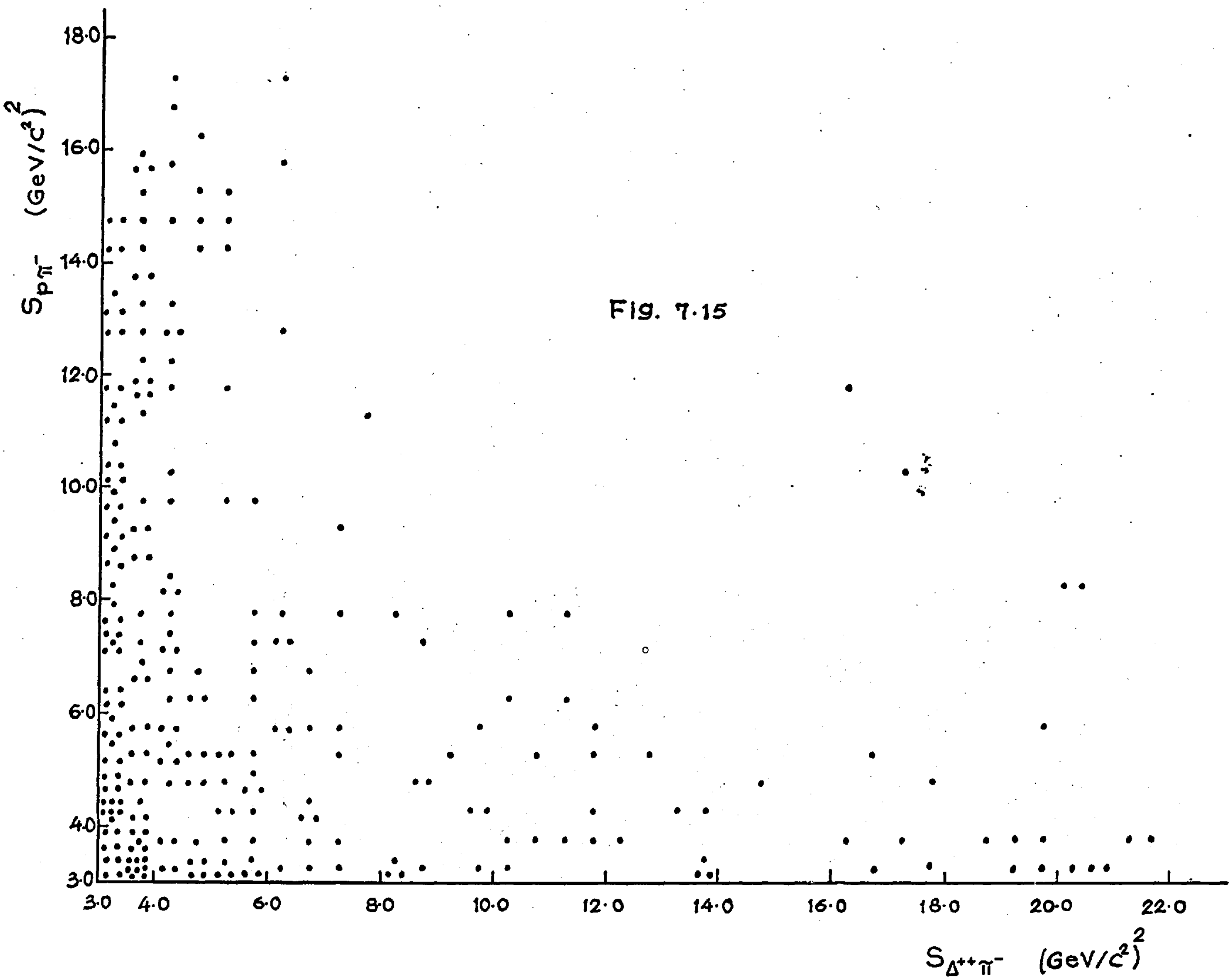
Fig. 7.15
$S_{p\pi^-}$ $(GeV/c^2)^2$
$S_{\Delta^{++}\pi^-}$ $(GeV/c^2)^2$
18·0
16·0
14·0
12·0
10·0
8·0
6·0
4·0
3·0
3·0
4·0
6·0
8·0
10·0
12·0
14·0
16·0
18·0
20·0
22·0

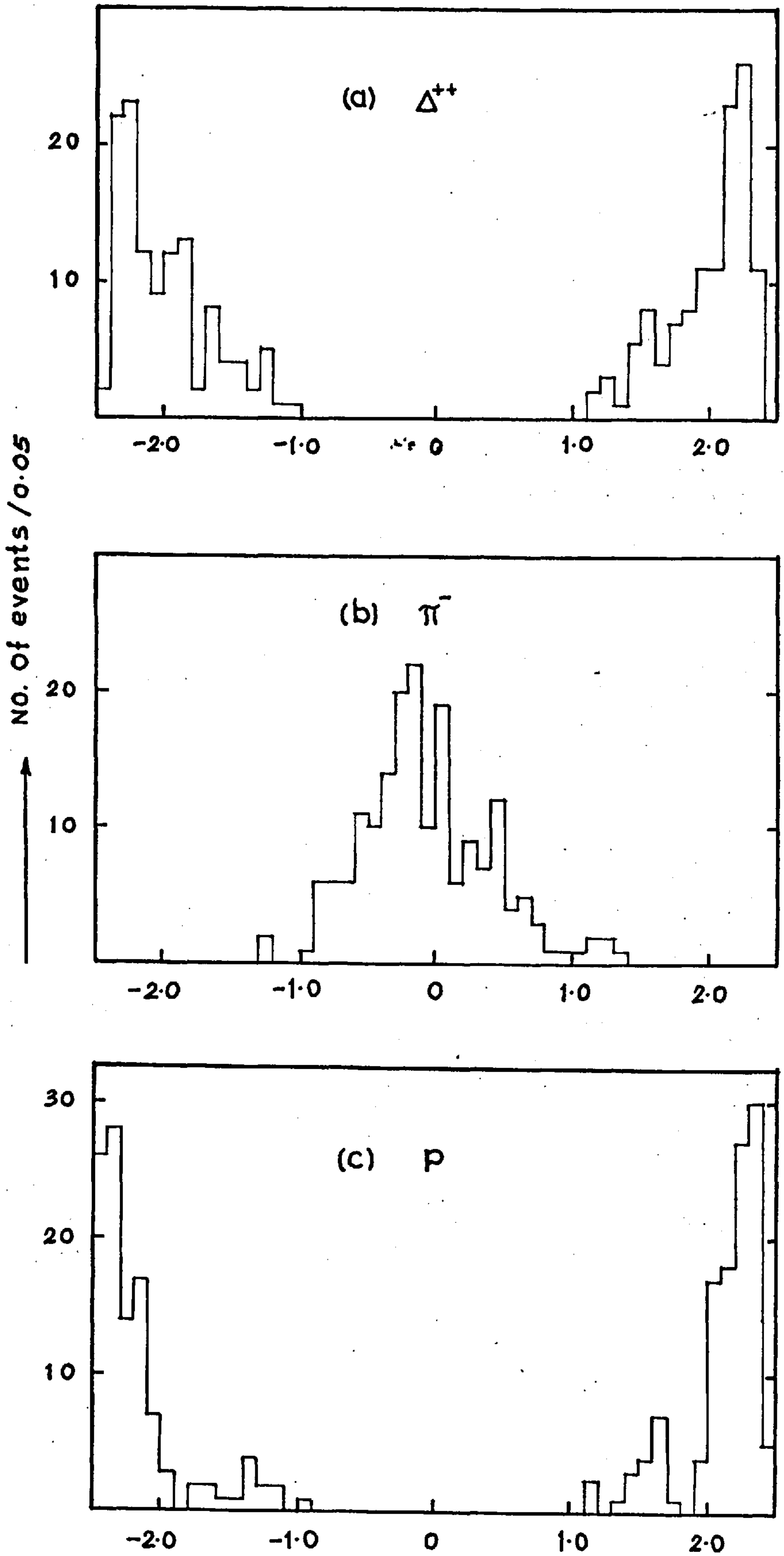

Fig. 7·16 p_l^* GeV/c

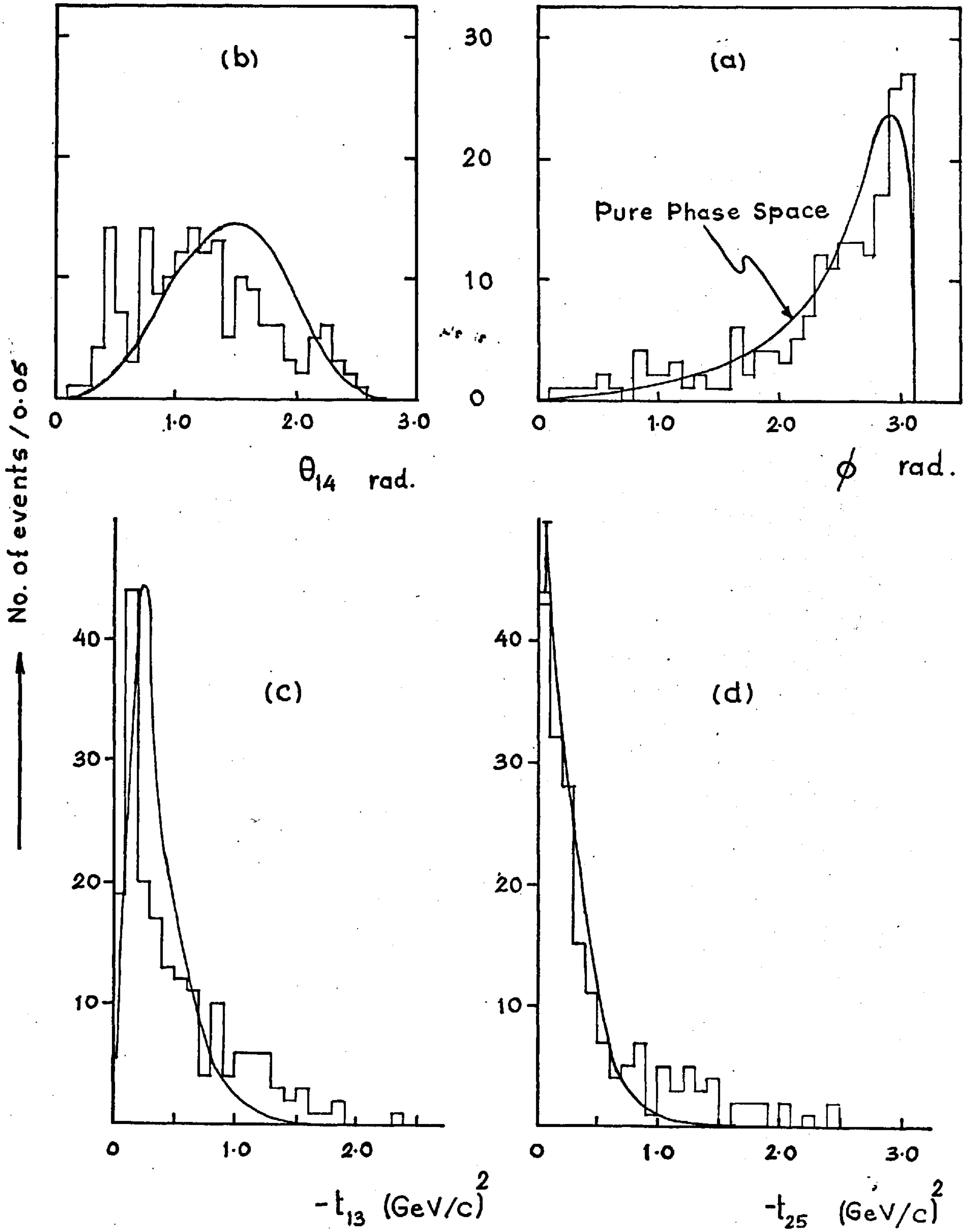

(b)
(a)
Pure Phase Space
No. of events / 0·05
θ14 rad.
φ rad.
(c)
(d)
-t13 (GeV/c)2
-t25 (GeV/c)2

Fig. 7·17

Double Regge graph, as this peak is also expected from peripheral phase space theory alone (see fitted curve in figure 7.17b).

7.4.2 <u>The C.L.A. Model</u> - Since a considerable number of events have been rejected due to the DRPM selection rule, the evidence is inconclusive. Therefore in order not to lose these events, a Reggeized Multi-peripheral analysis of Chan <u>et al</u> was carried out for the two final states:-

$$pp \longrightarrow \Delta^{++}\pi^{-}p \qquad \ldots\ldots\ldots \text{(1a)}$$

and $$pp \longrightarrow pp\pi^{+}\pi^{-} \qquad \ldots\ldots\ldots \text{(1b)}^{*}$$

in order to describe the full features of the experimental data. Once again, a Monte Carlo method was employed using the programme FOWL[60] to generate a large number of random "events". These were, in turn, weighted by the amplitude:-

$$|W|^2 = \sum_{i=1}^{n} |A|^2 \qquad \ldots\ldots\ldots \text{(7.12)}$$

where n is the number of permutations and

A_i is the amplitude corresponding to the i^{th} permutation of the final particle and is parameterised as described in equation (6.18) (page 169).

All the same constant parameters suggested in ref.72 were used here, except parameter b_i.

b_i describes the exponential t-dependence of the Regge couplings for the reggeons attached to the two external particles (two outer vertices). The corresponding constant can be estimated from known two-particle reactions[52].

* Excluding the events where a $p\pi^+$ mass combination is in the Δ^{++} mass region (1.15 - 1.30 GeV).

Because of the two identical particles in the initial state the parameters b_i are taken to be the same for both vertices (b_i = 0.5 (GeV)). Nothing is clearly known about the internal Regge Couplings which occur in higher multiplicity reactions and the couplings b_i are replaced by an effective constant b_I (taken as 1.2 (GeV)) as suggested by Chan et al.

The following constants were used in the calcula-tion of the present experiment:-

$$a = 1 \qquad b_i = 0.5 \qquad b_I = 1.2$$

$$\alpha_P = 1.0 \qquad \alpha_M = 0.5$$

$$g_N/g_M = 1.3 \qquad c/g_M = 1.4$$

For the same reason as described under the D.R.P.M. only one Double Regge graph was considered in the three-body processes with two permutations. The possible graphs for four-body process (1b) are illustrated in figure 7.18 with four permutations.

The predictions of the CLA Model after derivation by the Monte Carlo method were smoothed by hand and normalised to the data. The results are shown superimposed on the experimental distributions for $\mathrm{Cos}\theta^*$, P_t^* P_l^* and the four momentum transfer for reaction (1a) in figures 7.19 and 7.20, 7.21 and 7.22 respectively. The corresponding distributions and predicted results for reaction (1b) are depicted in figures 7.23, 7.24, 7.25 and 7.26. In most cases, it is apparent that the prediction is in good agreement with experi-mental data except for Δ^{++} where the prediction is less peripheral than the observed distribution. This effect is most probably due to the fact that the Δ^{++} was treated (unrealistically) as a particle with fixed mass at 1236 MeV. In general the model gives the best explanation to date for the nature of the particles produced. The peripheral back-ground is also well described.

The Multi-Peripheral Diagrams for Reactions:

$pp \longrightarrow \Delta^{++}\pi^{-}p$ and $pp \longrightarrow P_1 P_2 \pi^{+}\pi^{-}$

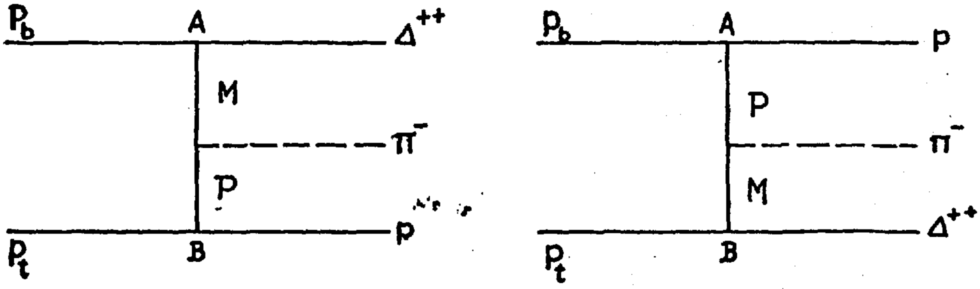

P_b = Beam Proton , P_t = Target Proton

M = Meson P = Pomeranchuk (i.e. Elastic Scattering)

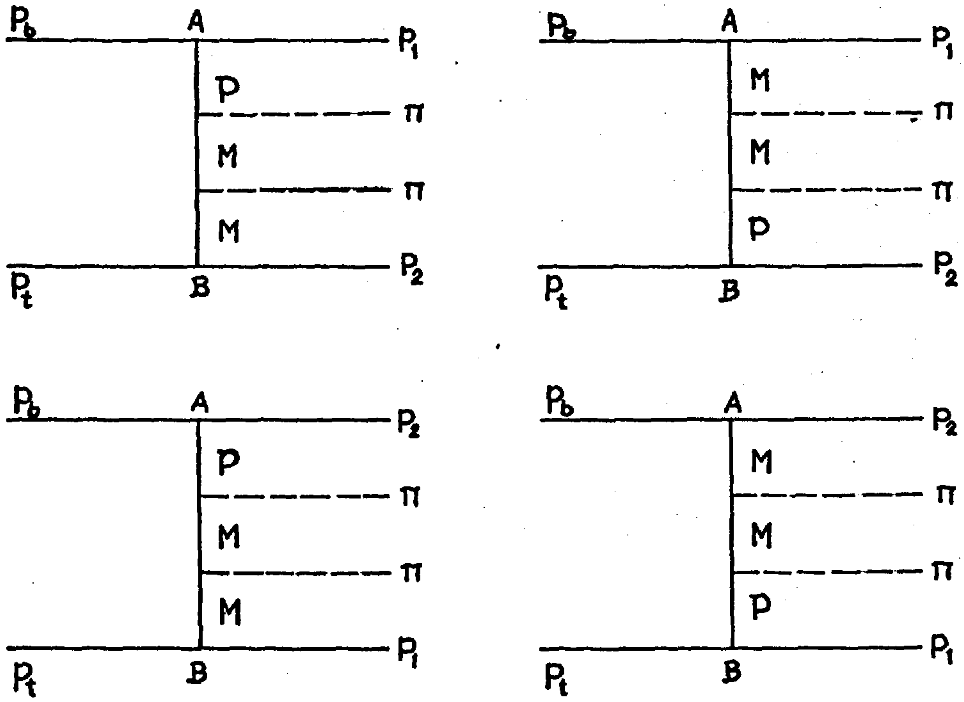

Fig. 7·18

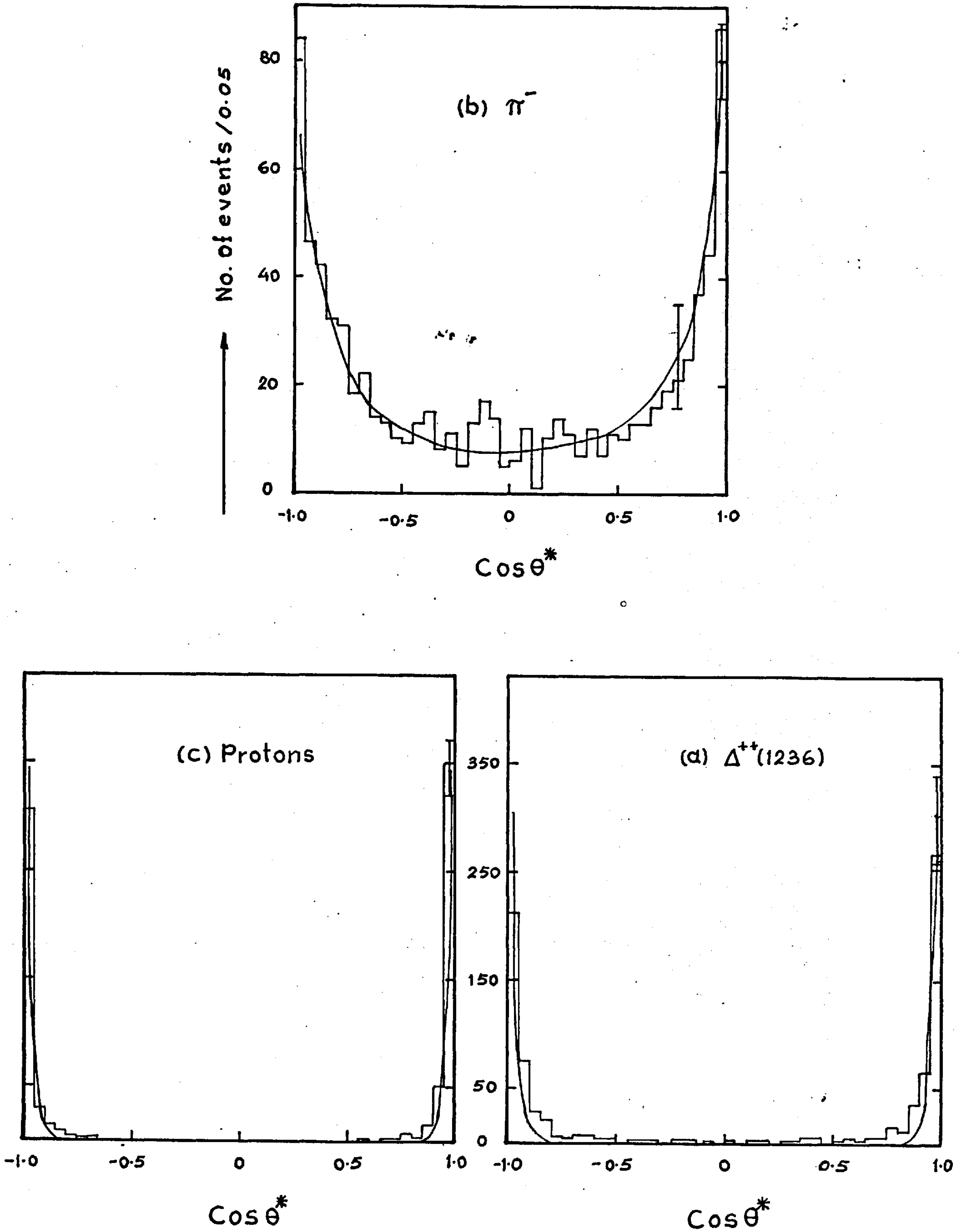
No. of events /0.05
(b) π⁻
80
60
40
20
0
-1.0
-0.5
0
0.5
1.0
Cos θ*
(c) Protons
-1.0
-0.5
0
0.5
1.0
Cos θ*
(d) Δ⁺⁺(1236)
350
250
150
50
0
-1.0
-0.5
0
0.5
1.0
Cos θ*

Fig. 7.19

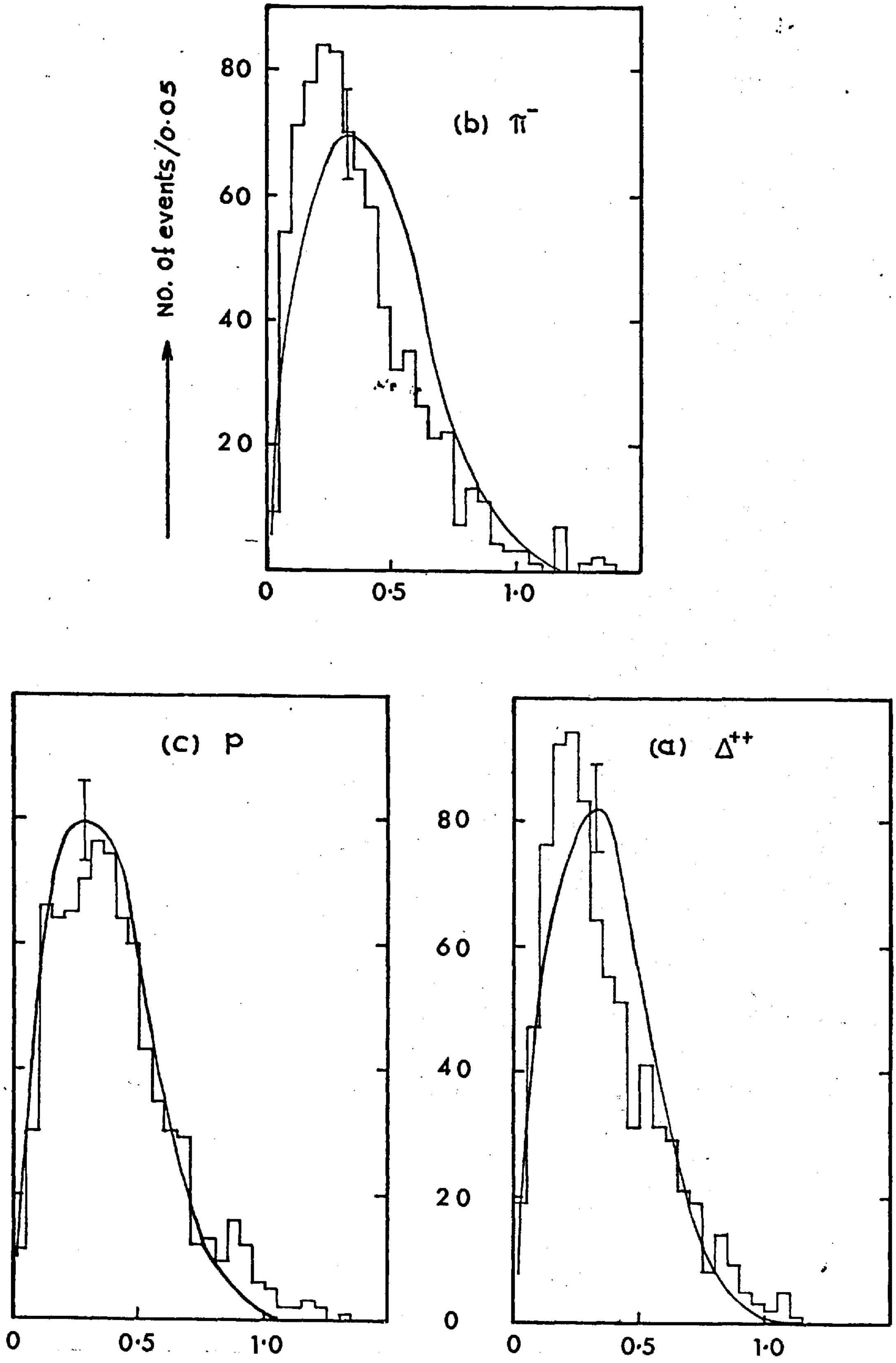

Fig. 7·20 P_t^* GeV/c

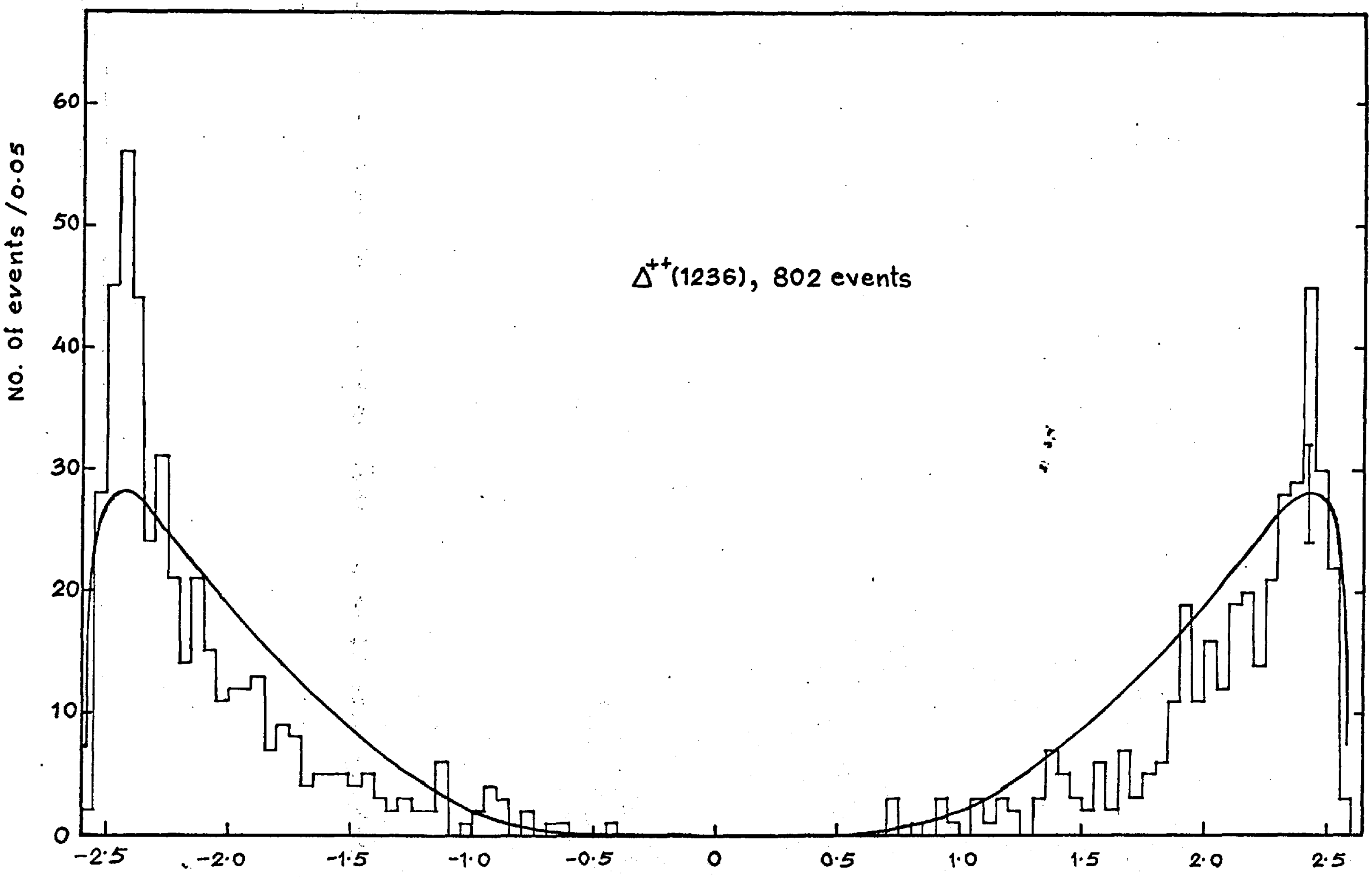

Fig. 7·21 a p_1^* GeV/c

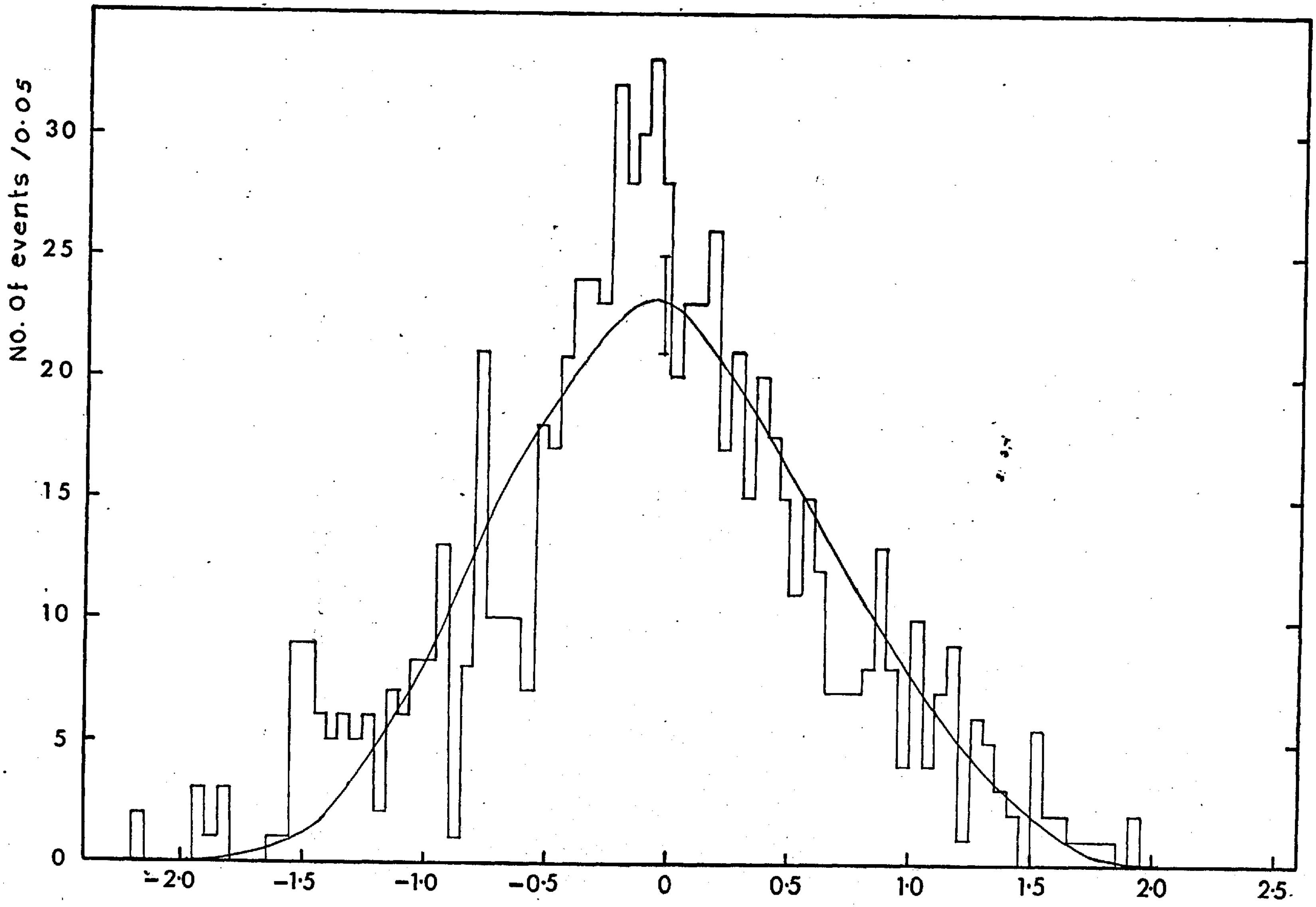

Fig. 7·21 b $P_l^*(\pi^-)$ GeV/c

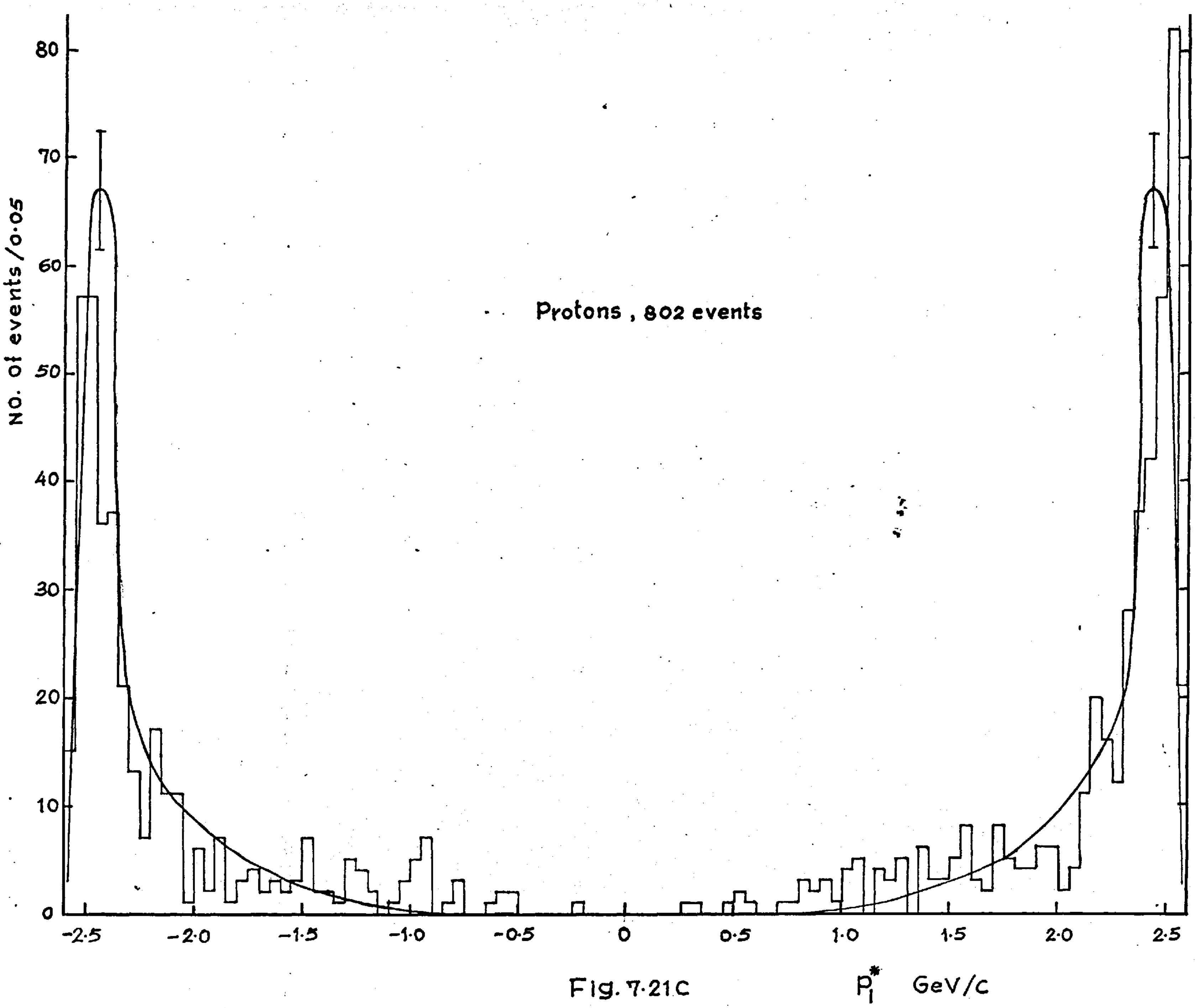
No. of events /0·05
Protons , 802 events
80
70
60
50
40
30
20
10
0
-2·5
-2·0
-1·5
-1·0
-0·5
0
0·5
1·0
1·5
2·0
2·5
p_l^* GeV/c

Fig. 7·21C

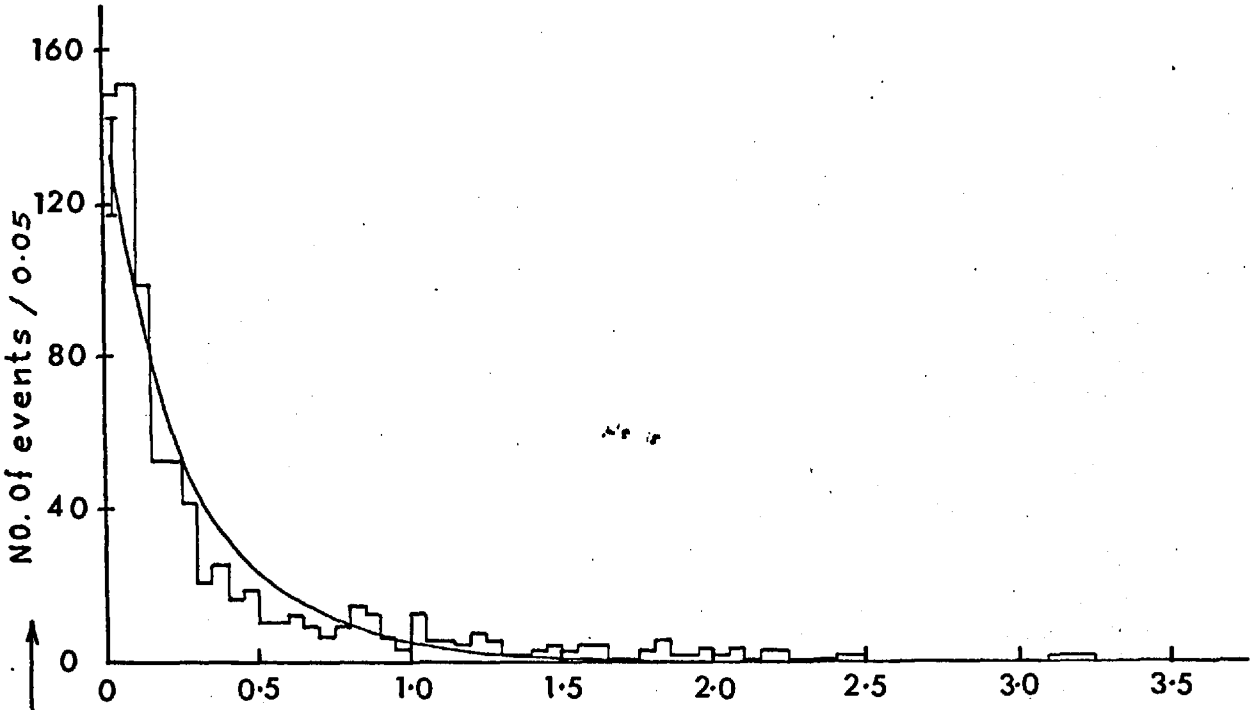

Fig. 7·22 a $-t(p-p), (GeV/c)^2$

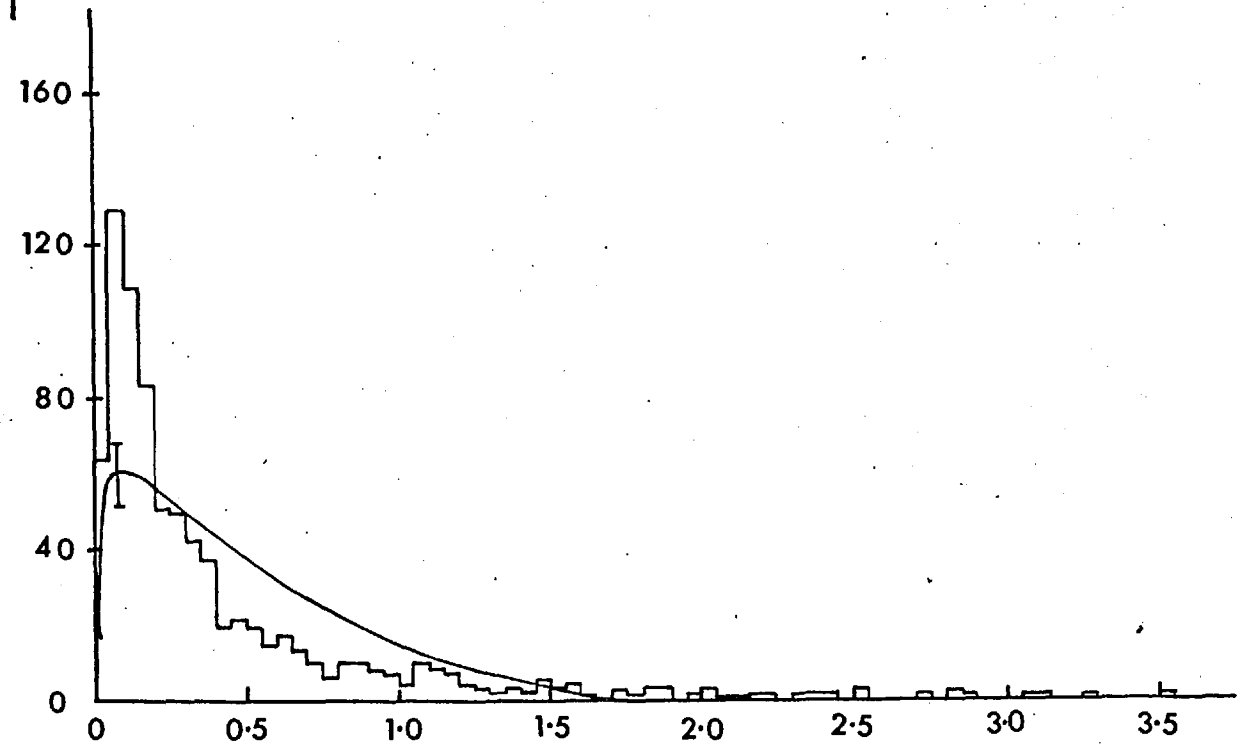

Fig. 7·22 b $-t(p-\Delta^{++}), (GeV/c)^2$

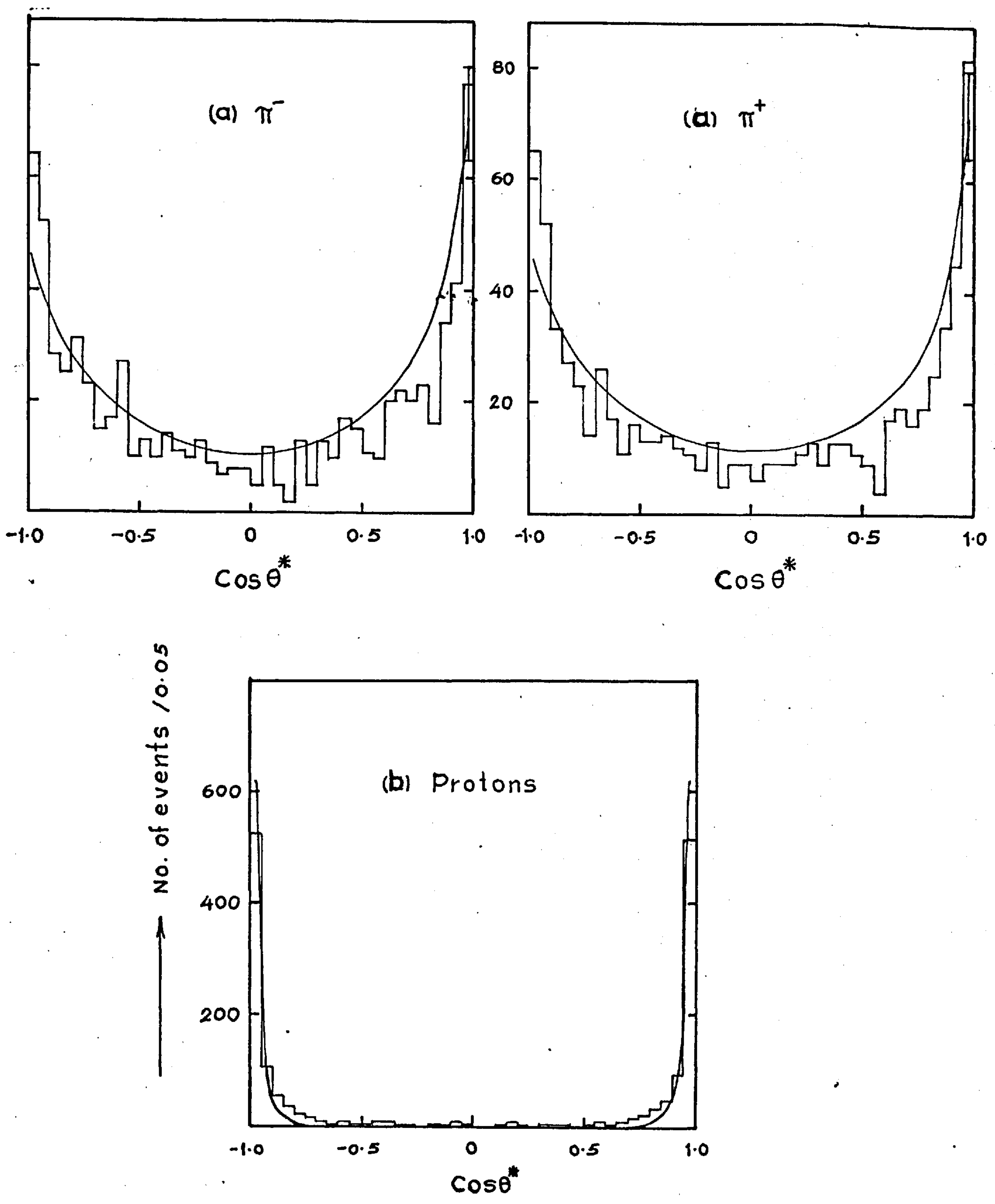
(a) π⁻
(a) π⁺
80
60
40
20
-1·0
-0·5
0
0·5
1·0
Cos θ*
No. of events /0·05
(b) Protons
600
400
200
Cosθ*

Fig. 7·23

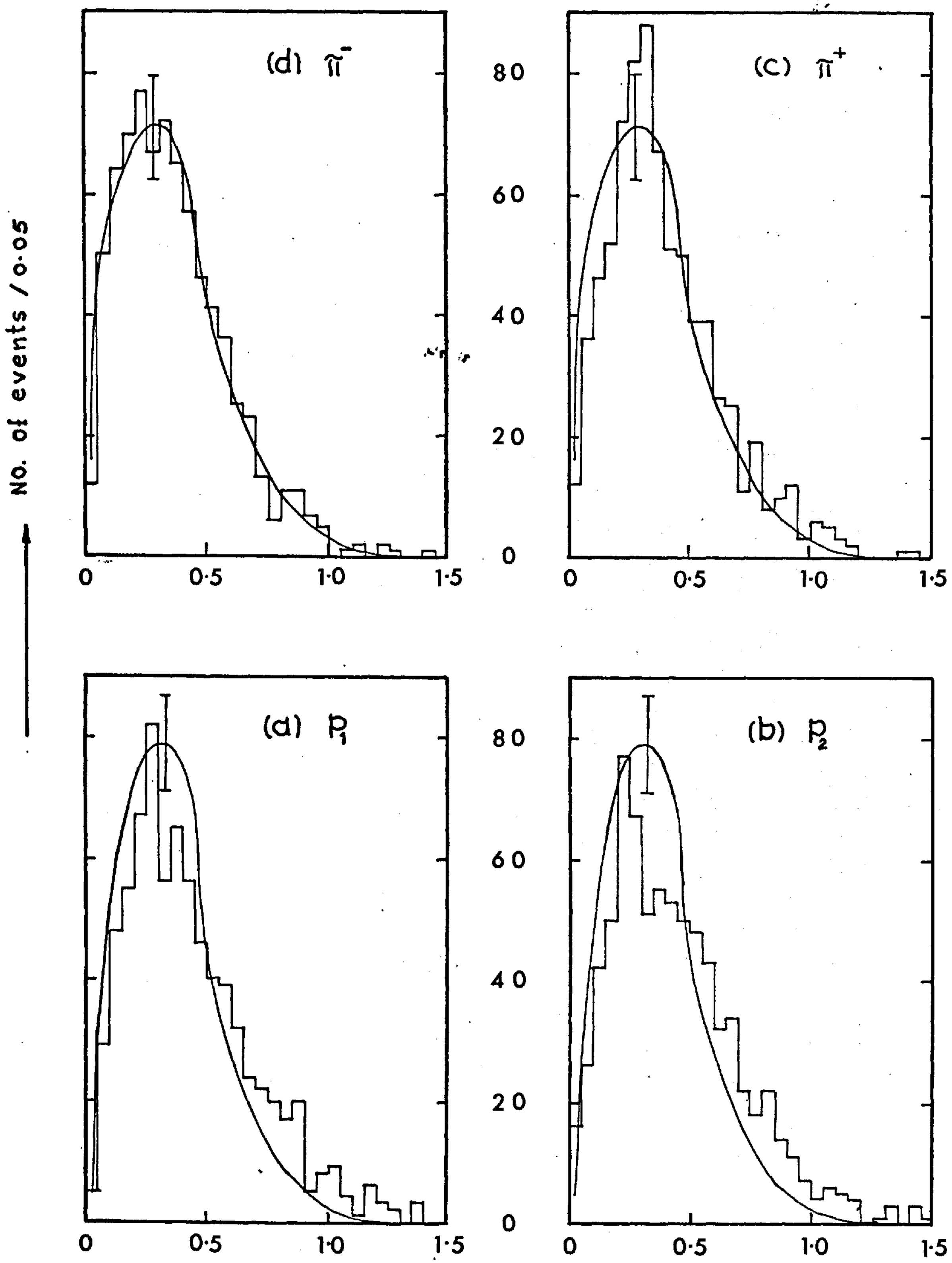

Fig. 7·24 P_t^* GeV/c

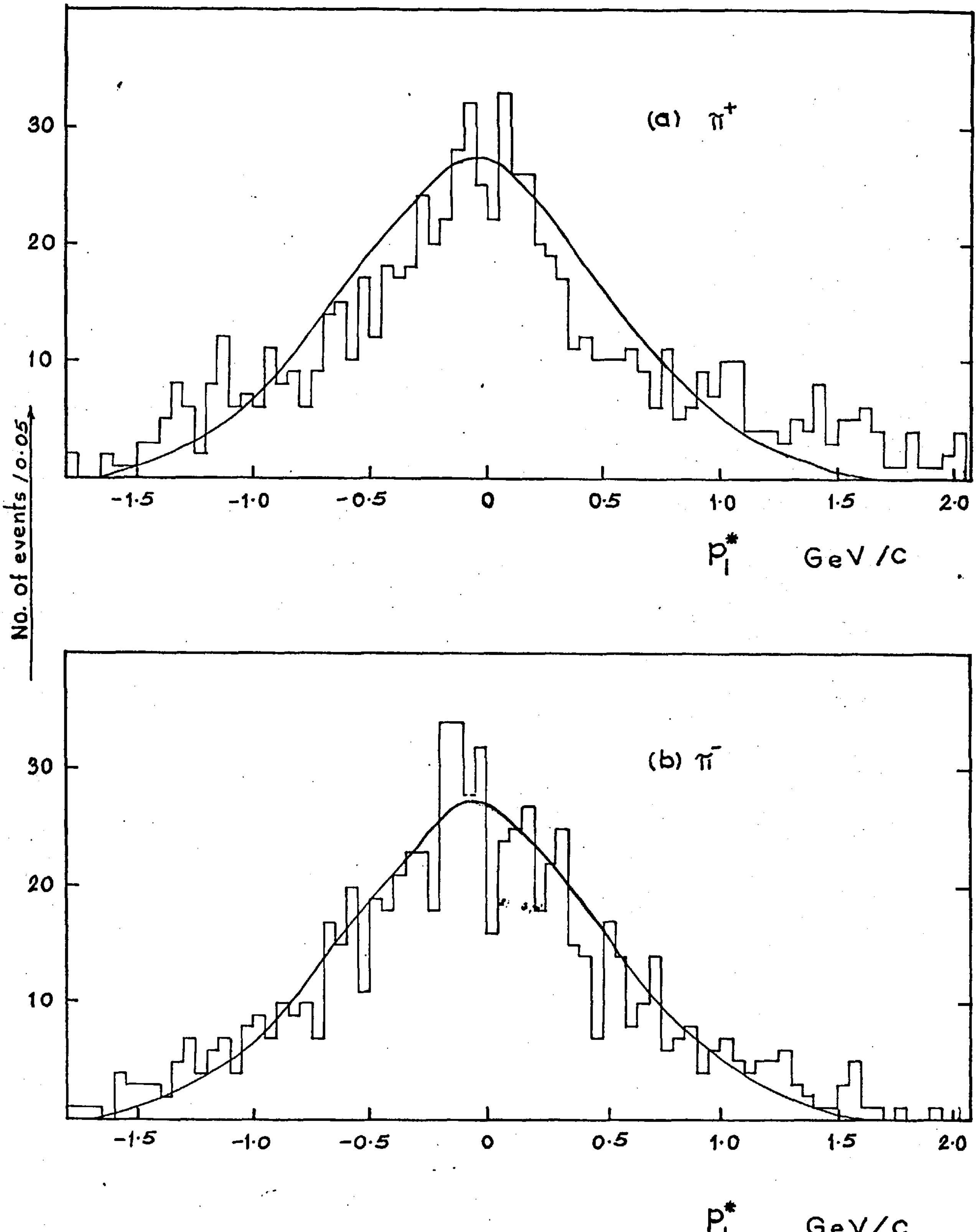
No. of events / 0·05
(a) π+
30
20
10
-1·5
-1·0
-0·5
0
0·5
1·0
1·5
2·0
p_l^* GeV/c
(b) π-
30
20
10
-1·5
-1·0
-0·5
0
0·5
1·0
1·5
2·0
p_l^* GeV/c

Fig. 7·25

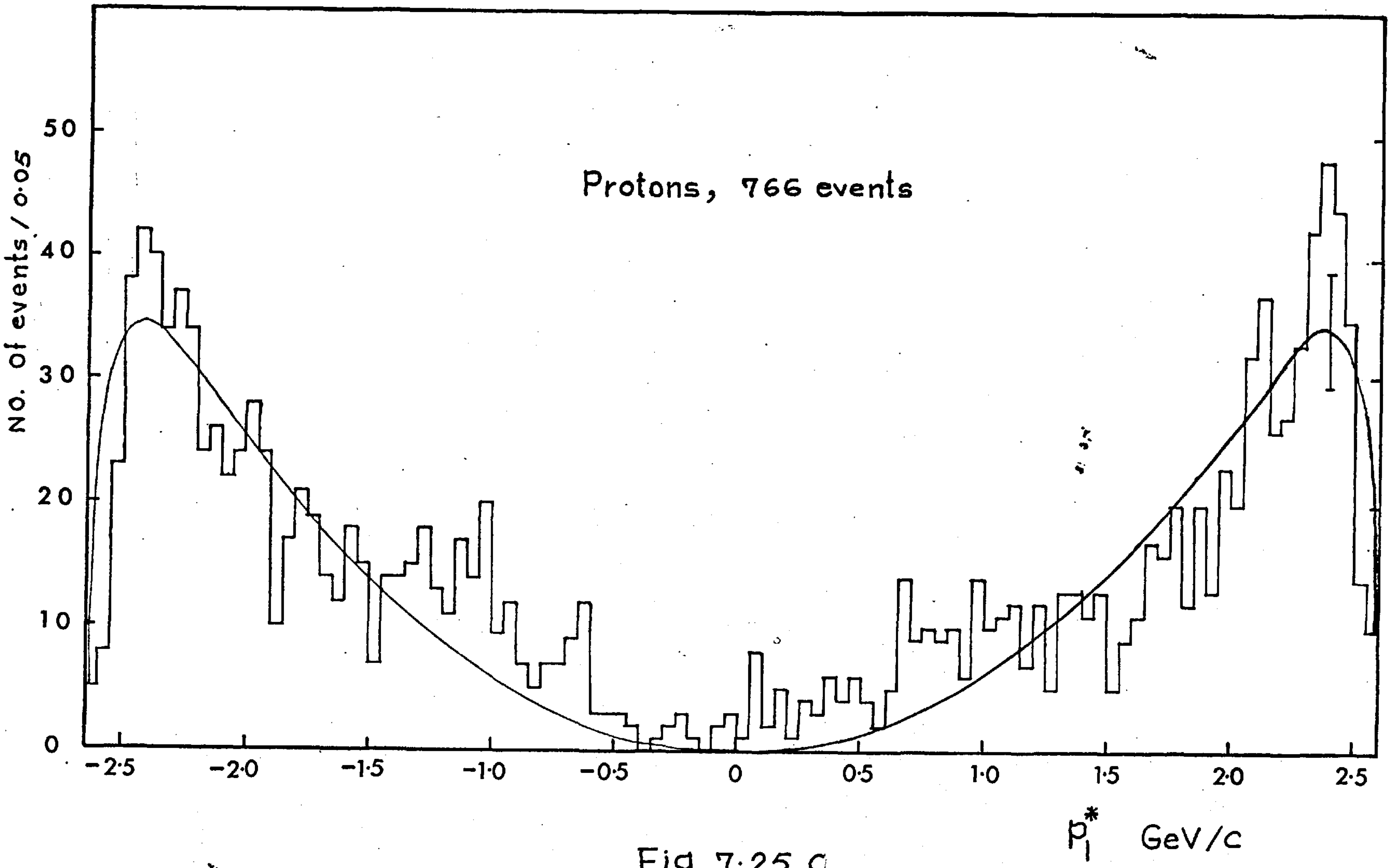
Protons, 766 events
No. of events / 0·05
50
40
30
20
10
0
-2·5
-2·0
-1·5
-1·0
-0·5
0
0·5
1·0
1·5
2·0
2·5
p_l^* GeV/c

Fig. 7·25 a

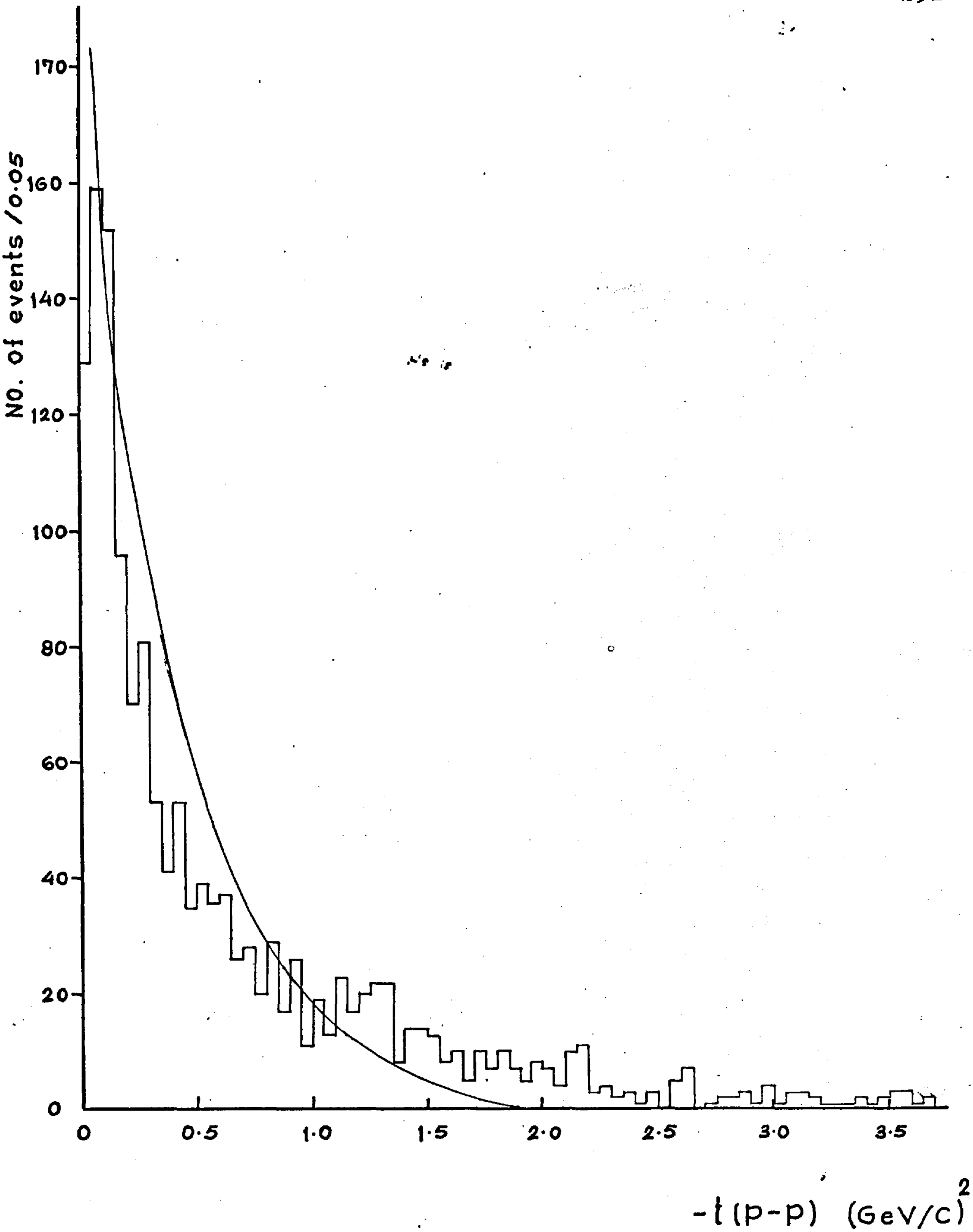

NO. of events /0.05
170
160
140
120
100
80
60
40
20
0
0
0.5
1.0
1.5
2.0
2.5
3.0
3.5
$-t\,(p-p)\ \ (GeV/c)^2$

Fig. 7.26

CHAPTER 8

COMPARISON AND DISCUSSION

Fortunately a comparison can be made between data from both counter and bubble chamber experiments on proton-proton interactions. This comparison can be made for several energies and is particularly useful in the case of resonance production. Some general limitations of high energy experiments are discussed in the following paragraphs with an emphasis on proton-proton interactions.

In section 8.3 a brief comparison is made between the writer's results and those derived from a sample of the Cavendis Laboratory data.

8.1 Resonance Production in Proton-Proton Collisions

We have examined the particular reaction

$$pp \longrightarrow pp\pi^+\pi^-$$

from proton-proton experiments in the energy range 5 - 28 GeV. Five general features of resonance production[38] can be summarized:-

(i) The dominant resonance produced at all energies is $\Delta^{++}(1236)$ and there is no significant evidence for any other $p\pi^+$ resonance.

(ii) For the double Isobar production of the type

$$\begin{array}{l} pp \longrightarrow \Delta^{++} + N^{*} \\ \qquad\qquad\quad \lfloor\!\longrightarrow p\pi^+ \quad \lfloor\!\longrightarrow p\pi^- \end{array}$$

the main $p\pi^-$ resonances are $\Delta^0(1236)$, N*(1470), N*(1520) and N*(1688). This process is strong at low energy but the differential cross section decreases with increasing energy. The same resonances are also produced in the $p\pi^-$ system but with the absence of Δ^{++}.

(iii) No bibaryon resonances are obtained except in one experiment at 4 GeV[85] where an enhancement of 120 MeV width at the effective mass of $M(pp\pi^+)$ near 2.520 GeV is claimed to be $D^{+++}(2520)$, ($y = 2$ and $s = 0$).

(iv) The feature of the $p\pi^+\pi^-$ system is still unclear due to a considerable variability in resonance production with the incident momentum.

a) Low Energy: in this case only N*(1520), N*(1688) are seen. However at 5.5 GeV[86] N*(1680) and N*(1920) have been reported as observed in the $p\pi^-$ system.

b) High Energy: the N*(1520) peak appears to be combined with a peak due to N*(1470). This may be partly due to the kinematic effect of the diffracted pion from another vertex (a broad peak at the low mass end of the $p\pi^+\pi^-$ system has been reported by Gellert <u>et al</u> at 6.6 GeV as Deck Effect[88], and partly associated with N*(1470), the P_{11} resonance which was predicted for the first time by Roper[94] in his πp phase shift analysis.

Some evidence has been reported at 10 GeV[40] to support this idea of P_{11} resonance and its production is consistent with counter experiment results[87]. Also a peak at

1500 MeV splits into two peaks near 1450 and 1520 with $|t| < 0.35$ (GeV)^2.

c) There is evidence to show that the N*(1688) peak shifts to a higher mass with increasing incident momentum (10 GeV). In the present experiment at 16 GeV an enhancement is seen at 1750 MeV which may be associated with this state. An enhancement is also apparent at 2030 MeV (see figure 7.7a).

The extent to which these different resonances are correlated with the $\Delta^{++}\pi^-$ system is a matter of some dispute and it is evident that the pattern of resonance formation is extremely complex.

(v) The f°, ω° resonances of the $\pi^+\pi^-$ system at all energies are produced very weakly or not at all.

Qualitatively there is some difficulty in drawing consistent conclusions from the different experiments. This is probably due to the presence of the two identical protons in the final state; for example, throughout the range 5 - 28 GeV the percentage of events in which Δ^{++} is formed is quoted as being between 50 and 65%. However, at 6 and 8.1 GeV figures of 100% and 82% have been obtained. Furthermore the background situation for $p\pi^-$ and the $p\pi^+\pi^-$ system are uncertain. Sometimes by varying the selection on the basis of t-value, we may reduce the background. At 5.5 and 6 GeV the estimated fraction for three body resonances varies from 52% to 0% and similar discrepancies appear in $p\pi^-$ system; for instance from 5 to 10 GeV the double isobar production is 20% - 30%.

More reliable results have been obtained from counter experiments, using the momentum and scattering angle of the detected proton. The missing mass resolution in the reaction:

$$p + p \longrightarrow p + N^{*} \qquad \ldots\ldots\ldots\ldots \quad (2)$$

varied from $\pm$ 20 MeV at 6 GeV to $\pm$ 60 MeV at 30 GeV.

The cross sections of resonances of isospin $\frac{1}{2}$ and natural parity observed in the energy range 2.85 to 30 GeV[87] are found to be almost constant (see figure 6.1c). All the resonances are consistent with a "diffraction-like" t-dependence of the form

$$\sigma(t) = \sigma(0)\, e^{-bt}$$

We can identify two sub-groups from the observed t-dependence:-

Sub-group (a) $\underline{|t| < 1.0\ (\mathrm{GeV})^2}$ - In this case the slopes of the resonances are about 5 $(\mathrm{GeV})^{-2}$ for N*(1520), N*(1690) and N*(2190).

For Δ^{++} (1236) and N*(1470) the slopes are in the order of 14 - 20 $(\mathrm{GeV})^{-2}$.

Sub-group (b) $\underline{|t| > 1.0\ (\mathrm{GeV})^2}$ - Here the slope, on average, is about 1.5 $(\mathrm{GeV})^{-2}$.

A summary of the resonances observed in the present experiment appears in table 8.1.

TABLE 8.1

OBSERVED RESONANCES

Final Reaction	Cross Section (mb)
$pp\pi^+\pi^-$	1.67 ± 1.0
$\Delta^{++}p\pi^-$	$0.48 \pm 0.02^*$
$\Delta^{++}\Delta^{\circ}(1236)$	0.06 ± 0.01
$\Delta^{++}N^*(1470/1520)$	0.04 ± 0.01
$\Delta^{++}N^*(1688/1750)$	0.20 ± 0.02
$p\ N^*(1470)$	0.29 ± 0.03
$p\ N^*(1750)$	0.05 ± 0.01
$p\ N^*(2030)$	0.09 ± 0.01
$p\pi^+\Delta^{\circ}(1236)$	$0.23 \pm 0.01^{\dagger}$
$p\pi^+N^*(1470/1520)$	$0.20 \pm 0.01^{\dagger}$
$p\pi^+N^*(1680)$	$0.06 \pm 0.01^{\dagger}$
$p\pi^+ N^*(2137)$? with a width of 214 MeV has been fitted later which resulted in an estimated cross section of 0.075 ± 0.025 mb. (in the case of $p_s\pi^-$ only).	

* Peripheral background was used.

† Visual estimation.

8.2 The General Limitations of High Energy Proton-Proton Collisions

There is no completely satisfactory theory for the interaction between protons of high energy. The problem is very complex and has usually been approached by making various simplifying assumptions. There may also be more meaningful parameters among the experimental data than is currently realised. As the experimental data is usually examined in the C.M.S., it is expected that it will then reflect the nature of the interaction with least disguise.

The achievement of a satisfactory kinematic analysis, with good identification of resonances, depends ultimately on the precision with which the angles and momenta of the relevant charged particle tracks are determined. There are certain inherent limitations in bubble chambers resulting, in particular, in limited precision in the determination of the momenta of charged particle from their track curvature. This leads to two fundamental limitations in the analysis.

(1) Event Identification Ambiguity - In general, in a high energy experiment it is not possible to obtain unbiased samples of events from a reaction without a background of incorrectly identified events from other channels. This inevitably produces spurious peaks in invariant mass plots and is confusing for the study of resonance formation. When one is searching for weak resonances in particular, their separation from background becomes a serious problem.

(2) The Limitation in Effective Mass Resolution

The resolution in effective mass which is currently achieved is low compared to the natural width of many known states (see Rosenfeld table) and a large number of measurements will not necessarily give an accurate mass value unless one can check for systematic mass shifts. The experimental resolution limits the precision with which this can be done.

8.2.1 Errors and Their Dependence on Chamber Parameters[49]

The errors in measurement can be discussed under two headings:-

(i) The errors in momentum measurements on charged particles

In the absence of an ionization loss, the trajectory of a charged particle moving in a magentic field (H), corresponding to a given momentum (P) is:-

$$P\cos\lambda = 0.3\,R\,H$$

If the errors in R and λ are uncorrelated, the total error in P is given by

$$(\Delta P/P)^2 = (\Delta R/R)^2 + \tan^2\lambda(\Delta\lambda)^2 + (\Delta H/H)^2$$

This error has two contributions arising from the multiple Coulomb scattering and the measurement precision. Its value depends on the number of points measured and their spacing along the track. Thus :-

$$(\Delta P/P)^2 = (\Delta P/P)^2_{Coul.} + (\Delta P/P)^2_{Meas.}$$

The error formulae given below are derived by Gluckstern[50].

$$(\Delta P/P)^2_{Coul.} = \frac{0.133\,(\ln 4.8P + \ln 145P/mc)}{H^2 L^2 \cos^2\lambda\ \beta^2} + \frac{5.0\times 10^{-2}\, L \tan^2\lambda}{P^2\beta^2} \qquad \text{.......... (8.1)}$$

$$(\Delta P/P)^2_{Meas.} = \frac{3.55\times 10^{-6}\, P^2 \varepsilon^2}{H^2 L^4 \cos^2\lambda} + \frac{0.5\times 10^{-6}\,\varepsilon^2 \sin^2\lambda}{L^2} \qquad \text{.......... (8.2)}$$

where

- λ = dip angle in degree
- L = total track length in cm
- P = momentum in MeV
- H = magnetic field in K gauss
- β = P/E where E = energy in MeV
- ε = the position errors in microns for a single conventional measurement in the chamber projected onto the median plane.

For high energy tracks having small dip angles with respect to the median plane, the second terms in both relations (8.1 and 8.2) can be neglected. This is readily justified since transverse components of momenta are always less than 500 MeV (see distribution in Chapter 4). Thus particles having momenta greater than 3 GeV are usually emitted at small angles.

Inspection of the expression for $(\Delta P/P)_{coul}$ and $(\Delta P/P)_{meas}$ shows that for high momenta and short tracks the measurement error dominates in the total error, this situation being typical for the present experiment, whereas for longer tracks or lower momenta the Coulomb term dominates. Figure 8.1 illustrates the 2-dimensional plot for the ratio of $(\Delta P)_{coul}$ to $(\Delta P)_{meas}$ versus the beam track length (L) for this experiment, assuming that roughly eight equally spaced points were measured on a track and that $= 70\,\mu$ in space (which corresponds to an error of $5\,\mu$ on the film).

(ii) The errors on angle measurements.

The angle errors also have contributions from both Coulomb scattering and position errors. The errors on the azimuthal and dip angles are given by[50] :-

$$\langle\Delta\theta\rangle^2 = \frac{2.8\times10^{-2}\,L}{P^2\,\beta^2\,\mathrm{Cos}\,\Lambda} + \frac{1.44\times10^{-7}\,\varepsilon^2}{L^2\,\mathrm{Cos}\,\Lambda} \quad \ldots\ldots\ldots \ (8.3)$$

$$\langle\Delta\Lambda\rangle^2 = \frac{5.0\times10^{-7}\,\varepsilon^2\,\mathrm{Cos}^2\Lambda}{L} + \frac{5.0\times10^{-2}\,L}{P^2\,\beta^2} \quad \ldots\ldots\ldots \ (8.4)$$

The following remarks are relevant:-

a) measurement errors in azimuthal angles are always smaller than errors in the dip angles.

b) The value of Λ or ϕ is rather insensitive to the variation of length L.

c) angle errors at high energies are always in the region where the measuring error contribution dominates, and are independent of the magnetic field.

d) errors in the angle between two tracks is approximately given by: $\langle\Delta\phi\rangle \approx 5.7\,\varepsilon / L^{3/2}$

where ϕ is the angle between two tracks
L is the length of the track (in cm)
and ε is the error in the position (in mm).

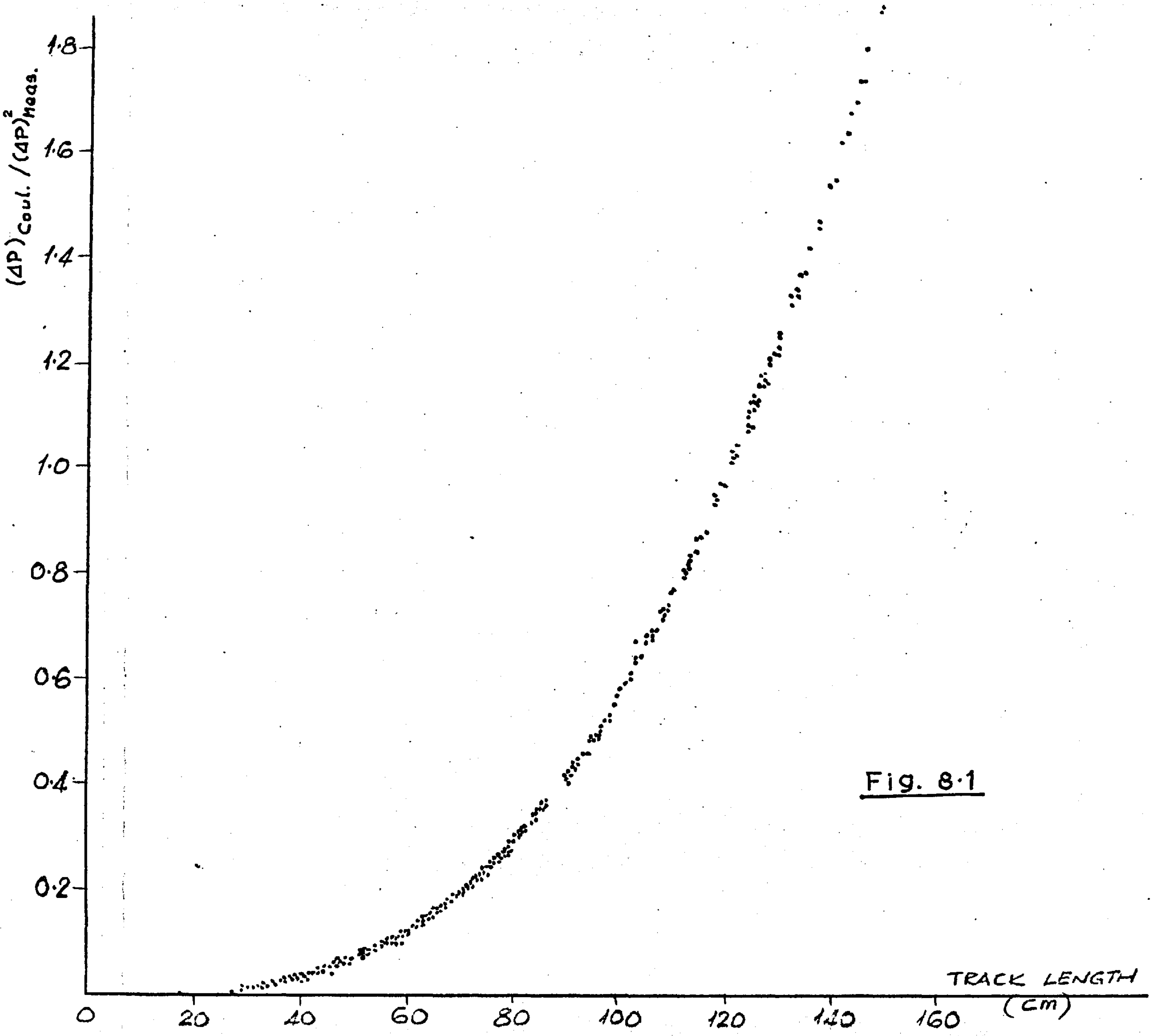

$(\Delta P)_{Coul.} / (\Delta P)^2_{Meas.}$
1·8
1·6
1·4
1·2
1·0
0·8
0·6
0·4
0·2
0
20
40
60
80
100
120
140
160
TRACK LENGTH (cm)

Fig. 8·1

For any given momentum p it is possible to find a track length L for a given ε such that, below p, the Coulomb term dominates, and the error is proportional to $1/H\sqrt{L}$. Above p the measurement error is essentially proportional to $\varepsilon P/HL^{5/2}$ If we define

$$L = 2.8\sqrt{P\varepsilon} \qquad \ldots\ldots\ldots\ldots (8.5)$$

with p in GeV ε in microns and L in cm, then from the momentum measurement point of view, with p = 16 GeV and $\varepsilon \approx 70\,\mu$ for example, we require about a metre of track length for each secondary particle from an interaction.

Hence, one can see that the inaccuracies in the measurement of momentum are the chief limiting factors affecting the conclusions that can be drawn from this experiment. Moreover, the main difficulties in the quantitative analysis of resonance production in this channel are: (i) the ambiguities caused by the presence of two protons in the final state; (ii) the influence of $p\pi^+\pi^-$ resonances on the $p\pi^+$ and $p\pi^-$ spectra and of Δ^{++} on the $p\pi^+\pi^-$ spectrum; and (iii) the overlapping of the different resonances with similar mass in the $p\pi^+\pi^-$ system, in particular between 1.4 - 1.8 GeV. (An example of overlapping of nucleon resonances from ref.95 is reproduced in figure 8.2).

The scatter plots of M ($p\pi^-$) versus ΔM($p\pi^-$) for the two protons in the final state for interactions of the present type experiment of $pp \longrightarrow p_s p_f \pi^+\pi^-$ are shown separately as figures 8.3a and 8.3b. A comparison of these two plots shows clearly the lack of accuracy in measuring the fast track particles. The corresponding estimated mass resolution for the effective mass of the combination is about 10 - 15 MeV for $p_s\pi^-$ and 20 - 40 MeV for $p_f\pi^-$.

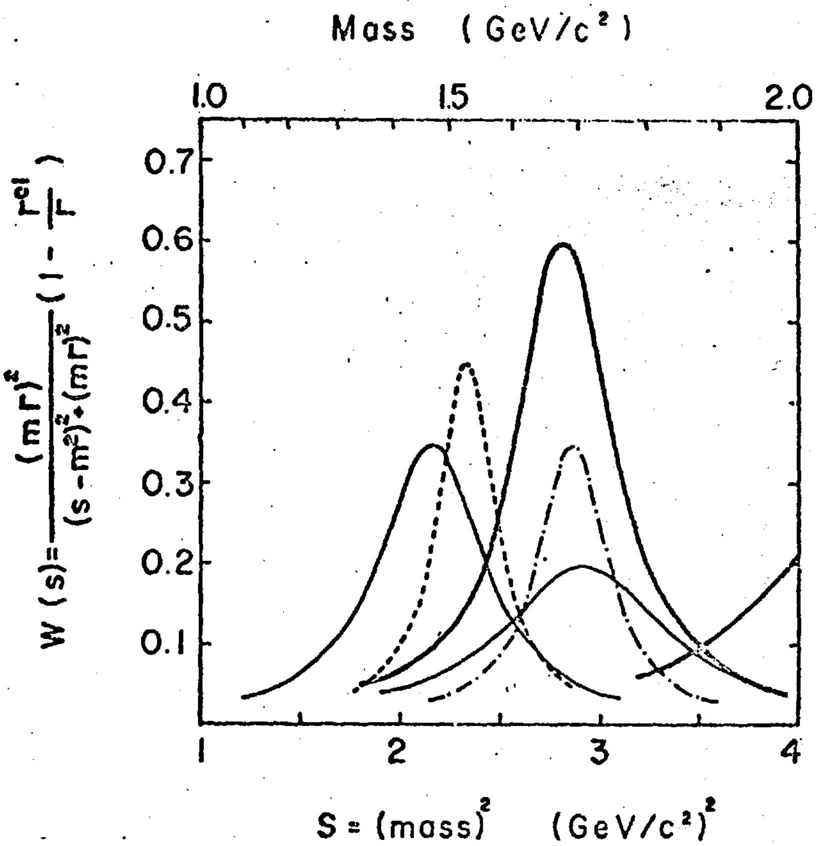

Fig. 8.2 Example of overlapping of nucleon resonances in the mass region 1.4 – 1.8 GeV/c^2 and decay channel $N\pi\pi$. The ordinate is proportional to the fraction of inelastic decays for each state.

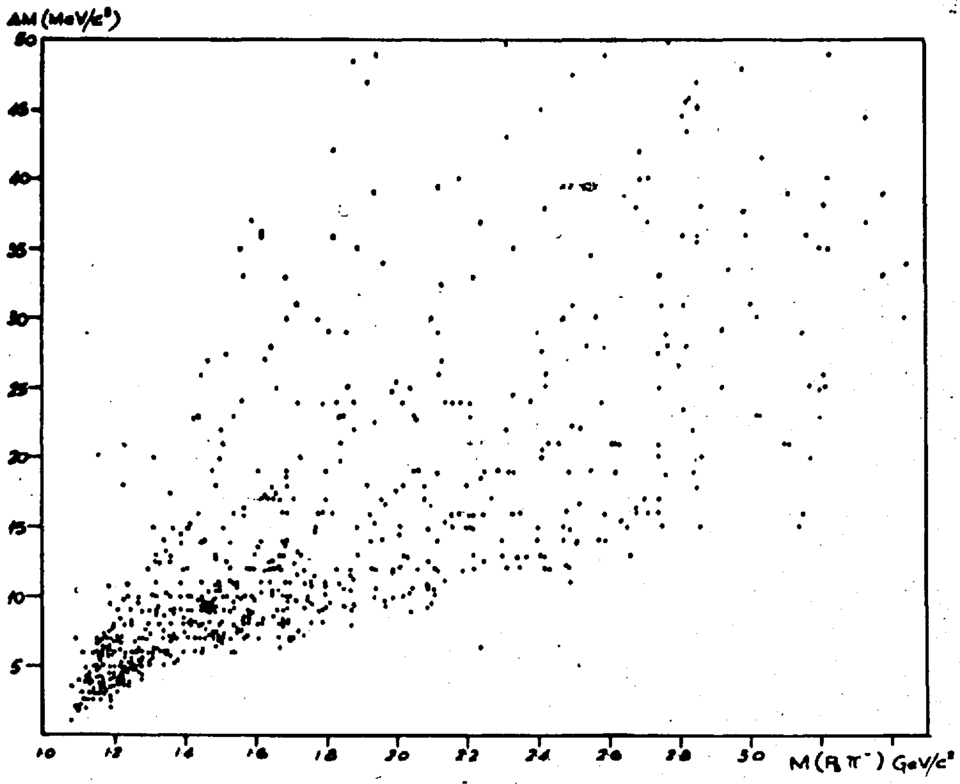

Fig. 8.3a

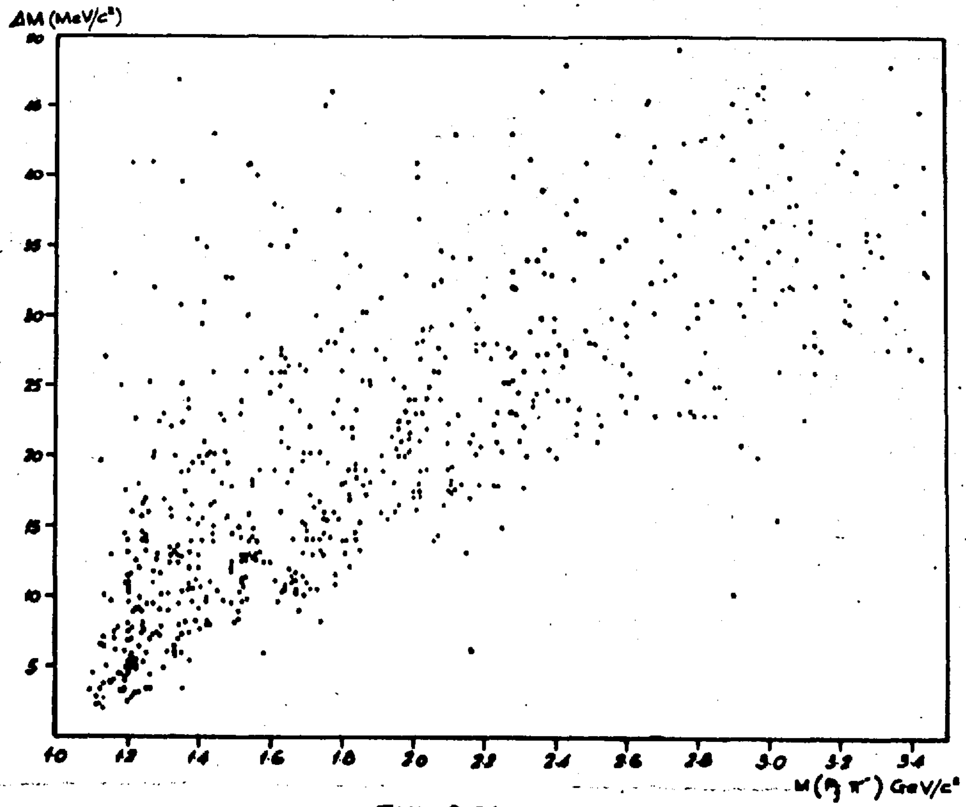

Fig. 8.3b

8.3 <u>Conclusion</u> - The unknown distortion(45) of the CERN 2M HBC during the operating period June 1966 - January 1967 and the low quality of the films are considered to be the chief difficulties in the data analysis described above. Since phase space cannot represent the background of high energy interactions, an arbitrary estimate of the background for any interaction was made on the basis of its peripheral nature. The effect is to make the partial cross-section calculations less certain.

Fortunately for proton-proton collisions, the difficulty of measuring high momentum tracks has been partially compensated by the symmetrical nature of the collision. An internal consistency argument makes possible a comparison of the C.M.S. forward and backward particles. However, because Imperial College and the collaborating group at the Cavendish Laboratory have used quite different analysis programmes, a very careful experimental study was necessary. Most of the results are in good agreement, e.g. :-

Cross-Section	Imperial College (I.C)	Cambridge
$pp \longrightarrow pp\pi^+\pi^-$	1.67 ± 0.10 mb.	$1.66 \pm {}^{0.13}_{0.06}$ mb.

However, the estimates for the partial cross-section are in disagreement especially for the $p\pi^-$ system. In this system a selection at low t-value has improved the sharpness of the resonance peak in the Cambridge analysis, but not so in the

I.C. case. The effect of t-cuts is simply to lower the statistical significance of Imperial College data. If we compare the $p\pi^-$ mass distributions for Imperial College and Cambridge, as shown in figures 8.4a and 8.4b, we find the following distinct differences:-

Imperial College

the M ($P_s\pi^-$) distribution has a clearer shape than that for the M ($P_f\pi^-$) distribution.

Cambridge

both the distributions are more or less the same but not as clear as those derived by I.C. for M ($P_s\pi^-$).

This could possibly be explained as follows:-

The Cambridge Group has simply used the measured beam momentum as the starting value for kinematic fitting. Figure 8.5 shows a plot of their final fitted beam momentum for 4C fit events with mean value at 16.11 GeV and about 600 MeV spread. At Imperial College, on the other hand, the beam momentum is found to be 16.08 GeV by measuring the beam tracks of all events. And from CERN we understand that a spread of $\pm$ 50 MeV on the fixed value to be used in GRIND is reasonable.

For four momentum transfer (t (p-p)), one expects the t-values of two protons to be the same for symmetry. Both Imperial College and Cambridge's data show a small loss of events having very slow protons in the laboratory system. The Imperial College loss is bigger than that of Cambridge and proably due to poor scanning efficiency and/or poor quality of film.

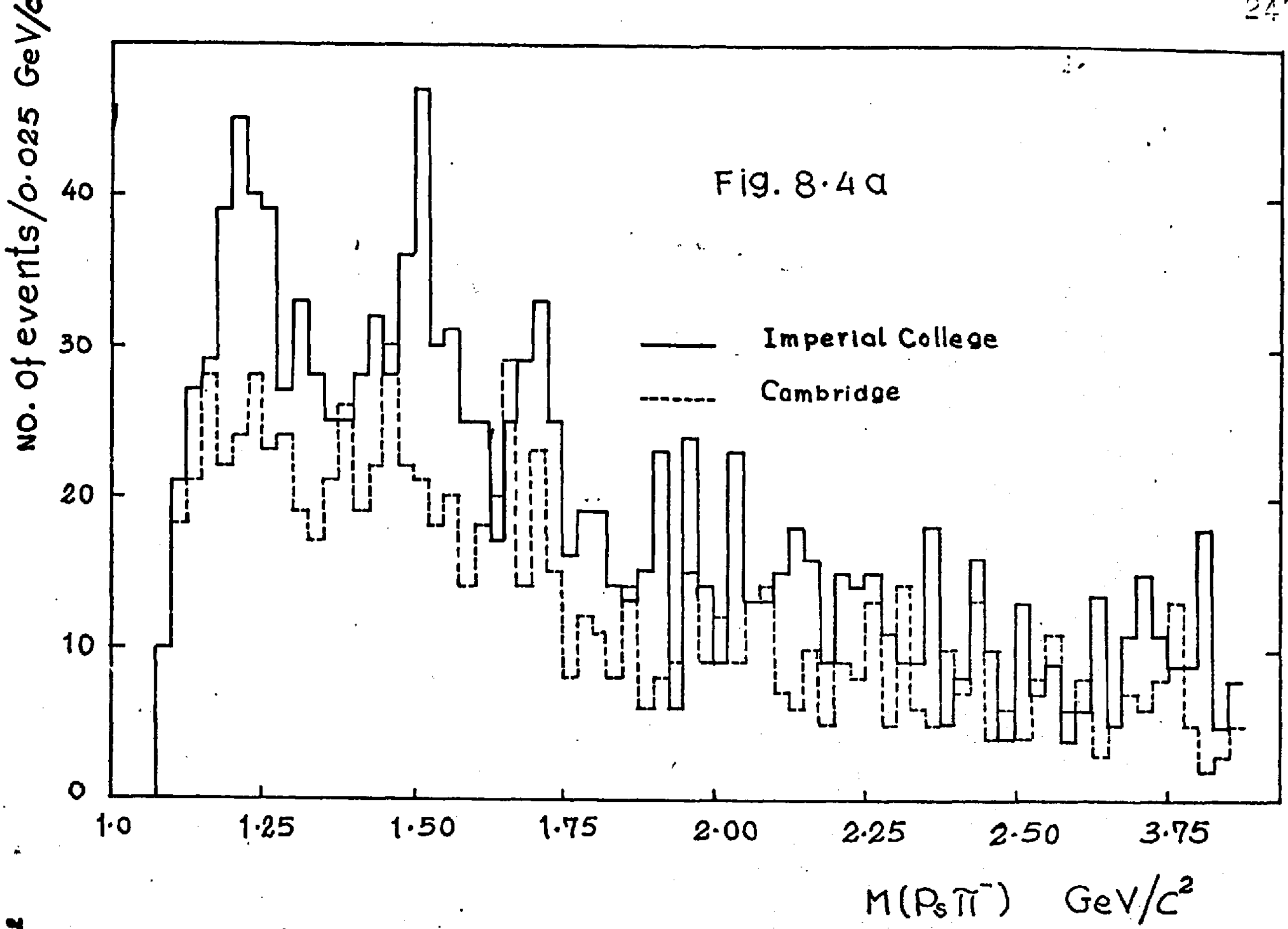

Fig. 8·4a
Imperial College
Cambridge
No. of events/0·025 GeV/c²
0
10
20
30
40
1·0
1·25
1·50
1·75
2·00
2·25
2·50
3·75
M(Psπ⁻) GeV/c²

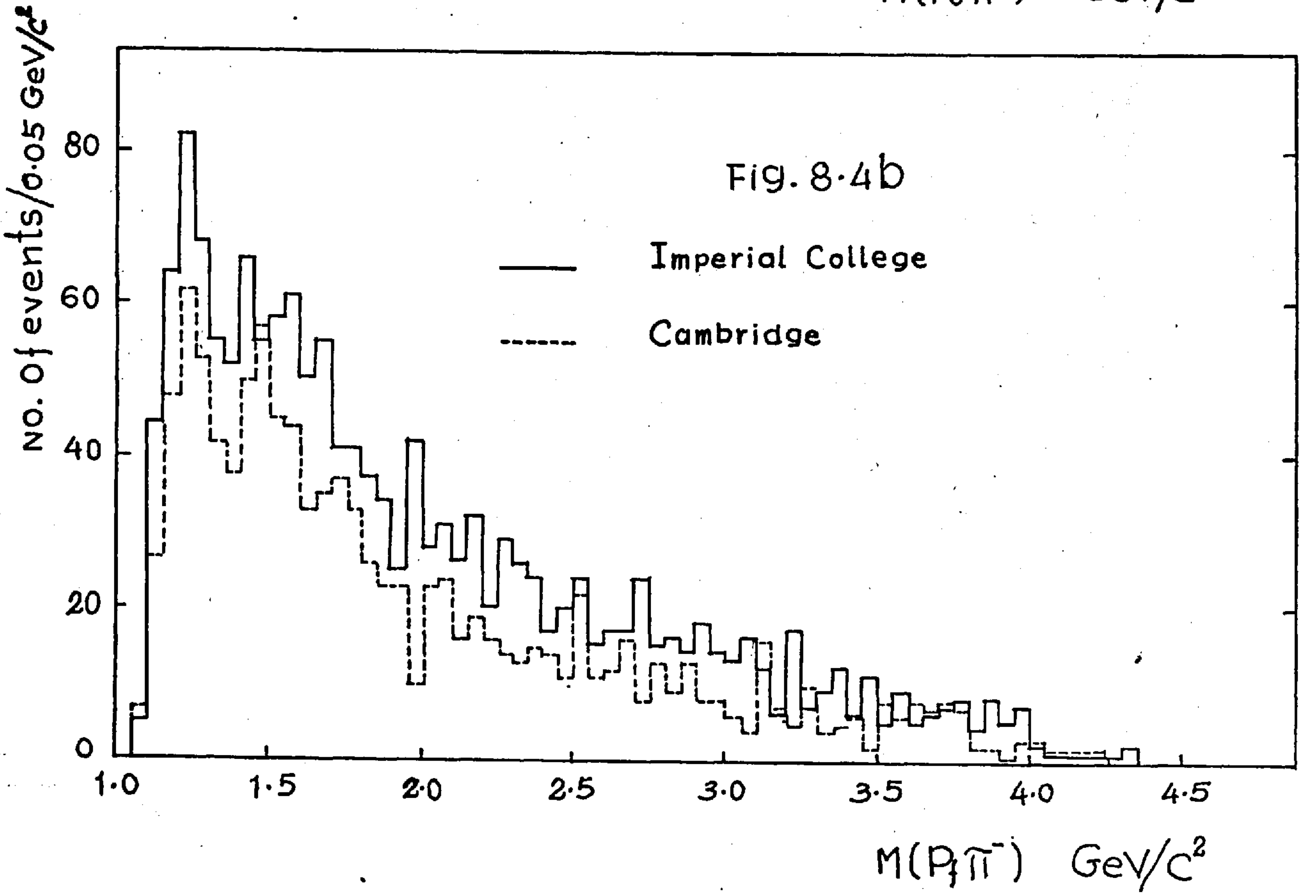

Fig. 8·4b
Imperial College
Cambridge
No. of events/0·05 GeV/c²
0
20
40
60
80
1·0
1·5
2·0
2·5
3·0
3·5
4·0
4·5
M(Pfπ⁻) GeV/c²

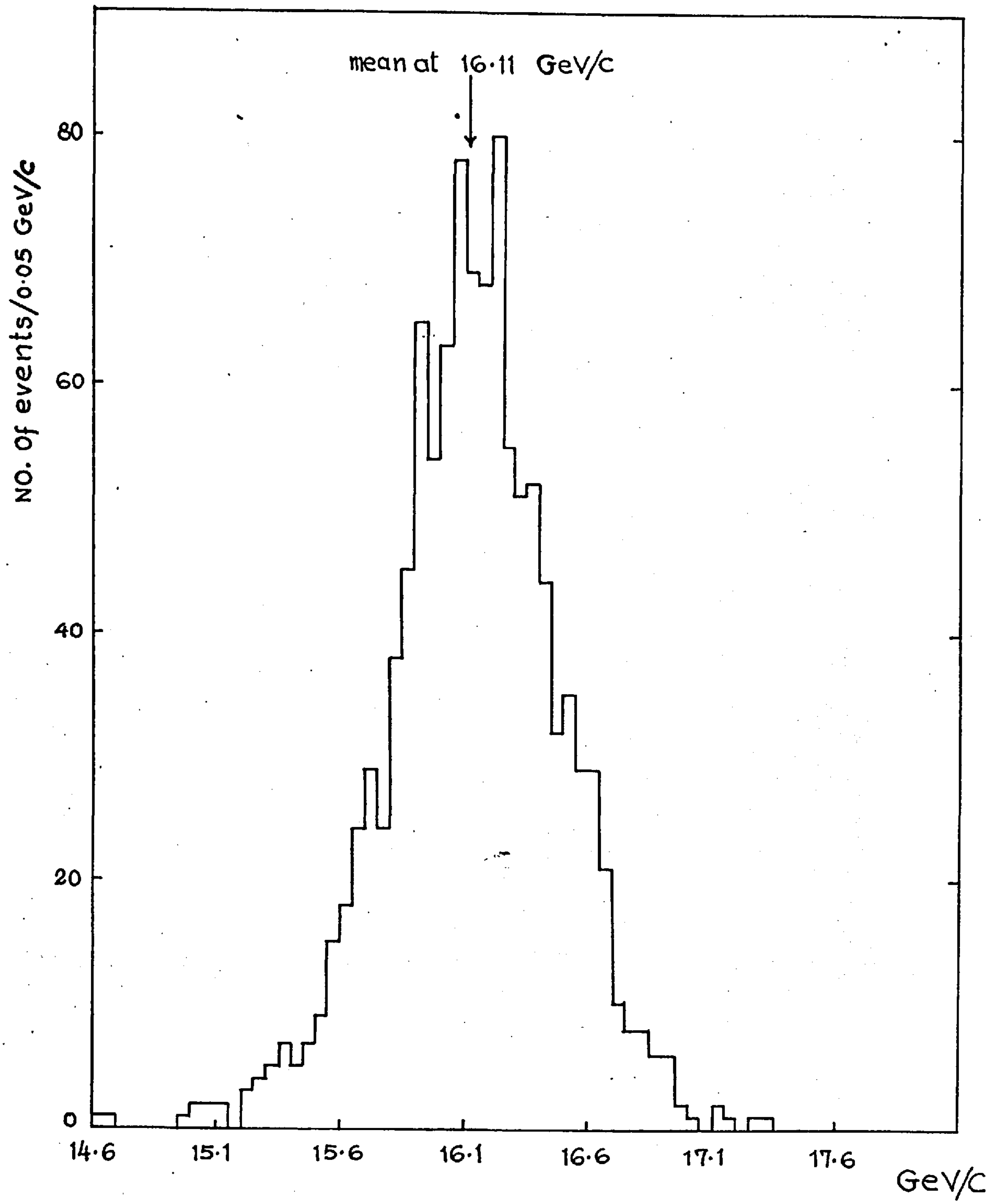

Cambridge: Final fitted beam momentum for 4c fit with ≈ 600 MeV spread

Fig. 8·5

Certain features of the interactions stand out clearly. For instances, the C.M.S. momentum and angular distribution argue strongly for the peripheral nature of the interaction. The consistency of the mean value and the distribution of the transverse momentum of the secondary particles is another interesting feature of the interaction.

It would be interesting to repeat the experiment with more statistics and better precision, and quantitative comparison with the multi-peripheral models[89-93] for inelastic reactions could be attempted as well as a study of the spin and parity of resonances.

An analysis of the four particles final state with one neutral particle missing (1-constraint fit) is under way at Tel-Aviv University[96], and will include some of the 7000 measured events which failed to give a 4-constraint fit at Imperial College. A study of strange particle production from the same experiment is in progress at Cambridge[97].

APPENDIX I

1. The procedure for rough predigitzation (D-MAC) is:-

   (i) set the whole frame of view 1 on the scanning table.

   (ii) set the information on the D-MAC keyboard corresponding to the frame, event number, etc., together with some comment information and then punch onto paper tape.

   (iii) measure the apex first as a common point.

   (iv) measure another two approximately equal space points on each track.

   (v) press "END EVENT" for separation purposes.

2. Measuring three approximately equal space points on each track, one can determin the radius of curvature (R) from:-

$$(X_i - X_o)^2 - (Y_i - Y_o)^2 = R^2$$

where X_o, Y_o represent the centre coordinate of the circle formed. X_i and Y_i (i = 1, 2, 3) are the coordinates of each measured point along the track. Three simultaneous equations give more than enough data to determine the two unknown variables X_o, Y_o. A conversion parameter of value 0.000066 GeV/c was derived after a large number of beam tracks (known as 16 GeV) has been measured.

3. Two exceptional cases were recognised at this stage and were not predigitzed. First, an event followed by one of more difficult long tracks. Secondly, those events with one or more straight short tracks (about 4 - 5 cms on the scanning table). These two types could be accepted for measurement on the conventional measuring machines having higher magnification; in the latter case the tracks are too difficult to measure as a segment of circle. If a very slow proton is produced with very short visible length and it stops in the chamber, then three arbitrary points formed a small circle were predigitized.

The relevant measurement information from the D-MAC was punched on conventional 5-hole paper tape. Thus the coordinate pairs were converted and computed by the IBM 7090 which produced a full listing of all the scanned events, each accompanied by its own characteristics.

APPENDIX II

Length Dependent Distortion Calculation

Suppose the distortion in the bubble chamber is such as to give a curvature of the XZ plane at the centre of the chamber of the form $z' = ax^2 + bx^3$

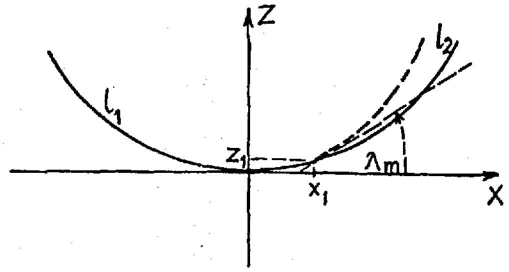

Let a track of length l start at (X_1, Z_1) and have a true projected angle of dip Λ_t. The true equation of its projection on the XZ plane is:-

$$Z_t = \Lambda_t (x - x_1)$$

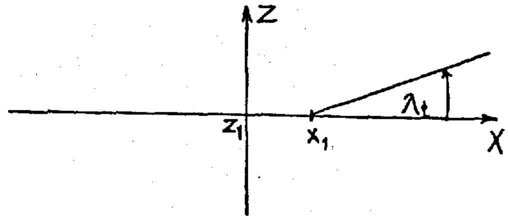

but because of the distortion, the measured projection will be

$$Z_m = z_t + z' = \Lambda_t (x - x_1) + ax^2 + bx^3$$

$$\text{at} \quad x = x_1, \; Z_m = Z_{m1} = ax_1^2 + bx_1^3$$

$$x = x_1 + l, \; Z_m = Z_{m2} = \Lambda_t l + a(x_1 + l)^2 + b(x_1 + l)^3$$

$\therefore$ The dip of the chord is:-

$$\Lambda_m = \frac{Z_{m2} - Z_{m1}}{l}$$

$$= \Lambda_t + \frac{a}{l}(2lx_1 + l^2) + \frac{b}{l}(3lx_1^2 + 3l^2x_1 + l^3)$$

$$= (\Lambda_t + al + bl^2) + (2a + 3bl)x_1 + 3bx_1^2$$

Thus if we have a track of (projected) length l_1 finishing at x_1

and another of length l_2 starting at x_1

$$\lambda_{1m} = \lambda_{1t} - al_1 + bl_1^2 + (2a - 3bl_1)x_1 + 3bx_1^2 \quad \ldots\ldots\ldots (1)$$

$$\lambda_{2m} = \lambda_{2t} + al_2 + bl_2^2 + (2a + 3bl_2)x_1 + 3bx_1^2 \quad \ldots\ldots\ldots (2)$$

$$\therefore \lambda_{2m} - \lambda_{1m} = \lambda_{2t} - \lambda_{1t} + a(l_2 + l_1) + b(l_2^2 - l_1^2) + 3b(l_2 + l_1)x_1$$

For beam track events we assumed that

$$l_1 + l_2 = L = \text{constant}, \qquad l_1 = \frac{L}{2} + x_1$$

$$\lambda_{1t} = \lambda_{2t}$$

and $\quad \lambda_{2m} - \lambda_{1m} = \epsilon_0 + \gamma l_1$

then $\quad \epsilon_0 + \gamma l_1 = aL + bL(L - 2l_1) + 3bL(l_1 - \frac{L}{2})$

$$= (aL - \tfrac{1}{2}bL^2) + bLl_1$$

$$\therefore \quad \epsilon_0 = aL - \tfrac{1}{2}bL^2, \qquad \gamma = bL$$

or $\quad b = \gamma/L \quad$ and $\quad a = \dfrac{\epsilon_0}{L} + \dfrac{\gamma}{2}$

substituting a and b into (1) and (2) it follows that

$$\lambda_{2m} - \lambda_{1m} = \epsilon_0 + \gamma l_1$$

ACKNOWLEDGEMENTS

The author would like to thank Professor C.C.Butler for the opportunity of working in the High Energy Nuclear Physics Group at Imperial College of Science and Technology. The writer wishes to express her deep gratitude to Mr N.C. Barford for his supervision of the work and to Dr S.J.Goldsack for his useful guidance and encouragement.

The assistance of all the members of the collaboration is acknowledged. The author is also thankful to Dr Y. Oren for assistance in writting the Proton-Proton experiment dependent post kinematical analysis programmes, and to Dr M. Mermikides for suggesting the Regge Multi-peripheral calculations presented in this thesis.

The author is greatly indebted to all her H.E.N.P. colleagues; especially M.Losty for all his co-operation and helpful discussions, and Miss M. Urquhart for her efficient book-keeping.

The painstaking work of all the scanners, measurers and technical staff has been greatly appreciated.

Sincere appreciation is extended to Mrs E.Speer for her excellent typing of this work and to Dr R.J. Speer for his valuable criticism, discussion and for reading the draft of this thesis.

Finally, the author is extremely grateful to her parents and her fiancé for their constant support and encouragement.

A generous grant on the Columbo Plan has been greatly appreciated and enabled the writer to study between October 1967 and February 1970.

REFERENCES

1. Regenstreiff, CERN 59-29 Report "The CERN Proton Synchrotron".

2. J.P. Blewett, Report of Progress Physics, p.37, 1956.

3. E.D. Courant & H.S. Snyder, Annual of Physics, 3, 1, 1958.

4. J.J. Livingood, Cyclic Particle Accelerator (Van Nostrand, 1961).

M.S.Livingston & J.P.Blewett, Particle Accelerator (McGraw Hill, 1962).

5. D.A. Glaser, Reprint from "Scientific America", Feb., 1955.

6. D.B.Vernon, et al, "Scientific America", December 1967, p.77.

7. A.H.Rosenfeld & W.E.Humphrey, Annual Review of Nuclear Sicence, 13, 103, 1963.

C.M. Fisher, Lecture notes for the 1968 Hercig Novi School of Elementary Particle Physics.

8. W.T. Welford, Applied Optics, 2, 981, 1963.

9. W.T. Welford, Applied Optics, 2, 1037, 1963.

10. F. Frungel, et al, Applied Optics, 2, 1017, 1963.

11. W.T. Welford, Bubble and Spark Chamber, 1, 233, 1967.

12. E. Keil & W.W.Neale, Proc. of Int. Conf., Dubna, 798, 1963.

13. W.W. Neale, Prog. in Nuc. Tech. and Instr., 2, 1965.

14. W.W. Neale, Prog. in Nuc. Tech. and Instr., 2, 1967.

15. E. Keil & W.W. Neale, CERN/TC/02, 63-3, 1963.

16. K.G. Seffen, Beam Optics; CERN School of Physics, 1967.

17. B. de Raad, et al, CERN 66-21, 43, 1966.

18. U3 Beam Line CERN/TC/BEAM 66-7, 1966.

19. H. Lengeter, CERN/TC/BEAM 65-4, 1965.

20. Achen-Berlin CERN Call. submitted to Phys. Letters.

21. N.C. Barford, et al, Int. Conf. on H.E. Acc. Instr. CERN, 1959.

22. H.P. Reinhard, CERN/TC/200 66-1, 1966
CERN/TC/200 65-11, 1965.

23. H.P. Reinhard, CERN/TC/200 66-11, 1966.

24. F. Wittgenstein, CERN/TC/200 65-5, 1965.

25. M. Schmitt, CERN/TCC/ 67-48, 1967.

26. G. Kellner, Private Communication.

27. Bertha, The British National Measuring Machine at I.C.

28. W.T. Welford, Applied Optics, 2, 1037, 1963.

29. C. Peyrou & H. Bridge, Proc. of the Int. Conf. on H.E. Acc. and Instr., CERN, 454, 1959.

30. F. Fuch, M.Sc. Thesis, Imperical College, 1967.

31. "Test Strip": In order to study the general quantities of the film, of the designed experiment, during the run. As soon as one roll of photographic film was finished, a sample of about 10 - 20 frames in each view is immediately developed and investigated visually at CERN.

32. "Proper Scan": The procedure consists of three scans; the first and second scans are made independently by scanners on the same amount of film. The scanning cards (records) from the two scans are compared and checked with the event on a scanning table by physicists. The existing events are recorded and transferred to be measured.

33. "NIRNS Programmes": The series of post kinematical analysis programmes written by J.M.Scarr (Rutherford Library programmes).

34. "POOR MAN SUMX": The experiment dependent post kinematical analysis programme was written by Dr Y. Oren* for 16 GeV proton-proton collisions at Imperial College.

35. W. Chinowsky, et al, Phys. Rev. Letter, 9, 330, 1962.
G. Goldhaver, et al, Phys. Letters, 6, 62, 1962.

36. D.R.O. Morrison, CERN/TC/Physics, 65-7, 1965.

37. V. Barger, & M. Olsson, Phys. Rev. Letters, 15, 930, 1965.
H.L. Anderson, et al, Phys. Rev. Letters, 18, 89, 1967.
W. Galbraith, et al, Phys. Review, 138B, 913, 1965.
V. Barger & M. Olsson, Phys. Review, 148, 1428, 1966.

38. F. Turkot, Proc. of the Topical Conf. on the Collision of Hadron, vol.I.
E. Ferrari, & F. Selleri, CERN 68-7, 1967
Nuovo Cimento 30, 240, 1963.

39. J.R. Williams, Private Communication.

40. S.P. Almieda, et al, Phys. Letters, 14, 240, 1965.
DESY 68/17, 1968.

* Dr Y. Oren is now at Tel-Aviv University.

41. V. Henry, Lecture notes for the 1968 Hercig Novi School of Elementary Particle Physics.

42. J. Jackson, et al, Nuovo Cimento, 34, 1644, 1964.

43. CERN Library programme: THRESH-GRIND Manual.

44. G.R. Moorhead, CERN 60-11, 1960
CERN 60-33, 1960.

R. Böck, CERN 61-29, 1961
CERN 61-30, 1961.

45. D. Drijard, Private Communication.

46. B. Ronne, CERN 64-13, p.87, 1964.

47. D. Hudson, CERN 63-29, 1963.

48. Report on the Design Study of Large H.B.C. for the CERN Proton-Synchrotron: TC/BEBC 66-73, October, 1966.

49. Int. Colloquium on B.B.C. held at Heidelberg, April, 1967; CERN 67-26, vol.I.

50. R.L.Gluckstern, Nuc. Instr. and Meth., 24, 381, 1963.

51. H. Bøggild, Private Communication.
(Copenhagen-Helsinki-Oslo-Stockholm Collaboration).

52. N.C. Barford, Experimental Measurement Precision Error and Truth. Addison-Wesley Publishing Co., 1967.

53. R. Böck, Lecture notes for the 1968 Hercig Novi School of Elementary Particle Physics.

54. M. Firebaugh, et al, Phys. Review, 172, 1354, 1967.

55. M. Szeptycka, Ph.D. Thesis, Warsaw University. 1963.

56. O. Ninakawa, Supp. Nuovo Cimento, 11, 125, 1959.

K. Pinkau, Phil. Magazine, 6, 657, 1961.

R.R. Danniel, Nuovo Cimento, 16, 1, 1960.

57. T.T. Wu & C.N. Yang, Phys. Review, 137B, 708, 1965.

K. Huang, Phys. Review, 156, 1555, 1967.

A.D. Krisch, et al Phys. Review Letters, 18, 1218, 1967.

E.F. Friedlander, et al, Nuovo Cimento, 41A, 417, 1966.

D.R.O. Morrison, CERN/TC/ 63-1, 1963
CERN/TC/ 61-22, 1961.

58. G. Cocconi, et al, Report UCID-1444, Lawrence Radiation Laboratory, California.

J. Orear, Phys. Letters, 13, 190, 1964.

59. A. Bigi, et al, Nuovo Cimento, 33, 1249, 1964.

H.H. Aly, et al, Nuovo Cimento, 32, 905, 1964.

60. F. James, A Monte-Carlo Phase Space, Programme FOWl.
CERN 68-15, 1968.

61. H.M. Chan, CERN 67-16, 1967

62. G.F. Chew & F.E. Low, Phys. Review, 113, 1640, 1962.

63. R.J.Eden, High Energy Collision. Cambridge Univ.Press,196

64. J.D. Jackson & H. Pilhuhn, Nuovo Cimento 33, 906, 1964.
Nuovo Cimento 34, 1841, 1964.

N. Schmitz, CERN 65-24, vol.I.

65. E. Ferrari & F. Selleri, Supp. Nuovo Cimento 24, 453, 1962.
Nuovo Cimento 21, 1028, 1961.

65. H.P. Durr & H. Pilkuhn, Nuovo Cimento, 40A, 899, 1965.

G. Wolf, Phys. Review Letters, 19, 925, 1967.

S.D. Drell, Phys. Review Letters, 5, 278, 1960.
Phys. Review Letters, 5, 342, 1960.

66. Z. Salewski, Lecture notes for the 1968 Hercig Novi School of Elementary Particle Physics.

H. Pilkuhn, CERN 67-24, vol. II.

67. K. Gottfried & J.D. Jackson, Rev. Mod. Ph., 37, 484, 1965.
Nuovo Cimento, 34, 735, 1964.

J.D. Jackson, et al, Phys. Review, 139B, 428, 1965.

68. M.L. Good & W.D. Walker, Phys. Review, 120, 1857, 1960.

S.D. Drell & K. Hiida, Phys. Review Letters, 7, 199, 1961.

69. B.E.Y. Svensson, Proceedings of the 1967 CERN School of Physcis; CERN 67-24, vol.II, December 1967.

70. Chan-Hong-Mo, et al, Nuovo Cimento, 49A, 3077, 1967.

E.L. Berger, et al, Phys. Review Letters, 20, 964, 1968.
Phys. Review, 166, 1525, 1968.
Phys. Review, 163, 1572, 1967.

71. R.T. Deck, Phys. Review Letters, 13, 169, 1964.

M.H. Ross & Y.Y. Yam, Phys. Review Letters, 19, 546, 1967.

V.Maor & T.A. O'Halloran, Phys. Letters, 15, 281, 1965.

72. Chan Hong-Mo, et al, CERN 66/845/5-TH, 679, 1966.
CERN 66/1060/5-TH, 719, 1966.
CERN 67/533/5-TH, 764, 1967.
CERN 67/1542/5-TH, 688, 1967.
Nuovo Cimento, 57A, 93, 1968.

73. N. Byers & C. Yang, Phys. Review, 142, 976, 1966.
A. Bialas, Phys. Letters, 19, 604, 1965.

74. K. Gottfried & J. Jackson, Nuovo Cimento, 33, 309, 1964.
A. Daudin, et al, Ann. Phys. 26, 322, 1964.
D.F. Jackson & B.K. Jain, Phys. Letters 27B, 174, 1968.
A. Daudin, et al, Phys. Letters, 7, 125, 1963.

75. F. Fermi, Prog. Theo. Phy. 5, 570, 1950.
Phys. Review, 92, 452, 1953.

76. O. Skjeggestad, CERN 64-13, vol. II, page 1-73.

77. S.J. Lindenbaum & R.M. Sternhumer, Phys. Review, 105, 1874, 1953.

78. L.M. Beer, et al, Phys. Review Letters, 20, 340, 1964.
P. Bareyre, et al, Phys. Letters, 18, 342, 1965.

79. D.R.O. Morrison, CERN/TC/PHYSICS, 66-20, 1966.

80. G. Ranft, Private Communication.

81. R.B. Bell, et al, Phys. Review Letters, 20, 79, 1968.
J. Wolfson, et al, Bull. Am. Phy. Soc., 13, 704, 1968.

82. C. Lovelace, Int. Conf., Heidelberg, 1967.

83. "MALIK": CERN Fitting Programme.

84. "MINUIT": CERN Fitting Programme.

85. J. Kidd, et al, Phys. Letters, 16, 75, 1965.

86. R. Ehrlich, et al, Phys. Review Letters, 21, 1839, 1968.
Bull. Am. Physic. Soc. 13, 682, 1968.
R.A. Jesperson, Phys. Review Letters, 21, 1368, 1968.

86. G. Alexandra, Nuovo Cimento, 40A, 839, 1965.

G. Kayas, et al; Scandinavian Collaboration. pp at 19 GeV/c. Contribution to the Heidelberg Conf. September 1967.

87. E.W. Anderson, et al, Phys. Review Letters, 16, 855, 1966.

I.M. Blair, et al, Phys. Review Letters, 17, 789, 1966.

88. E. Gellert, Phys. Review Letters, 17, 884, 1966.

89. S. Frautschi, Nuovo Cimento, 28, 409, 1963.

90. M.S.K. Razmi, Nuovo Cimento, 31, 615, 1964. Nuc. Phy. 68, 591, 1965.

91. Chan-Hong-Mo, et al, CERN Report TH 719, 1966.

92. G. Zweig, et al, Phys. Review, 160, 1322, 1967.

93. N. Bali, et al, Phys. Review Letters, 19, 614, 1967.

94. L.D. Roper, et al, Phys. Review Letters, 12, 340, 1964.

R.H. Dalitz, et al, Phys. Letters, 14, 159, 1965.

95. S. Nelssion, Lecture notes for the 1968 Hercig Novi School of Elementary Particle Physics.

96. Dr Y. Oren, Private Communication. Tel-Aviv University.

97. R. Walgate, Private Communication. Cambridge.